FABRICATION AND ANALYSIS OF MAGNETIC NANOSTRUCTURES FOR SENSOR APPLICATIONS

Thesis submitted to

University of Calicut
in partial fulfillment of the requirements
for the award of the degree of
Doctor of Philosophy in Physics

By
NIMISHA O K
Under the guidance of
Dr. Reena Mary AP

Department of Physics
Government Victoria College, Palakkad
August 2024

Ph.D. Thesis
Entitled

FABRICATION AND ANALYSIS OF MAGNETIC NANOSTRUCTURES FOR SENSOR APPLICATIONS

Author

NIMISHA O K

Department of Physics

Govt. Victoria College, Palakkad

(Affiliated to the University of Calicut)

Kerala, India-678001

E-mail: nimmykrishnangvc@gmail.com

Guide

Dr. REENA MARY A P

Professor

Department of Physics

Govt. Victoria College, Palakkad

E-mail: reenamaryap@gmail.com

Co-guide

Dr. PRADEESH K

Assistant Professor

Department of Physics

Govt. Victoria College, Palakkad

Email: pradeeshk@gvc.ac.in

DEPARTMENT OF PHYSICS
GOVERNMENT VICTORIA COLLEGE, PALAKKAD
Kerala, India, PIN 678001
Affiliated to the University of Calicut
NAAC Accreditation - A Grade
NIRF Rank- 84
Email: physics@gvc.ac.in | Web: www.gvc.ac.in/physics

CERTIFICATE

Certified that the thesis entitled **"FABRICATION AND ANALYSIS OF MAGNETIC NANOSTRUCTURES FOR SENSOR APPLICATIONS"** submitted by **Mrs. NIMISHA O K** in partial fulfillment of the requirements for the award of the degree of Doctor of Philosophy under the faculty of science, Department of Physics, Govt. Victoria College, Palakkad under the University of Calicut and the work embodied in the thesis has not been included in any other thesis submitted previously for the award of any other degree.

Palakkad
13/06/2025
~~24/08/2024~~

Date ....

13/06/25.
Principal
and Head of the Research Centre
Govt. Victoria College, Palakkad

PRINCIPAL
GOVT. VICTORIA COLLEGE
PALAKKAD

DEPARTMENT OF PHYSICS
GOVERNMENT VICTORIA COLLEGE, PALAKKAD
Kerala, India, PIN 678001
Affiliated to the University of Calicut
NAAC Accreditation - A Grade
NIRF Rank- 84
Email: physics@gvc.ac.in | Web: www.gvc.ac.in/physics

CERTIFICATE

Certified that the thesis entitled **"FABRICATION AND ANALYSIS OF MAGNETIC NANOSTRUCTURES FOR SENSOR APPLICATIONS"** submitted by **Mrs. NIMISHA O K** under my guidance at the Department of Physics in partial fulfillment of the requirements for the award of the degree of Doctor of Philosophy under the faculty of science, Department of Physics, Govt. Victoria College, Palakkad under the University of Calicut and the work embodied in the thesis has not been included in any other thesis submitted previously for the award of any other degree.

Palakkad

24/08/2024

Date ....

Dr. REENA MARY A P

Professor

Department of Physics

Govt. Victoria College, Palakkad

Prof.Reena Mary A P
DEPARTMENT OF PHYSICS
GOVERNMENT VICTORIA COLLEGE, PALAKKAD
Kerala, India, PIN 678001
Affiliated to the University of Calicut
NAAC Accreditation - A Grade NIRF Rank- 84
Email: reenamaryap@gvc.ac.in | Web: www.gvc.ac.in/physics

CERTIFICATE

This is to certify that the corrections recommended by both adjudicators have been incorporated in the thesis entitled **"FABRICATION AND ANALYSIS OF MAGNETIC NANOSTRUCTURES FOR SENSOR APPLICATIONS"**, submitted by Mrs. NIMISHA O K , Department of Physics, Government Victoria College Palakkad.

Place: Palakkad

Date: 04/06/2025

Dr. REENA MARY A P

(Supervising Guide)

DEPARTMENT OF PHYSICS
GOVERNMENT VICTORIA COLLEGE, PALAKKAD
Kerala, India, PIN 678001
Affiliated to the University of Calicut
NAAC Accreditation - A Grade
NIRF Rank- 84
Email: physics@gvc.ac.in | Web: www.gvc.ac.in/physics

CERTIFICATE

Certified that the thesis entitled **"FABRICATION AND ANALYSIS OF MAGNETIC NANOSTRUCTURES FOR SENSOR APPLICATIONS"** submitted by **Mrs. NIMISHA O K** under my co-guidance at the Department of Physics in partial fulfillment of the requirements for the award of the degree of Doctor of Philosophy under the faculty of science, Department of Physics, Govt. Victoria College, Palakkad under the University of Calicut and the work embodied in the thesis has not been included in any other thesis submitted previously for the award of any other degree.

Palakkad
24/08/2024

Dr. PRADEESH K
Assistant Professor
Department of Physics
Govt. Victoria College, Palakkad

DECLARATION

I hereby declare that the work presented in the thesis entitled **"FABRICATION AND ANALYSIS OF MAGNETIC NANOSTRUCTURES FOR SENSOR APPLICATIONS"** is based on the original research work carried out by me under the guidance and supervision of Dr. Reena Mary A P (Guide) and Dr. Pradeesh K (Co-guide), Department of Physics, Govt. Victoria College, Palakkad under the University of Calicut and no part of the work reported in this thesis has been presented for the award of any other degree. The thesis is free from AI generated contents.

Nimisha.O.K

NIMISHA O K

Palakkad

24/08/2024

ACKNOWLEDGEMENTS

I wish to express my grateful appreciation to all who have helped me in completing this work, and made it a remarkable experience for me. First and foremost, I praise the almighty for giving me the opportunity and vitality to undertake this challenging process of research work.

At this juncture I would like to express my deep sense of gratitude to my research guide and teacher Dr. Reena Mary A P for all the support and persistent encouragement extended to me throughout my research period. I am always grateful for her competent advice, keen observation, sustained guidance, humanity, readiness to share her knowledge as well as personal attention given to me during the entire course of work, without which the successful completion of this work would not have been possible. She opened in front of me the doors of research. It was really a blessing to get an opportunity to work with her.

I express my sincere gratitude to my Co-guide, Dr. Pradeesh K for sustained support and timely advice. His professional guidance and valuable comments have been very helpful to prompt my research quality.

I acknowledge University Grant Commission, India for the financial support in the form of fellowship.

I express my sincere thanks to Mr. Ramesan O K, former Head of the Department of Physics for providing the laboratory and library facilities during my research period. I thank with love and gratitude to Dr. Ambily Krishnan, my teacher and present Head of the department of Physics for her care, support and advise, which helped me a lot at the time of difficulties. I extend my gratitude to all teaching and non-teaching staff of Dept. of Physics, GVC, Palakkad for their support and help, without which it would have been difficult for me to complete my degree. Special thanks to Mr. Vijayakumar, my teacher for care, support and advice during initial stage of my research work.

I thank with love and gratitude to all teaching and non-teaching staff of Dept. of Chemistry for their help and advice. Special thanks to all non-teaching staff of Dept. of Chemistry for creating a good working environment during my initial research work. I would like to thank all teaching and non-teaching staff of Dept. of Zoology for their help and support. I am gratefully thankful to Dr. Lakshmi Priyadharsani, Dept. of Zoology for invaluable support, advice and inspiration in this pursuit of knowledge for one of my work during the research period. Thankful to Dr. Sindhu S L, present Head of the Research Centre and Head of the

Institute and to all former principals of GVC, for their immense support and for providing me with the necessary facilities to carry out my research. I would like to thank all the present and former office staff of the GVC, Palakkad for the cordial atmosphere during y research days. I thank with love and gratitude to all my research fellows Dr. Ambily Krishnan, Dr. Shaheera M, Dr. Resmi K R, Dr. Lisha, Dr. Anlin Lazar, Dr, Smiya John, Nayana K, Ajeesh P V, Athulya Jayakumar, Nandhitha Pauly, Athulprasad A J, Ramya M, Sajeev K F, Roshni Prabhakaran, Sukesh C, for their help and support during my research. Let me express my thanks with love to Kavya P, Gopika K Y, Divya P, Anugraha S N, Priya S, Nikhila G, Greeshma Varma, Sajini K P, Syama P S, Aneesha U, Shahila Ismail K I, Maya Ammathil Manoharan, Jayalekshmi C V, Aswani V J, research scholars in various department at GVC, Palakkad for their support and help in different stages of my research work. I express my feeling of gratitude towards all my friends.

I thank DST-FIST, New Delhi, India, for providing research funding to the Research Dept. of Physics, Govt. Victoria College institution. Also, thank DCE, Kerala, India, for the fund provided to this Research Centre under the Centre of Excellence head. I am grateful to the faculty and scientists in various institutions around the world. Let me thank Dr. T N Narayanan, TIFR, Hyderabad for providing lab facilities and made a fruitful discussion during my research days. I acknowledge with thanks Dr. Imad-al-Omari of Sultan Qaboos University Muscat for magnetic measurements. I am thankful to Dr. Saji K J and Dr. Praveen C S, International School of Photonics, Cusat for helping me at various stages of my work. I thank the scientists at STIC, CUSAT for their technical help. I am thankful to Dr. Shubhadeep Pal, TIFR, Hyderabad for helping instability study.

I will not thank my husband, Sanesh, but owe him my life in all my life. A doctorate would have been a distant dream without their immense motivation, love, support, care and patience. Thanks for being a bliss in my life. Words are insufficient to express my acknowledgement for my ever-loving parents, especially my father, without his blessing I won’t be able to chase my dreams. They have been the inspiring force behind me. I am deeply indebted to my compassionate in-laws who provided me with all the support for such a long time. I humbly remember their hardships at the time of research. I thank my brother Nishanth & his family, sister-in-law Sahitha & her family, my cousins and relatives for their support and encouragement.

Kunjappi, the little one who arrived as I shaped these pages, your grace reminded me of life’s truest purpose. You are my greatest chapter.

Once again, I thank God Almighty for offering me with all these wonders.

NIMISHA O K

PREFACE

Nanoscience and nanotechnology are innovative fields of research that has accomplished a great deal in the decades since Nobel Prize Laureate Richard Feynman introduced the concept in 1959. In 1960 he presented a visionary and prophetic lecture at a meeting of the American Physical Society, entitled “There is Plenty of Room at the Bottom”, where he speculated on the possibility and potential of nanosized materials. The prefix nano in the word nanotechnology means a billionth ($1x10^{-9}$). Nanotechnology deals with various structures of matter having dimensions of the order of billionth of a meter. In general, we can say that nanotechnology is the act of purposefully manipulating matter at the atomic scale. Nanotechnology has a significant impact on other interdisciplinary fields of science, which will eventually and also have a seminal role in human day-to-day life. Materials in the micrometer scale mostly exhibit physical properties the same as that of bulk form; however, materials in the nanometer scale may exhibit superlative chemical and physical properties distinctively different from that of bulk. The fundamental physical, chemical and biological properties of materials are surprisingly altered as their constituent grains are decreased to nano meter scale owing to their size, shape, space, surface chemistry and topology. Therefore, nano technology has generated much interest in the scientific community and it has become a very active area of research. In order to explore novel physical properties and phenomena and realize potential applications of nanostructures and nanomaterials, the ability to fabricate and process nanomaterials and nanostructures is the first cornerstone in nanotechnology. Nanostructured materials are those with at least one dimension falling in nanometer scale, and include nanoparticles, nanorods, nanowires, thin films, and bulk materials made of nanoscale building block or consisted of nanoscale structures.

Recent advancement in magnetism and magnetic materials has made magnetic nanostructures a matter of immense research interest because of their wide scientific and technological applications such as in magnetic fluids, magnetic random access memory (MRAM), magnetic switches, magnetic recording, catalysis, biotechnology/biomedicine, contrast agents in magnetic resonance imaging (MRI), water treatment, gas sensor, protein separation, cancer cell destruction, hyperthermia therapy etc. Although intensive research on magnetic fluids did not start until the 1960, the preparation of water based magnetic fluids had already been described in 1938 by Elmore. Technological applications of nanomaterials and nanofluids are numerous. Among nanofluids, a magnetic nanofluid popularly known as ferrofluid is a unique material that has both the liquid and magnetic properties. The ferrofluid technology finds increasingly great applications in industrial, space and medical fields. As the particle size of a magnetic material decreases, enormous changes in the properties occur. The magnetic nanostructures exhibit curious properties with size, shape and surface modification, which have immense applications and are of interest from the aspect of fundamental properties at atomic, molecular, electronic level of interactions.

The investigation of ferrofluid is began by NASA in USA. But the successful preparation of ferrofluid was done by Pappel in 1960. Later on Rosensweig put forward a novel technique for synthesizing stable ferrofluid as compared to one prepared by Pappel. Rosensweig contribution to the depth knowledge of fluid dynamics leads to the development of Ferrohydrodynamics. Ferrofluids are stable colloidal suspension of nanomagnetic single domain particles suspended in a liquid carrier medium. It is a new functional material, which has the fluidity of a liquid and the magnetism of solid magnetic material at the same time. The unique property of fluidity and the capability of interacting with a magnetic field is due to their composition. It mainly consists of three components: base fluid, single-domain magnetic nanoparticles and surfactant. The Brownian motion must be present in a fully developed magnetic nanofluid in order to prevent particles from coalescing and from collapsing when subjected to gravity. This means that it is necessary to take into account the interaction of numerous forces, including thermal, gravitational, magnetic, and surface tension. The average particle density is 10^{23} per liter, and the average particle diameter is 10 nm. They adhere to the ferrohydrodynamics laws and a modified Bernoulli's equation. Actually, the ferrofluid behaves as a non-newtonian in the high-concentration regime and newtonian in the low-concentration regime. A stable ferrofluid offers a wide range of applications. The magnetic nanoparticles can be suspended in any solvent by employing new techniques. Kerosene is the solvent for the majority of technical applications such as lubricants, coolants, heat exchangers, magnetic inks etc. For biomedical applications, like drug delivery, magnetic cell separation, hyperthermia, Magnetic Resonance Imaging etc., the solvents are dispersed in water. The quality of a fluid depends on stability and shelf life. To avoid agglomeration caused by attractive Van der Waals interaction, the magnetic particles have to be surfaced with suitable surfactant either by steric repulsion or electrostatic repulsion. Surface instability studies are a kind of icon in ferrofluid research. The instability of a fluid surface is an aggravation in many technical applications, where stability is of great importance. Nevertheless, the study leads to understanding the fundamental properties of the fluid in detail. Hence investigating the normal magnetic field on the free horizontal surface of a fluid paves the way for technological applications.

One of the important advantages of combining magneto-optical materials with plasmonics is the degree of engineering control that is attainable by modifying the design of the metal structure. Such control of light-matter interaction has been possible in metamaterials over the last decade. Furthermore, carefully chosen plasmonic devices may be able to disrupt the rotational symmetry of polarization space, which creates an artificial magnetic field that imparts circular birefringence to transmitted light. One of the most exciting aspects of nanoscience is the size and shape-dependent properties of matter. Due to the spatial confinement of electrons, phonons and electrical fields surrounding the particles as well as the material exhibits a variety of unique features. Ferrofluid is optically isotropic in the absence of an external magnetic field; once the external field is applied, they show anisotropic behaviour and exhibit magneto-optic phenomena like linear dichroism, faraday rotation, birefringence, magneto-optical transmission etc. Linear dichroism arises due to the intrinsic optical anisotropy or the shape anisotropy of individual magnetic particles. In a ferrofluid the random orientation of particles does not show any anisotropy in the fluid as a whole; hence the particles would not be expected to give rise to dichroism. But when a magnetic field is applied the particles may orient in the field direction; this causes the magnetic fluids to be structurally anisotropic. If the transmitted light intensity is different from the polarization of light perpendicular and parallel to the applied magnetic field, it is called the magneto-optic linear dichroism effect. In a ferrofluid, the particles in aggregate forms can act as oscillating dipoles. The interaction of two dipoles produces anisotropic polarizability giving rise to magnetic field-induced optical effects. When a magnetic field is applied to a ferrofluid, some pre-existing aggregates align along the direction of the applied magnetic field and with increasing field strength these clusters grow in size resulting in long periodic chains are formed, which are responsible for magneto-optical effects of ferrofluids. Surface plasmon resonance is a detection method, where excited fluorophores are coupled with plasmon resonance oscillations of electrons in metal films. Surface plasmon resonance-based sensor (SPR sensor) is a powerful tool for the study of biomolecular interactions. Conventional SPR sensor is limited in their ability to resolve complex samples, extremely dilute concentrations, or small molecular weight. The Surface plasmon resonance sensitivity can be enhanced using a magnetoplasmonic material in the presence of a magnetic field. The effect of iron oxide nanoparticles in the presence of an external magnetic field on SPR is quite interesting from both a fundamental and application point of view.

Hematite is the most stable form of iron oxide in the air at ambient conditions. It was attracted by researchers due to its abundance, low cost, low toxicity, high chemical stability, and tunable optical and magnetic properties in catalytic reactions, gas sensors, magnetic storage systems, photoelectron chemical water splitting and biological applications. The increase of infectious disorders caused by different harmful bacteria and the appearance of novel bacterial strains resistant to existing medications are major public health concerns. With the outbreaks of infectious diseases caused by pathogenic bacteria and the rise of antibiotic resistance of bacteria much attention in pharmaceutical and medical fields has been focused on creating new antibacterial agents. Iron oxide nanoparticles have received a lot of attention as a potential candidate for antibacterial agents, due to the generation of reactive oxygen species, which damage the cellular and viral components that ultimately lead to bacterial growth. Water is essential to life, rapid industrialization growth and an expanding human population have made the quality of water wrecked. The presence of various contaminants in wastewater discharge from industries is a global concern. The use of metal oxide nanoparticles in photocatalytic degradation is one of the simple and effective methods for purifying water. Hematite nanoparticles are a potential candidate for photocatalytic application due to their adequate band gap, high surface-to-volume ratio and recyclability after the reaction.

A significant development in the field of carbon nanomaterials was the successful mechanical exfoliation of graphene that was one atom thick from graphite using the Scotch tape technique. Since then, we have seen a surge in two-dimensional (2D) material research, which has resulted in the discovery of novel 2D materials. Two-dimensional materials have been a cradle for extensive scientific research both in fundamental and applied perspectives, due to their predominant quantum effects and fascinating material properties. Hematene, a 2D material is exfoliated from a bio synthesized Hematite nanoparticles. Energy scarcity is a great problem in our society, the development of sustainable energy technologies grabbed the attention of society. Photoelectrochemical water splitting is one of the promising processes to solve the problem of the energy crisis. In 1972, Fujishima and Honda discovered a TiO_2 photoanode that could photoelectrochemically split water molecules into H_2 and O_2 under UV illumination. TiO_2 is an efficient material for water splitting, but due to wide band gap restricts its photoactivity to the UV- region. This difficulty can be overcome by forming heterojunction with small band gap material.

The Density Functional Theory (DFT) has been commonly used to understand the dynamics of electrons in a solid. DFT is a very useful method to predict the structural, electronic, magnetic, mechanical, thermal and optical properties. The complex systems that are otherwise impossible by experimental methods can also be studied with the aid of DFT. The electronic properties such as electronic band structure and density of energy states of Hematite nanoparticles is studied using DFT in this work.

The title of the thesis is **"FABRICATION AND ANALYSIS OF MAGNETIC NANOSTRUCTURES FOR SENSOR APPLICATIONS"** and the thesis is divided into eight chapters as follows.

Chapter 1 gives a brief introduction to 2D material and the physics of magnetism. It outlines the magnetic properties of nanoparticles and ferrofluid in particular. Various instabilities exhibited by ferrofluid are also dealt with in this chapter. Finally, a scanty introduction to DFT and the motivation for this study is outlined.

Chapter 2 discusses the various synthesis methods and analytical tools used for this study. The principle behind these state-of-the-art analytical tools is also briefly discussed in this chapter.

Chapter 3 deals with the synthesis of ferrofluid by co-precipitation method. The Rosensweig instability study of ferrofluid under a uniform magnetic field is also studied.

The magneto-optical property of hydrocarbon and aqueous-based ferrofluid at different field strengths is described in **Chapter 4**. The synthesis of a hybrid iron oxide nanofluid based on silver and the effect of the applied magnetic field on the hybrid fluid is also investigated in this chapter. The fabrication of magneto plasmonic nanostructure and investigation of surface coupled plasmon emission (SPCE) with magnetic field is also carried out in this chapter. The Reverse Kretschmann (RK) configuration is used for the SPCE study.

Chapter 5 presents the synthesis of Hematite nanoparticles through the hydrothermal method using black tea extract as the reducing agent. The photocatalytic properties, antibacterial property and cytotoxicity of Hematite nanoparticles are also studied.

The exfoliation of 2D hematene from synthesized hematite nanoparticles is explained in **Chapter 6**. The anodization of Ti foil is also described. The visible light photoelectrochemical activity of hematene -TiO_2 heterostructure for energy applications is also carried out in this chapter.

Theoretical prediction of important properties such as density of states and band gap of hematite nanoparticles using Density functional theory is discussed in **Chapter 7**.

Chapter 8 contains the conclusions drawn from this study. The scope for further studies is also highlighted in this chapter.

LIST OF FIGURES

LIST OF PUBLICATIONS

1. **Nimisha O K**, Pal Shubhadeep, Divya D, Al-Omari Imadin, Pradeesh Kannan and Reena Mary A P, 2023, “Rosensweig instability study of iron oxide nanofluid under uniform magnetic field”, *Journal of Nanofluids*, doi:10.1166/jon.2023.1944.
2. **Nimisha O K**, Akshay M, Mannya S and Reena Mary A P, 2022, “Synthesis and photocatalytic activity of nickel doped zinc ferrite”, *Materials Today: Proceedings*, doi.org/10.1016/j.matpr.2022.06.332.
3. **Nimisha O K**, Pradeesh Kannan and Reena Mary A P, 2022, “Magneto-optical studies of kerosene based ferrofluid”, *Journal of Physics: Conference Series,* doi:10.1088/1742-6596/2312/1/012070.
4. **Nimisha O K**, Rajita Ramanarayanan, Pradeesh Kannan and Reena Mary A P, 2023, “Synthesis of iron oxide nanoparticles using black tea extract”. *In AIP Conference Proceedings*, doi.org/10.1063/5.0163277.
5. **Nimisha O K**, Reena Mary A P and Rajita Ramanarayanan, 2022, “Template assisted green synthesis of nickel oxide nanoparticles for photocatalytic applications”, *IOP conference series: Materials science and engineering*, doi:10.1088/1757-899X/1258/1/012010.
6. **Nimisha O K**, Pradeesh Kannan and Reena Mary A P, “Fluorescence quenching of fluorescein dye using silver nanoparticles”, *Materials Today: Proceedings*, https://doi.org/10.1016/j.matpr.2023.11.156.
7. **Nimisha O K**, Al-Omari Imadin, Pradeesh Kannan and Reena Mary A P, “Magneto-optical studies of magneto plasmonic nanofluid based on silver” (To be communicated).
8. **Nimisha O K**, Athulya Jayakumar, Ambily Krishnan, Pradeesh Kannan and Reena Mary A P, “Hematene- TiO_2 nanostructure for energy applications” (To be communicated).
9. **Nimisha O K**, Pradeesh Kannan and Reena Mary A P “Iron oxide mediated surface plasmon coupled emission enhancement for sensor applications” (To be communicated).
10. **Nimisha O K**, Nikhila G, Lakshmi Priyadarshini, Pradeesh Kannan and Reena Mary A P “Evauation of biological applications of green synthesized α-Fe_2O_3 nanoparticles” (To be communicated).

CONFERENCE PRESENTATIONS

1. **Nimisha O K**, Pal Shubhadeep, Divya D, Al-Omari Imadin, Pradeesh Kannan and Reena Mary A P ‘Rosensweig Instability Studies of Hydrocarbon-based Ferrofluid Under Uniform Magnetic Field at the International Conference on Magnetic Fluids (ICMF 2019) organized by Premc from 8th to 12th July 2019 at the Sorbonne University in Paris (Oral Presentation)
2. **Nimisha O K**, Pradeesh Kannan and Reena Mary A P ‘Magneto optical studies of water based ferrofluid’ at the International Conference on Magnetics Around-the-Clock Around-the-Globe Magnetics Conference (AtC-AtG), organized by IEEE Magnetics on 24th August 2021 (Poster Presentation)
3. **Nimisha O K**, Pradeesh Kannan and Reena Mary A P ‘Magneto optical studies of kerosene based ferrofluid’ at the International Conference on Emerging Electrical Energy, Electronics and Computing Technologies 2021 (ICE4CT2021) organized by faculty of Electrical engineering technology from 16th to 17th December 2021 at the University of Malaysia Perlis (UniMAP) (Oral Presentation).
4. **Nimisha O K**, Rajita Ramanarayanan, Pradeesh Kannan and Reena Mary A P ‘Synthesis of iron oxide nanoparticles using black tea extract’ at the International Conference on Materials for Emerging Technologies (ICMET 2021) organized by Department of Research Impact & Outcome, Division of Research & Development from 18th to 19th February 2022 at Lovely Professional University, Punjab, India (Oral Presentation).
5. **Nimisha O K**, Reena Mary A P and Rajita Ramanarayanan ‘Template assisted synthesis of nickel oxide nanoparticles for photocatalytic applications’ at the International Conference on Materials Science and Manufacturing Technology (ICMSMT 2022) organized by the Akshaya College of Engineering and Technology (Academic Partner), Coimbatore, Tamil Nadu India and Diligentec Solutions (Industry Partner), Coimbatore, Tamil Nadu, India, from 8th to 9th April 2022 at Akshaya College of Engineering and Technology, Tamil Nadu, India (Oral Presentation).
6. **Nimisha O K**, Akshay M, Mannya S and Reena Mary A P ‘Synthesis and photocatalytic activity of Nickel doped Zinc ferrite’ at the International Conference on Recent Advances Engineering Materials (ICRAEM 2022) organized by Alvas Institute of Engineering and Technology, Moodbidri, Karnataka, India from 3rd to 5th March

2022 at Alva’s Institute of Engineering & Technology, Moodbidri, Karnataka, India (Oral Presentation).

7. **Nimisha O K**, Pradeesh Kannan and Reena Mary A P ‘Fluorescence quenching of fluorescein dye using silver nanoparticles’ at the International Conference on Science and Technology of Advanced Materials (STAM23) from 18th to 20th April 2023 at Mar Athanasius College(Autonomous), Kothamangalam, Kerala, India (Oral Presentation).
8. **Nimisha O K**, Pradeesh Kannan and Reena Mary A P ‘Initial investigations of Hematene’ at the International Conference on Magnetics Around-the-Clock Around-the-Globe Magnetics Conference (AtC-AtG), organized by IEEE Magnetics on 27th September 2023 (Poster Presentation).

TABLE OF CONTENTS

Chapter 1: Introduction

Chapter 2: Experimental Techniques

Chapter 3: Rosensweig Instability Study of Iron Oxide Nano Fluid Under Uniform Magnetic field

3.4 Experimental

3.5 Results and Discussions

Chapter 4: Magneto-Optical and Magneto-Plasmonic Study of Iron Oxide fluid based on Silver

4.5 Experimental

4.6 Results and Discussions

Chapter 5: Bio-synthesis of Hematite nanoparticles for photocatalytic and biological applications

5.3 Experimental

5.4 Results and Discussions

Chapter 6: Hematene-TiO_2 heterostructures for energy applications

Chapter 7: Fundamental study of α-Fe_2O_3 using DFT

Chapter 8: Conclusions and recommendations

ABSTRACT

FABRICATION AND ANALYSIS OF MAGNETIC NANOSTRUCTURES FOR SENSOR APPLICATIONS

NIMISHA O K

Recent advancement in magnetism and magnetic materials has made magnetic nanostructures a matter of immense research interest because of their wide range of applications such as in magnetic fluids, magnetic sensors, magnetic recording, catalysis, biomedicine, contrast agents in magnetic resonance imaging, hyperthermia therapy etc. In the current work, we studied the various fields of applications of iron oxide in different forms such as solid, liquid and film. Ferrofluids are of great interest since they possess the properties of a fluid and act as a ferromagnetic material and their motion can be controlled by a magnetic field. Surface instability studies are a kind of icon in ferrofluid research. From a fundamental perspective, magnetic nanofluid is an ideal platform for investigating Rosensweig instability and pattern formation. Using a home-made experimental set up we studied the Rosensweig instability in detail. Investigation of magneto-optical characteristics of ferrofluid is important for the development of optoelectronic devices such as optical modulators, optical switches, sensors etc. Combining the effects of magnetism with plasmonic structure can lead to many applications, especially in the medical field. Surface plasmon resonance-based sensor is a powerful tool for the study of biomolecular interactions. However, the conventional SPR sensor is limited in its ability to resolve complex samples, extremely dilute concentrations or small molecular weight. The surface plasmon resonance sensitivity can be enhanced using a magnetic material in the presence of a magnetic field, using the phenomena of surface coupled emission is also carried out in this work. Among the various nanometal oxides, hematite nanoparticles are promising compounds due to their wide range of applications as antioxidant, antibiofilm and antibacterial agents. Hence in the present work, the photocatalytic activity, antibacterial property and cytotoxicity of bio synthesized hematite nanoparticles is studied. Energy scarcity is a great problem in our society, hence the development of sustainable energy technologies grabbed the attention of society. Photoelectrochemical water splitting is a promising process to solve the problem of energy crisis. Here we exfoliated a hematene 2D material, from hematite particles, quantum confinement in the 2D regime leads to modification of optical bandgap and could be useful materials for water splitting. At the end the fundamental study of hematite using DFT theory is also carried out.

സംഗ്രഹം

സെൻസർ ആപ്ലിക്കേഷനുകൾക്കായുള്ള മാഗ്നെറ്റിക് നാനോസ്ട്രക്ചറുകളുടെ ഫാബ്രിക്കേഷനും വിശകലനവും

നിമിഷ ഒ കെ

കാന്തിക ദ്രാവകങ്ങൾ, കാന്തിക സെൻസറുകൾ, കാന്തിക റെക്കോർഡിംഗ്, കാറ്റലിസിസ്, ബയോമെഡിസിൻ, മാഗ്നറ്റിക് റെസൊണൻസ് ഇമേജിംഗിലെ കോൺട്രാസ്റ്റ് ഏജന്റുകൾ, ഹൈപ്പർതെർമിയ തെറാപ്പി തുടങ്ങിയ വിശാലമായ പ്രയോഗമേഖലകൾ നിലവിലുള്ളതിനാൽ, കാന്തിക നാനോസ്ട്രക്ചറുകളെ കാന്തികത്വത്തിലെയും കാന്തിക വസ്തുക്കളിലെയും സമീപകാല പുരോഗതി വളരെയധികം ഗവേഷണ താൽപ്പര്യമുള്ള വിഷയമായി ഉയർന്നിരിക്കുന്നു. ഖരാവസ്ഥയിലും ദ്രവാവസ്ഥയിലും നേരിയ പാളിരൂപത്തിലുള്ള പദാർത്ഥങ്ങളായും വിവിധ രൂപങ്ങളിൽ ഇരുമ്പ് ഓക്സൈഡിന്റെ പ്രയോഗങ്ങളുടെ വിവിധ പഠനങ്ങൾ ഈ പ്രബന്ധത്തിൽ പ്രതിപാദിക്കുന്നു . ഒരു ദ്രാവകത്തിന്റെ ഗുണങ്ങൾ ഉള്ളതിനാൽ ഫെറോ ഫ്ലൂയിഡുകൾക്ക് വലിയ പ്രാധാന്യമുണ്ട് , അവ കാന്തിക വസ്തുവായി പ്രവർത്തിക്കുകയും അവയുടെ ചലനം ഒരു കാന്തികക്ഷേത്രത്തിലൂടെ നിയന്ത്രിക്കുകയും ചെയ്യാം. ഉപരിതല അസ്ഥിരത പഠനങ്ങൾ ഫെറോ ഫ്ലൂയിഡ് ഗവേഷണത്തിലെ ഒരുതരം ചിഹ്നമാണ്. അടിസ്ഥാനപരമായ കാഴ്ചപ്പാടിൽ, റോസൻസ്വീഗ് അസ്ഥിരതയും തദ്വാരാ വിന്യാസരൂപീകരണവും അന്വേഷിക്കുന്നതിനുള്ള അനുയോജ്യമായ മാതൃകയാണ് കാന്തികദ്രവങ്ങൾ അഥവാ മാഗ്നറ്റിക് നാനോഫ്ലൂയിഡ്. ഗവേഷണശാലയിൽ തന്നെ പരീക്ഷണാത്മക സജ്ജീകരണം ഉപയോഗിച്ച് ഞങ്ങൾ റോസൻസ്വീഗ് അസ്ഥിരതയെക്കുറിച്ച് വിശദമായി പഠിച്ചു. ഒപ്റ്റിക്കൽ മോഡുലേറ്ററുകൾ, ഒപ്റ്റിക്കൽ സ്വിച്ചുകൾ, സെൻസറുകൾ തുടങ്ങിയ ഒപ്റ്റോ ഇലക്ട്രോണിക് ഉപകരണങ്ങളുടെ വികസനത്തിന് ഫെറോ ഫ്ലൂയിഡിന്റെ മാഗ്നെറ്റോ-ഒപ്റ്റിക്കൽ സ്വഭാവസവിശേഷതകളെക്കുറിച്ചുള്ള അന്വേഷണം പ്രധാനമാണ്. കാന്തികതയുടെ ഫലങ്ങൾ പ്ലാസ്മോണിക് ഘടനയുമായി സംയോജിപ്പിക്കുന്നത് നിരവധി പ്രയോഗങ്ങൾക്ക് കാരണമാകും, പ്രത്യേകിച്ച് മെഡിക്കൽ മേഖലയിൽ. ജൈവ തന്മാത്രാ ഇടപെടലുകളെക്കുറിച്ചുള്ള പഠനത്തിനുള്ള ശക്തമായ ഉപകരണമാണ് ഉപരിതല പ്ലാസ്മോൺ അനുരണനം അടിസ്ഥാനമാക്കിയുള്ള സെൻസർ. എന്നിരുന്നാലും, സങ്കീർണ്ണമായ സാമ്പിളുകൾ, വളരെ നേർപ്പിച്ച അളവിലോ അല്ലെങ്കിൽ ചെറിയ തന്മാത്രാ ഭാരം എന്നിവയുടെ കഴിവിൽ പരമ്പരാഗത എസ്പിആർ സെൻസർ പരിമിതമാണ്. ഒരു കാന്തികക്ഷേത്രത്തിന്റെ സാന്നിധ്യത്തിൽ ഒരു കാന്തികവസ്തു ഉപയോഗിച്ച് ഉപരിതല പ്ലാസ്മോൺ റെസൊണൻസ് സംവേദനക്ഷമത വർദ്ധിപ്പിക്കാൻ കഴിയും, ഉപരിതല സംയോജിത പ്രസാരണ പ്രതിഭാസങ്ങളും ഈ പ്രബന്ധത്തിൽ വിശകലനം ചെയ്യുന്നു. വിവിധ നാനോമെറ്റൽ ഓക്സൈഡുകളിൽ, ആന്റിഓക്സിഡന്റ്, ആൻറിബയോഫിലിം, ആൻറി ബാക്ടീരിയൽ ഏജന്റുകൾ തുടങ്ങിയ വിശാലമായ ഉപയോഗങ്ങൾ കാരണം ഹെമറ്റൈറ്റ് നാനോകണങ്ങൾ മികച്ച സംയുക്തങ്ങളാണ്. അതിനാൽ ഇപ്പോഴത്തെ പഠനത്തിൽ, ജൈവനിർമ്മിത ഹെമറ്റൈറ്റ് നാനോകണങ്ങളുടെ പ്രകാശരാസത്വരക പ്രവർത്തനങ്ങൾ, സൂക്ഷ്മജീവികളുമായുള്ള പ്രതിപ്രവർത്തനം, ജൈവകോശങ്ങളിൽ അവയേൽപ്പിക്കുന്ന വിഷലിപ്തത എന്നിവയും ഇവിടെ പഠനവിഷയമാക്കിയിരിക്കുന്നു. ഊർജ്ജ ദൌർലഭ്യം നമ്മുടെ സമൂഹത്തിൽ ഒരു വലിയ പ്രശ്നമാണ്, അതിനാൽ സുസ്ഥിര ഊർജ്ജ സാങ്കേതികവിദ്യകളുടെ വികസനം സമൂഹത്തിന്റെ. ഊർജ്ജ പ്രതിസന്ധി പരിഹരിക്കുന്നതിനുള്ള ഒരു നല്ല പ്രക്രിയയാണ് പ്രകാശ-വൈദ്യുത രാസ സഹായിതമായി ജലത്തെ അതിന്റെ മൂലകങ്ങളായ ഹൈഡ്രജനും ഓക്സിജനുമായി വേർതിരിക്കുന്ന പ്രവത്തനം (ഫോട്ടോ ഇലക്ട്രോകെമിക്കൽ വാട്ടർ സ്പ്ലിറ്റിംഗ്). ഇവിടെ ഹെമറ്റൈറ്റ് കണങ്ങളിൽ നിന്ന് ദ്വിമാന പദാർത്ഥമായ ഹേമാറ്റിൻ പാളികൾ ഉതിർത്തെടുക്കുന്നു , 2 ഡി ദ്വിമാനവസ്തുക്കളിൽ / കുഞ്ഞു കണങ്ങളിലും പ്രകടമായി കണ്ടുവരുന്ന ക്വാണ്ടം തടങ്കൽ മൂലം ഇത്തരം വസ്തുക്കളിലെ ഒപ്റ്റിക്കൽ ഊർജ്ജന്തരം പരിഷ്കരിക്കപ്പെടുകയും, ഇത് ജല വിഭജനത്തിന് ഉപയോഗപ്രദമായ പദാർത്ഥങ്ങളായി രൂപപ്പെടുകയും ചെയ്യുന്നു . കൂടാതെ ഡി. എഫ്. ടി സിദ്ധാന്തം ഉപയോഗിച്ച് ഹെമറ്റൈറ്റിനെക്കുറിച്ചുള്ള അടിസ്ഥാന പഠനവും ഈ പ്രബന്ധത്തിൽ ഉൾക്കൊള്ളിച്ചിട്ടുണ്ട്.

Chapter 1

Introduction

Modern society's living conditions have greatly improved as a result of the development of nanotechnology, which plays a significant part in all scientific and technological advancements. The technology of the twenty-first century is the multidisciplinary field of nanoscience and nanotechnology, which is growing quickly and having a big social influence. Throughout human history, exploration, migration, and travel were made possible by the discovery of lodestone, one of the first magnetic materials. Even though scientists were aware of the magnetic phenomena as early as 600 BC, a complete understanding of magnetism could not be attained until the discovery of quantum mechanics. Magnetism is a natural phenomenon that is primarily caused by the orbital and spin movements of electrons and their interactions. For scientists, magnetism is an endless field of study. The fundamentals of magnetism, ferrofluid physics, and a brief overview of density functional theory for fundamental research are covered in this chapter. The goals and rationale for the current investigation are highlighted at the conclusion.

1.1 Introduction

Developments in magnetic materials have traditionally been associated with advances in the field of magnetism. Better-performing nanomagnetic materials are gradually replacing outdated ones. This is demonstrated by the advent of new kinds of materials, including spin valve transistors, giant magnetocaloric materials, giant magnetoresistive materials, and ferrofluids. Ferrofluid technology is finding extensive applications in the fields of space exploration, manufacturing, and medicine. Scientists and engineers made unsuccessful attempts to create magnetic fluid a long time ago. In the nascent phases of NASA's lunar exploration initiatives, Papell is acknowledged for being the first to create a magnetic fluid in 1960. Since magnetic fluid does not exist in nature, it must be produced. Melting a magnetic substance won't produce a fluid since its ordering temperature is far greater than the surrounding air temperature. It must therefore be produced by appropriate surface modification. The emergence of nanotechnology simplified matters, and a variety of synthesis methods are now accessible for the production of stable fluids. The mere dispersion of magnetic particles does not guarantee the presence of magnetism in a fluid. For a fully evolved magnetic nanofluid to be free of collapsing and coalescing when exposed to gravity, Brownian motion is required. This implies that the interaction of many forces, such as thermal, gravitational, magnetic, and surface tension, must be considered. The average particle diameter is 10 nm, and the average particle density is 1023 particles per litre. They follow a modified version of Bernoulli's equation and the laws of ferro-hydrodynamics. Actually, in the high-concentration regime, the ferrofluid exhibits non-Newtonian behavior, while in the low-concentration domain, it exhibits Newtonian behavior. The uses for a stable ferrofluid are numerous. By using novel methods, the magnetic nanoparticles can be suspended in any kind of fluid. Most technical applications, including lubricants, coolants, heat exchangers, magnetic inks, etc., use paraffin as their solvent. The solvents are distributed for use in biomedical applications such as drug delivery, magnetic cell separation, hyperthermia, magnetic resonance imaging, etc.

Scientists and engineers have been studying two-dimensional materials lately. The discovery in 2004 of the graphene monolayer, which was isolated from the bulk graphite by mechanical exfoliation, opened up new avenues for the research of 2D materials. It is found that these materials are more effective for use in future electronics applications. The monolayer of graphene has subsequently developed into the ideal material for the production and investigation of many 2D layered and non-layered materials because of its special electrical, electronic, and other properties. Graphene's electronic spectra lack an energy band gap, which prevents it from being employed in nano-electronic devices, despite its benefits. This has led to the study and discovery of a variety of 2D nanomaterials, including transition metal chalcogenides and oxides. In a broad range of possible applications, such as energy storage, field effect transistors, sensors, and optoelectronics, a number of 2D materials have demonstrated promising performance. The majority of 2D materials research focuses on layered materials with weak Van der Waals interlayer bonding and high covalent intralayer interaction. Making 2D materials from their non-layered predecessors would be an interesting endeavour, especially considering the advantages of 2D geometry. The enhanced characteristics arising from 2D morphology can emulate the existing layered 2D materials, in addition to other important intrinsic material attributes. Typically, bulk counterparts of 2D materials have layered structures with weak Vander Waals contacts between the layers and strong covalent bonds inside the planes. Therefore, exfoliating them chemically or physically from their stacked bulk counterparts is easier. However, because of their high surface energy and lack of bonding anisotropy, 2D Non-Van der Waals materials are very difficult to exfoliate from their non-layer structure. Exfoliation of the bulk material down to atomically thin sheets alters its physical properties due to quantum confinement, providing intriguing opportunities for a range of applications. Since dangling bonds are present in non-layered 2D materials but not in layered 2D materials, this is their most notable characteristic. The primary characteristic of non-layered 2D materials is the existence of dangling bonds, which are not present in layered 2D materials. This enhances the surface reactivity of non-layered 2D materials, making them appropriate for sensing and catalytic applications. It can be difficult to disrupt the crystalline arrangement of atoms without upsetting the 3D bonding network, even when it crosses the unit cell axes. The majority of synthesis techniques used to produce 2D non-layered materials are bottom-up strategies that combine dry and wet chemical pathways.

To achieve the necessary anisotropic growth, the procedure includes perturbing thermodynamic equilibrium and intentionally controlling atom dynamics. Achieving controlled growth is essential for creating novel materials. Unlike their Van der Waals predecessors, the synthesis of Non-Van der Waals 2D materials is by no means simple, yet these materials have a strong propensity to satisfy surface dangling connections and form 3D structures. However, techniques that deviate from the thermodynamic equilibrium are needed to synthesize Non-Vander Waals 2D materials. As a result, bottom-up techniques are utilized in the majority of procedures used to synthesize Non-Van der Waals 2D materials. According to Balan et al., in certain circumstances, traditional liquid phase exfoliation can even be used to exfoliate covalent and ionic crystals. This approach is a relatively new and significant development in this developing field of study. Because of their strong physical and chemical characteristics, transition metal oxides that are found in abundance on Earth are thought to be perfect progenitors for 2D materials. Because of the well-known sensitivity of the electrical and magnetic properties of transition metal oxides to their dimensionality, researchers and engineers can modify these materials' ground states by confining their thickness to a single or small number of atomic layers. Therefore, 2D magnetism is still an emerging topic of study with potential applications in spintronics and storage. Nevertheless, 2D magnetism is still in its infancy, and further basic research is needed.

1.2 Basics of magnetism

Magnetism is a microcosm of the history of science. The results of William Gilbert's research with lodestones and iron magnets were published in his book "De Magnete" in 1600 [1, 2]. This marked the start of the study of magnetism. His ability to precisely define Earth's magnetism led to the debunking of many other widely held notions about it. Hans Christian Oersted's discovery that an electric current produces a magnetic field in 1825 marked a momentous advance in the history of magnetism since it allowed researchers to reach strong fields that were previously unattainable with conventional, permanent magnets [3]. For thousands of years, magnetism has captivated humans due to its ability to utilize magnetic properties creatively. Magnetic discoveries have yielded a vast array of applications, ranging from magnetic storage medium to the compass needle. Human intelligence has never stopped searching for ground-breaking innovations, whether it is through the fusion of naturally existing magnetic materials or the creation of intricate artificial magnetic structures. An atom's or an ion's magnetic moment is the total of two contributions. They derive one from the quantized orbital angular momentum and the other from the angular momentum of their intrinsic spin [1]. While electrons revolve around the nucleus to produce the orbital magnetic moment, they process about their axes to produce the spin magnetic moment. The interaction between the orbital and spin magnetic moments of the individual atoms in a substance determines its magnetic properties. Magnetic material is any substance that reacts to an external magnetic field. The way that electrons and atomic moments are arranged affects how a material reacts to an external magnetic field. On the other hand, the materials' interactions and ordering are used to classify them. The following sections examine several magnetic forms.

1.2.1 Diamagnetism

Since all of the atoms in diamagnetic materials have full orbital shells and no unpaired electrons, their net magnetic moment is zero. Every substance has diamagnetism to some extent. The mutual interaction between the applied magnetic field and orbiting electrons produces a magnetic moment that opposes the applied magnetic field when it is present. It seems contradictory, yet a diamagnetic substance typically expels the applied field. This is a result of the law of Lenz [4]. Magnetic induction causes additional currents to flow through the atoms of a diamagnetic substance when it is subjected to an external magnetic field. The susceptibility is negative because of the way these generated currents are orientated, which produces a field that opposes the applied field (**Figure 1a**). The susceptibility of diamagnetic materials is temperature-independent, which is another crucial property (**Figure 1b**). Diamagnetic materials include things like quartz, calcite, water, copper, silver, etc.

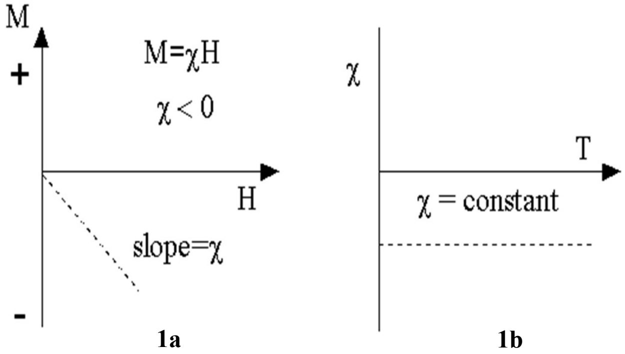

Figure 1.1 Magnetic response of a diamagnetic material in the presence of a magnetic field: (1a) shows the magnetization curve, and (1b) shows the variation of susceptibility with temperature [5]

1.2.2 Paramagnetism

Materials with net magnetic moments because of unpaired electrons are said to be paramagnetic. Nevertheless, because of the thermal energy-induced random orientation of magnetic moments, there is no externally imposed magnetic field and magnetization is zero [6] (**Figure 1.2a**). A net positive susceptibility is produced when a magnetic field is applied because the magnetic moments tend to align in that direction. Curie's law, which is derived from Langevin's theory of localized moments, represents the temperature-dependent susceptibility of paramagnetic materials (**Figure 1.2b**).

$$\chi = \frac{C}{T} \tag{1.1}$$

Where C and T are Curie's constant and Temperature respectively. Typical examples for paramagnetic materials are sulphide, silicate, carbonate, clay etc.

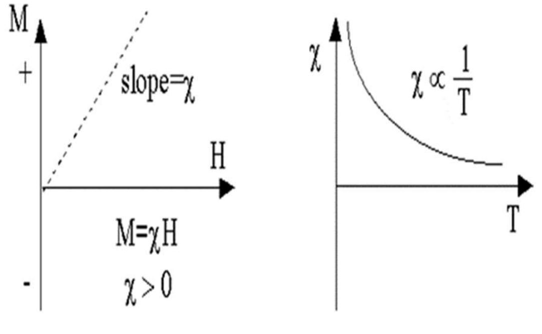

1.2a **1.2b**

Figure 1.2 Magnetic response of a paramagnetic material in the presence of a magnetic field: (1.2a) shows the magnetization curve, and (1.2b) shows the variation of susceptibility with temperature [5]

1.2.3 Ferromagnetism

Because of the interaction between a ferromagnet's spins, the materials show spontaneous magnetization even in the absence of an external magnetic field [7]. Moments aligned in paralle due to electronic exchange pressures. A ferromagnetic material's special properties include the presence of an ordering temperature and spontaneous magnetization. Their distinctive temperature is known as ferromagnetic Curie temperature, below which a material exhibits ferromagnetic behaviour and above which a substance becomes paramagnetic, with the primary heat influences disrupting the aligned spins [8]. The relationship between temperature and susceptibility is explained by the Curie-Weiss theory. A ferromagnetic substance has an extremely high susceptibility and follows the Curie-Weiss law.

$$\chi = \frac{C}{T-T_c} \tag{1.2}$$

Where C is the Curie constant, T temperature and T_c the Curie temperature. Cobalt, Nickel, and Iron are some examples of ferromagnetic materials. The alignment of magnetic moments in a ferromagnetic material is illustrated in **Figure 1.3**.

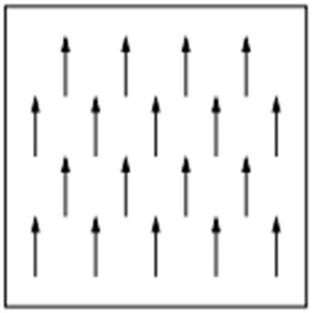

Figure 1.3 The alignment of magnetic moments in a ferromagnetic material [9]

Weiss put up the ferromagnetism domain theory in 1907 [10]. This hypothesis states that a ferromagnetic material has several tiny, spontaneously magnetised areas termed domains. However, the vector sum of the magnetic moments of the various domains determines the net magnetisation. In addition, he proposed the possibility of a molecular field acting in ferromagnetic materials to magnetise them even in the absence of a magnetic field, but he was unable to explain the molecular field's origin. Heisenberg attempted to use the exchange interaction of quantum mechanics to explain ferromagnetism in 1928. The expression for the interaction energy between two atoms is

$$E_{ex} = -2J_{ex}S_i.S_j \text{ [11]} \tag{1.3}$$

Where S_i and S_j are the spins of two atoms, and J_{ex} is the exchange integral. E_{ex} has a minimum at parallel spins and a maximum at antiparallel spins if J_{ex}positive. On the other hand, the lowest energy state is produced by J_{ex}, a negative antiparallel spin. We already know that the alignment of spin moments on neighbouring atoms is the cause of ferromagnetism. Therefore, with ferromagnetic material, the exchange integral needs to be positive. The exchange integral varies with $\frac{r_{ab}}{r_d}$ ratio, where $r_{ab}$and r_d are the radii of an atom and its 3d shell of electrons, respectively. This is illustrated by the Bethe-Slater curve (**Figure 1.4**).

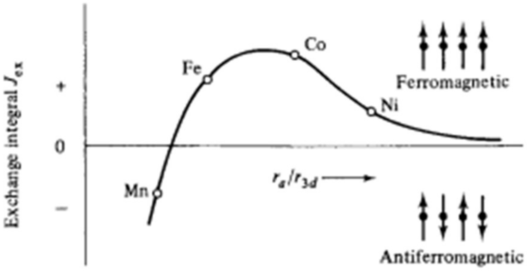

Figure 1.4 The Bethe-Slater curve [1]

Slater states that ferromagnetic materials must satisfy the ratio $\frac{r_{ab}}{r_d} \geq 3$. In this case, ferromagnetic materials are discovered to be Fe, Co, and Ni, while non-ferromagnetic materials are Mn and Cr. The Heisenberg theory and domain theory provided a satisfactory explanation for the ideas of domains, exchange interactions, and temperature-dependent susceptibility, but they were unable to explain the exact value of the magnetic moment in metals. Both of these ideas, which go by the name "localised moment theory," contend that ferromagnetism is caused by electrons that are fixed to atoms and immovable within crystals. Every atom has a unique magnetic moment that is localised due to the contribution of these electrons. The Band theory of magnetism has solved this [1]. Band theory discards the idea that an electron is localised to a single atom and instead assumes that electrons are part of the entire crystal and are mobile across atoms. According to band theory, electrons are thought to be part of the entire crystal and are mobile, meaning they are not limited to a particular atom. Atoms cannot be brought together to violate Pauli's exclusion principle since the electron clouds overlap and the distinct energy levels of different atoms with the same energy should separate. For different energy levels, the amount of splitting varies, and the levels spread out to form bands as seen in **Figure 1.5**. The band theory states that in order for ferromagnetism to occur, the electrons must be partially filled bands with empty levels. To ensure a negligible gain in energy due to spin alignment, the bands' level density must be high. The atoms must be at the proper distance for the exchange forces to cause electron contact.

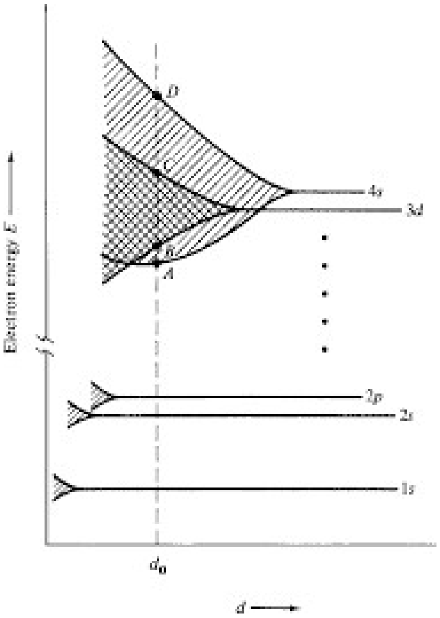

Figure 1.5 Splitting of electron energy levels as the interatomic distance decreases [1]

1.2.4 Antiferromagnetism

The materials are those in which the net magnetisation is zero because the neighbouring spins align antiparallel to one another (**Figure 1.6**) as a result of negative exchange interaction. Two sublattice models can be used to describe the distinctive behaviour of antiferromagnetic materials. The magnetic atom lattice is split into two equivalent interpenetrating sublattices in this concept. The spins on the sublattice only interact with the closest spins on the adjoining sublattice; only the nearest neighbour interactions are taken into account. The net magnetisation is zero because the two sublattices spontaneously magnetised in the opposite direction due to the negative exchange interaction [12]. A tiny magnetisation is created when the temperature rises because the field can rotate spins and cause a slight upset in spin alignment. The magnetisation increases with temperature, reaching its maximum value at a specific temperature known as the Neel temperature. As the temperature rises more, the magnetisation gradually decreases and the material behaves like a paramagnetic one. Curie-Weiss law (with a negative value of θ) is followed by the material. For an antiferromagnet, the susceptibility is modest and positive because of the antiparallel alignment of moments. Examples of antiferromagnets include ferrous oxide, manganese oxide, manganese sulphite, chromium oxide, etc.

$$\chi = \frac{1}{T-\theta} \tag{1.4}$$

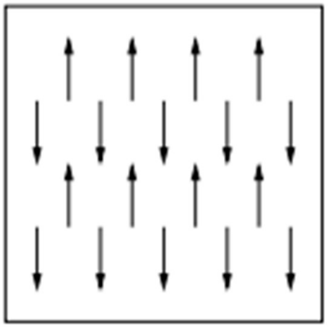

Figure 1.6 The alignment of magnetic moments in a ferromagnetic material [9]

1.2.5 Ferrimagnetism

The ferrimagnetic materials, which have two interpenetrating sublattices, are microscopically identical to the antiferromagnetic materials [13]. However, the magnetic structure is not similar because multiple types of magnetic atoms or crystallographic sites are present throughout the entire magnetic structure. There will be a net magnetisation as a result of the spontaneous magnetisation being distinct in each sublattice. Even in the case of a tiny external magnetic field, net magnetisation is higher. Thermal energy over a specific temperature known as the Curie temperature prevents spontaneous magnetisation. At and below the Curie temperature, they exhibit paramagnetic and ferromagnetic properties. The magnetic moment alignment in a ferrimagnetic material is shown in **Figure 1.7**. Ferrimagnetic materials include Fe_3O_4, $MgFe_2O_4$, $ZnFe_2O_4$ and others.

.

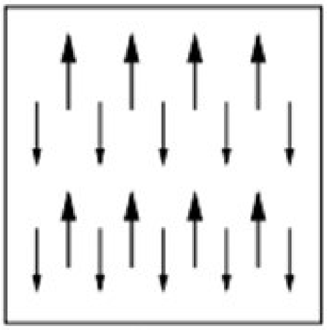

Figure 1.7 The alignment of magnetic moments in a ferrimagnetic material [14]

1.3 Magnetic Interactions

The kind of interaction between the magnetic moments in a solid substance determines its magnetic behaviour. The moments interact with one another through these magnetic interactions to establish long-range order. The collective behaviour of magnetic moments gives rise to all kinds of magnetic phenomena that are manifested by solids. In this context, we address several kinds of interactions between solid-state magnetic moments.

1.3.1 Magnetic dipolar interactions

The long-range magnetic dipolar interactions between magnetic moments are always present. The interaction energy between two magnetic dipoles $\mu_1$and μ_2 are separated by a distance r given by

$$E = \frac{\mu_0}{4\pi r^3}\left[\mu_1.\mu_2 - \frac{3}{r^2}(\mu_1.r)(\mu_2.r)\right] \quad (1.5)$$

This energy cannot contribute to any magnetic ordering in solid magnetic materials at room temperature since it is insignificant in contrast to thermal energy. Near absolute zero, however, magnetic dipolar interaction becomes substantial at very low temperatures.

1.3.2 Exchange interactions

One of the most significant phenomena in molecular magnetism is exchange contact. Its electrostatic character has a foundation in quantum mechanics. Strong exchange interactions only occur between the closest neighbours. With distance, the interaction's strength quickly decreases. Four different kinds of exchange interactions can happen, depending on the solid's metallic characteristics and the degree of magnetic moment delocalization.

a. Direct exchange interactions

It results from the electronic wave functions' spatial overlap. Strong localization of the magnetic moments occurs on the magnetic centers, and direct interaction between the electrons of adjacent magnetic ions occurs without the need for any intermediary [15]. The Direct Exchange Interaction is schematically represented in **Figure 1.8**. This kind of interaction is explained by Heisenberg's model.

$$H = -J \sum S_i \, . S_j \tag{1.6}$$

Certain metals are antiferromagnetic (J<0) and some are ferromagnetic (J>0) based on their J values. Since there is not enough direct overlap between nearby magnetic orbitals, as there is in the case of rare earth and transition metals, this form of interaction is relatively weak and cannot be a significant factor in determining the magnetic properties. Additionally, when dealing with such magnetic materials, some sort of indirect exchange interaction.

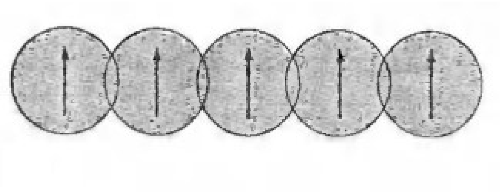

.

Figure 1.8 Schematic illustration of direct exchange interaction [16]

b. Indirect exchange interactions

The interaction between the magnetic moments over a long distance through a mediator. Mainly two types of indirect exchange interactions exist.

1. Superexchange interactions

A common non-magnetic ion mediates the interaction between two magnetic ions (**Figure 1.9**). In ionic solids, this kind of indirect exchange contact mostly happens via the occupied oxygen 2p orbital between two magnetic ions of the same valence. Because the exchange interaction occurs over a significant distance, the superexchange is named. It appears to be more common in difluorides of transition metals or magnetic oxides. According to Pauli's exclusion principle, this interaction is a virtual exchange of electrons from the same 2p orbital of oxygen, which possesses antiparallel spins, with electrons from magnetic ions [17]. Consequently, antiferromagnetic coupling results from the antiparallel spin orientation of magnetic ions. When electrons from magnetic ions interact with electrons from various oxygen orbitals, ferromagnetic ordering can also result from this interaction.

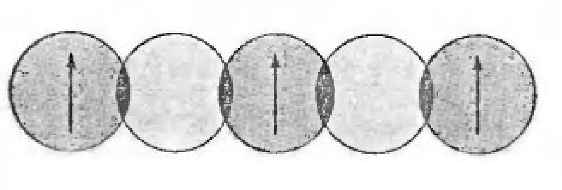

Figure 1.9 Schematic representation of superexchange interaction [16]

2. RKKY interactions

The RKKY interaction (**Figure 1.10**) is a conduction electron-mediated interaction between two localised spins that plays a key role in the magnetic coupling between localised moments in metals. Conduction electrons interact with the crystal lattice's ith site's effective magnetic field and develop a spin polarisation of sorts. The spin polarisation and spin of the lattice site will both change mutually when the electron relaxes its magnetic moments and passes through the next lattice site. The connection is indirect since there is no direct coupling between magnetic moments. The coupling is expressed as an exchange interaction that depends on distance, as given by

$$J_{RKKY(r)} \propto \frac{\cos(2k_F r)}{r^3} \qquad (1.7)$$

where r and k_F stand for the fermi surface radius and the distance between two rare earth ions, respectively. The long-range interaction depends oscillatorily on the distance between the magnetic moments. Therefore, it can be either ferromagnetic or antiferromagnetic, depending on the separation. If k_F is modest, the interaction results in ferromagnetism, and if $k_F \sim \frac{\pi}{a}$, in antiferromagnetism. The sign of the exchange integral J varies with the separation between the localised moments. **Figure 1.11** displays the fluctuation of the exchange integral with interatomic distance.

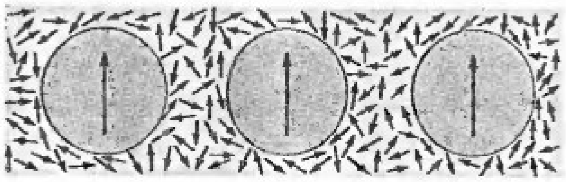

Figure 1.10 Schematic illustration of RKKY interaction [16]

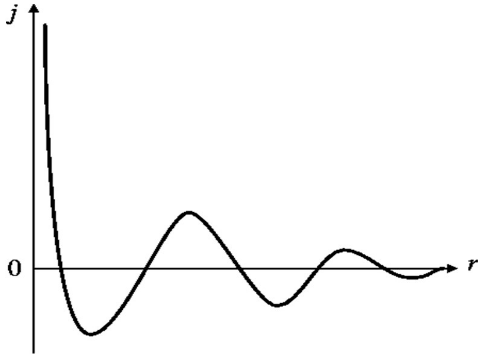

Figure 1.11 Variation of exchange integral with interatomic distance [3]

c. Double exchange interactions

It is the most common interaction between oxides with different valence states. Zener suggested using the nearby oxygen ion to explain the interaction between neighbouring ions with parallel spins (**Figure 1.12**). One electron simultaneously hops from the third shell of one magnetic cation to the oxygen's second p orbital, and from there it hops to the third shell of another magnetic cation. The ferromagnetic order of magnetic cations results from this interaction since the hopping happens while the spin sign is conserved [18].

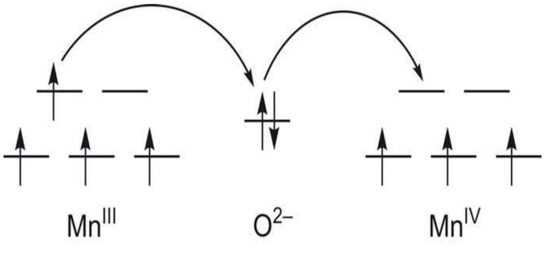

Figure 1.12 Schematic illustration of Double exchange interaction [19]

d. Anisotropic exchange interactions

Magnetic exchange interactions can produce orders that are not necessarily ferromagnetic or antiferromagnetic, in addition to being extremely complex. Instead of collinear spins, some magnetic systems contain canted spins. In these magnetic systems, the exchange Hamiltonian is antisymmetric under the exchange of two spins and moreover incorporates an anisotropic term. The spin-orbit interaction in conjunction with the lack of inversion symmetry produces this anisotropic exchange interaction, also referred to as the Dzyaloshinsky-Moriya interaction [20], in which the excited state of one ion interacts with the ground state of another ion. One way to express the interaction Hamiltonian is as:

$$H = D_{12}(S_1 X S_2) \tag{1.8}$$

With D_{12}=$-D_{21}$. However, this kind of interaction tries to force two spins to be at right angles in a plane perpendicular to vector D to ensure that the energy is negative. Because of this, the interaction favours a small canting of the spins, which is the foundation of all chiral magnetic structures, including skyrmion. The fundamental conditions for the existence of Dzyaloshinsky-Moriya interaction in a system are strong spin-orbit interaction and the absence of inversion symmetry. A non-collinear spin structure is significant because for both parallel and antiparallel spins, the cross-product disappears. It was discovered that the interaction is maximised in rhombohedral and perovskite oxides like α-Fe_2O_3, $MnCO_3$, $CoCO_3$ etc, because it causes the phenomenon of weak ferromagnetism depending on how vector D is arranged.

Collinear AFM

Spin canted AFM

1.4 Magnetic anisotropy

Magnetic anisotropy is the term used to describe a material's magnetic property that changes as it crystallographically orients. This is a crucial characteristic of magnets that are permanent. Magnetic anisotropy controls coercivity and remanence and has a major effect on hysteresis loop forms. This reliance produces both simple and complex instructions. Since the easy axis is an energetically advantageous direction of magnetisation, it is easier to magnetise material in easy directions than in hard directions, where the system's total magnetisation will tend to lie along it. Due to its exploitation for material with significant commercial value, this topic is often very interesting. The following sections examine several forms of magnetic anisotropy.

1.4.1 Magnetocrystalline anisotropy

An intrinsic anisotropy known as magnetocrystalline anisotropy can be thought of as a force that pushes the magnetization to align in a specific crystallographic direction. The spin-orbit interaction and crystal field interaction are the sources of this type of anisotropy. Actually, the material is magnetized by the energy differential between hard and easy directions. As an illustration, magnetite has hard and easy directions [100] and [111] respectively [5].

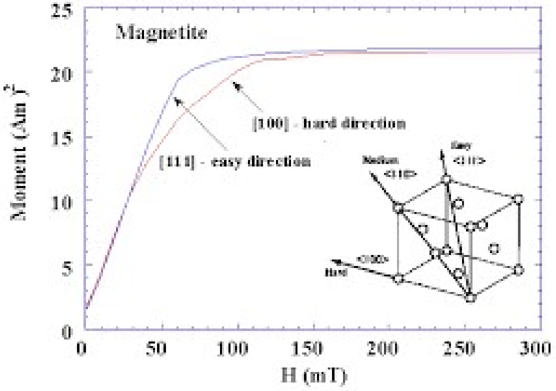

Here, we can see that, regardless of the axis along which it is applied, the saturation magnetisation remains constant, but the field needed to reach the value varies. Since the applied field must work against the anisotropy force in order to move the magnetisation vector away from an easy direction, anisotropy energy, also known as crystal anisotropy energy, needs to be stored. The anisotropy energy for cubic crystals is expressed as

$$E = K_0 + K_1(\alpha_1^2\alpha_2^2 + \alpha_2^2\alpha_3^2 + \alpha_3^2\alpha_1^2) + K_2(\alpha_1^2\alpha_2^2\alpha_3^2) + \ldots\ldots\ldots\ldots$$

Where K_0, K_1, K_2 are anisotropy constants at a particular temperature and $\alpha_1, \alpha_2, \alpha_3$ are direction cosines of the magnetization vectors with respect to the crystallographic axes. The term K_0 is independent of angle and is usually neglected. The sign of K_1 determines the direction of the easy magnetization when K_2 is zero. If K_1 is positive $E_{100} < E_{110} < E_{111}$, hence E_{100} is the easy direction because it has minimum energy as compared to other crystallographic directions. Similarly, if K_1 is negative, $E_{100} > E_{110} > E_{111,}$ and the easy direction is E_{111}. When K_2 is not zero, the values of both K_1 and K_2 determine the easy direction. The anisotropy decreases with increasing temperature and vanishes at the Curie temperature.

1.4.2 Shape anisotropy

An extrinsic anisotropy is shape anisotropy. It results from long-range dipolar interaction and is caused by the magnetic specimen's form. The demagnetising field will not be equal in all directions when a particle is not perfectly spherical, resulting in the creation of one or more easy axes. Because of their form, non-spherical polycrystalline materials with no preferred orientation can cause anisotropy. Compared to a short axis, a long axis is easier to magnetise. because a short axis has a stronger demagnetising field. The shape anisotropy of a spherically shaped object is zero. Utilising this type of anisotropy, one-dimensional nanostructures are employed for high-density data storage.

1.4.3 Exchange anisotropy

When a ferromagnet and an antiferromagnet interact, exchange anisotropy results. This interaction is often seen in a single-domain particle system. Under an applied field, the antiferromagnets drop below their Neel temperature, causing the exchange anisotropy, which is unidirectional and includes the pinning of moments in a ferromagnetic layer by an adjacent antiferromagnetic layer. Exchange anisotropy is the cause of the hysteresis loop shift. Because ferromagnetic-antiferromagnetic bilayers have so many uses, including high-density data storage, spin valves, and spintronics, there has been a lot of interest in their combination.

1.4.4 Surface anisotropy

Surface anisotropy is important in nanoparticle systems, because the relative spins at the surface are bigger in nanoparticle systems, surface anisotropy is significant. Less coordination with neighbouring spins and symmetry breaking at the surface are the causes of it. Surface anisotropy is largely determined by surface ligands and other components of the electrical environment. Neel's surface anisotropy, which considers the symmetry of the nearby atoms at the surface, sheds more light on surface anisotropy. The surface anisotropy expression is provided by

$$H_{surf} = \sum_{i \in sur} K_{surf} (S_i . v_i)^2 \tag{1.9}$$

$$v_i = \sum_{j \in neighb} r_{ij} \tag{1.10}$$

Where K_{surf} is a surface anisotropy constant and v_i is the anisotropy axis direction.

1.4.5 Induced anisotropy

When applied stress creates an easy direction of magnetisation, the outcome is induced anisotropy. It can be created through processes like annealing, casting, etc. It isn't inherent in the substance.

1.5 Magnetism at nano level

In the research sector, nanoscale magnetism is a lively and incredibly exciting issue. Because of their finite size and surface effect, the nanoparticles display a wide range of peculiar and fascinating magnetic properties, such as single domain nature, superparamagnetism, and modulation in coercivity with particle size. We examine the magnetism of nanoparticles in the next section.

1.5.1 Single domain particles

A domain wall made of bulk magnetic material divides each domain in order to lower the net free energy of the system. Below the critical size, the production of domain walls requires more energy than the decrease in magneto-static energy, making the development of domains energetically unfavourable [21]. As a result, only the construction of a single domain is encouraged. In fact, ferromagnetic materials have a minimum domain size; further reduction of the grain size will lead to a critical size at which the grain can no longer support a wall. This suggests that domains could not form from a single particle of a size comparable to the minimum domain size. The critical size of the domain is determined by the balance of the magnetostatic energy, anisotropy energy, and exchange energy. The diameter of the critical single-domain is provided by

$$D = \frac{72\sqrt{A_{ex}K}}{\mu_0 M_s^2} \tag{1.11}$$

Where A_{ex}, K and M_s are exchange stiffness, magnetic anisotropy constant and saturation magnetization respectively. The incredibly difficult process of spin rotation will cause the magnetisation of a single domain particle to vary. because single domain particles are magnetically hard and have higher coercivity and remanence than multidomain particles. The magnetisation for the single-domain particles comes from the Stoner-Wohlfarth model [22]. Given a system whose magnetisation is at an angle to the direction of the magnetic field and a magnetic field of strength H applied at an angle with the domain's easy axis, the system's energy density is given by

$$E = KSin^2(\theta - \varphi) - \mu H M_s Cos\varphi \qquad (1.12)$$

1.5.2 Superparamagnetism

In ferromagnetic or ferrimagnetic single-domain particles, superparamagnetism is a significant finite-size effect. The anisotropy energy causes the magnetisation in a single-domain particle to hold in a specific direction. However, when the particle size falls, the anisotropic energy reduces and the thermal energy increases [23]. Therefore, even in the absence of an applied field, thermal fluctuations lead a particle's magnetisation to flip from one easy direction to the other. Superparamagnetism is the state in which a material exhibits paramagnet-like behaviour with an extremely high effective magnetic moment per atom when the thermal energy exceeds the anisotropy energy. Because heat energy flips the magnetisation, the systems show zero remanence and coercivity. The average relaxation time required to flip the magnetization is given by the Neel-Brown expression [24].

$$\tau = \tau_0 exp\left(\frac{KV}{k_B T}\right) \qquad (1.13)$$

Where τ_0, K, V, k_B, T represent the pre-exponential factor, anisotropy constant, volume of the particle, Boltzmann constant and temperature respectively. A particle's superparamagnetism depends on the measurement time in addition to temperature. The particles exhibit superparamagnetic behaviour if the measurement time is much greater than the relaxation time. If the measurement time is significantly shorter than the relaxation period, the nanoparticle's magnetic moment is said to be in the blocked condition. The superparamagnetic blocking temperature is the temperature at which the relaxing time and the measurement time are equal. For a measurement time of 100 s, the blocking temperature T_B can be computed using the formula

$$T_B = \frac{KV}{25k_B} \qquad (1.14)$$

Below T_B the anisotropy obstructs the free movement of the magnetic moment, while beyond T_B, the system exhibits superparamagnetic behaviour.

1.5.3 Variation of coercivity with particle size

The Coercivity of tiny particles is very sensitive to size variation. When the particle size reduces, the coercivity usually rises, achieves a maximum value at a specific size, and then tends to zero as the particle size continues to drop. The schematic representation of the coercivity variation with particle size in fig. There are three regions in it.

1. Multidomain: The domain wall motion changes the magnetization. The size dependence of coercivity is experimentally found to be given by

$$H_c = a + \frac{b}{D} \tag{1.15}$$

Where a and b are constants and D is the particle diameter.

2. Single domain: The coercivity reaches its maximum value in this size range and the particles become a single domain below a critical diameter D_s. Here the smaller changes in their magnetization by domain rotation. As the particle size further decreases below D_s the coercivity decreases, due to thermal effects. The variation of coercivity in this range is given by

$$H_c = g - \frac{h}{D^{3/2}} \tag{1.16}$$

3. Superparamagnetic region: At a sufficiently small size the particle exhibit superparamagnetism with zero coercivity. Thermal effects are now powerful enough to spontaneously demagnetise a previously saturated assembly of particles.

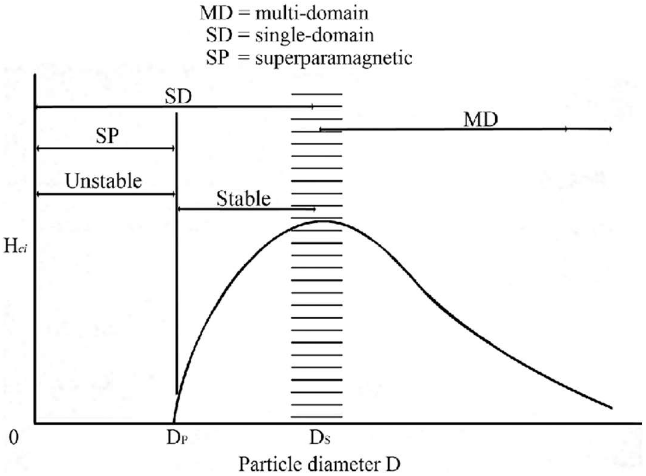

Figure 1.13 Variation of coercivity with particle size [25]

As the particle diameter shrinks, a magnetic multi-domain state transforms into a single-domain size, as can be understood from the schematic representation of a variation of coercivity with particle size. D_s represents the diameter at which this change from a multi-domain to a single domain occurs. A Single Domain particle's coercivity value is often high, indicating that reversing its magnetisation is more challenging. As a result, a magnetic field stronger than the

Single Domain particle's demagnetisation field must be applied. Particle size reduction below D_s causes the coercivity to drop because the thermal agitation energy outweighs the magnetic anisotropy energy and randomises the magnetisation [26]. In an extreme situation where the particle size decreases further, the coercivity is zero, resulting in a superparamagnetic state. The zero-coercivity diameter is indicated by D_p.

1.6 Ferrites

Ferrites are ferrimagnetic oxides made up of trivalent iron oxide combined with one or more bivalent oxides. Because ferrites have both simultaneous electrical and magnetic properties, they are commonly referred to as magnetic insulators. They are significant prospects for industrial applications because of their great mechanical hardness, high thermal stability, low eddy current, low dielectric loss, high magnetic permeability, and high electrical resistivity [27]. Researchers have focused on ferrites because of the need for electrical and magnetic qualities in the realm of advanced electronics and microwave devices. As of right now, ferrites are the greatest option for both traditional and novel applications.

1.6.1 Structure of ferrites

The typical formula for ferrites, according to Neel, is AB_2O_4, where A and B are metallic cations that are situated at tetrahedral (A site) and octahedral (B site) sites, respectively [28, 29]. Four groups are distinguished among ferrites based on their crystal structure**.**

a. Spinel ferrites

It is the ferrites' most significant category. Bragg and Nishikawa were the first to determine the spinel structure. They are represented by the formula MFe_2O_4, where M is any divalent ion, such as Mg^{2+}, Ni^{2+}, Co^{2+}, Fe^{2+}, etc., and they have a cubic structure. Al^{3+}, Cr^{3+}, Ga^{3+}, and other trivalent ions can also be used in place of Fe^{3+} ions. Octahedral and tetrahedral crystallographic sites are the two different forms found in spinel ferrites. There are eight MFe_2O_4 formula units in a unit cell. There are 64 tetrahedral sites in each unit cell, of which 8 are occupied, and 32 octahedral sites, of which 16 are occupied [30]. The distribution of cations in each site is dictated by the electronic configuration, electrostatic energy, and ionic radii. For spinel ferrite, the precise formula is $(M_{1-x}^{2+}Fe_x^{3+})[M_x^{2+}Fe_{2-x}^{3+}]O_4^{2-}$, the tetrahedral and octahedral sites are represented by the parentheses and square brackets respectively. Here x represents the degree of inversion defined as a fraction of A-sites (tetrahedral) occupied by Fe^{3+} ions. A unit cell of spinel ferrite is shown in **Figure 1.14**. Spinel ferrites are classified as:

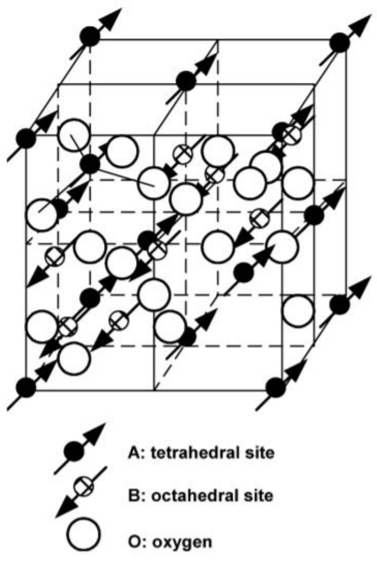

Figure 1.14 Unit cell of spinel ferrite [31]

1. Normal spinel ferrites

Tetrahedral sites are inhabited by all divalent metal cations, while octahedral sites are occupied by trivalent cations [32]. There is only one kind of cation that can fit at each location. In these kinds of structures, x equals to zero and the basic formula is $M^{2+}Fe_2^{3+}O_4^{2-}$. $ZnFe_2O_4$, $CdFe_2O_4$ are two examples of normal spinel ferrites.

2. Inverse spinel ferrites

Trivalent cations occupy both octahedral and tetrahedral sites, whereas divalent cations only fit into octahedral sites [32]. In this type of structure, x equals to one and the cation distribution can be written as $Fe^{3+}[M^{2+}Fe^{3+}]O_4^{-2}$. Fe_3O_4, $NiFe_2O_4$ are two examples of inverse spinel ferrites.

3. Mixed spinel ferrites

The divalent cations and trivalent cations are distributed at both tetrahedral and octahedral sites. Here the value of x lies between zero and one [33]. The cation distribution can be written as $M_{1-x}^{2+}Fe_x^{3+}[M_x^{2+}Fe_{2-x}^{3+}]O_4^{2-}$. $Ni_xZn_{1-x}Fe_2O_4$, $Cu_xZn_{1-x}Fe_2O_4$ are two examples of mixed spinel ferrites. Most cubic ferrites at the nanosized scale have mixed structures.

b. Hexagonal ferrites (Magnetoplumbite)

Particularly, ferrimagnetic oxides with a hexagonal magnetoplumbite-type crystal structure are hard magnetic materials. $MFe_{12}O_{19}$, where M is an element such as barium, strontium, lead, calcium, etc., can be used to represent them [34]. Because of their strong coercivity, hexagonal ferrites are difficult to magnetise in a different direction. Due to their high electrical resistivity, high magnetic permeability, and moderate permittivity, hexagonal ferrites are used in a variety of applications such as magnetic recording media, military aircraft radar absorbing paints, permanent magnets, and microwave devices like filters, resonance isolators, circulators, and phase shifters.

c. Garnet

It is a class of hard magnets with an orthorhombic crystal structure. The general formula for garnet is $M_3Fe_5O_{12}$, where M is one of the rare earth elements like Sm, Eu, Gd, Tb, Dy, Er, Tm, Lu, or Y [35]. It can only tolerate trivalent iron and trivalent rare earth elements. The absence of additional valencies results in extraordinarily high electrical resistivity and very low losses in the microwave area. As single crystals, these are transparent and display fascinating magneto-optical properties. Yitrium ferrite is a well-known example of garnet. Garnet ferrites are used in microwave technology, optical, magneto-optical and acoustic applications.

d. Ortho-ferrite

It has an orthorhombic crystal structure. It can be represented by a chemical formula $MFeO_3$, where M is the rare earth element. Most of the Ortho-ferrites are weak ferromagnetic materials [36]. Lanthanum orthoferrite, Gadolinium orthoferrite, Dysprosium orthoferrite are some examples of Ortho-ferrite. Ortho-ferrites are used in communication techniques, in sensors of magnetic fields and in optical internet.

1.6.2 Magnetic properties of ferrites

The existence of irregular 3d electrons dispersed in an uneven amount at the tetrahedral and octahedral sites in ferrites is the cause of magnetism. Neel's two-sub lattice model of ferrimagnetism describes the ferrimagnetic type ordering of spinels in general. The interchange of cations between the two sites and their occupancy have a significant impact on the magnetic characteristics of ferrites. Because of the great separation between the cations, direct interactions are minimal in spinel ferrites. Even at low temperatures, the saturation magnetisation of all ferrites is relatively modest. The magnetisation will be greater than the reported value if every spin is parallel. Based on Heisenberg's exchange forces, Neel's two-sub lattice model of ferrimagnetism was able to provide a reasonable explanation for the low saturation magnetisation in 1948 on the basis of Heisenberg's exchange forces. Ferrites, according to Neel, have a magnetic structure that is quite distinct from any structure that has been identified previously. Using Heisenberg's exchange forces as a foundation, Neel explained the ferrites' spontaneous magnetisation. The following formula provides the exchange energy between two nearby atoms with spin angular momentum, $E_{ex} = -2J_{ex}S_i.S_j$, where $E_{ex}$is the exchange energy, S_i and S_j are the total spins of adjacent atoms and J_{ex} is the exchange integral. If $J_{ex}>0$ favours parallel spin and $J_{ex}<0$ favours antiparallel spin. The magnetic ions in spinel ferrites have the potential to interact in three different ways, and the superexchange process allows for these interactions to occur between the intermediate O^{2-}ions. Three types of interactions can occur: A-O-A, B-O-B and A-O-B. Among them, the strongest superexchange interaction is A–O–B [37, 38]. The weakest interaction is A-O-A, which is about ten times weaker than B-O-B. Both the angle between the magnetic ions and the distance between the metallic ions and the oxygen determine how much of these interactions occur. The largest exchange energy will occur at an angle of 180, and as distance increases, the energy rapidly declines. The difference between the ions at the A and B sites is therefore equal to the resulting magnetic moment. Since the saturation magnetic moment for the B lattice (M_B) is generally greater than that of the A lattice (M_A), the resulting saturation magnetisation (M_s) can be stated as $M_s = M_B - M_A$. Ferrites are divided into the following categories according to their magnetic properties:

a. Soft ferrites

All soft ferrites are given by the formula MFe_2O_4, where M is an ion of a transition metal. Soft ferrites are ferrimagnetic materials with inverse spinel structures that belong to a cubic crystal system. They have low coercivity and remanence because they are easily magnetized and demagnetized by introducing a modest magnetic field. The material may change its magnetization orientation without using a lot of energy. Soft ferrites are frequently used in radio frequency inductors, electromagnetic cores of transformers, and switching circuits in computers due to their high magnetic permeability, intrinsic high resistivity, low eddy current losses over a wide frequency range, and stability over a broad temperature range. Examples of soft ferrites are manganese-zinc ferrite and nickel-zinc ferrite.

b. Hard ferrites

Hard ferrites are permanently magnetized and exhibit magnetoplumbite structures. They are challenging to magnetize and demagnetize due to their high coercivity and remanence values. They have a harsh magnetic property because of large magnetocrystalline anisotropy caused by spin-orbit interaction. Permanent magnets are one of the main uses for hard ferrites. Hard ferrites include, for example, barium ferrites and strontium ferrites.

1.7 Ferrofluids

Ferrofluids are liquid carrier medium-suspended nanomagnetic single domain particles in a stable colloidal suspension [39]. It is a novel functional material that possesses both the magnetism of a solid magnetic substance and the fluidity of a liquid. Their composition gives them the special capacity to interact with a magnetic field and to have fluidity. The three main parts of it are the surfactant, base fluid, and single-domain magnetic nanoparticles [40]. Depending on the uses, the carrier liquid may be polar or nonpolar. Stephen Pappel created ferrofluid in 1960 to use it in space applications. To keep the particles from settling in a magnetic or gravitational environment, Brownian motion is adequate [41]. The particles are superparamagnetic due to their small size; each one functions as a single magnetic domain that is randomly capable of flipping its magnetisation in response to temperature. Because of this Neel relaxation and rotating Brownian relaxation, ferrofluids show no remanent magnetisation at room temperature once the external magnetic field is withdrawn. By volume, a typical ferrofluid has roughly 5% magnetic particles, 10% surfactant, and 85% carrier. Ferrofluids offer the benefit of having a high degree of fluidity as well as the ability to modify their performance and attributes with the use of an external magnetic field. A fluid's shelf life and stability determine its quality. To prevent the magnetic particles from clumping together due to the attractive Van der Waals contact, they must be surfaces using an appropriate surfactant by either electrostatic or steric repulsion. Ferrofluid research is driven by both fundamental and practical interests**. Figure 1.15** illustrates ferrofluid's reaction in the presence of a non-uniform magnetic field.

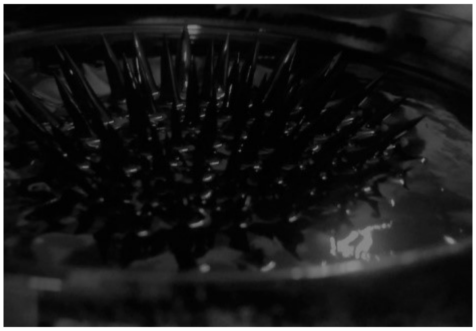

Figure 1.15 The response of ferrofluid in the presence of a non-uniform field

1.7.1 Stability criteria of ferrofluid

One of the most important factors in determining a fluid's applicability for different uses is its stability. The stability of the ferrofluid is determined by the thermal contribution and the equilibrium between repulsive and attractive interaction [42]. To avoid particle sedimentation and preserve a well-dispersed suspension, the particles' thermal energy must be high enough to allow for sufficient mixing of the suspensions.

a. Stability in a magnetic field

When ferrofluid is subjected to an external magnetic field, a magnetic field's greater intensity areas attract particles, whereas thermal movements balance the field's pull and give statistical movements that enable the particle to move the entire volume of the fluid. A high ratio of thermal energy to magnetic energy provides stability against segregation.

$$\frac{Ther \quad energy}{Magnetic\ energy} = \frac{k_B T}{\mu_o MHV} \geq 1 \tag{1.17}$$

Substituting the volume of a sphere and rearranging it gives an expression for particle size for stability.

$$D \leq \left(\frac{6k_B T}{\pi \mu_o MH}\right)^{1/3} \tag{1.18}$$

b. Stability in a gravitational field

Gravitational force forces the particles downward continually, and heat agitation prevents sedimentation by stabilising the particles. Gravitational energy is negligible when one accounts for magnetic energy. For stable fluid, the gravitational to magnetic energy ratio is therefore smaller than one.

$$\frac{Gravitational\ energy}{Magnetic\ energy} = \frac{\Delta\rho g L}{\mu_0 MH} < 1 \tag{1.19}$$

c. Stability against magnetic agglomeration

Particle collisions occur often in ferrofluids because they typically contain 10^{23} particles per cubic metre. This leads the particles to stick together and create clumps. Because the particles are permanently magnetised, when they are aligned and there may be a dipolar exchange that results in a dipole-dipole pair energy, the maximum energy to overcome the magnetic attraction between a pair of particles occurs. When the surface of the particles come into contact, this energy is given by

$$E_{dipole} = \frac{\mu M^2 V}{12} \tag{1.20}$$

To prevent particle agglomeration, thermal agitation must be stronger than this dipolar energy, and this stability condition necessitates the ratio, Thermal energy/dipole- dipole pair energy;

$$\frac{24kT}{\mu M^2 V} > 1 \tag{1.21}$$

This provides the fluid's steady particle size as,

$$d < \left(\frac{144 k_B T}{\pi \mu_o M^2}\right)^{1/3} \tag{1.22}$$

The particle size in a ferrofluid with a long shelf life is often found to be around 10 nm.

d. Stability against Van der Waals forces

Additionally, constant fluctuating electric dipole-induced dipole forces result in the existence of Van der Waals forces of attraction between neutral particles. Through a quantum mechanical interaction, the oscillating orbital electrons in one particle cause dipoles in the neighbouring particle. Taking precautions against these factors is also crucial. London's model predicts inverse sixth power laws between point particles, which Hamer extended to equal spheres. For spherical particles of diameter d and distance x, the interaction energy can be expressed as

$$|E_v| = \frac{A}{6}\left[\frac{2}{a^2+4a} + \frac{2}{(a+2)^2} + ln\frac{a^2+4a}{(a+2)^2}\right] \tag{1.23}$$

Where a=2x/d and A is Hamaker constant. This constant has a value of 10^{-19} Nm for magnetite in water. Unlike the magnetic dipole-dipole interaction energy, the interaction energy diverges at decreasing interparticle distance. Therefore, as long as the Hamaker constant has a finite value, thermal energy cannot stop coagulation. Thus, in order to maintain the colloidal stability of the system, particle contact must be avoided. The net interaction curve is shown in **Figure 1.16** for different energies.

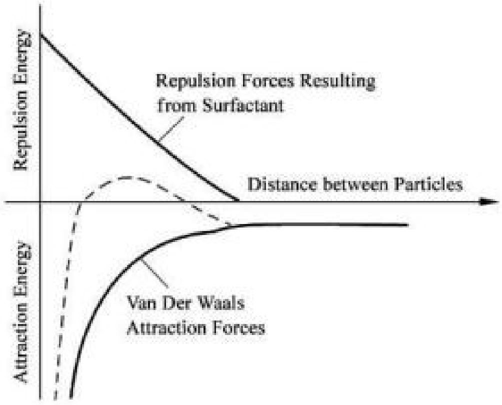

Figure 1.16 The net interaction energy curve [42]

1.7.2 Stabilization Techniques

The two main stabilisation methods for colloidal stability are steric repulsion and electrostatic repulsion [43]. The reason behind steric repulsion is the existence of long-chain molecules that have been adsorbed onto the surface of the particles, preventing them from contacting. To act as an effective solvent for polymer expansion, the linked polymer chains must be well suited to the base fluid. The inner particle core is typically better screened when grafting long polymer chains and high surface coverage. The freedom of the surface polymer chains decreases with the proximity of the grafted particles, which in turn lowers the mixing entropy. An osmotic action is also produced concurrently by the increased concentration of polymeric molecules in the space between the grafted nanoparticles. The physical foundation for steric stabilisation is mostly provided by the combined effects of lowered entropy and induced osmotic action. The most popular steric surfactants are oleic acid and related compounds. Through the application of basic or acidic radicals to form charges at the particle surfaces, electrostatic stabilisation works by causing the coulomb interaction between the particles to resist one another. Water-based systems make use of it. Citric acid and tetra methyl ammonium hydroxide are surfactants that offer ionic repulsion.

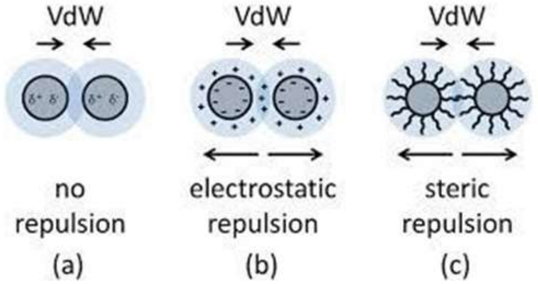

1.7.3 Classification of Ferrofluid

Based on the steric and electrostatic stabilization the ferrofluid is classified into two: surfacted ferrofluid and Ionic ferrofluid respectively.

1. Ionic ferrofluids

Ionic ferrofluids use electrically charged nanoparticles to keep the colloidal system stable [44]. Here, the particles' surfaces are exposed to basic or acidic radicals, which causes charges to form at the surfaces of the particles that oppose one another because of coulomb interaction. The liquid carrier of choice is usually water, and the pH of the solution can vary from 2 to 12, depending on which way the surface charge of the particle is orientated. Acid ionic ferrofluid (pH 7) contains positively charged nanoparticles, and alkaline ionic ferrofluid (pH > 7) has negatively charged particles. Citric acid and tetramethylammonium hydroxide are surfactants that provide ionic repulsion.

2. Surfacted ferrofluid

In order to prevent aggregation, surfactants such as aerosol sodium di-2 ethylhexyl-sulfosuccinate and oleic acid are deposited on magnetic particles to create surfactacted ferrofluids. Steric repulsion creates a physical barrier that stabilises the colloid and keeps the grains in the fluid [45]. A long-chain molecule adsorbs onto the particles, physically preventing them from approaching. A stable ferrofluid is produced when the magnetic particles are stopped from moving about in the solution by a physical barrier known as steric repulsion between the particles. It's crucial to employ adequate surfactants because not enough will result in a coating that isn't strong enough to resist van der Waals attractions. The particle is in contact with the fluid carrier, and the polar head of the surfactant is adhered to the particle. The zeta potential is generated by the surface charge of the suspended particles in the base fluid, resulting in a repulsive force between the particles. Since the repulsive energy of small particles is less, a large amount of zeta potential is required for a stable suspension repulsive force between suspended particles.

To generate an exterior hydrophobic layer, one layer of surfactant is required if the particles are dispersed in a nonpolar media like oil. The carbonic chain is in touch with the fluid carrier, and the surfactant's polar head is affixed to the particle surface. On the other hand, a double surfactation of the particles is required to produce a hydrophilic layer surrounding them if they are dispersed in a polar liquid like water. Surfactant molecules can have nonionic, anionic, or cationic polar heads. **Figure 1.17** displays the drawings of the ionic ferrofluid grain and the surfacted ferrofluid grain.

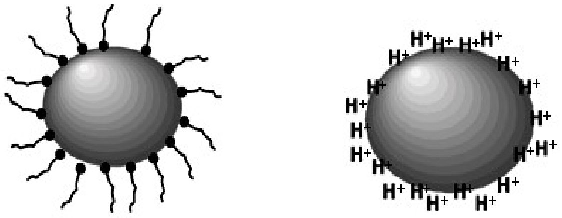

1a **1b**

Figure 1.17 Sketches of surfacted ferrofluid grain(1a) and ionic ferrofluid grain(1b) [43]

1.7.4 Surface Instabilities

The scientific community is drawn to ferrofluids because of their various instabilities, which allow for the suggestion of novel uses. Because they may generate a variety of patterns when subjected to magnetic fields, ferrofluids, for instance, can be utilised as tunable soft templates. These kinds of applications can be suggested by the way magnetic nanoparticles self-organise in ferrofluid when exposed to a magnetic field. Following are some examples of the various instabilities that can occur in ferrofluid:

1. Rosensweig Instability

Rosensweig instability is the interfacial instability on a ferrofluid's free horizontal surface when there is a continuous magnetic field perpendicular to the surface [46]. The magnetisation of the ferrofluid and the intensity of the applied magnetic field determine surface instability. When the applied magnetic field is greater than the stabilising forces resulting from surface tension and gravitational force, the instability mechanism takes place. The spikes begin to form at the container's boundaries and spread towards the centre when the field reaches a critical amount. The initial disturbance of the surface decreases towards a flat surface as the applied field strength approaches the critical field. Ridges replace the flat surface when the magnetic field is increased in a quasi-static manner [47]. Moreover, the pattern changes to a hexagonal shape as the magnetic field increases. The applied field strength increases and the spike height increases at the critical wave number condition. The pattern changes from hexagonal to square when the applied magnetic field reaches a second threshold value.

2. Labyrinthine pattern

Not specific to ferrofluids, but another kind of pattern that can be produced by them is the labyrinth. When a ferrofluid containing an immiscible nonmagnetic fluid is put between two closely separated glass plates and a vertical magnetic field is applied, a pattern emerges [48]. The conflict between the fluid's surface tension and the magnetic dipolar interaction causes it to arise. With a rise in the applied magnetic field, the pattern's shape gradually changes from a circular drop to several bifurcation configurations. More precisely twisted patterns were obtained by systematically varying the horizontal cell wall spacing and applying a stronger magnetic field. Using an energy minimisation approach, Rosensweig et al. (1983) estimated the Labyrinth spacing and concluded that Labyrinthine patterns are at equilibrium. In reality, a steady state response produces the labyrinthine structure. Goldstein et al. investigated the matter using a "dynamic theory" method, showing how different final states of ferrofluids under the same magnetic field can arise from the same initial configuration. In a global energy landscape, these analogous states are steady states that are not in equilibrium.

3. Benard-Marangoni instability

This type of instability is brought about by the temperature dependency of surface tension, which is additionally impacted by the fluid's rheological properties [49]. Consider a scenario in which a free surface surrounds a liquid layer that is heated from below. Fluid rising at a particular point in the layer will cause a hot spot to form on the free surface. Surface tension thus decreases, causing a flow to diverge at the free surface and drive the fluid upward even farther.

4. Rayleigh-Taylor instability

This type of fingering instability happens when a magnetorheologically active fluid is positioned above a less dense fluid, causing fingering at their interface [50]. The fluids are of different densities.

1.8 Fundamental study of theoretical calculation using DFT

In order to approximate wave functions and energy for atoms and ions, Hartree developed the Hartree function in 1927 [51]. A few years later, his pupils Fock and Slater each put forth a self-consistent function that took into account the multi-electron wave function and Pauli principles. This was done in the form of a determinant of one-particle orbitals, or Slater-determinant, in order to overcome the electron system's complete disregard for anti-symmetry.

The Hartree-Fock model was not widely employed until the 1950s due to its difficult computations. The underlying premise of the Hartree-Fock model, however, asserts that the actual outcome can only be approximately predicted. In the same year 1927, Thomas and Fermi created a statistical model to compute the energy of atoms by estimating the electron distribution in an atom as the Hartree function. They were able to calculate the atom's energy by defining its kinetic energy as a function of electron density and adding two standard terms for nuclear-electron and electron-electron interactions (both of which can be represented in terms of electron density). It did not have the atom's exchange energy at first, which comes from the Pauli principle and is represented by the Hartree-Fock theory. Dirac expanded the theory in 1928 by including an exchange energy functional factor. The Thomas-Fermi model is an important initial step, however at the moment it has relatively few applications because it is not very precise for most of them. The approximation of the kinetic energy functional term is the main source of mistake; the total disregard of the electron correlation effect is the source of inaccuracy in the exchange energy. On the other hand, it serves as the forerunner of the Density Functional Theory (DFT). The DFT Mansion Corporation was founded by Hohenberg and Kohn after they published a paper in 1964. The basic idea underlying DFT is to use the functional of electron density, which has only three variables, in place of the complex and challenging-to-compute many-electron wave function, which has three N variables (N is the number of electrons, and each electron has three spatial variables). A function that transfers a number to another function is called a functional. Consequently, the new system reduces the number of variables we need to manage from the massive 3N variables to just 3. This makes managing only three variables much easier. The first theorem published by Hohenberg and Kohn states that the ground state energy is a function of electron density and solely depends on electron density. their second theorem showed that by minimising the energy of the system according to the electron density, the ground state energy could be obtained [52]. It is important to recognise that H-K theorems do not specify the nature of the one-to-one mapping relations that exist between electron density functional and system properties. So, instead of "minimising the system energy," the most widely used method is the Kohn-Sham technique. In a work published just a year after the important study by Hohenberg and Kohn, Kohn and Sham reduced the multi-electron problem to one of non-interacting electrons in an effective potential. This potential consists of the external potential as well as the results of the electron-electron Coulomb interactions, such as the exchange and correlation interactions [53].

Handling the exchange and correlation relationship is difficult with KS-DFT. As of right now, there isn't a systematic way to solve the energy exchange and correlation problem. On the other hand, the easiest approximation is the Local-Density Approximation (LDA). The foundation of LDA is the uniform electron gas model, which is used to derive the exchange energy—whose exact value can be found in the Thomas-Fermi model and the correlation energy from fits to the uniform electron gas. A Slater determinant of orbitals can be used to exactly define the wave function of the system, which can be simply described as a non-interacting system in an effective potential. On the other hand, the exchange-correlation part of the total energy functional is poorly understood.

DFT has been more and more common for solid-state physics computations since the 1970s. Unlike other methods for solving multi-body problems in quantum mechanics, LDA yields strong conclusions backed by experimental data. However, DFT was still unreliable in the field of quantum chemistry until the 1990s, when approximation techniques were significantly improved to better explain the exchange-correlation interaction. DFT is currently commonly utilised for electrical structure simulations. It is still difficult to use DFT to tackle strongly correlated systems, semiconductor band gaps, and strong dispersion systems. DFT is still being developed as a result.

1.9 Motivation of the present study

For a long time, scientists and researchers have had the ambition of creating a homogeneous fluid with magnetic properties, but their efforts to melt metallic magnets in order to turn a solid into a liquid have been unsuccessful because, when heated over a certain temperature known as the Curie Temperature, all magnetic materials have the potential to lose their magnetic characteristics. Since ferrobluids behave like ferromagnetic materials and have fluid characteristics while being able to be moved by a magnetic field, they are quite interesting. Ferrofluids have become more and more sought after in a variety of technological and biomedical area applications during the past 50 years. Ferrofluids applications in our society increasing day by day from space technology to the medical field and even our daily life. Ferrofluid could play a crucial role in making stronger and more affordable armour as part of the effort to make India as self-reliant in the defence sector. Natural patterns exhibit remarkable intricacy and similarity over length scales that can span from the individual component to the ecosystems that comprise them. The ferrofluid also exhibits a richness of different patterns, which depends on the strength of the applied magnetic field and the interfacial tension of the fluid. From a fundamental perspective, magnetic nanofluid is an ideal platform for investigating Rosensweig instability and pattern formation. The ferrofluid can also be used to create patterns for computer-aided art by applying an external magnetic field, which is something that contemporary technological artists are exploring. Due to their superparamagnetic nature, the constituents exhibit complex relaxation behaviour under a magnetic field and also they exhibit a variety of altered optical characteristics in the presence of a magnetic field. These factors contribute to enhancing the interest to study fundamental magnetism at the nanolevel.

Iron oxide oxides play a very important role in material science. Among them, Hematite is the most stable form of iron oxide in the air at ambient conditions. Hematite nanoparticles have attracted a lot of interest due to their abundance, low cost, low toxicity, high chemical stability, and tunable optical and magnetic properties in catalytic reactions, gas sensors, magnetic storage systems, photoelectron chemical water splitting and biological applications. Nanoparticle synthesis is one of the most interesting areas in the research field. The nanoparticles can be synthesized through different chemical, physical and biological methods. Among them, the green method has gained more attention as a reliable, sustainable and eco-friendly protocol for synthesizing a wide range of nanoparticles. A significant public health concern is the growth of infectious diseases brought on by various dangerous bacteria and the emergence of new bacterial stains that are resistant to already available medicines. Since bacteria show opposition against several common antibacterial agents, contagious diseases continue to be one of the greatest threats to human health worldwide. Thus, there is a clear motivation to create new antibacterial agents. Due to the spread of antibiotic resistance among microbial pathogens, the interest in studying the antimicrobial activity of nanoparticles are also increased. Water is essential to life and is therefore necessary for all living things. However, the quality of water has been severely compromised due to the swift expansion of industrialisation and an increasing human population. It is a worldwide problem because industrial wastewater discharges contain a variety of toxins.

Among all of these contaminants, dyes are the most persistent and difficult to break down. Due to the fact that these contaminants do not mineralise as well using conventional procedures. Many novel techniques are used for the removal of contaminants from water, like coagulation, ozonation, electrochemical degradation, and photocatalytic degradation. Among them, photocatalytic degradation is one of the simplest and most efficient methods for purifying water. This fact encouraged to me for doing photocatalysis. Since magnetic nanoparticles have a higher surface area to volume ratio and may be recovered and recycled after a reaction, their application as catalysts in organic transformations has garnered a lot of attention lately. This is another objective of the present study.

A significant development in the field of carbon nanomaterials was the successful mechanical exfoliation of graphene that was one atom thick from graphite using the Scotch tape technique. Since then, we have seen a surge in two-dimensional (2D) material research, which has resulted in the discovery of novel 2D materials. The exfoliation of a few layers of a 2D material from its layered counterpart is quite easy. But the scientist has faced trouble in extracting a monolayer or a few layers from a Non-van der Waals material. But in 2018 Balan etal. Successfully exfoliated freestanding 2D sheets with intrinsic magnetism from bulk Hematite material. Different techniques have been used in order to induce magnetism in 2D atomic layers. Till that time the research community believed that theoretically, the magnetic ground state is impossible in 2D. Yet because of their intriguing material characteristics and predominance of quantum phenomena, two-dimensional materials have served as a breeding ground for a great deal of basic and applied scientific inquiry. So yet another motive for the present study is to synthesize 2D hematene material from a synthesized non-layered material, not from a commercially available bulk material. As environmental deterioration and energy scarcity issues became significant barriers influencing human progress, people's attention has been drawn to the development of sustainable energy technology. By using solar energy to produce clean and renewable hydrogen fuel, photoelectrochemical water splitting is a highly sustainable approach to mitigating the impending catastrophe. The integration of different components with unique structure features can effectively promote the PEC process. Hence we made a heterojunction with an extracted layer of Hematite and Titanium nanotube and studied the PEC performance, which is another motive of the present study.

Investigation of magneto-optical characteristics of ferrofluid is important for the development of optoelectronic devices such as optical modulators, optical switches, tunable grating, wavelength-division multiplexers, holographic optical tweezers, sensors etc. Ferrofluid is optically isotropic in the absence of an external magnetic field, once the external magnetic field is applied, they show anisotropic behaviour and exhibit magneto-optic phenomena like linear dichroism, faraday rotation, birefringence, magneto-optical transmission etc. A field-induced clustering or chain formation is found to explain the variation of the optical transmission with the applied field. The light's intensity changes with polarisation potentially provide information on the kinetics of relaxation and particle-particle interaction.

Analysing the light transmission as a function of the applied field allows one to assess the relative strength of the interparticle interaction and the particle's interaction with the field. Both ionic and steric ferrofluid’s linear dichroism behavior will be studied. They are of interest from a fundamental perspective since the light-matter interaction of magnetic particles can be studied. This is an area rich in Physics and offers an appropriate platform for studying such interactions. A hybrid fluid that has both the properties of plasmonics and magnetism will be a novel area of investigation. Due to the development of plasmonics, it is now possible to create a hybrid magnetic nanofluid based on magnetic iron oxide particles and noble metals like Ag, Au etc. It provides many applications in sensors, batteries, imaging and the medical field etc. One of the motivations of the present study is to synthesize magneto-plasmonic nanofluids using isotropic Ag nanoparticles. The effect of the magnetic field on different concentrations of Ag nanoparticles will be investigated in detail. Here we intend to study the magneto-optical properties of hybrid nanofluid using a homemade setup. Surface plasmon resonance is a promising technique for detecting biological and chemical objects, based on refractive index sensing through optical detection method. The effect of iron oxide nanoparticles in the presence of an external magnetic field on SPR is quiet interesting in both fundamental and application point of view. There are many works reported on the SPR, but very few works are reported on the effect of the external magnetic field on the SPR phenomenon. This is another motive of the present study. Nanostructure-based sensors are widely used in numerous fields including manufacturing, environmental monitoring, the chemical and petrochemical sector, food and beverage processing and industrial production.

Haematite has a tightly correlated electron system with 3d electrons and exhibits fascinating features due to spin, charge, and lattice degrees of freedom. Electronic structure computations using on-site The Coulomb interaction has been rigorously carried out in density functional theory using the Hubbard U technique (DFT + U), where the U value takes into account the high correlation effect. Theoretical prediction of densities of states and optical bandgap is yet another motive of the present investigation.

1.9.1 Objectives

1. Synthesis of iron oxide nanoparticles, fluids and films based on iron oxide.
2. Structural, magnetic, surface tension and magneto-optical characterization of the prepared nanoparticles, fluids and films.
3. Correlation of results.

References

[1]. Cullity, B.D. and Graham, C.D., 2011. *Introduction to magnetic materials*. John Wiley & Sons.

[2]. Peregrinus, P., 2020. The letter of petrus peregrinus on the magnet, ad 1269 (Vol. 1). Library of Alexandria.

[3]. Coey, J.M., 2010. *Magnetism and magnetic materials*. Cambridge university press.

[4]. Reis, M., 2013. *Fundamentals of magnetism*. Elsevier.

[5]. Moskowitz, B.M., 1991, June. Hitchhiker's guide to magnetism. In *Environmental magnetism workshop (IRM)* (Vol. 279, No. 1, p. 48). Univ. of Minn., Minneapolis, Minn: Inst. for Rock Magnetism.

[6]. Chikazumi, S., 1955. Physics of Magnetism (Wiley, New York, 1964), p. 554. *W. Känzig, Phys. Rev.*, *9*, pp.98-549.

[7]. Blundell, S., 2001. *Magnetism in condensed matter*. OUP Oxford.

[8]. Theiner, W.A. and Willems, H.H., 1984. Determination of microstructural parameters by magnetic and ultrasonic quantitative NDE. In *Nondestructive Methods for Material Property Determination* (pp. 249-258). Boston, MA: Springer US.

[9]. Spaldin, N.A. and Mathur, N.D., 2003. Magnetic materials: fundamentals and device applications. *Physics Today*, *56*(12), pp.62-63.

[10]. Weiss, P., 1907. L'hypothèse du champ moléculaire et la propriété ferromagnétique. *J. Phys. Theor. Appl.*, *6*(1), pp.661-690.

[11]. Heisenberg, W., 1985. *Zur theorie des ferromagnetismus* (pp. 580-597). Springer Berlin Heidelberg.

[12]. Pillai, S.O., 2006. *Solid state physics*. New Age International.

[13]. Jiles, D., 2015. *Introduction to magnetism and magnetic materials*. CRC press.

[14]. Goldman, A., 2012. *Handbook of modern ferromagnetic materials* (Vol. 505). Springer Science & Business Media.

[15]. Nolting, W. and Ramakanth, A., 2009. *Quantum theory of magnetism*. Springer Science & Business Media.

[16]. Roelofs, L.D., 1996. Phase transitions and kinetics of ordering. In *Handbook of Surface Science* (Vol. 1, pp. 713-807). North-Holland.

[17]. [16]. Anderson, P.W., 1950. Antiferromagnetism. Theory of superexchange interaction. *Physical Review*, *79*(2), p.350.

[18]. Heisenberg, W., 1985. *Zur theorie des ferromagnetismus* (pp. 580-597). Springer Berlin Heidelberg

[19]. Staruch, M.L., 2013. *Magnetotransport and multiferroic properties of perovskite rare-earth manganites*. University of Connecticut.

[20]. Moriya, T., 1960. Anisotropic superexchange interaction and weak ferromagnetism. *Physical review*, *120*(1), p.91.

[21]. Lee, E.W. and Bishop, J.E.L., 1966. Magnetic behaviour of single-domain particles. *Proceedings of the Physical Society*, *89*(3), p.661.

[22]. Tannous, C. and Gieraltowski, J., 2008. The Stoner–Wohlfarth model of ferromagnetism. *European journal of physics*, *29*(3), p.475.

[23]. Cullity, B.D., 1972. Introduction to Magnetic Materials, Addison.

[24]. Knobel, M., Nunes, W.C., Socolovsky, L.M., De Biasi, E., Vargas, J.M. and Denardin, J.C., 2008. Superparamagnetism and other magnetic features in granular materials: a review on ideal and real systems. *Journal of nanoscience and nanotechnology*, *8*(6), pp.2836-2857.

[25]. Osouli-Bostanabad, K., Aghajani, H., Hosseinzade, E., Maleki-Ghaleh, H. and Shakeri, M., 2016. High microwave absorption of nano-Fe3O4 deposited electrophoretically on carbon fiber. *Materials and Manufacturing Processes*, *31*(10), pp.1351-1356.

[26]. Park, Y., Adenwalla, S., Felcher, G.P. and Bader, S.D., 1995. Superparamagnetic relaxation of Fe deposited on MgO (001). *Physical Review B*, *52*(17), p.12779.

[27]. Dastjerdi, O.D., Shokrollahi, H. and Mirshekari, S., 2023. A review of synthesis, characterization, and magnetic properties of soft spinel ferrites. *Inorganic Chemistry Communications*, *153*, p.110797.

[28]. Snelling, E.C., 2002. Magnetic Materials. *Electrical Engineer's Reference Book*.

[29]. Reddy, D.H.K. and Yun, Y.S., 2016. Spinel ferrite magnetic adsorbents: alternative future materials for water purification?. *Coordination Chemistry Reviews*, *315*, pp.90-111.

[30]. Mmelesi, O.K., Masunga, N., Kuvarega, A., Nkambule, T.T., Mamba, B.B. and Kefeni, K.K., 2021. Cobalt ferrite nanoparticles and nanocomposites: Photocatalytic, antimicrobial activity and toxicity in water treatment. *Materials Science in Semiconductor Processing*, *123*, p.105523

[31]. Mathew, D.S. and Juang, R.S., 2007. An overview of the structure and magnetism of spinel ferrite nanoparticles and their synthesis in microemulsions. *Chemical engineering journal*, *129*(1-3), pp.51-65.

.[32]. Smit, J. and Wijn, H.P.J., 1954. Physical properties of ferrites. In *Advances in Electronics and Electron Physics* (Vol. 6, pp. 69-136). Academic Press.

[33]. Dekker, A.J., 1981. The Band Theory of Solids. In *Solid State Physics* (pp. 238-274). Palgrave, London.

[34]. Gerber, R., Šimša, Z. and Jenšovský, L., 1994. A note on the magnetoplumbite crystal structure. *Czechoslovak Journal of Physics*, *44*(10), pp.937-940.

[35]. Akhtar, M.N., Saleem, M. and Khan, M.A., 2018. Al doped spinel and garnet nanostructured ferrites for microwave frequency C and X-band applications. *Journal of Physics and Chemistry of Solids*, *123*, pp.260-265.

[36]. Birajdar, A.A., 2012. Introduction, types and applications of ferrites. *SMP College Murom Osama Bad, India*.

[37]. Valenzuela, R., 1994. Magnetic ceramics. *(No Title)*.

[38]. Murthy, V.R.K., Raju, K.J. and Viswanathan, B., 1992. Characteristics of materials for microwave devices. *Bulletin of Materials Science*, *15*, pp.213-217.

[39]. Rosensweig, R.E., 1988. An introduction to ferrohydrodynamics. *Chemical Engineering Communications*, *67*(1), pp.1-18.

[40]. Berkovsky, B.M., Medvedev, V.F. and Krakov, M.S., 1993. Magnetic fluids: engineering applications.

[41]. Bacri, J.C., Perzynski, R. and Salin, D., 1988. Magnetic liquids. *Endeavour*, *12*(2), pp.76-83.

[42]. Rosensweig, R.E., 1979. Fluid dynamics and science of magnetic liquids. In *Advances in electronics and electron physics* (Vol. 48, pp. 103-199). Academic Press.

[43]. Scherer, C. and Figueiredo Neto, A.M., 2005. Ferrofluids: properties and applications. *Brazilian journal of physics*, *35*, pp.718-727.

[44]. Massart, R., 1981. Preparation of aqueous magnetic liquids in alkaline and acidic media. *IEEE transactions on magnetics*, *17*(2), pp.1247-1248.

[45]. Clark, A.E., 1980. Ferromagnetic materials. *Magnetostrictive rare earth-Fe_2 compounds*, pp.531-589.

[46]. Cowley, M.D. and Rosensweig, R.E., 1967. The interfacial stability of a ferromagnetic fluid. *Journal of Fluid mechanics*, *30*(4), pp.671-688.

[47]. Gailītis, A., 1977. Formation of the hexagonal pattern on the surface of a ferromagnetic fluid in an applied magnetic field. *Journal of Fluid Mechanics*, *82*(3), pp.401-413.

[48]. Rosensweig, R.E., Zahn, M. and Shumovich, R., 1983. Labyrinthine instability in magnetic and dielectric fluids. *Journal of Magnetism and Magnetic Materials*, *39*(1-2), pp.127-132.

[49]. Cerisier, P., Perez-Garcia, C., Jamond, C. and Pantaloni, J., 1987. Wavelength selection in Bénard-Marangoni convection. *Physical Review A*, *35*(4), p.1949.

[50]. Sharp, D.H., 1984. An overview of Rayleigh-Taylor instability. *Physica D: Nonlinear Phenomena*, *12*(1-3), pp.3-18.

[51]. Szabo, A. and Ostlund, N.S., 2012. *Modern quantum chemistry: introduction to advanced electronic structure theory*. Courier Corporation.

[52]. Hohenberg, P. and Kohn, W., 1964. Inhomogeneous electron gas. *Physical review*, *136*(3B), p.B864.

[53]. Kohn, W. and Sham, L.J., 1965. Self-consistent equations including exchange and correlation effects. *Physical review*, *140*(4A), p.A1133.

Chapter 2

Experimental Techniques

Any investigation of materials involves the careful selection of experimental methods to guarantee the purity and easiness of the synthesis. Before any experimental research, proper characterization is also required to avoid drawing erroneous conclusions. The present chapter describes the synthesis methodologies and analytical techniques used to characterize the prepared samples in this investigation.

2.1 Co-precipitation

Chemical co-precipitation is one of the prominent methods of synthesizing uniform magnetic nanoparticles. This method has several advantages as compared to other methods such as high homogeneity of the final product, low-temperature and control morphology, large-scale synthesis of the product and high product field. In this method, a homogeneous composition is obtained by precipitation reaction of two or more cations. It typically involves the precipitation of Fe^{3+} and Fe^{2+} salts in the ratio 2:1 in an aqueous medium using a strong base such as NH_4OH, KOH etc; at room temperature or elevated temperature [1-3]. Stabilization methods like electrostatic stabilization or steric stabilization can be utilized to prevent the agglomeration of magnetic nanoparticles. The solution is then put through several processes like decantation and magnetic separation. A stable magnetic nanofluid is created by diluting and ultrasonically processing the cleaned precipitate. The nanoparticle formation can be explained based on LaMer's theory of nucleation and growth process. According to LaMer theory, the process can be divided into three stages, are shown in **Figure 2.1**[4, 5]; (I) A rapid increase in the concentration of free monomers in solution, which goes to critical value for nucleation, (II) burst nucleation of the monomer causes a large decrease in the concentration of free monomers in solution. After this threshold, the low concentration of monomers virtually eliminates nucleation, and the rate of nucleation is characterised as practically limitless; (III) after nucleation, growth is regulated by the monomer's diffusion through the solution [6].

At this point, the curve starts to fall due to an increase in the amount of solute needed for the expansion of produced nuclei before it once more reaches the critical threshold for nucleation. The nucleation step is complete at this point. The expansion of the generated stable nuclei under supersaturation below the critical level for nucleation without renucleation then continues to lower the solute concentration. The nucleation and development processes should produce monodispersed particles because of this distinct separation. Size control should be carried out during the nucleation step in such a system since the final number of monodispersed particles is only determined during the nucleation stage and maintained constant in the growth stage, and because controlling particle size is equivalent to controlling particle number. However, the reaction parameters such as temperature, pH, ionic strength, kind of basic solution, etc., have a significant impact on the produced particles' properties, including size, shape, and composition. Additionally, the iron oxide particles produced in this technique are frequently unstable; as a result, they need to be stabilized with functionalized polymers or low-molecular-weight surfactants. The crystallinity, size, and size distribution are determined by nucleation and growth. A smaller particle size can be attained by accelerating nucleation, changing the supersaturation, and adding surfactants to stop the growth. However, Co-precipitation is an excellent method for rapid production, but pH, temperature control and purity are crucial to maintaining their stoichiometry.

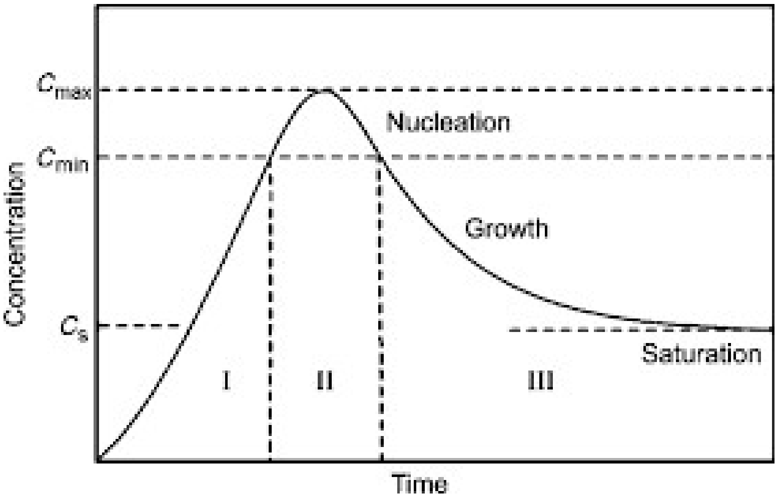

Figure 2.1 Lamer and Dinegar's model [7]

2.2 Hydrothermal Method

In the past ten years, hydrothermal synthesis has become a cutting-edge method for processing sophisticated materials for nanotechnology. Any heterogeneous reaction used to synthesise inorganic material in an aqueous medium above room temperature and pressure is referred to as hydrothermal [8-10]. In this case, a securely sealed stainless steel autoclave containing an aqueous mixture of precursors is heated to the boiling point of water, significantly increasing the autoclave's internal pressure over atmospheric pressure for the reaction. Without the need for post-annealing processes, high temperature and pressure combine to create extremely crystalline materials in a single step. Hydrothermal methods can now be used to create a wide range of nanomaterials, including magnetic nanoparticles. By modifying the parameters, such as the type and concentration of the precursors, the solvent, the stabilising agents, the reaction temperature, and the reaction time, this approach offers simple and accurate control over the end product's form, size, and crystallinity [11]. The direct crystallisation method known as hydrothermal synthesis typically entails two stages: nucleation and crystal development. Processing variables like as temperature, pH, reactant concentrations, and additives can be adjusted to obtain the desired final product morphologies and particle sizes. The phenomena behind the size and morphological control attained by varying the process parameters are the general nucleation and growth rates, which rely on supersaturation. Supersaturation is the ratio of the species' actual concentration to its saturation concentration. Nucleation occurs when the solute's solubility in the solution exceeds its limit or when the solution is supersaturated. The solute precipitates in crystal clusters with the potential to attain macroscopic size, and the process is irreversible. Following nucleation, the crystals go through a sequence of processes that include the integration of growth units—which are composed of the same materials as crystal entities but differ in their structures from the bulk solution—into the already-formed crystal entities, leading to larger crystals. Particle size reduces at higher temperatures because the nucleation process proceeds more quickly than the crystal formation. Longer reaction times lead to a dominant crystal development. Particle size reduces at higher temperatures because the nucleation process proceeds more quickly than the crystal formation. Larger particles are produced when the reaction period is extended because crystal formation takes precedence [12]. The most common solvent for hydrothermal reactions is water. Water's characteristics vary with temperature and pressure, particularly above the critical point. The water's critical temperature is 374°C, and its critical pressure is 22.1 MPa. The temperature and pressure-related decline in the water's dielectric constant is significant. The solute species' solubility is significantly decreased as a result of the dielectric constant's abrupt change, which raises the solution's supersaturation and promotes the nucleation and development of crystals. Ferrites are formed under hydrothermal circumstances primarily by the hydrolysis and oxidation of mixed metal hydroxides. The following is the mechanism by which metal oxide particles form from metal nitrate solution: Metal hydroxide is first produced by hydrolysing hydrated metal ions. After that, metal hydroxides undergo dehydration and precipitate as metal oxides [13].

$$M(NO_3)x + xH_2O = M(OH)x + xHNO_3 \qquad (2.1)$$

$$M(OH)x = MOx/2 + x/2\ H_2O \qquad (2.2)$$

2.3 Liquid exfoliation

Liquid exfoliation technologies are extremely promising and highly scalable approach to creating vast quantities of high-grade exfoliated 2D materials in an economically feasible way [14]. Traditionally, the fragmentation and exfoliation mechanisms have been just ascribed to the force generated by ultrasonic waves and their interaction with the solvent molecules. To create a suspension of matching 2D sheets, this method involves dispersing the bulk material in an appropriate solvent, sonicating it in an ultrasonic bath, and then centrifuging the mixture

[15]. To employ these 2D sheets for a variety of applications, they can be removed from the suspension using the appropriate techniques. Liquid exfoliation is just a broad term because there are several mechanics for various methods. The three primary liquid exfoliation techniques-ion intercalation, ion exchange, and sonication-assisted are depicted in **Figure. 2.2** [16]. The ability of layered materials to adsorb guest molecules in the gaps between their layers is exploited by the ion intercalation process. In a liquid environment, the ions are intercalated between the layers, which causes the swelling of the crystal and it reduces the energy barrier for exfoliation and diminishes the inter-layer Van der Waals attraction. The layers can then be entirely separated by thermal shock or ultra-sonication in an appropriate solvent. Electrostatic stabilisation of exfoliated sheets is possible by adding surfactants or surface charge. Ion intercalation techniques have a significant disadvantage in that they are sensitive to the ambient conditions [17].

Ion exchange technique makes use of the characteristic that various metal oxides, clays, and layered double hydroxides have an interchangeable interlayer of cationic counter ions. Such counter ions can exchange with protons by being soaked in an acidic solution. Large organic ions may later replace these protons, causing significant swelling. This type of swelling makes it easier to create negatively charged nanosheets by effective exfoliation using ultra sonication or shear mixing [18].

Applying ultrasonic energy to layered materials in a suitable solvent is a relatively contemporary method of liquid phase exfoliation. Exfoliation occurs when cavitation bubbles produced by ultrasonic waves burst and separate the stacked crystallites into high-energy jets. Modelling indicates that the solvent's surface energy needs to be similar to the layered materials in order to guarantee that the energy difference between the exfoliated and reaggregated states is negligible and ultimately removes the driving force for reaggregation. When the multilayer crystal is sonicated in a solvent, it exfoliates and forms nanosheets. Solvents having the appropriate surface energy, or "good" solvents, prevent the reaggregation of the exfoliated nanosheets. If "bad" solvents are used, reaggregation and sedimentation will occur [19, 20]. Using liquid exfoliation seems to be very simple. Nanosheets can be created by simply combining a few solvents with the bulk materials and using the right ultrasonic treatments. Nonetheless, choosing the appropriate solvent is essential because there are numerous varieties accessible. According to the classic solution theory, the ionization and polarizability of various components can be used to gauge the stability of a mixed solution.

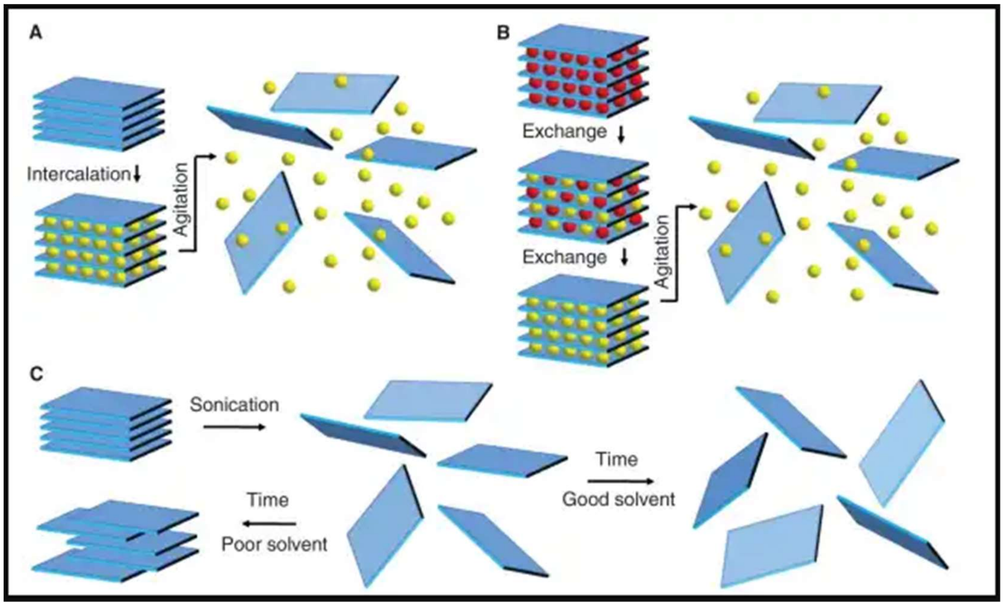

Figure 2.2 Schematics illustration of liquid exfoliation techniques [15]

2.4 Anodization

Anodization is a widely employed synthesis technique for preparing ordered TiO_2 nanotubes. The metal's surface oxide layer, which acts as the electrolytic cell's anode, is thickened via an electrolytic process [21]. This technique has several benefits, including the ability to generate nanotubes in a single step, the creation of highly ordered nanotube structures that are consistent in size, and simple control over tube shape and size. Nearly all anodization parameters, including the kind of electrolyte, pH, temperature, applied voltage, and current density, will have an impact on the results of a nanotube [22]. The oxidation and dissolution kinetics under a constant applied voltage is connected to the formation of TiO_2 nanotubes. In the process of forming oxides, water undergoes electrolysis to produce the anions O^{2-} and OH^- at the electrolyte or oxide interface. To interact with the metal surface, these anions diffuse through the oxide layer [23]. While this is happening, Ti^{4+} is moving through the oxide layer in the other direction and reacting with oxygen anions directly. TiO_2 is produced eventually as indicated by the equation below.

$$\mathbf{Ti+2H_2O \rightarrow TiO_2+4H^++4e^-} \quad (2.3)$$

During the dissolution reaction, F^- ions directly interact with TiO_2 at the electrolyte or oxide interface to generate $[TiF_6]^{2-}$, which is easily dissolved into the electrolyte due to its high solubility in water [24]. The F^- ions can interact and react with Ti^{4+} directly at the oxide or metal interface because they move at a speed roughly equivalent to that of the oxygen ions. The following are the necessary reaction equations [25].

$$\mathbf{TiO_2 + 4H^+ + 6F^- \rightarrow [TiF_6]^{2-} + H_2O} \tag{2.4}$$

$$\mathbf{Ti^{4+} + 6F^- \rightarrow [TiF_6]^{2-}} \tag{2.5}$$

The honeycomb-like porous structure changes into a collection of tubes with an F^- rich layer between the TiO_2 layer and the Ti metal due to the involvement of F^-. A hemispherical oxide or metal interfacial structure is created as a result. The difference between the rates of oxide production and dissolution response controls the overall growth rate and the length of the nanotubes. The current density drops significantly in this stage. The electrolyte's ion F^- reacts with TiO_2 to create the complex $[TiF_6]^{2-}$, which causes pits the size of nanometres to grow on the surface. In this step, the current density will slightly rise. The nano-size pits grow larger and form a tubular structure as a result of simultaneous oxidation and dissolution, and the process's current density again drops. The length and diameter of the nanotube will develop as long as the growth rate exceeds the rate of dissolution; otherwise, the growth will cease.

2.5 X-Ray Diffraction Analysis

X-ray diffraction technique is one of the most widely employed non-destructive techniques to study various parameters of the crystals such as crystal structure, crystallite size, lattice constants and strain. Each crystalline solid has a unique X-ray diffraction pattern. Electromagnetic radiation with energy between 200 eV and 1 MeV is referred to as X-rays. Debye and Scherrer developed the XRD powder technique in 1916. In a crystal, the atoms are organized in a periodic array. When an X-ray beam strikes a crystal surface, crystal atoms occupying specific locations in the crystal lattices operate as X-ray scattering centers. The phenomenon of diffraction takes place from the scattering centers and obtains a diffraction pattern, which gives information about the atomic arrangement within the crystal. Under some circumstances, X-rays that are scattered from various atoms reinforce one another and emit in particular directions [26]. An X-ray diffractometer is made up of three fundamental parts: an X-ray source, a sample holder and an X-ray detector. A non-diffracting glass slide is covered with a thin coating of powder sample, which is then exposed to an X-ray beam. The X-rays will be strongly absorbed and the intensity of the diffracted beam will diminish if an element in the specimen has an atomic number that is somewhat lower than that of the target metal. In X-ray diffraction (XRD), a specimen is exposed to a collimated X-ray beam with a wavelength of 1.5406 Å. The specimen's crystallographic planes diffract the beam in accordance with Bragg's law [27].

$$n\lambda = 2dsin\theta \tag{2.6}$$

Where n, λ, d and θ represent the order of diffraction, X-ray wavelength, interplanar spacing and diffraction angle respectively and it holds only if $\lambda \leq 2d$. Those X-rays that satisfy the Bragg Equation (equation 2.1) undergo constructive interference and a peak in intensity occurs. These signals are gathered by a detector, which produces an output in counts. Every material has a unique X-ray diffraction spectrum that makes it possible for researchers to recognize a specific substance by examining its diffraction peaks. The intensity of the diffracted X-rays was measured and plotted as a function of diffraction angle 2θ. From the 2θ values of the peaks, the lattice spacing (d) values are calculated using the equation. We have for any plane with index (h k l)

$$d_{hkl} = \frac{1}{\sqrt{\frac{h^2}{a^2}+\frac{k^2}{b^2}+\frac{l^2}{c^2}}} \tag{2.7}$$

For cubic crystal, $a = b = c$,

$$d_{hk} = \frac{a}{\sqrt{h^2+k^2+l^2}} \tag{2.8}$$

By comparing the experimental pattern to that in the International Centre for Diffraction Data (ICDD) file, the sample can be easily identified. Except for single crystalline particles, the randomly orientated crystals in nanoparticles produce widening of the diffraction patterns. The effect becomes more evident when the crystallite size is on the order of a few nanometres. The Full Width at Half Maximum approach [28] is the simplest and most extensively used for measuring crystallite size.

2.6 UV-Visible Absorption Spectroscopy

The UV-visible absorption spectroscopy is used to do the optical characterisation. Ultraviolet-visible spectroscopy is the spectroscopy of photons in the UV-visible region. It utilises near-infrared and near-ultraviolet wavelengths in addition to visible light. It calculates the total spectrum's absorbance of electromagnetic radiation in the visible and ultraviolet wavelengths. In this area of the electromagnetic spectrum, the molecules go through an electronic transition. The atom may undergo an electronic transition from one energy level to another by the absorption of electromagnetic radiation with a high enough frequency. The energy that is absorbed in this area matches the valence electron's excitation from an occupied molecular orbit [29]. The wavelength of the radiation and the material's characteristics determine how much is absorbed. The wavelength at which absorption is strongest and its maximum wavelength are both recorded in the spectrum as a function of the input light's wavelength. The instrument used to obtain the ultraviolet-visible spectrum is the UV-Vis spectrophotometer. **Figure 2.3** shows a schematic diagram of UV-visible spectroscopy. The operation of this device is rather straightforward. A prism or diffraction grating separates the wavelengths of a visible or ultraviolet light beam. A half-mirrored system divides each monochromatic (single wavelength) beam into two beams of equal intensity. One beam, known as the sample beam, travels through a small, transparent cuvette containing the chemical under study in a clear solvent solution. Through a comparable cuvette that is solely filled with solvent, the reference beam passes. The intensity of the reference beam, denoted by I0, which should have had little to no light absorption, is then measured and compared by the electronic detectors. The letter I represents the intensity of the sample beam. In this approach, during a little time, the spectrometer automatically scans all of the component wavelengths. The UV portion is normally between 200 and 400 nm, while the visible section is commonly between 400 and 800 nm. I will always be less than I0 because part of the light that passes through the specimen is absorbed. The absorbance of the sample is provided by

$$\boldsymbol{A = \frac{I_0}{I}} \text{ or } \boldsymbol{A = -\log(\%T)} \tag{2.9}$$

With the right methods and the acquired absorption spectra, we can determine the specimen's bandgap. Tauc et al. developed a method for estimating the band gap using optical absorbance data shown precisely in terms of energy; the resulting figure is known as the Tauc plot. The energy-dependent absorption coefficient in this plot can be written as follows:

$$\boldsymbol{(\alpha h\vartheta)^{\frac{1}{n}} = A(h\vartheta - E_g)} \text{ [29]} \tag{2.10}$$

The absorption coefficient, Planck's constant, photon frequency, a constant, and band gap energy are represented by the values of α, h, ϑ, A and $E_g$respectively. The sort of electrical transition—direct or indirect—is indicated by the exponent's n value. In the case of indirect (forbidden), indirect (allowed), direct (forbidden), and direct (allowed) transitions, respectively, n can have values of 3, 2, 3/2, or 1/2.

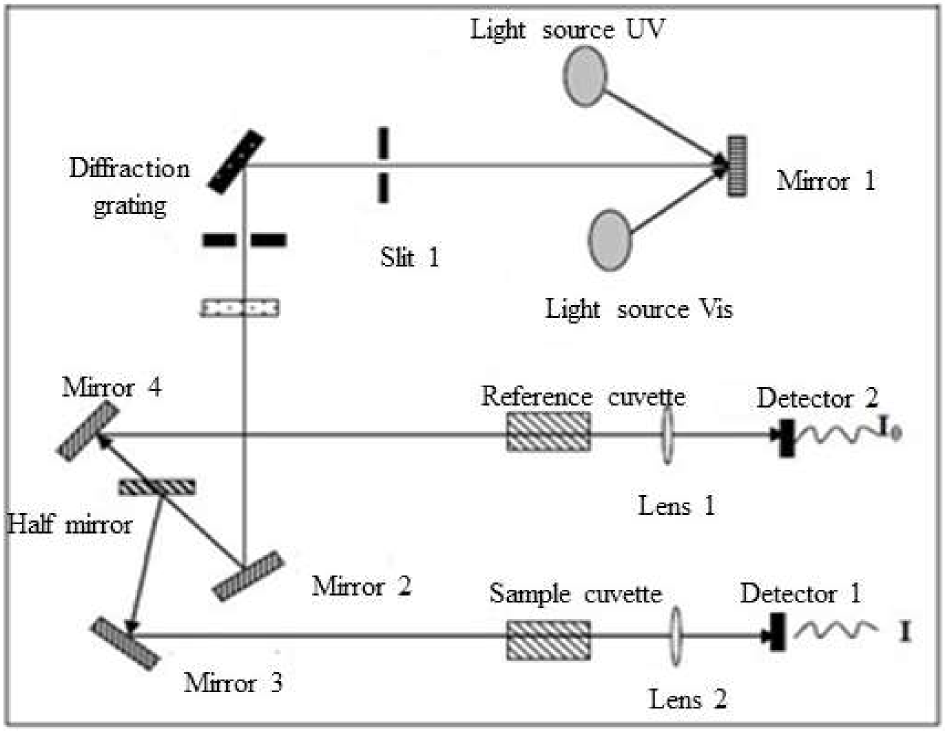

Figure 2.3 Schematic illustration of UV-visible absorption spectroscopy [31]

2.7 Fourier Transform Infrared Spectroscopy

The vibration and rotation of chemical bonds as well as the molecular structures of both organic and inorganic materials can be studied using FTIR, a non-destructive analytical technique. When exposed to infrared light, a molecule absorbs energy at frequencies unique to that molecule. A reverse-peaks infrared absorption plot that shows the sample's transmittance and reflectance at different frequencies of infrared light. It cannot directly evaluate the measured interferogram, hence a decoding is necessary. To do this, a mathematical technique called Fourier transformation is applied. After that, the acquired FTIR spectrum is scrutinised and contrasted with the acknowledged signatures of recognised objects in the FTIR library. Since neither nitrogen nor oxygen absorb infrared light, FTlR spectroscopy can be performed without a vacuum. **Figure 2.4** displays the FTIR spectrometer block diagram.The foundation of FTIR spectroscopy is the idea that interference between two radiation beams results in an interferogram signal, or signal as we refer to it. This is often generated via a Michelson interferometer, which splits the incoming infrared beam into two optical beams using a beam splitter [32]. An interferometer, a detector, and a radiation source are the three essential parts of an FTIR spectrometer. A glowing black body source emits infrared light, which travels through an aperture. Next, the parallel beam enters the interferometer, which is made up of a beam splitter and two mirrors. The light is sent in two directions at a right angle by the beam splitter. The light is sent in two directions at a right angle by the beam splitter. One beam is directed at the stationary mirror, and the other towards the moving mirror. After travelling the same route back from both of these mirrors, the radiation is combined once more into a single beam at the beam splitter. As a result, the two beams are merged again when they reunite at the beam splitter, and the radiation that comes out of the interferometer eventually reaches the detector and sample compartment. Following the amplification of the signal, the data is digitally transformed by an analog-to-digital converter and then transferred to a computer, where the Fourier transform generates the required infrared spectrum.

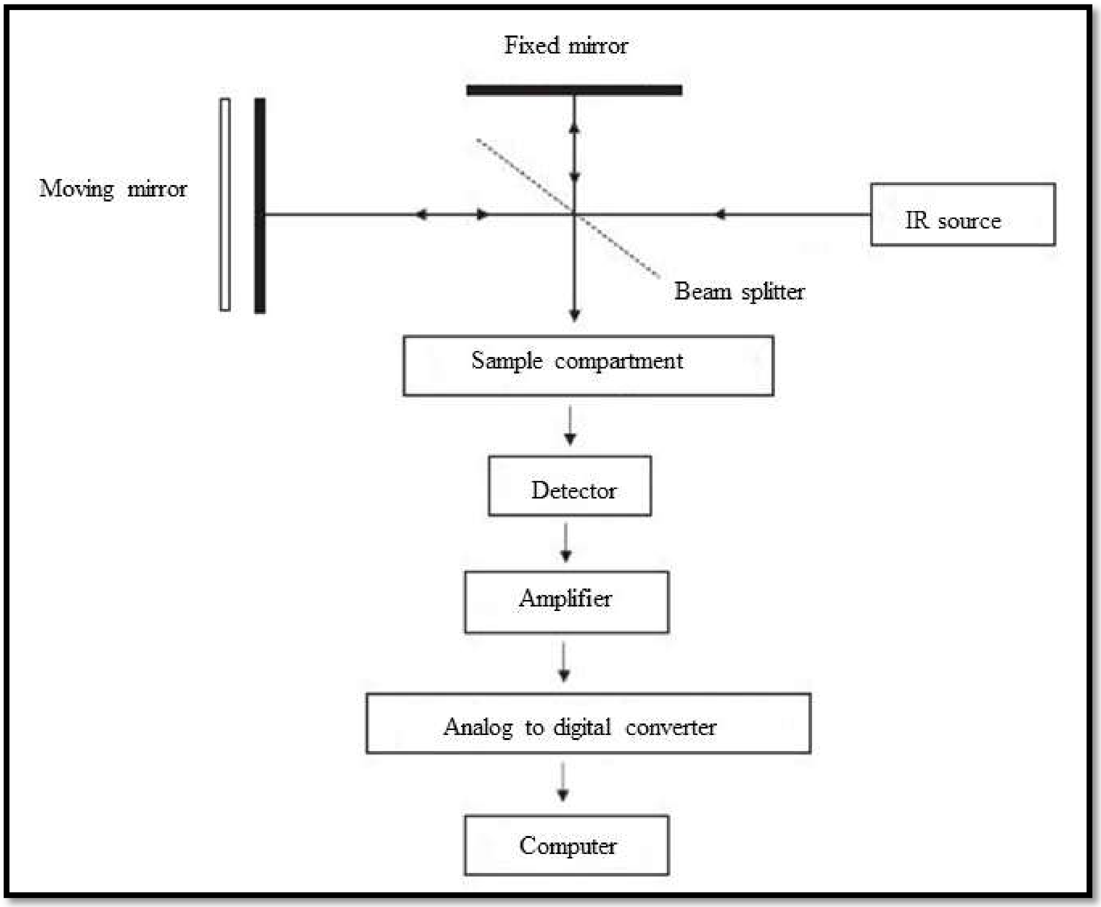

Figure 2.4 Schematic illustration of Fourier transform infrared spectroscopy [32]

2.8 Raman Spectroscopy

A quick and non-destructive method for determining a molecule's structural fingerprint is Raman spectroscopy. Raman scattering, or the shift in frequency of scattered light caused by molecular vibrations, is the fundamental concept behind the Raman spectrum [33]. By analysing the molecular vibrations, we may ascertain the chemical composition of the substance as well as other significant details. Since the Raman effect is too weak to be detected with the human eye, a very sensitive spectrometer is used to study the scattered light. A schematic of a contemporary Raman spectrometer is shown in **Figure 2.5**. Photons can scatter or absorb light, which allows them to interact with materials at the molecular level. Either inelastic or elastic scattering can happen. The inelastic process is known as Raman scattering, and the elastic process is known as Rayleigh scattering [34]. The electric field component of the scattering photon disturbs the molecule's electron cloud, exciting the system into a virtual state. Raman scattering results from the system decaying to vibrational energy levels above or below the starting state after exchanging energy with the photon. The term "Raman shift" refers to the frequency shift that results from the energy difference caused by Raman scattering between the entering and scattered photons. Depending on whether the system has lost or acquired vibrational energy, the Raman shift might be either positive or negative. The components that have been up- and down-shifted are referred to as the Stokes and anti-Stokes lines, respectively [35]. A Raman spectrum can be obtained by plotting the number of photons detected against the Raman shift from the incident laser energy. Because various materials have distinct vibrational modes, they all exhibit distinctive Raman spectra. Raman spectroscopy is therefore a helpful method for identifying materials.

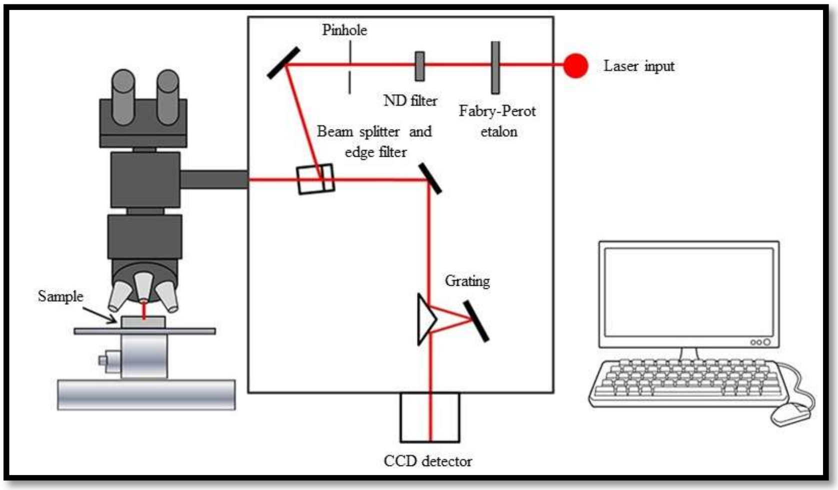

Figure 2.5 Schematic illustration of Raman spectroscopy [34]

2.9 Dynamic Light Scattering

DLS or photon correlation spectroscopy has been widely used to assess the hydrodynamic size of colloidal systems [36]. There are various benefits to this method. Firstly, the experiment takes a short time, and practically everything is automated, so a lot of experience is not needed for routine measurements. Moreover, the sample can be used for other purposes following the measurement because this procedure is non-invasive. Furthermore, because the scattering strength is directly proportional to the sixth power of the particle radius, this approach is extremely sensitive to the presence of small aggregates. Thus, even in the case of minor aggregation, imprecise measurement can be reasonably avoided. This unique feature makes DLS one of the best techniques for determining the colloidal stability of magnetic fluids [37].

The Brownian motion of scattered particles is the foundation of dynamic light scattering (DLS). Particles scattered in a liquid flow arbitrarily in every direction [38]. Particles and solvent molecules collide constantly, according to the theory of Brownian motion. Particles move as a result of the energy that is imparted during these collisions. Smaller particles are more affected by the energy transfer since it is more or less constant. Smaller particles are therefore travelling faster than larger particles. In the DLS experiment, a solution containing minute particles moving in a Brownian motion is exposed to monochromatic incident light, which is usually produced by a laser. The Rayleigh scattering process will then cause the incident light to be scattered in all directions with different wavelengths and intensities as a function of time by particles whose sizes are tiny enough in relation to the incident light's wavelength [39]. Either mutually destructive or mutually constructive phases will arise from the scattered light, cancelling each other out and producing a visible signal. The intensity of the diffracted light is determined by the following formula, per Rayleigh scattering theory:

$$I = I_0 \frac{1+cos^2\theta}{2R^2}\left(\frac{2\pi}{\lambda}\right)^4\left(\frac{n^2-1}{n^2+2}\right)^2 r^6 \tag{2.11}$$

Where $I_0, \theta, R, \lambda, n, r$ represents the intensity of unpolarised light, scattering angle, distance to the particle, wavelength of the incident light, refractive index of the particle and radius of the particle respectively. Because of the Brownian motion, the frequency of the incident light and the frequency of the scattered light experience a Doppler shift, resulting in a continuous fluctuation in the particle's distance. Correlating the scattered light intensity changes over time allows one to identify the speed at which the intensity fluctuates, which is related to the behaviour of macromolecules during diffusion. The speed at which the particles move affects the pace of this intensity fluctuation, which is connected to the way macromolecules diffuse. Next, the digital auto-correlator connects the dispersed light's intensity variations over time. The scattered light's autocorrelation function, G(τ), can be found as follows:

$$G(\tau) = \frac{\langle I(t) * I(t+\tau)\rangle}{\langle I(t)\rangle^2} \tag{2.12}$$

Where I is the intensity, t and τ represent the time and delayed time respectively. The hydrodynamic radius R_h or the diameter of a hypothetical sphere that diffuses at the same rate as the particle under study, can be found using the Stokes-Einstein equation.

$$R_h = \frac{k_B T}{6\pi\eta D} \tag{2.13}$$

Where k_B is the Boltzmann coefficient, T is the absolute temperature, η is the viscosity of the medium and D is the diffusion coefficient respectively. The schematic depiction of DLS is shown in **Figure 2.6**.

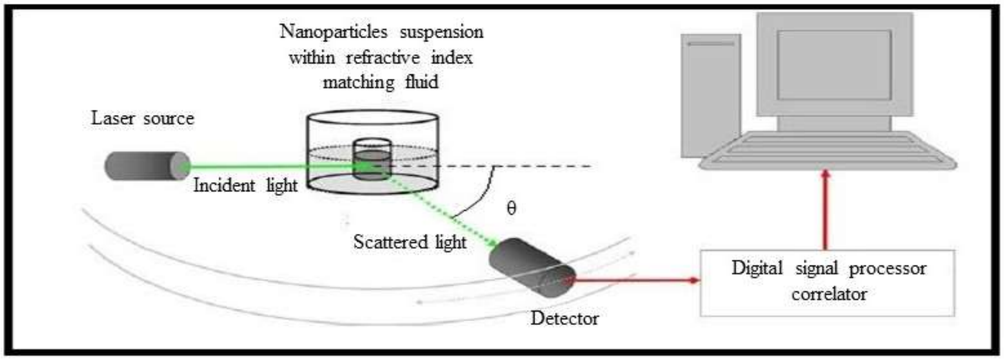

Figure 2.6 Schematic illustration of Dynamic light scattering [39]

2.10 Vibrating Sample Magnetometer

A vibrating sample magnetometer is a tool used to measure the magnetic properties of materials [40]. Using VSM, the saturation magnetisation, coercive field, and remanence of the measurement were used to calculate the hysteresis loop parameters. A vibrating sample magnetometer operates on the basis of Faraday's Law of Induction, which states that a changing magnetic field generates an electric field [41]. This electric field is measurable, and we can utilise the measurement to find out more about the changes in the magnetic field. The schematic diagram of a vibrating sample magnetometer is displayed in **Figure 2.7**. The samples that need to be evaluated are exposed to a constant magnetic field in a VSM. If the sample is magnetic, it will become magnetic due to the alignment of the individual magnetic spins or magnetic domains with the field. A higher magnetisation will be the outcome of a higher constant field. Because of its magnetic dipole moment, the sample will be surrounded by a magnetic field, also referred to as the magnetic stray field. This magnetic stray field, which changes over time as the sample is moved up and down, can be detected by a sequence of pick-up coils. A transducer converts a sinusoidal AC driving signal from a console-based circuit into a sinusoidal vertical vibration of the sample, which moves sinusoidally in a continuous magnetic field. The signal produced by the motion of the sample is detected by coils attached to the magnet's pole components. Due to the alternating magnetic field and Faraday's law of induction, the pickup coil will experience an electric field since the current will be proportionate to the sample's magnetisation. As magnetisation grows, so does the resultant current's magnitude. The induction current is increased by a lock-in amplifier and a transimpedence amplifier. The interface between the various components is a computer. The amount of magnetisation in the sample and how it changes with the intensity of the applied constant magnetic field can both be determined by the operating and monitoring software of the system. The probe's corresponding signal is transformed into a number that indicates the magnetic moment of the material. A plot of magnetisation against a steady magnetic field varies with time. When subjected to a uniform magnetic field, a sample material develops a dipole moment. This dipole moment is proportional to the sample's susceptibility to the applied field. This dipole moment is proportional to the sample's susceptibility to the applied field. A pickup coil may produce an electrical signal if the sample vibrates on a regular basis. Any coil positioned close to this magnetic moment will have a magnetic flux associated with it that is determined by

$$\phi = \mu_0 n \alpha M \tag{2.14}$$

Where μ_0 is the permeability of free space, n is the number of turns per unit length of the coil, α represents the geometric moment decided by the position of the moment concerning the coil as well as the shape of the coil and M is the magnetic moment of the sample. An emf is induced in the stationary detection coil by an anharmonic oscillator of the type $\boldsymbol{z = z_0 + Ae^{j\omega t}}$. And the induced emf is given by

$$V = \frac{-d\phi}{dt} = -j\omega\mu_0 nMA\frac{\partial\alpha}{\partial Z}e^{j\omega t} \tag{2.15}$$

The magnetic moment of the sample is directly proportional to the induced voltage if the vibration amplitude (A), frequency (ω), and $\frac{\partial\alpha}{\partial Z}$ remain constant across the sample zone. This is VSM's fundamental concept.

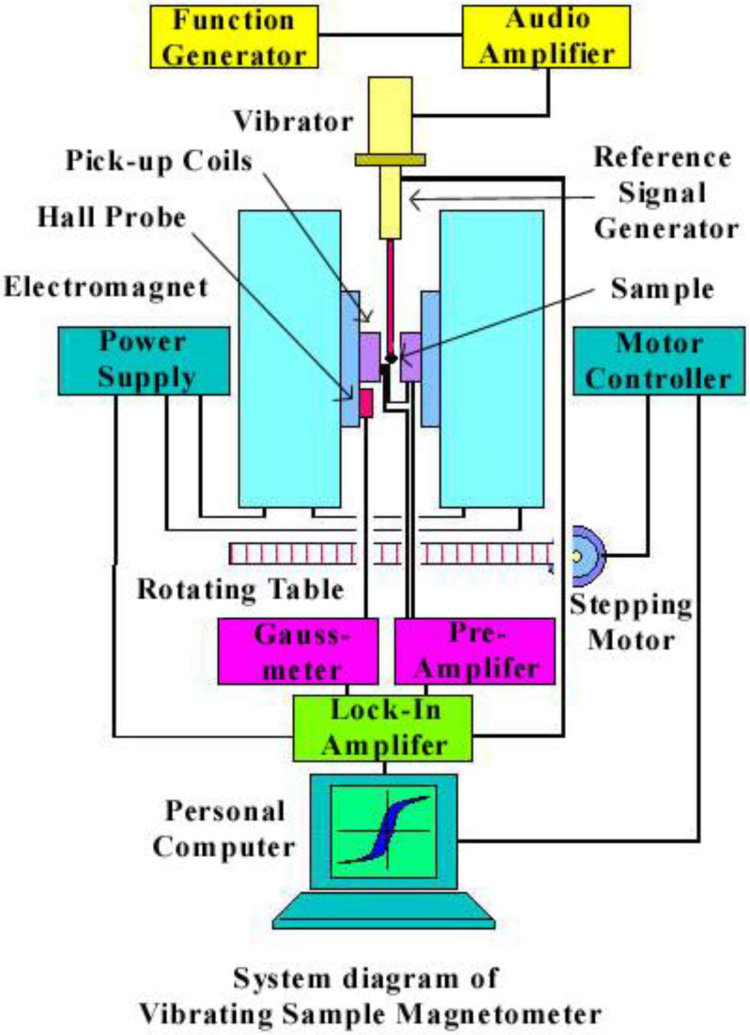

Figure 2.7 Schematic illustration of Vibrating Sample Magnetometer [42]

2.11 Superconducting Quantum Interference Device

A superconducting quantum interference device is the most precise and sensitive instrument for measuring the magnetic moment of a sample (SQUID). The fundamental idea behind SQUID's ability to detect extremely tiny magnetic fields is the DC Josephson effect and flux quantisation [43]. It is made up of two parallel Josephson junctions made of superconducting magnets spaced apart by thin insulating layers. It is possible to set up SQUID to measure magnetic fields on the order of 10^{-14} T. The capacity of SQUID devices to detect changes in the magnetic field due to a single flux quantum (h/2e) is connected to their great sensitivity. The basic principle of a SQUID magnetometer is that, provided that the SQUID device maintains a constant biassing current, the measured voltage will oscillate in response to phase shifts at the two junctions, which are contingent upon variations in the magnetic flux

[44]. Monitoring the oscillations allows one to evaluate the actual or perceived change in flow. Consequently, when the sample passes through the superconducting magnetic coils, a flux shift occurs in the pickup coils. Measurement in a SQUID is possible by passing the sample through the superconducting detecting coil with connections. Even the tiniest variation in magnetic flux brought on by the sample moving while keeping the current constant might be detected using the resulting voltage changes between the junctions. With the right electronics, it is possible to manipulate the change in voltage across the junctions that is proportionate to the change in flux and therefore acquire the specimen's magnetisation.

2.12 Thermogravimetric Analysis

Thermogravimetric analysis is a type of thermal analysis in which a material is heated to a specific temperature and its mass is determined as a function of temperature [45]. The weight variation of a sample with respect to temperature is represented by the thermogravimetric (TGA) curve. It can be used to investigate changes in weight brought on by volatiles' absorption or desorption, breakdown, oxidation and reduction, stability, purity, and solvent loss during heating [46]. Thermally generated transition-related weight changes are quantitatively assessed using TGA. The procedure is heating a sample at a predetermined rate, gradually raising the temperature for a substance whose beginning weight is known, and recording the weight changes over time as a function of temperature at different intervals. There are two possible ways to show the results [47]:

- TG Curve: Weight variations are seen in relation to temperature.
- DTG Curve: Plotting the first derivative of the TG curve against temperature or time.

Because of the exact sequence in which physical transitions and chemical reactions take place over predetermined temperature ranges, the TG curve is unique to a given substance or material. Physical alterations and the creation and breaking of chemical bonds at high temperatures also result in weight changes. TG typically operates in reactive or inert atmospheres within the temperature range of 1200°C. Molecule structure often affects the rates of thermally induced reactions. The most important experimental component in the TGA study is the heating rate. The samples are usually heated at a rate of 10 or 20°C per minute. By lowering the heating rate, the resolution of overlapping weight losses is improved. Technology developments have made it possible to use variable heating rates in studies to increase resolution by automatically reducing the heating rate when weight is reduced. Because nitrogen is inert, it is the gas most often employed to purge samples in TGA. Air is known to improve resolution since the sample's constituents' oxidative stability fluctuates. In the event that the samples catch fire, using a hoover is a possibility. **Figure 2.8** depicts a basic internal diagram of a standard TGA.

The TGA has two pans: a sample pan and a reference pan. Aluminium and platinum are suitable substitute materials for the pan. The pan utilised depends on the maximum temperature that a certain run may achieve. Platinum pans are used when the maximum temperature is higher than 660 °C since platinum melts at 1760 °C and aluminium melts at 660 °C. Beneath every pan is a thermocouple that senses the temperature. Before each run starts, each pan is balanced on a balancing arm. The balance arms need to be adjusted to take into consideration the arms' varying rates of thermal expansion. The gadget will only record the temperature at which an event happens if the arms are not calibrated; it will not record the change in mass at that same moment. The empty pans are zeroed, weighed, and set on the balancing arms to calibrate the apparatus.

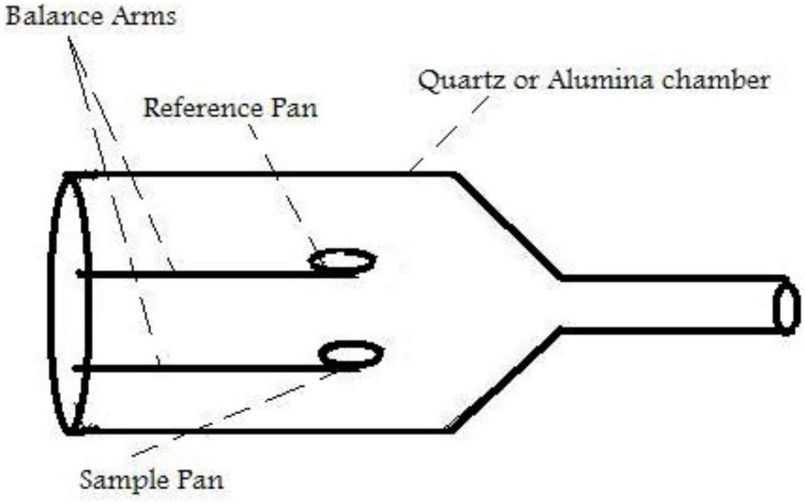

Figure 2.8 Schematic illustration of Thermogravimetric analysis [46]

2.13 Spin coating unit

One popular and efficient method for depositing uniform films on a flat substrate is spin coating. It is a solution-based method in which a specific material's solution is spun at very high speeds, using the liquid's surface tension and centripetal force to produce a homogeneous coating on the substrate [48]. After the extra solvent evaporates, a thin coating with a thickness of a few nanometres is produced. One of the main benefits of this method for creating thin films is its simplicity, which makes it less dangerous and relatively simple to set up. It also produces thin and consistent films. A typical spin process consists of three major steps as depicted in the Figure:

1. **Dispensing stage**

On the substrate surface, the resin fluid is deposited in this location. Static and dynamic dispensing are the two popular dispensing techniques. The fluid is dispensed onto the substrate while it is stationary in a static dispense. A dynamic dispense involves rotating the substrate until it reaches the desired speed, at which point the solution is dispensed in the middle of the substrate.

2. **Rotation dominated thinning**

This is the point where the rotating motion allows the excess fluid to escape from the substrate. Depending on the fluid and substrate, the typical spin speed for this step is between 500 and 6000 rpm. The final film thickness for this step will be determined by the combined effect of spin speed and time.

3. **Solvent evaporation**

The solvent evaporating takes over the thinning process after the fluid stream stops. The solvent vapour pressure, volatility, and surrounding temperature all affect the rate of solvent evaporation [49].

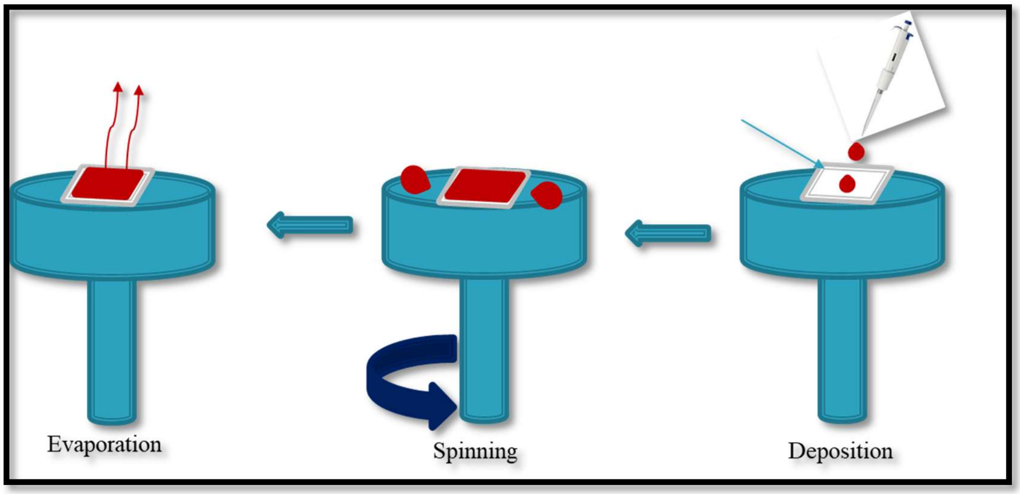

Figure 2.9 Schematic illustration of Spin coating unit

2.14 Field Emission Scanning Electron Microscopy

The field emission scanning electron microscope is an enhanced microscope capable of producing images with extremely high resolution at low accelerating voltages, with magnifications ranging from 10x to 500000x, it offers both elemental and topographical information, and its depth of field is almost infinite. The sample surface topology of any material in the nanoscale regime can be imaged by means of a high-energy electron beam supplied via a variety of electromagnetic lenses and apertures in a high vacuum. FESEM uses electron beams as an illumination source rather than light [50]. Target materials like tungsten or lanthanum hexaboride are heated or subjected to a large electric potential difference in order to produce the electron beam. Because FESEM uses field emission, which generates electron beams of greater quality than traditional SEM, it creates images with a spatial resolution of at least 1.5 nm that are sharper and less statistically deformed. The in-lens detectors of FESEM are engineered to function at low acceleration potential and high resolution for optimal resolution. Their outstanding resolution and suitability for low-voltage applications make them unique for high-resolution imaging. In a field emission source, electrons are liberated and accelerated within a strong gradient of electric field in a FESEM. These so-called primary electrons are concentrated and deflected by electronic lenses within the high vacuum column, creating a narrow scan beam that bombards the target. This causes secondary electrons to release from the thing everywhere. There is a connection between the item's surface structure and the secondary electrons' angle and velocity. Next, an electric signal is produced by a detector that finds the secondary electrons. After being amplified, this signal is converted into a digital image that can be further processed, stored, and displayed on a monitor or video scan image.

References

[1]. Charles, S.W., 2002. The preparation of magnetic fluids. *Ferrofluids: magnetically controllable fluids and their applications*, pp.3-18.

[2]. Jolivet, J.P., Chanéac, C. and Tronc, E., 2004. Iron oxide chemistry. From molecular clusters to extended solid networks. *Chemical communications*, (5), pp.481-483.

[3]. Schwertmann, U. and Cornell, R.M., 2008. *Iron oxides in the laboratory: preparation and characterization*. John Wiley & Sons.

[4]. Marian S. Carson Collection (Library of Congress), 1914. *Journal of the American Chemical Society* (Vol. 36). American Chemical Society.

[5]. Thanh, N.T., Maclean, N. and Mahiddine, S., 2014. Mechanisms of nucleation and growth of nanoparticles in solution. *Chemical reviews*, *114*(15), pp.7610-7630.

[6]. Vreeland, E.C., Watt, J., Schober, G.B., Hance, B.G., Austin, M.J., Price, A.D., Fellows, B.D., Monson, T.C., Hudak, N.S., Maldonado-Camargo, L. and Bohorquez, A.C., 2015. Enhanced nanoparticle size control by extending LaMer's mechanism. *Chemistry of Materials*, *27*(17), pp.6059-6066.

[7]. Bahrig, L., Hickey, S.G. and Eychmüller, A., 2014. Mesocrystalline materials and the involvement of oriented attachment–a review. *CrystEngComm*, *16*(40), pp.9408-9424.

[8]. Rabenau, A., 1985. The role of hydrothermal synthesis in preparative chemistry. *Angewandte Chemie International Edition in English*, *24*(12), pp.1026-1040.

[9]. Coppola, P., Da Silva, F.G., Gomide, G., Paula, F.L.O., Campos, A.F.C., Perzynski, R., Kern, C., Depeyrot, J. and Aquino, R., 2016. Hydrothermal synthesis of mixed zinc–cobalt ferrite nanoparticles: structural and magnetic properties. *Journal of Nanoparticle Research*, *18*, pp.1-15.

[10]. Ismael, M., 2021. Ferrites as solar photocatalytic materials and their activities in solar energy conversion and environmental protection: a review. *Solar energy materials and solar cells*, *219*, p.110786.

[11]. Huang, G., Lu, C.H. and Yang, H.H., 2019. Magnetic nanomaterials for magnetic bioanalysis. In *Novel nanomaterials for biomedical, environmental and energy applications* (pp. 89-109). Elsevier.

[12]. Fu, C. and Ravindra, N.M., 2012. Magnetic iron oxide nanoparticles: synthesis and applications. *Bioinspired, Biomimetic and Nanobiomaterials*, *1*(4), pp.229-244.

[13]. Hayashi, H. and Hakuta, Y., 2010. Hydrothermal synthesis of metal oxide nanoparticles in supercritical water. *Materials*, *3*(7), pp.3794-3817.

[14]. Li, Z., Young, R.J., Backes, C., Zhao, W., Zhang, X., Zhukov, A.A., Tillotson, E., Conlan, A.P., Ding, F., Haigh, S.J. and Novoselov, K.S., 2020. Mechanisms of liquid-phase exfoliation for the production of graphene. *ACS nano*, *14*(9), pp.10976-10985.

[15]. Hernandez, Y., Nicolosi, V., Lotya, M., Blighe, F.M., Sun, Z., De, S., McGovern, I.T., Holland, B., Byrne, M., Gun'Ko, Y.K. and Boland, J.J., 2008. High-yield production of graphene by liquid-phase exfoliation of graphite. *Nature nanotechnology*, *3*(9), pp.563-568.

[16]. Nicolosi, V., Chhowalla, M., Kanatzidis, M.G., Strano, M.S. and Coleman, J.N., 2013. Liquid exfoliation of layered materials. *Science*, *340*(6139), p.1226419.

[17]. Fu, L., Yan, Z., Zhao, Q. and Yang, H., 2018. Novel 2D nanosheets with potential applications in heavy metal purification: A review. *Advanced Materials Interfaces*, *5*(23), p.1801094.

[18]. Ma, R. and Sasaki, T., 2010. Nanosheets of oxides and hydroxides: ultimate 2D charge-bearing functional crystallites. *Advanced materials*, *22*(45), pp.5082-5104

[19]. Wang, J., Li, G. and Li, L., 2016. Synthesis strategies about 2D materials. *Two-dimensional Materials-Synthesis, Characterization and Potential Applications*, *1*, pp.1-20.

[20]. Kaur, H. and Coleman, J.N., 2022. Liquid-phase exfoliation of nonlayered non-van-der-waals crystals into nanoplatelets. *Advanced Materials*, *34*(35), p.2202164.

[21]. Masuda, H., Yanagishita, T. and Kondo, T., 2018. Fabrication of anodic porous alumina. *Encyclopedia of Interfacial Chemistry*, pp.226-235.

[22]. Arifin, K., Yunus, R.M., Minggu, L.J. and Kassim, M.B., 2021. Improvement of TiO2 nanotubes for photoelectrochemical water splitting. *International Journal of Hydrogen Energy*, *46*(7), pp.4998-5024.

[23]. Yoo, H., Kim, M., Kim, Y.T., Lee, K. and Choi, J., 2018. Catalyst-doped anodic TiO2 nanotubes: binder-free electrodes for (photo) electrochemical reactions. *Catalysts*, *8*(11), p.555.

[24]. Lee, K., Mazare, A. and Schmuki, P., 2014. One-dimensional titanium dioxide nanomaterials: nanotubes. *Chemical reviews*, *114*(19), pp.9385-9454.

[25]. Nie, X., Chen, J., Li, G., Shi, H., Zhao, H., Wong, P.K. and An, T., 2013. Synthesis and characterization of TiO_2 nanotube photoanode and its application in photoelectrocatalytic degradation of model environmental pharmaceuticals. *Journal of Chemical Technology & Biotechnology*, *88*(8), pp.1488-1497.

[26]. Arroyo, M., Lopez-Manchado, M.A., Valentin, J.L. and Carretero, J., 2007. Morphology/behaviour relationship of nanocomposites based on natural rubber/epoxidized natural rubber blends. *Composites science and technology*, *67*(7-8), pp.1330-1339.

[27]. Kittel, C. and McEuen, P., 2018. *Introduction to solid state physics*. John Wiley & Sons.

[28]. Cullity, B.D., 1978. Elements of X-ray diffraction, Addison. *Wesley Mass*, pp.127-31.

[29]. Marcì, G. and Palmisano, L. eds., 2019. *Heterogeneous photocatalysis: Relationships with heterogeneous catalysis and perspectives*. Elsevier.

[30]. Sze, S.M., Li, Y. and Ng, K.K., 2021. *Physics of semiconductor devices*. John wiley & sons.

[31]. Jiulong, S., 2014. *Development of Inorganic-Organic Hybrid Materials for Waste Water Treatment* (Doctoral dissertation, National University of Singapore (Singapore)).

[32]. Stuart, B.H., 2004. *Infrared spectroscopy: fundamentals and applications*. John Wiley & Sons.

[33]. Colthup, N., 2012. *Introduction to infrared and Raman spectroscopy*. Elsevier.

[34]. Raman, C.V. and Krishnan, K.S., 1928. A new type of secondary radiation. *Nature*, *121*(3048), pp.501-502.

[35]. Aravind, P.B., 2019. *Exfoliation of Non-van der Waals Materials and Investigations on the Magnetic Bistability of 2D Nanostructures on Curved Surfaces* (Doctoral dissertation, Cochin University of Science and Technology).

[36]. Berne, B.J. and Pecora, R., 2000. *Dynamic light scattering: with applications to chemistry, biology, and physics*. Courier Corporation.

[37]. Grob, C., Buscher, K., Romanus, E., Helm, C.A. and Weitschies, W., 2002. Characterization of a ferrofluid by atomic force microscopy and photon correlation spectroscopy after magnetic fractionation. *European cells and Materials*, *3*(supplement 2), pp.163-166.

[38]. Yerin, C.V., 2017. Particles size distribution in diluted magnetic fluids. *Journal of Magnetism and Magnetic Materials*, *431*, pp.27-29.

[39]. Lim, J., Yeap, S.P., Che, H.X. and Low, S.C., 2013. Characterization of magnetic nanoparticle by dynamic light scattering. *Nanoscale research letters*, *8*, pp.1-14.

[40]. Foner, S., 1959. Versatile and sensitive vibrating-sample magnetometer. *Review of Scientific Instruments*, *30*(7), pp.548-557.

[41]. Kirupakar, B.R., Vishwanath, B.A., Sree, M.P. and Deenadayalan, D., 2016. Vibrating sample magnetometer and its application in characterisation of magnetic property of the anticancer drug magnetic microspheres. *International Journal of Pharmaceutics and Drug Analysis*, *4*(5), pp.227-233.
[42]. Reena Mary, A.P. and Anantharaman, M.R., 2011. *Investigations on Magnetic, Optical and Transport Properties of Magnetic Nanofluids for Engineering and Biomedical Applications* (Doctoral dissertation, Cochin University of Science & Technology).
[43]. Fagaly, R.L., 2006. Superconducting quantum interference device instruments and applications. *Review of scientific instruments*, *77*(10).
[44]. Khalid, A., Salman, R. and Anwar, S., 2010. Principles and Applications of Superconducting Quantum Interference Devices (SQUIDs).
[45]. Prime, R.B., Bair, H.E., Vyazovkin, S., Gallagher, P.K. and Riga, A., 2009. Thermogravimetric analysis (TGA). *Thermal analysis of polymers: Fundamentals and applications*, pp.241-317.
[46]. Chartoff, R.P. and Sircar, A.K., 2002. Thermal analysis of polymers. *Encyclopedia of polymer science and technology*.
[47]. Barron, A.R., 2015. Physical methods in chemistry and nano science.
[48]. Resmi, K.R., Investigation on surface plasmon resonance and its coupled emission tuning for bio chemical sensing applications.
[49]. Tyona, M.D., 2013. A theoritical study on spin coating technique. *Advances in materials Research*, *2*(4), p.195.
[50]. Afshari, M. ed., 2016. *Electrospun nanofibers*. Woodhead Publishing.

Chapter 3

Rosensweig Instability Study of Iron Oxide Nano Fluid Under Uniform Magnetic Field

Magnetically controllable fluids paved way to the new branch of Ferrohydrodynamics. To investigate the Rosensweig instability on a horizontal free surface of a ferrofluid under the influence of a normal uniform magnetic field is very interesting. This chapter deals with the synthesis, characterization and study of Rosensweig instability under uniform magnetic field of hydrocarbon based ferrofluid. They are characterized using X- ray diffraction technique, Dynamic light scattering and Fourier Transform Infrared Spectroscopy. The magnetic properties have been analyzed by the Superconducting Quantum Interference Device. The temperature-dependent relaxation studies were carried out by field-cooled (FC) and zero-field-cooled (ZFC) moment measurements at a constant applied field. We have demonstrated the Rosensweig instability experimentally and observed the pattern transition. The surface tension of the fluid is measured by the pendant drop method and is correlated with the results obtained through instability measurement. The magnetic concentration of the sample is determined from the Thermogravimetric analysis.

3.1 Introduction

Nanomagnetic single-domain particles contained in a liquid carrier medium form stable colloidal suspensions known as ferrofluids [1]. The applications will determine whether the carrier liquid is polar or nonpolar. Usually, the suspended particles are about 10 nm in size [2]. Brownian motion is sufficient to prevent the particles from settling in a magnetic or gravitational field [3, 4]. The small size makes the particles to be superparamagnetic; each particle acts as a single magnetic domain that can flip its magnetization randomly under the influence of temperature [5, 6]. The quality of a fluid depends on stability and shelf life. To avoid agglomeration caused by attractive Vander Waals interaction the magnetic particles have to be surfaced with suitable surfactant either by steric repulsion or electrostatic repulsion [7]. Surface instability studies are a kind of icon in ferrofluid research. The opaque nature of magnetic fluids limits applying standard measurement techniques of fluid dynamics such as Shadography or Laser Doppler Anemometry. Hence the instability studies of magnetic fluids are an excellent tool to enhance the understanding of the physics behind the fluids. The instability of a fluid surface is an aggravation in many technical applications, where stability is of great importance. Nevertheless, the study leads to understanding the fundamental properties of the fluid in detail. Hence investigating the normal magnetic field on the free horizontal surface of a fluid paves the way for technological applications. Rosensweig instability studies are an excellent choice for the study of surface pattern formation in the equilibrium system because field-induced instability studies are easier to conduct and using an external magnetic field, we are able to control the experiment.

Rosensweig instability is a perturbation on the free surface of a ferrofluid. On the surface of the magnetic fluid, a uniform vertical magnetic field causes a wavy disturbance. Comparing the field intensity with the free surface value, it is lower in the valley but increases near the perturbation bulges. Consequently, there is a tendency for the magnetic force perturbation to be amplified near the surface, with the perturbation directed downward at valleys and upward at bulges. The surface-tension and gravity forces, on the other hand, work in opposition to the displacement of the surface's components from equilibrium; in other words, they obstruct the displacement. All of the forces caused by a surface that is slightly warped are proportionate to the displacement value. Nonetheless, the square of the magnetic fluid's magnetisation also determines the coefficient of the magnetic force perturbation. Consequently, instability sets at sufficiently high magnetisation because the destabilizing magnetic force is greater than the sum of the other two forces [8]. When a uniform magnetic field is applied normally on the horizontal free surface of a ferrofluid causes a huddling of magnetic field lines on the surface which represents a spatial gradient in the field strength. Hence the ferrofluid is drawn towards the strong field region [9]. As a result, the height of the perturbation of fluid will be increased and more field lines are concentrated at the tip. Rosensweig instability can also create discrete peaks having no fluids between the peaks, depending on the depth of the ferrofluid. Even a small magnetic field is applied on the fluid surface producing large deformation on the fluid surface, because the deformed surface has larger surface and hydrostatic energy as compared to the free surface. The increase is caused by the costs of energy to lift up the fluid against the gravitation and to create more surface area. Hence the surface tension and gravitation acts as stabilizing forces and the magnetic field serve as destabilizing force [10].

When a uniform vertical magnetic field is applied to the horizontal free surface of the magnetic fluid, surface may be unstable when the field strength exceeds a critical value and a static periodic pattern appears on the surface [11, 12]. Surface instability depends on the strength of applied magnetic field and magnetization of ferrofluid [13], the instability mechanism occurs when the applied magnetic field exceeds the stabilizing forces due to surface tension and gravitational force [14, 15]. The surface deformation of the fluid surface first occurs at the edge of the container, due to the field inhomogeneity induced by the container. When the magnetic field is increased in a quasistatic way the flat surface changes to ridges. Further increase in the magnetic field results in a transition to a hexagonal pattern [16]. At the critical wave number condition, the increase in applied field strength causes increase in spike height. When the applied magnetic field increased to a second threshold value the hexagonal pattern gets changed to a square pattern. For hexagonal pattern the distance between the two peaks under critical condition is given by $d = \frac{4\pi}{\sqrt{3}k_{hex}}$ [9] and for square pattern $d = \frac{2\pi}{k_{squ}}$ [12]. Using the linear analysis, the wave number under this condition is $k_{crit} = \frac{\sqrt{\Delta\rho g}}{\sqrt{\gamma}}$, where $\Delta\rho$ is the density difference between the interfaces γ is the surface tension and g is the acceleration due to gravity [16]. The distance between the peaks is reported to vary from 9.5 mme to 12 mm with air interface [9]. Gailitis (1977) theoretically studied the relative stability of a hexagonal pattern and a square pattern, both at k_{crit}. He predicted that near the onset of instability, the hexagonal pattern has a lower energy as compared to square pattern and hence is assumed to be the stable state of the system [17, 18]. When the strength of the applied field is smaller than the critical field, the initial surface perturbation declines towards a flat surface [19]. When the field increases to a critical value, the spikes start developing from edges and grow to the centre of the container [20]. The hexagonal pattern becomes less stable and gives way to the square pattern at increasing magnetic field values. Compression of the hexagonal pattern results in the square pattern, which is a metastable state. Growth and decay rate of the newly formed spikes are different. During the growth of the spikes new surface area is generated and the diffusion of surfactant from the bulk of the ferrofluid towards the surfactant may lag behind, but in case of decay process the surface area is annihilated and the surface density of surfactant may exceed the equilibrium concentration [21]. For the hexagonal pattern, the distance between the two peaks under critical conditions is given by $d = \frac{4\pi}{\sqrt{3}k_{hex}}$ and for the square pattern $d = \frac{2\pi}{k_{squ}}$. Using the linear analysis, the wave number under this condition is $k_{crit} = \frac{\sqrt{\Delta\rho g}}{\sqrt{\gamma}}$, where $\Delta\rho$ is the density difference between the interfaces γ is the surface tension and $g$is the acceleration due to gravity. The distance between the peaks is reported to vary from 9.5 mm to 12 mm with air interface. Gailitis (1977) theoretically studied the relative stability of a hexagonal pattern and a square pattern, both at k_{crit}. He predicted that near the onset of instability, the hexagonal pattern has lower energy as compared to the square pattern and hence is assumed to be the stable state of the system. When the strength of the applied field is smaller than the critical field, the initial surface perturbation declines towards a flat surface. When the field increases to a critical value, the spikes start developing from the edges and grow to the center of the container. For higher values of the magnetic field, the hexagonal pattern losses stability in favour of the square pattern. The square pattern is a metastable state induced by compression of the hexagonal pattern. The growth and decay rates of the newly formed spikes are different. During the growth of the spikes new surface area is generated and the diffusion of surfactant from the bulk of the ferrofluid towards the surfactant may lag behind, but in case of the decay process the surface area is annihilated and the surface density of surfactant may exceed the equilibrium concentration [22].

3.1.1 Dispersion relation for linear medium

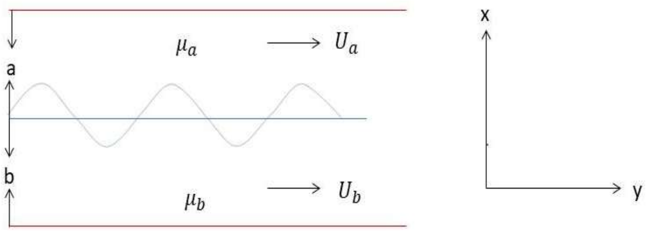

Consider an incompressible, non-conducting and viscous magnetic fluid of thickness h and density ρ. The fluid is bounded from below by the bottom of the container, and has a free surface with air above the fluid. Let $U_a$and U_b represents the fluid velocities from above and below the equilibrium condition. A dispersion relation describing the spatial wavelength of peaks can be obtained by balancing gravitational, surface tension and magnetic energy. The dispersion relation is given by [8],

$$\begin{aligned}(\omega - k_y U_a)^2 \rho_a cothk_a a + (\omega - k_y U_b)^2 \rho_b cothk_b \\ = gk(\rho_b - \rho_a) + k^3\sigma \\ - \left\{ \frac{k^2 \mu_a \mu_b (H_x^a - H_x^b)^2}{\mu_b tanhka + \mu_a tanhkb} - \frac{k_y^2 H_y^2 (\mu_a - \mu_b)^2}{\mu_b cothkb + \mu_a cothka} \right\}\end{aligned} \tag{3.1}$$

For thick layers or infinite depth, $a \to \infty, b \to \infty$

$$\begin{aligned}(\omega - k_y U_a)^2 \rho_a + (\omega - k_y U_b)^2 \rho_b \\ = gk(\rho_b - \rho_a) + k^3\sigma - \left\{ \frac{k^2 \mu_a \mu_b (H_x^a - H_x^b)^2}{\mu_b + \mu_a} - \frac{k_y^2 H_y^2 (\mu_a - \mu_b)^2}{\mu_b + \mu_a} \right\}\end{aligned} \tag{3.2}$$

The parameters expressed in equation 2 areω-the growth rate of peaks, k_y-the wavenumber along y direction, $\rho_b - \rho_a$the density difference between the interface, U_a and $U_b$are the fluid velocities, $\mu_a$and μ_b are the permeability of fluid, H_x-the perpendicular field,H_y-the tangential field, g- the acceleration due to gravity,k-the wave number, σ-the surface tension, subscript a and b denotes above and below the fluid interface respectively.

Assume that the fluid velocity at a and b are zero, then $U_a = U_b = 0, H_y = 0, \mu_a = \mu_0, \mu_b = \mu$, Substituting these values in equation **(2)**, we obtain

$$\begin{aligned}\omega^2(\rho_a + \rho_b) \\ = gk(\rho_b - \rho_a) + k^3\sigma - \frac{k^2 \mu_0 \mu (H_x^a - H_x^b)^2}{\mu_0 + \mu}\end{aligned} \tag{3.3}$$

$$\begin{aligned}\frac{\omega^2(\rho_a + \rho_b)}{k^2} \\ = \frac{g(\rho_b - \rho_a)}{k} + k\sigma - \frac{\mu_0 \mu (H_x^a - H_x^b)^2}{\mu_0 + \mu}\end{aligned} \tag{3.4}$$

From the above equation we can say that the value of ω is either zero or imaginary. At the onset of instability

$$\omega^2 = 0 \tag{3.4a}$$

$$\frac{\partial \omega^2}{\partial k} = 0 \tag{3.4b}$$

Substituting the value of 3.4b in equation 3.4, we obtain

$$\frac{-g(\rho_b - \rho_a)}{k^2} + \sigma = 0 \tag{3.5}$$

$$k = \left(\frac{g(\rho_b - \rho_a)}{\sigma}\right)^{1/2} \tag{3.6}$$

Putting the value of $k_c$and applying the condition of 3.4b in equation 4, we get the critical value of saturation magnetization,

$$M_{c=}^2 \frac{2}{\mu_0}\left(1 + \frac{\mu_0}{\mu}\right)[g(\rho_b - \rho_a)\sigma]^{1/2} \tag{3.7}$$

This is the minimum value of magnetization at which the phenomenon can be observed. When the applied magnetic field is increased from zero correspondingly the magnetization is also increased. If the saturation magnetization is less than the critical magnetization, the fluid will never display the instability patterns. However, the fluid interface remains unchanged until a critical point at which the transition occurs [8].

3.2 Rosensweig instability

The interfacial instability on the free horizontal surface of a ferrofluid under a constant magnetic field normal to the surface is referred to as Rosensweig instability [11]. Surface instability depends on the strength of the applied magnetic field and the magnetization of the ferrofluid. The instability mechanism occurs when the applied magnetic field exceeds the stabilizing forces due to surface tension and gravitational force. When the field increases to a critical value, the spikes start developing from the edges and grow to the centre of the container. The strength of the applied field is smaller than the critical field, the initial surface perturbation declines towards a flat surface. When the magnetic field is increased in a quasi-static way the flat surface changes to ridges. Further, an increase in the magnetic field results in a transition to a hexagonal pattern. At the critical wave number condition, the increase in applied field strength causes an increase in spike height. When the applied magnetic field increases to a second threshold value, the hexagonal pattern gets changed to a square pattern. Actually, it is a perturbation on the free surface of a ferrofluid. A uniform vertical magnetic field produces a wavy perturbation on the magnetic fluid surface. The field intensity near the bulges of the perturbations is increased, but in the valley, it is decreased in comparison with the free surface value. Therefore, the perturbation of the magnetic force is directed upward at the bulges but downward at the valleys; that is a tendency to amplify the perturbation of the surface. On the other hand, the surface tension and gravity forces are directed opposite to the displacement of the parts of the surface from the equilibrium; that is, they impede the displacement. As long as the warping of the surface is small, all the forces produced by it are proportional to the value of the displacement. However, the coefficient in the perturbation of the magnetic force is also proportional to the square of the magnetization of the magnetic fluid. Therefore, at sufficiently large magnetization, the destabilizing magnetic force exceeds the sum of the other two forces and hence instability sets. When a uniform magnetic field is applied normally on the horizontal free surface of a ferrofluid causes a huddling of magnetic field lines on the surface which represents a spatial gradient in the field strength. Hence the ferrofluid is drawn towards the strong field region. As a result, the height of the perturbation of fluid will be increased and more field lines are concentrated at the tip. Rosensweig instability can also create discrete peaks having no fluids between the peaks, depending on the depth of the ferrofluid. Even a small magnetic field is applied on the fluid surface producing large deformation on the fluid surface because the deformed surface has a larger surface and hydrostatic energy as compared to the free surface. The increase is caused by the costs of energy to lift up the fluid against the gravitation and to create more surface area. Hence the surface tension and gravitation acts as stabilizing forces and the magnetic field serves as destabilizing force. The Rosensweig instability possessed by a hydrocarbon-based ferrofluid is illustrated in **Figure 3.1**.

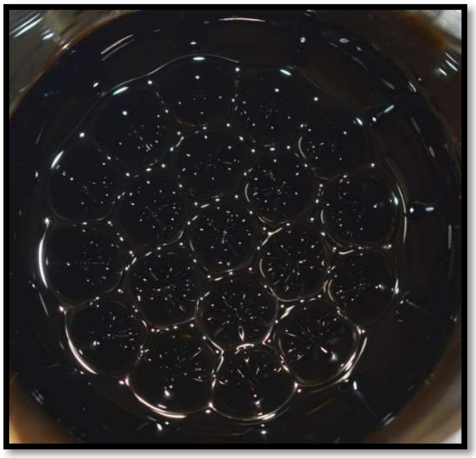

Figure 3.1 Rosensweig instability possessed by a hydrocarbon based ferrofluid in the presence of a uniform magnetic field

3.3 Characterization

The synthesized magnetic nanoparticles were characterized by XRD for structural identification and determination of crystallite size. The diffraction pattern of the sample was recorded at room temperature from 10° to 80° in the 2θ scale with a scanning speed of 3° (per minute) using Bruker AXS D8 Advance X ray diffractometer employing Cu–Kα X-rays of wavelength 1.5406 Å. Fourier Transform Infrared Spectroscopy is a non-destructive analytical technique. FTIR is employed to identify the structure and chemical bonds of a material. FTIR was performed on the dried sample of magnetite using an FTIR Bruker spectrophotometer in the wavelength range of 3500–400 cm^{-1} with a resolution of 4 cm^{-1}. The dried sample was mixed with KBr and compressed into a pellet, whose spectrum was recorded. The hydrodynamic size of the Fe_3O_4 nanoparticles was determined using DLS (Horiba Scientific, SZ-100 at 532 nm) principle. The concentrations of A, B, C and D are 0.33, 0.66, 1.33, 2 mg/cc respectively. The Pendant drop method was employed to determine the surface tension of the prepared ferrofluid using VCA Optima (Model S/N, 1021046135). The particle concentration is determined from TGA analysis (Perkin Elmer STA6000, at a heating rate of 10°C per minute and up to a maximum temperature of 1000°C). The magnetization measurement was carried out via SQUID, (Quantum design, VSM_HW_VERSION-3101-150 F0).

3.3 Experimental

3.3.1 Synthesis of hydrocarbon based ferrofluid

Chemical co-precipitation is one of the most prominent methods to synthesize ferrofluid. In this method, ferrous sulphate heptahydrate ($FeSO_4 \cdot 7H_2O$) and anhydrous ferric chloride ($FeCl_3$) with a molar ratio of 1:2 are dissolved in deionized water separately. The equimolar (1:2) solution of $FeSO_4 \cdot 7H_2O$ and $FeCl_3$ was mixed together and homogenized by using magnetic stirring for 30 minutes. Then the NH_4OH solution was added dropwise under vigorous magnetic stirring until the pH of the solution reached 10.5. Oleic acid was added to the solution to prevent the agglomeration of magnetic nanoparticles; this was heated to 50°C and subjected to continuous stirring while heating for 30 minutes. Further, the solution was allowed to cool while stirring for 60 minutes. Dilute hydrochloric acid was added dropwise until the pH of the mixture was reduced to below 7. The suspended particles were separated by magnetic decantation and washed repeatedly with deionized water to remove the impurities and free radicals. Finally, the unreacted oleic acid and water were removed by washing with acetone and the slurry was placed in the oven at 70°C until the oleic acid-coated magnetite fine powder was formed. Then the coated particles are dispersed in kerosene by sonication for 30 minutes at room temperature in order to obtain stable ferrofluid.

3.3.2 Analysis Techniques

Rosensweig instability studies were performed on the synthesized fluid in an indigenous experimental arrangement **(Figure 3.2(a))**. The synthesized ferrofluid is taken in a cylindrical glass container with a flat circular bottom of 70 mm in diameter, to a thickness of 4 mm, and was placed at the center of a pair of Helmholtz coils. A DLS camera was positioned above the vessel for image observation. A digital gauss meter (Model: DGM-102) is used for measuring the field. The Pendant drop method is one of the standard methods used to determine the surface tension of a liquid [23]. The experimental setup for the pendant drop method is shown in **(Figure 3.2(b))**. This technique involves the acquisition of a profile of an axisymmetric fluid droplet and iterative fitting of the Young-Laplace equation with a high digital camera (Model: UI-3240CP) automated with the computer for the purpose.

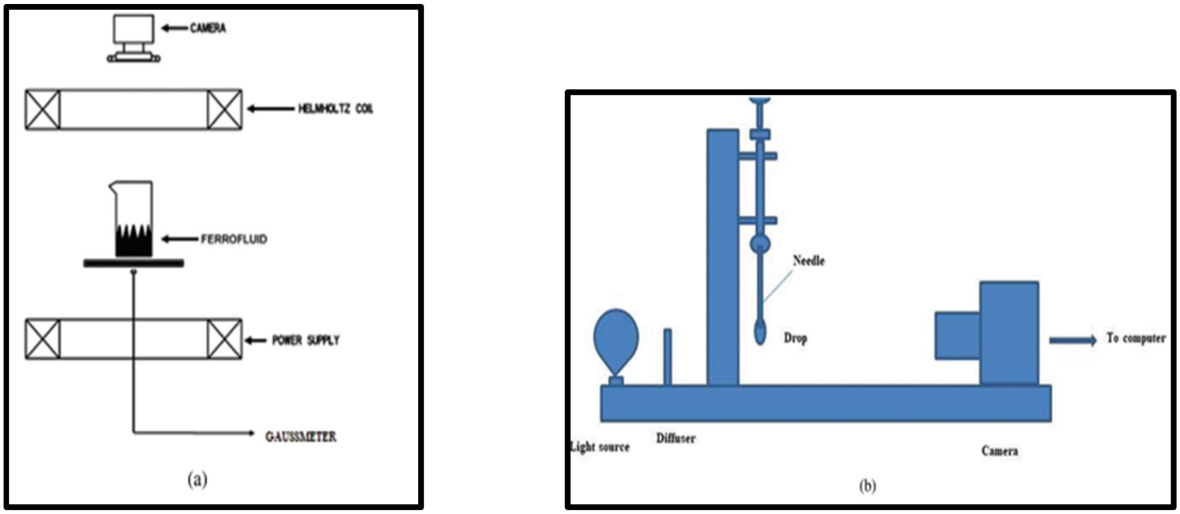

Figure 3.2 Experimental set up for (a) Rosensweig instability and (b) Pendant drop method for surface tension measurement

3.4 Results and Discussions

3.4.1 Structural characterization

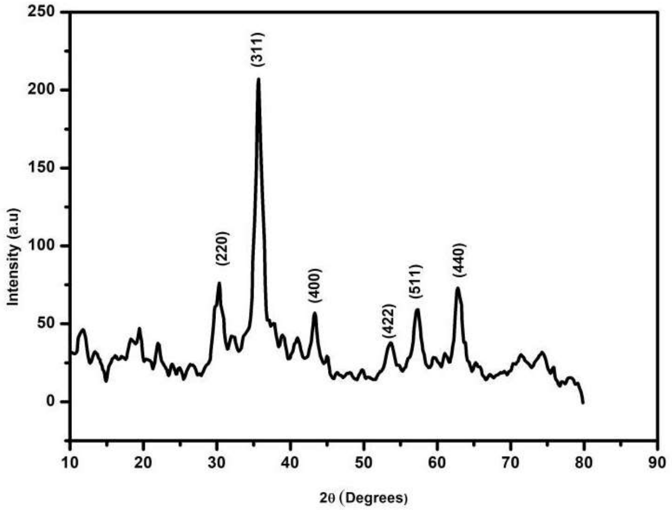

Figure (3.3a) X-ray diffraction pattern of Fe_3O_4

Figure 3.3a depicts the XRD pattern of the synthesized magnetic particles. All the characteristic peaks of the Fe_3O_4 crystal with a cubic inverse spinel structure could be seen in the pattern and are in good agreement with the database in JCPDS file no: 19-0629. No extra peaks have been observed in the XRD pattern, which indicates the high purity of the synthesized particles [24]. The broadening of the diffraction lines indicates the nanocrystalline nature of the particles in the sample [25]. The average crystallite size of the particles was estimated from the line width of the various diffraction peaks by Debye Scherrer's formula [26].

$$D = \frac{K\lambda}{\beta \cos\theta} \qquad (3.8)$$

Here, D is the mean crystallite size, K is a Debye constant, λ is the wavelength of the radiation (1.5406 Å), β is the full width at half maximum in radians, and θ is the Bragg angle. The crystallite size is approximately found to be (9 ± 1.8) nm. The Lattice constant of the synthesized Fe_3O_4 particle is calculated to be 8.33 Å. The lattice parameter is slightly lesser than the standard value of 8.39 Å indicating the strain in the nanocrystal. The strain induced in the material is determined by the Williamson-Hall method [27].

3.4.2 Williamson-Hall Plot

The induced micro strain was calculated from the Williamson-Hall method, using the equation [28].

$$\beta \cos\theta = \frac{.9\lambda}{D} + 4\varepsilon \sin\theta \qquad (3.9)$$

Where λ is the wavelength of X-ray, β is the full width at half maximum of the diffraction peaks; θ is the Bragg angle in degree and ε is the strain. By plotting $\beta\cos\theta$ versus $4\sin\theta$, the strain component is obtained from the slope and the size component from the intercept.

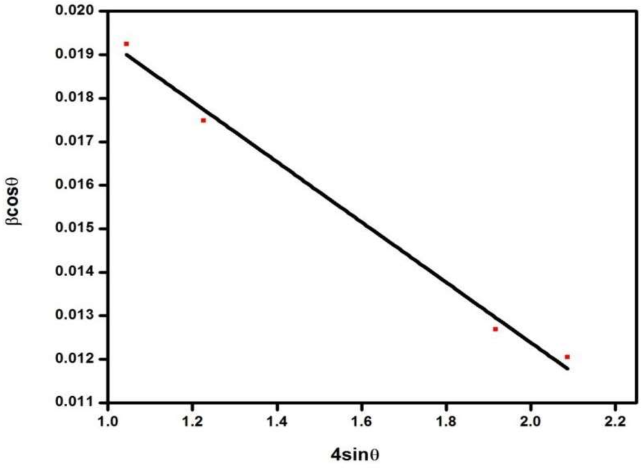

Figure (3.3b) W-H plot of Fe_3O_4 nanoparticles

Figure (3.3b) shows the W-H plot, variation of $\beta\cos\theta$ versus $4\sin\theta$ for the synthesized sample. The induced strain calculated from the plot is -0.00692. The negative value of the strain indicates lattice compression of the synthesized particles, which is in agreement with the reduced lattice parameter as calculated from the interplanar distance [29].

3.4.3 FTIR Spectra

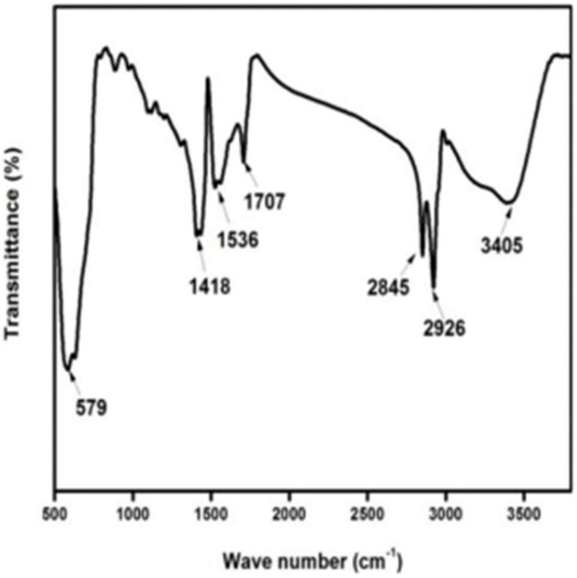

Figure 3.4 FTIR Spectra of Oleic acid coated Fe_3O_4 nanoparticles

The FTIR spectrum is illustrated in **Figure 3.4.** The absorption lines are summarised in Table I. In oleic acid-coated Fe_3O_4 nanoparticles, the CH_2 asymmetric stretching vibration is shifted to 2926 cm^{-1} and the symmetric stretching vibration is shifted to 2845 cm^{-1}. These shifts of characteristic bands to a lower frequency indicate that the oleic acid molecules were adsorbed onto the solid surface, and the hydrocarbon chains in the monolayer surrounding the nanoparticles, in a close-packed crystalline state. Two new bands appear at 1536 cm^{-1} and 1418 cm^{-1} which indicates the asymmetric and symmetric stretching of the carboxylic group of oleic acid attached to the Fe atoms [30]. A weak band at 1707 cm^{-1}, indicates that most of the oleic acid in the nanoparticle system is adsorbed on Fe_3O_4 nanoparticles. The band at 579 cm^{-1} is the characteristic band of the Fe–O bond [31]. FTIR study confirms the presence of functional groups on Fe_3O_4 nanoparticles. The absorption lines of Oleic acid coated Fe_3O_4 nanoparticles is shown in **Table 3.1**.

Wave number (cm^{-1})	Peak assessment
3405	Hydroxyl group
2926	C-H_2 asymmetric stretching
2845	C-H_2 symmetric stretching
1707	Adsorbed Oleic acid
1536	Asymmetric stretching of carboxyl group of Oleic acid
1418	Symmetric stretching of carboxyl group of Oleic acid
579	Fe-O bond

Table 3.1 The absorption lines of Oleic acid coated Fe_3O_4 nanoparticles

3.4.4 DLS Measurement

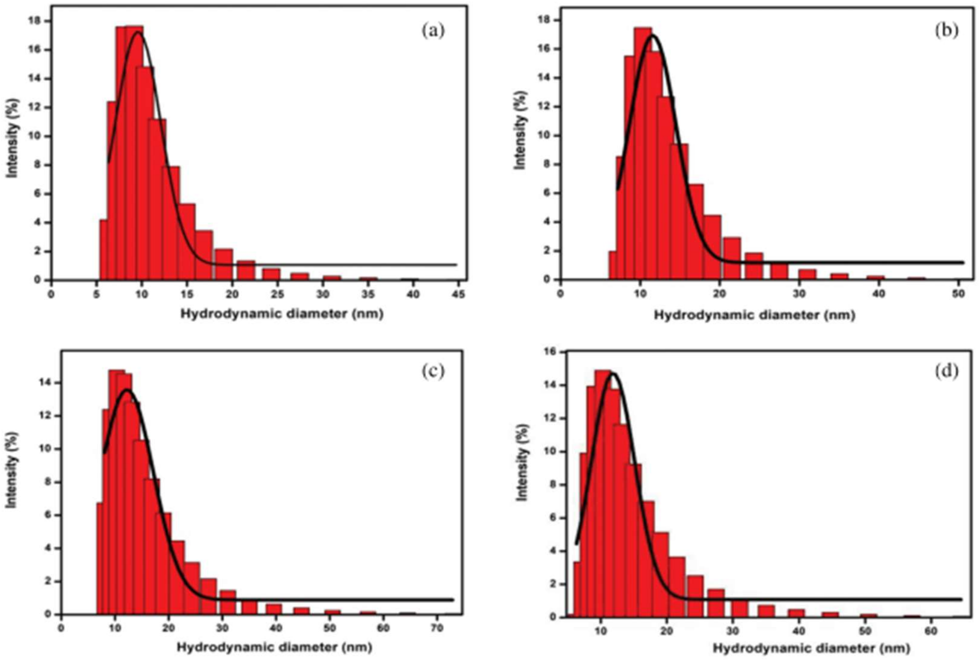

Figure 3.5 Hydrodynamic size of Fe_3O_4 nanoparticles of different concentrations

The DLS measurements were carried out on ferrofluid of different concentrations. The sample D has the highest concentration and A the lowest. It can be seen that in all these cases the size was found to be around 11 nm with a standard deviation of 1.7 nm as shown in **(Figure 3.5)**, which means that the agglomeration among nanoparticles is negligible and no clustering has occurred in the fluid [32]. The presence of surfactant on the surface of nanoparticles affects the diffusion speed, which will change the apparent size of the particles. Hence a slight variation in the size of the particle as compared to the value of average crystallite size obtained from XRD i.e., 9 nm. The asymmetry in the Gaussian fit is due to the variation of the size of particles. The asymmetry inclined towards the left indicates the presence of smaller particles is larger than that of the bigger ones.

3.4.5 Thermogravimetric Analysis (TGA)

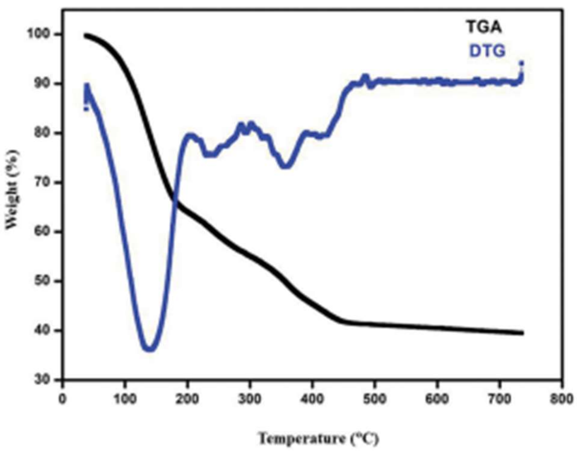

Figure 3.6 TGA curve of oleic acid coated Fe_3O_4 nanoparticles

The TGA curve of oleic acid-coated Fe_3O_4 nanoparticles are shown in **Figure 3.6**. In the TGA curve, a weight loss below 150°C indicates the removal of adsorbed kerosene on the surface of Fe_3O_4. The major weight loss is observed between 200 and 400°C, which is due to the degradation of oleic acid. The peak is around 237°C, which is associated with the presence of free oleic acid [33]. The weight loss around 360°C arises due to the decomposition of oleic acid directly attached to the surface, which confirms the strong binding between the oleic acid molecules and Fe_3O_4 nanoparticles. There is no significant weight change from around 460°C, indicating that only iron oxide is present [34]. From the TGA curve the magnetic content of the iron oxide is about 36.8 wt%.

3.4.6 Magnetization Measurement

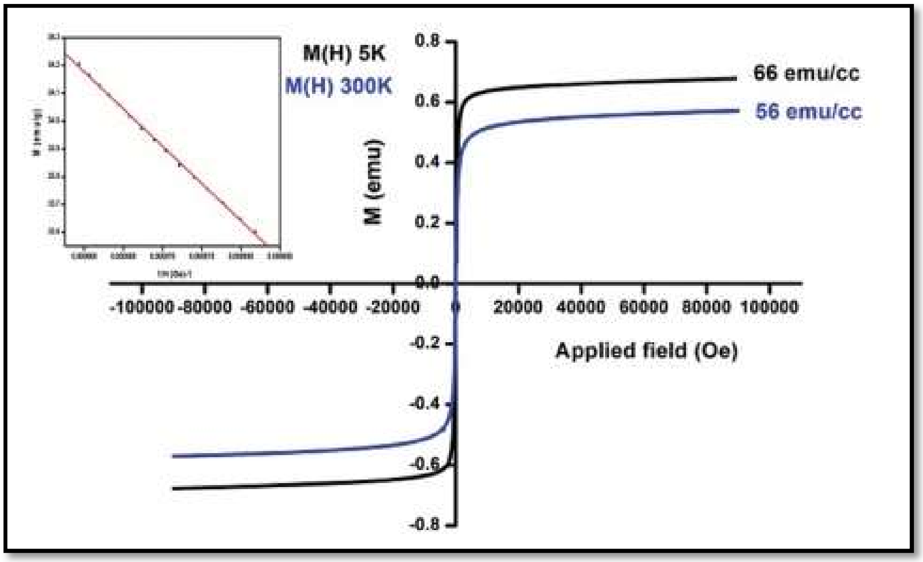

Figure 3.7 M-H curve at 5 K and 300 K. (Inset: Magnetization—H^{-1} plot for iron oxide)

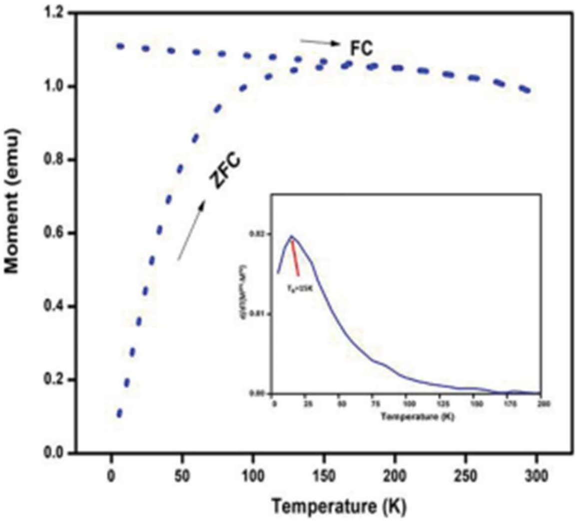

Figure 3.8 FC-ZFC moment variation with temperature (Inset: The derivative plot showing blocking temperature)

The magnetic measurements were carried out using a SQUID magnetometer. The hysteresis curves measured at room temperature and 5 K, are depicted in **Figure 3.7**. The M-H curve exhibits negligible coercivity and remanence, which signifies the superparamagnetic nature of particles. The saturation magnetization at room temperature is calculated by extrapolating the magnetization versus the inverse of the applied field, plotted in the inset of **Figure 3.7**. The field cooled (FC) and zero field cooled (ZFC) measurements are carried out at an applied field of 10 mT **(Figure 3.8)**. In ZFC measurement the sample was cooled down from a temperature of 300 K to 5 K without applying a magnetic field. After reaching 5 K, a field of 10 mT was applied and the magnetization was measured as a function of temperature upon heating up to 300 K. In FC measurement, the sample is cooled in a field of 10 mT up to 5 K and the moment is evaluated while warming up to a temperature of 300 K. The ZFC measurements exhibit a qualitative indication of the size distribution of the particles. The broad peak of ZFC reflects the relatively wide size distribution of magnetic nanoparticles, existence of randomly oriented surface spins, variation in magnetic anisotropic energy, magnetic interactions among the nanoparticles, which also suggests the polydispersion and the spin glass behaviour of the nanoparticles [35-39]. In ZFC measurement the magnetic moment increases with temperature and at a particular temperature the magnetic moment becomes maximum, the corresponding temperature is known as blocking temperature, where the thermal energy equals the anisotropy energy. A blocked state is reached by the nanoparticles at temperatures lower than the blocking temperature, in which their magnetic moments are fixed in orientation. They exhibit intrinsic ferrimagnetic ordering, which is reflected in their irreversible magnetization behaviour [40]. Temperature has a significant impact on the anisotropy energy, which is essential in deciding whether magnetic nanoparticles exhibit superparamagnetic nature or are in a blocked state. At high temperatures, superparamagnetism occurs when thermal fluctuations surpass the anisotropy energy. The anisotropy energy dominates at low temperatures, preventing magnetization variations and resulting in a blocked or frozen state [41]. The blocking temperature depends on the effective anisotropy and particle size. The blocking temperature obtained from the first derivative of the difference between ZFC and FC moments to temperature is plotted in the inset of **Figure 3.8**. The curve exhibits a maximum of 15 K, which corresponds to the average blocking temperature. In ZFC measurement, as the temperature increases the thermal energy disturbs the system, and more particles acquire enough energy to align along the field direction, hence the magnetization increases. But when the thermal energy is greater than the anisotropy energy the magnetic moments of the particles are randomized and the magnetic moment decreases monotonically with temperature [42]. The FC curve is measured from room temperature down to 5 K. The magnetic moment decreases with the increase in temperature. When the temperature is lowered the thermal fluctuation decreases and the magnetic moments are aligned along the field direction, hence an increase in the magnetic moment. For weakly interacting systems with a relatively large increase in the FC magnetization at low temperatures, this tendency has been reduced by the effects of interaction among the nanoparticles [43].

3.4.7 Surface Tension Measurement

The Pendant drop method is employed to determine the surface tension of the synthesized ferrofluid and the value of surface tension is found to be $22 \times 10^{-3}\text{Nm}^{-1}$. The image of the pendant drop of the prepared sample captured by a CCD camera is shown in **Figure 3.9**.

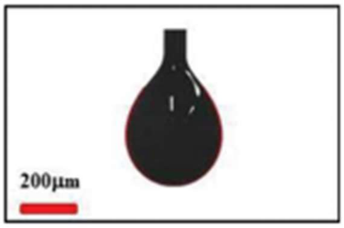

Figure 3.9 Image of the ferrofluid drop captured by a digital camera

3.4.8 Rosensweig instability measurement

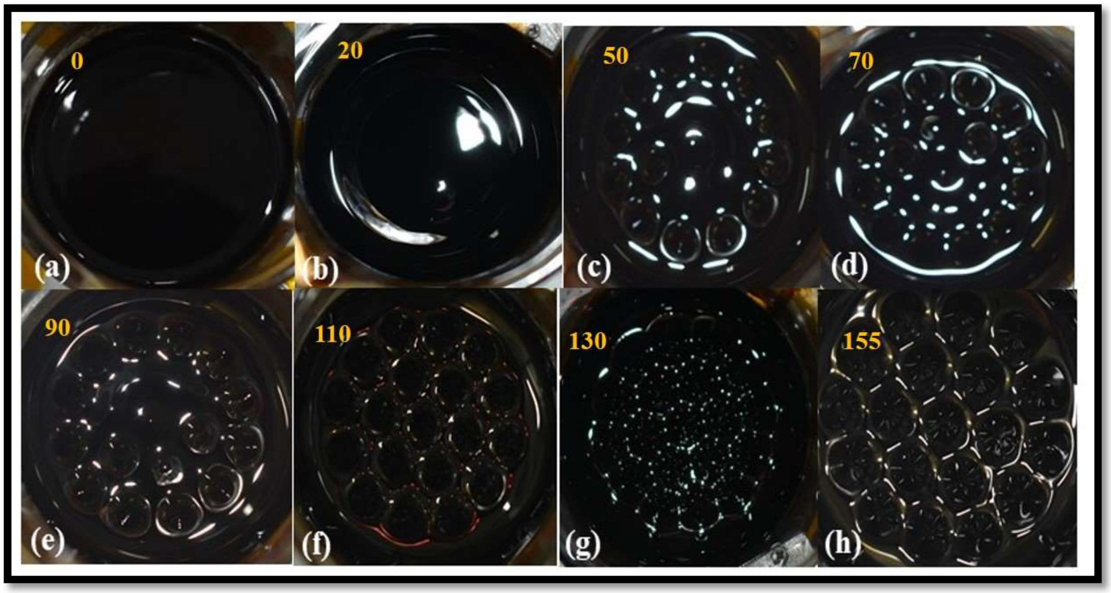

Figure 3.10 Progression of ferrofluid pattern in the presence of different magnetic field

Rosensweig instability studies were carried out in the experimental arrangement depicted in **Figure 3.2(a)**. The surface of the fluid exhibited different microstructures in the external applied uniform magnetic field normal to the surface of the fluid. The strength of the uniform magnetic field varies slowly and the formation of various surface patterns are studied and analyzed. The ferrofluid surface may distort into peaks and valleys to produce a patterned lattice in the presence of a vertical homogeneous magnetic field. At initial field strength, the applied field acts as a perturbation on the surface of the ferrofluid, which is in equilibrium by forces of surface tension. As the field is increased and when the magnetic force exceeds the stabilizing forces due to surface tension and gravitation, instability occurs in the fluid. In the absence of a magnetic field, the fluid surface remains stable as shown in (Fig. 3.10(a)). The progression of the ferrofluid pattern in the presence of different magnetic fields is depicted in **Figure 3.10**. When the applied field was increased in a quasistatic way with step of 5 Gauss, the perturbation was increased and the flat surface changed to ridges, (Fig. 3.10(b)). The magnetization of the ferrofluid increases with an increase in the applied magnetic field. When the critical magnetization is reached, the ferrofluid surface starts to deform yielding an outer ring, which is evident in the white reflection showing involutions and internal islands. The white reflections are due to light scattering from peaks and valleys of the emerging topographical elements. The magnetic flux gets concentrated at the peaks which drive the perturbation. At a critical field, no wave propagation is possible, but the surface becomes unstable with respect to the stationary surface of the fluid. Further increase in the applied field resulted in a transition to a well-ordered hexagonal pattern at a field of 120 Gauss (Fig. 9(c)) [39]. Above this threshold field, the wavenumber remained constant while the spike height increased with the field until it reached the second threshold of 155 Gauss when the hexagonal pattern started to disappear and the square pattern slowly started emerging (Fig. 9(d)). When the applied field strength was gradually decreased; the transition from the square pattern to hexagonal occurs at a higher field. This can be called inverse hysteresis. For a hexagonal pattern the distance between two spikes under critical conditions and surface tension is given by eqs. (1) and (3) respectively. The average spike distance was found to be 9.9 mm for the hexagonal pattern, and the corresponding wavenumber was 0.73 mm^{-1}. The surface tension is calculated to be $(21 \pm .62) \times 10^{-3}$ Nm^{-1}. The value of surface tension obtained from the Rosensweig instability study is in good agreement with the value obtained from the Pendant drop method.

3.5 Conclusions

Stable kerosene-based ferrofluid has been successfully synthesized by the controlled chemical Co-precipitation method. The structural characterization was performed by XRD, FTIR and DLS. The XRD pattern shows that the synthesized magnetic nanoparticles are crystallized in a cubic inverse spinel structure with an average crystallite size of 9 nm. The line broadening of XRD shows the ultra-fine nature of Fe_3O_4 nanoparticles. The size and strain contribution to line broadening was also analyzed by the W-H method. From the DLS measurement of the prepared fluid at different concentrations, the fluid was found to be stable and free of clusters. The hydrodynamic size of the ferrofluid was found to be 11 nm in good agreement with the value obtained from the XRD measurement. FTIR analysis reveals that the oleic acid has been successfully coated onto the surface of Fe_3O_4 nanoparticles by chemical adsorption. The magnetic content of the iron oxide is about 36.8 wt% from TGA. The M-H curve exhibits negligible coercivity and remanence, which signifies the superparamagnetic nature of particles. The ZFC measurements exhibit the size distribution of particles. For a collection of particles with a large size distribution, there would be a broad maximum in the ZFC curve. From the Pendant drop method, the surface tension of the prepared ferrofluid was found to be 22×10^{-3} Nm^{-1} which is confirmed in the analysis of instability measurements. In this work, we have demonstrated the Rosensweig instability experimentally. The Instability mechanism occurs only when the applied magnetic field exceeds the stabilizing forces due to surface tension and gravitational force. When the applied field becomes greater than the critical field the surface changes to a hexagonal pattern and when the applied field reaches a second threshold the hexagonal pattern changes to a square pattern. The hexagonal pattern won't be transformed to the square pattern until or unless the instrument capacity is beyond 155 Gauss. It is also observed that on reducing the applied magnetic field, the hexagonal pattern reappears at a higher field and is attributed to inverse hysteresis. From the Rosensweig instability measurement the surface tension of the prepared ferrofluid was calculated and found to be in good agreement with the value obtained from the Pendant drop method. The interplay of an external magnetic field, surface tension, and gravitational force forms a pattern of characteristic spikes. The Rosensweig instability in higher magnetic field is under progress. The combined effect of electric and magnetic fields on the instability of ferrofluid for ferrofluid thrusters is under experimental optimization. Studying the fluid properties in an external magnetic field is exploited in a wide range of applications, especially for designing ferrofluid actuator. The Rosensweig instability studies on different non-magnetic interfaces and the dependence of spike height on-field strength is a prospect.

References

[1]. Berger, P., Adelman, N.B., Beckman, K.J., Campbell, D.J., Ellis, A.B. and Lisensky, G.C., 1999. Preparation and properties of an aqueous ferrofluid. Journal of chemical education, 76(7), p.943.

[2]. Scherer, C. and Figueiredo Neto, A.M., 2005. Ferrofluids: properties and applications. Brazilian journal of physics, 35, pp.718-727.

[3]. Borglin, S.E., Moridis, G.J. and Oldenburg, C.M., 1998. Experimental studies of magnetically-driven flow of ferrofluids in porous media. Report LBNL-40126, Lawrence Berkeley National Laboratory, Berkeley, California.

[4]. Charles, S.W. and Popplewell, J., 1980. Ferromagnetic liquids. Handbook of Ferromagnetic Materials, 2, pp.509-559.

[5]. Coey, J.M., 2010. Magnetism and magnetic materials. Cambridge university press.

[6]. Benz, M., 2012. Superparamagnetism: theory and applications. Superparamagnetism Theory Appl, pp.1-27.

[7]. Kaiser, R. and Rosensweig, R.E., 1969. Study of ferromagnetic liquid (No. NASA-CR-1407). NASA.

[8]. Rosensweig, R.E., 1979. Fluid dynamics and science of magnetic liquids. In *Advances in electronics and electron physics* (Vol. 48, pp. 103-199). Academic Press.

[9]. IV, E.J.M., King, L.B., Jain, N. and Hawkett, B.S., 2013. Ionic liquid ferrofluid electrospray with EMIM-NTf2 and ferrofluid mode studies with FerroTec EFH-1 in a non-uniform magnetic field.

[10]. Odenbach, S. ed., 2009. *Colloidal magnetic fluids: basics, development and application of ferrofluids* (Vol. 763). Springer Science & Business Media.

[11]. Cowley, M.D. and Rosensweig, R.E., 1967. The interfacial stability of a ferromagnetic fluid. *Journal of Fluid mechanics*, *30*(4), pp.671-688.

[12]. Zakinyan, A. and Mkrtchyan, L., 2013. Instability of the ferrofluid layer on a magnetizable substrate in a perpendicular magnetic field. *arXiv preprint arXiv:1307.7481*.

[13]. Popplewell, J., 1984. Technological applications of ferrofluids. *Physics in technology*, *15*(3), p.150.

[14]. Abou, B., Wesfreid, J.E. and Roux, S., 2000. The normal field instability in ferrofluids: hexagon–square transition mechanism and wavenumber selection. *Journal of Fluid Mechanics*, *416*, pp.217-237.

[15]. Zakinyan, A., Mkrtchyan, L. and Dikansky, Y., 2016. Experimental investigation of surface instability of a thin layer of a magnetic fluid. *European Journal of Mechanics-B/Fluids*, *56*, pp.172-177.

[16]. Gollwitzer, C., Rehberg, I. and Richter, R., 2006. Via hexagons to squares in ferrofluids: experiments on hysteretic surface transformations under variation of the normal magnetic field. *Journal of Physics: Condensed Matter*, *18*(38), p.S2643.

[17]. Bohlius, S., Brand, H.R. and Pleiner, H., 2008. Amplitude equation for the Rosensweig instability. *Progress of Theoretical Physics Supplement*, *175*, pp.27-36.

[18]. Gailītis, A., 1977. Formation of the hexagonal pattern on the surface of a ferromagnetic fluid in an applied magnetic field. *Journal of Fluid Mechanics*, *82*(3), pp.401-413.

[19]. Knieling, H., Richter, R., Rehberg, I., Matthies, G. and Lange, A., 2007. Growth of surface undulations at the Rosensweig instability. *Physical Review E—Statistical, Nonlinear, and Soft Matter Physics*, *76*(6), p.066301.

[20]. Browaeys, J., Bacri, J.C., Flament, C., Neveu, S. and Perzynski, R., 1999. Surface waves in ferrofluids under vertical magnetic field. *The European Physical Journal B-Condensed Matter and Complex Systems*, *9*(2), pp.335-341.

[21]. Lange, A., Gollwitzer, C., Maretzki, R., Rehberg, I. and Richter, R., 2016. Retarding the growth of the Rosensweig instability unveils a new scaling regime. *Physical Review E*, *93*(4), p.043106.

[22]. Lange, A., Gollwitzer, C., Maretzki, R., Rehberg, I. and Richter, R., 2016. Retarding the growth of the Rosensweig instability unveils a new scaling regime. *Physical Review E*, *93*(4), p.043106.

[23]. Berry, J.D., Neeson, M.J., Dagastine, R.R., Chan, D.Y. and Tabor, R.F., 2015. Measurement of surface and interfacial tension using pendant drop tensiometry. *Journal of colloid and interface science*, *454*, pp.226-237.

[24]. Arora, A.K., Sharma, M., Kumari, R., Jaswal, V.S. and Kumar, P., 2014. Synthesis, Characterization, and Magnetic Studies of α-Fe2O3 Nanoparticles. *Journal of Nanotechnology*, *2014*(1), p.474909.

[25]. Reena Mary, A.P. and Anantharaman, M.R., 2011. *Investigations on Magnetic, Optical and Transport Properties of Magnetic Nanofluids for Engineering and Biomedical Applications* (Doctoral dissertation, Cochin University of Science & Technology).

[26]. Wahab, M.A., 2005. *Solid state physics: structure and properties of materials*. Alpha Science Int'l Ltd..

[27]. Dhumal, J., Bandgar, S., Zipare, K. and Shahane, G., 2015. Fe_3O_4 ferrofluid nanoparticles: synthesis and rheological behavior. *Int J Mater Chem Phys*, *1*, pp.141-145.

[28]. Izumi, F. and Ikeda, T., 2015. *Implementation of the Williamson-Hall and Halder-Wagner methods into RIETAN-FP* (Doctoral dissertation, Nagoya Institute of Technology).

[29]. Gonçalves, N.S., Carvalho, J.A., Lima, Z.M. and Sasaki, J.M., 2012. Size–strain study of NiO nanoparticles by X-ray powder diffraction line broadening. *Materials Letters*, *72*, pp.36-38.

[30]. Ibarra, J., Melendres, J., Almada, M., Burboa, M.G., Taboada, P., Juárez, J. and Valdez, M.A., 2015. Synthesis and characterization of magnetite/PLGA/chitosan nanoparticles. *Materials Research Express*, *2*(9), p.095010.

[31]. Lobato, N.C.C., Mansur, M.B. and Ferreira, A.D.M., 2017. Characterization and chemical stability of hydrophilic and hydrophobic magnetic nanoparticles. *Materials Research*, *20*(3), pp.736-746.

[32]. Regmi, R., Black, C., Sudakar, C., Keyes, P.H., Naik, R., Lawes, G., Vaishnava, P., Rablau, C., Kahn, D., Lavoie, M. and Garg, V.K., 2009. Effects of fatty acid surfactants on the magnetic and magnetohydrodynamic properties of ferrofluids. *Journal of Applied Physics*, *106*(11).

[33]. Tenório-Neto, E.T., Jamshaid, T., Eissa, M., Kunita, M.H., Zine, N., Agusti, G., Fessi, H., El-Salhi, A.E. and Elaissari, A., 2015. TGA and magnetization measurements for determination of composition and polymer conversion of magnetic hybrid particles. *Polymers for Advanced Technologies*, *26*(10), pp.1199-1208.

[34]. Arévalo, P., Isasi, J., Caballero, A.C., Marco, J.F. and Martín-Hernández, F., 2017. Magnetic and structural studies of Fe_3O_4 nanoparticles synthesized via coprecipitation and dispersed in different surfactants. *Ceramics International*, *43*(13), pp.10333-10340.

[35]. Joy, P.A. and Date, S.K., 2000. Comparison of the zero-field-cooled magnetization behavior of some ferromagnetic and ferrimagnetic systems. *Journal of magnetism and magnetic materials*, *218*(2-3), pp.229-237.

[36]. Bhattacharya, S., Roychowdhury, A., Tiwari, V., Prasad, A., Ningthoujam, R.S., Patel, A.B., Das, D. and Nayar, S., 2015. Effect of biomimetic templates on the magneto-structural properties of Fe 3 O 4 nanoparticles. *RSC Advances*, *5*(18), pp.13777-13786.

[37]. Nasirpouri, F., Nogaret, A. and Bending, S.J., 2011. Effect of size and configuration on the magnetization of nickel dot arrays. *IEEE transactions on magnetics*, *47*(12), pp.4695-4700.

[38]. Martins, C., Rolo, C., Cacho, V.R., Pereira, L.C., Borges, J.P., Silva, J.C., Vieira, T. and Soares, P.I., 2025. Enhancing the magnetic properties of superparamagnetic iron oxide nanoparticles using hydrothermal treatment for magnetic hyperthermia application. *Materials Advances*.

[39]. Sappey, R., Vincent, E., Hadacek, N. and Boilot, J.P., 1997. Non-monotonic field-dependence of the ZFC magnetization peak in some systems of magnetic nanoparticles. *arXiv preprint cond-mat/9705245*.

[40]. Etemadi, H. and Plieger, P.G., 2020. Improvements in the Organic-Phase Hydrothermal Synthesis of Monodisperse M x Fe3–x O4 (M= Fe, Mg, Zn) Spinel Nanoferrites for Magnetic Fluid Hyperthermia Application. *ACS omega*, *5*(29), pp.18091-18104.

[41]. Denardin, J.C., Brandl, A.L., Knobel, M., Panissod, P., Pakhomov, A.B., Liu, H. and Zhang, X.X., 2002. Thermoremanence and zero-field-cooled/field-cooled magnetization study of Co x (SiO 2) 1− x granular films. *Physical Review B*, *65*(6), p.064422.

[42]. Ozkaya, T., Toprak, M.S., Baykal, A., Kavas, H., Köseoğlu, Y. and Aktaş, B., 2009. Synthesis of Fe3O4 nanoparticles at 100 C and its magnetic characterization. *Journal of Alloys and Compounds*, *472*(1-2), pp.18-23.

[43]. Chantrell, R.W., Walmsley, N.S., Gore, J. and Maylin, M., 1999. Theoretical studies of the field-cooled and zero-field cooled magnetization of interacting fine particles. *Journal of applied physics*, *85*(8), pp.4340-4342.

[44]. Nimisha, O.K., Pal, S., Divya, D., Al-Omari, I.A., Pradeesh, K. and Reena Mary, A.P., 2023. Rosensweig Instability Study of Iron Oxide Nano Fluid Under Uniform Magnetic Field. *Journal of Nanofluids*, *12*(1), pp.183-191.

Chapter 4

Magneto-Optical and Magneto-Plasmonic study of Iron Oxide Fluid based on Silver

Ferrofluids have caught the attention of many due to their unique magnetic, electrical and optical properties. Under the influence of an external magnetic field, ferrofluid exhibits different phenomena, like linear dichroism, faraday rotation, birefringence, magneto-optical transmission etc. The magneto-optical phenomena are interesting to study the aggregate formation and inter-particle interaction in ferrofluid. The magneto-optical dichroism measurements are carried out on hydrocarbon and aqueous-based ferrofluid. The present chapter also includes the synthesis of a hybrid iron oxide nanofluid based on silver and the effect of the applied magnetic field on the hybrid fluid. Combining the effects of magnetism with plasmonic structure can lead to many applications, especially in the medical field. Surface plasmon resonance-based sensor (SPR sensor) is a powerful tool for the study of biomolecular interactions. However, the conventional SPR sensor is limited in its ability to resolve complex samples, extremely dilute concentrations or small molecular weight. The surface plasmon resonance sensitivity can be enhanced using a magnetic material in the presence of a magnetic field. The present chapter discusses the effect of an external magnetic field on the surface plasmon coupled emission using reverse Kretschmann configuration.

4.1 Introduction

The magnetic state of the medium and the electronic structure of the matter are factors that influence how light interacts with matter. These interactions produce magneto-optical effects when electromagnetic energy interacts with magnetically polarised materials. Michael Faraday made the initial discovery of this phenomena in 1842 [1, 2]. He observed that when a linearly polarised light beam propagates parallel to an externally applied magnetic field, it experiences a polarisation rotation [3]. John Kerr later detected the magneto-optical phenomenon in reflection mode in 1888 [4, 5]. These effects were crucial to the development of electromagnetism in the early years since they supported the electromagnetic theory of light and the classical and quantum theories of matter, including the spin-orbit coupling and electron spin movements. Magneto-optical effects are instrumental in exploring the electronic structure and properties of atomic, molecular, and solid-state systems. These effects arise from the interaction between a material's magnetic moment and light passing through it. One of the earliest observations in this field was made by Faraday, who noticed that polarized light undergoes rotation when it passes through a magneto-responsive medium subjected to an external magnetic field, a phenomenon known as Faraday rotation [6]. In this instance, the incident light follows the longitudinal mode, which is the direction in which the applied magnetic field travels. This rotation results from an interaction between the medium's magnetisation vector and the incoming light's electric field vector. In the reflection mode, magneto-optical phenomena are also utilised, especially in the construction of magneto-optical recording systems and the research of domain dynamics, which gives rise to the Magneto-Optical Kerr effect (MOKE). Depending on the direction of the incident light and the magnetic field's orientation, different types of Kerr effects, including transverse, longitudinal, and polar Kerr effects, can be observed. These phenomena can be understood by considering the effective dielectric tensor of the material, with complex, skew-symmetric elements, and their effects can be explained using Maxwell's equations [7]. Magneto-optical effects in the transmission mode are characterized by the way light passing through a magnetized medium is influenced by the strength and direction of an applied magnetic field or the medium's magnetization. Several significant magneto-optical effects manifest in this scenario, including Faraday rotation, field-induced dichroism, magnetic birefringence, and Cotton-Mouton rotation. These effects collectively alter the behaviour of transmitted light in terms of absorption, refraction, scattering, and the rotation of its plane of polarization. The extent and nature of these alterations depend on the prevailing magnetic field strength and the magnetization of the medium, with the most prominent effect taking precedence in a given situation. This interplay between light and magnetized materials finds applications in various optical devices, such as Faraday rotators, optical isolators, kerr microscopy [8], where precise control over light's properties is essential.

A significant benefit of integrating plasmonics with magneto-optical materials is the level of engineering control that can be achieved by altering the metal structure's design. Such control of light-matter interaction has been possible in metamaterials over the last decade. Furthermore, carefully chosen plasmonic devices may be able to disrupt the rotational symmetry of polarization space, which creates an artificial magnetic field that imparts circular birefringence to transmitted light. One of the most exciting aspects of nanoscience is the size and shape-dependent properties of matter. Due to the spatial confinement of electrons, phonons and electrical fields surrounding the particles, as well as the material, exhibits a variety of unique features. The confinement of electrons and ensuring changes in electronic energy levels cause the most significant change to be seen in colour. In the case of isotropic particles, the properties will be mostly unaffected by direction. The ferrofluid offers a unique possibility of tuning the particle interaction by an external magnetic field. In the presence of an external magnetic field, magnetic fluids exhibit field-induced optical anisotropy, which gives rise to numerous extraordinary magneto-optical properties like magnetic birefringence, dichroism, magnetically tunable refractive index, the photonic hall effect and negative refractivity [9]. A thorough knowledge of field-induced aggregation dynamics and related magneto-optical characteristics in ferrofluid still has to be developed, which is crucial for practical applications. Hence the primary goal of the present work was to gain a further understanding of the complex aggregation. When an external magnetic field is present, the nanoparticles in magnetic fluids encounter an attracting attraction parallel to the field direction and a repulsive force perpendicular to it. Head-to-tail aggregation of the randomly orientated scattered Brownian nanosized particles results in the formation of chain-like structures aligned along the direction of the magnetic field. As a result of the chains' lateral coalescence, they go through secondary aggregation to produce thick columns. Field-induced aggregation in magnetic fluids is mostly caused by the dipolar interaction between the distributed nano-sized magnetic particles. The magnetic particles exhibit optical isotropy and exhibit characteristics of permanent magnetic dipoles. The static magnetic forces between them lead to the formation of certain linear head-to-tail aggregates. It is believed that these individual particles in the aggregates become oscillating dipoles in the laser beam's electric field and interact with each other due to their close proximity. Depending on how the aggregates are oriented in relation to the polarisation direction of the light beam, the interaction is asymmetric. The optical anisotropy that results from the asymmetry is what causes the dichroism and birefringence effects in magnetic fluids. Ferrofluid is optically isotropic in the absence of an external magnetic field; once the external field is applied, they show anisotropic behaviour and exhibit magneto-optic phenomena like linear dichroism, faraday rotation, birefringence, magneto-optical transmission etc. Linear dichroism arises due to the intrinsic optical anisotropy or the shape anisotropy of individual magnetic particles. In a ferrofluid the random orientation of particles does not show any anisotropy in the fluid as a whole; hence the particles would not be expected to give rise to dichroism. But when a magnetic field is applied the particles may orient in the field direction; this causes the magnetic fluids to be structurally anisotropic. If the transmitted light intensity is different from the polarization of light perpendicular and parallel to the applied magnetic field, it is called the magneto-optic linear dichroism effect. In a ferrofluid, the particles in aggregate forms can act as oscillating dipoles. Optical effects caused by magnetic fields are created when two dipoles interact to produce anisotropic polarizability. Ferrofluids have magneto-optical effects because when a magnetic field is applied, some pre-existing aggregates align along the direction of the applied magnetic field. As the strength of the field increases, these clusters get bigger and form long periodic chains [10].

Recently researchers have investigated the remarkable localized surface plasmon resonance properties of metallic nanoparticles. In metallic nanoparticles, the conduction electrons move freely and moved toward the nanoparticle surface when the particle is irradiated by the electromagnetic field of light. Due to the confinement of these electrons inside the nanoparticle, when a positive charge accumulates on one side and a negative charge accumulates on the other, an electric dipole will form. The dipole forces the electrons to revert to their equilibrium position by producing an internal electric field inside the nanoparticle that is opposite to the one the light creates. When the field is withdrawn after the electrons have been shifted from their equilibrium position, they will oscillate at a frequency known as plasmonic frequency [11]. Scientists have long wished for a magnetic plasmonic nanofluid because it opens up a wide range of potential uses, including sensors, batteries, a substrate for surface-enhanced Raman spectroscopy (SERS), imaging, and therapies. They are also important from a fundamental perspective. One of the best plasmonic materials is silver, which exhibits relatively little magneto-optical activity at moderate magnetic fields. But if we add plasmonic components with ferro or ferrimagnetic materials, it exhibits a strong magneto-optical effect.

Thus, magnetism in plasmonics opens up new possibilities for creating effective and adaptable magneto-plasmonic structure. A magneto-plasmonic nanofluid, a hybrid fluid, offers a novel framework for investigating the magneto-optical effects. When such a nanofluid is exposed to an externally supplied magnetic field, important new information about the nature of light-matter interactions will emerge. The combination of magnetic and optical response produces high SAR values (Specific absorption rate), which means a considerable increment in heating power compared to the value obtained from individual responses used in medical applications. Some of the important magneto-optic phenomena are described here:

1. Magnetic circular dichroism

When a medium propagates circularly polarised light with unequal absorption on the left and right, it is said to display circular dichroism. In the absence of a magnetic field, these two components would experience the same absorption coefficient, and there would be no difference in their absorption [12]. Due to its solenoidal nature, a magnetic field can cause circular dichroism in a medium when applied along a direction of propagation for circularly polarised light; this phenomenon is known as magnetic circular dichroism. When a magnetic field is applied, it interacts with the magnetic moments of electrons in the material, leading to the Zeeman effect, which splits the energy levels for electrons with different spin orientations. As a result of this energy level splitting, the LCP and RCP components of the incident light may experience different absorption coefficients. This difference in absorption between LCP and RCP is the essence of magnetic circular dichroism. While MCD is a characteristic of all matter, natural CD is a quite uncommon occurrence. This provides valuable information about the electronic structure of the material, such as the energy-level splitting due to the magnetic field and the nature of transitions that occur in the presence of the field.

2. Faraday rotation

The Faraday effect is the rotation of the plane of polarization of light as it passes through a material in a direction parallel to an applied magnetic field [13]. Faraday effect can be explained in terms of the space anisotropy that the magnetic field introduces. The right and left circularly polarised components are affected by the magnetic field in various ways. As a result, there is a rotation of the linearly polarised wave's plane of polarisation and distinct refractive indices and propagation constants for each sense of polarisation. The emerging beam will be elliptically polarised if there is absorption in the medium, since the absorption coefficient will vary for each sense of circular polarization. This effect has practical applications in optical devices and magnetic field measurements.

3. Cotton-mouton rotation

The light path in this transverse M O effect is perpendicular to the direction of the applied field. Once through a magnetised substance, the plane polarised light becomes elliptically polarised. The field-induced change in refractive index is the cause of this.

4. Linear dichroism

The term "linear dichroism" describes a situation in which the direction of polarisation affects how much light is absorbed. This dependence results from the fact that the angle between a transition moment M and the polarised field E determines the molecular absorbance due to that moment [16, 17]. Materials with orientated molecules, whose absorbance changes with orientation, demonstrate this. The intensity of absorption is directly related to the square of the scalar product formed by the light's electric field vector and a transition moment vector unique to the molecule. The absorption is greatest when the light vector is polarised parallel to the transition moment and zero when it is perpendicular to it. Thus, in situations when the orientation of the molecule is known, linear dichroism can yield either directions of transition moments or information on molecular orientation when the transition moments are known [18]. Linear dichroism and birefringence are linked by the dispersion equations and, hence, theoretically, share the same fundamental data. However, as linear dichroism is more easily related to roughly well-separated quanta1 transitions, it is more useful in practical applications than birefringence, which is an intricate average over all of the molecule's transitions. The dichroism of linearly polarised light created in a material by an external magnetic field or magnetization is known as magnetic linear dichroism. The variation in the optical absorption indices for linearly polarised light parallel `and perpendicular to magnetization is the source of the effect [19]. In the presence of a magnetic field applied perpendicular to the direction of the incident light, the energy levels of the electrons in the material are modified due to the Zeeman effect, which is a splitting of electron energy levels caused by the magnetic field. The modified energy levels influence the material's absorption properties. As a result, the material may exhibit different levels of absorption for linearly polarized light, depending on the orientation of the polarization concerning the applied magnetic field. This is known as magneto-optical linear dichroism.

4.2 Magneto-optical effects in ferrofluid

Ferrofluids are isotropic in nature due to the randomly oriented particles. But when an external magnetic field is applied, the ferrofluid shows anisotropic behaviour and exhibits magneto-optical phenomena like linear dichroism. The light changes in intensity after passing through the sample. The transmitted light intensity depends on the direction of polarization under the applied magnetic field [20]. If the direction of polarization is perpendicular to the applied magnetic field, the number of particles obstructing the flow of light drops. As a result, there is less absorption and more easy particle transmission since fewer particles interact with the applied magnetic field. More particles interact with the applied magnetic field when the direction of polarisation is parallel to it. This results in a decrease in the intensity of light transmitted and an increase in absorption. In a ferrofluid, a chain structure often forms when an external magnetic field is present [21, 22]. These chains would spin their magnetic moment along the direction of the applied external magnetic field. As the field's strength rises, the chain's length varies dynamically. If the applied field is zero, no clear chain arrangement forms because the ferrofluid is isotropic at that point. However, due of the comparatively lower particle-to-particle interactions, a configuration with shorter chains forms in the field direction when a smaller magnetic field is applied. If the field intensity is raised, a configuration with longer chains can result. As the field strength rises, so do the chain lengths. When the ferrofluid reaches its saturation magnetisation, the process tends to stop, and that is when the chains have the longest lengths. This dynamic chain-growing mechanism implies a dynamic rise in the ferrofluid’s anisotropy with the field. This procedure suggests that the fluid's anisotropy will dynamically grow with the field. Field energy plus dipole interaction energy adds up to the chain's total energy [23]. As a result, the chains' lengths are varied in the field direction and perpendicular to it.

The total chain length in the applied field direction can be written as:

$$L = NPde^{\left(\frac{-U}{KT}\right)} \tag{4.1}$$

Where N, P, d, K, T, U are the total number of particles, a constant, mean diameter of the particles, Boltzmann constant, absolute temperature and the potential energy respectively. Where the potential energy consists of two parts: U_0 due to an external field and U_i due to the dipole-dipole interaction among the particles. The chain length in the parallel and perpendicular direction is given by:

$$L_{\parallel} = NPde^{\left[-\left(\frac{U_0+U_i}{KT}\right)\right]} \tag{4.2a}$$

$$L_{\perp} = NPde\left[\frac{-U_i}{KT}\right] \tag{4.2b}$$

$$\frac{L_{\perp}}{L_{\parallel}} = e\left(\frac{U_0}{KT}\right)=e\frac{mH_0}{KT} \tag{4.2c}$$

Where m is the magnetic moment of a particle. When H_0 =0, $L_{\perp}$=$L_{\parallel}$, aggregates are nearly spherical in shape and no obvious chain configuration is formed. Hence the ferrofluid is isotropic at that time. When $H_0 = \infty$, $L_{\perp} \ll L_{\parallel}$.

An optical anisotropy is produced by the dielectric that is created by the field-induced structural anisotropy. Anisotropy is caused by the moments' attempt to align in the direction of the applied field. Under various assumptions, the dielectric properties of a ferrofluid exposed to a magnetic field are investigated. Finally, solving the dielectric constant of the ferrofluid in a magnetic field is obtained as:

$$\varepsilon_{perp} = \varepsilon_c + \varphi C\left[1 - \frac{L(a)}{a}\varepsilon_{\xi} + \frac{L(a)}{a}\varepsilon_{\zeta} - \varepsilon_0\right] \tag{4.3}$$

$$\varepsilon_{para} = \varepsilon_c + \varphi C\left[2\frac{L(a)}{a}\varepsilon_{\xi} + \left((1 - 2\frac{L(a)}{a}\right)\varepsilon_{\zeta} - \varepsilon_0\right] \tag{4.4}$$

Where φ, C, L(a) the packing density of the chains, the volume concentration of the particles in the fluid and the Langevin function with a=(mH/k_BT) respectively. The relation between the dielectric constant and complex refractive indices is given by the relations

$$\varepsilon_{\perp} = N_{\perp}^2 = (n_{\perp} + jk_{\perp})^2 \text{ and } \qquad \varepsilon_{\parallel} = N_{\parallel}^2 = (n_{\parallel} + jk_{\parallel})^2 \tag{4.5}$$

Where n and k represent the refractive indices and the extinction coefficient in the two directions. The change in the absorbance of the sample when the plane polarized light parallel and perpendicular to the applied magnetic field is given by [24]

$$\Delta A_{\parallel} = -ln\left(\frac{I_{\parallel}}{I_0}\right) \tag{4.6a}$$

$$\Delta A_{\perp} = -ln\left(\frac{I_{\perp}}{I_0}\right) \tag{4.6b}$$

Where $I_{\perp}$ and $I_{\parallel}$ represents the transmitted light intensities in the directions perpendicular and parallel to the field direction. I_0 is the intensity of the incident light. The transmitted light intensity in terms of extinction coefficient is given by:

$$I_{\perp} = I_0 \alpha_{\perp} = I_0 exp\left[\frac{-(4\pi)cLk_{\perp}}{\lambda}\right] \tag{4.7a}$$

$$I_{\parallel} = I_0 \alpha_{\parallel} = I_0 exp\left[\frac{-(4\pi)cLk_{\parallel}}{\lambda}\right] \tag{4.7b}$$

Where $\alpha_{\perp}$and $\alpha_{\parallel}$ depict transmission coefficient of ferrofluid in the directions perpendicular and parallel to the field direction, c is the concentration, L is the path length in the sample, $k_{\perp}$and $k_{\parallel}$ represents the extinction indices in the two directions, λ is the wavelength of the incident light.

The difference in absorption coefficients of two orthogonal polarizations is known as linear dichroism, which can be written as [25]:

$$\Delta K = (\Delta A_{\parallel} - \Delta A_{\perp})\left(\frac{\lambda}{4\pi l}\right) \tag{4.8}$$

The degree of moment orientation in a fluid under an applied field is reflected in dichroism. This reflects the creation of the microstructure and its relaxation in the field. Fundamentally, the dichroism measurements in both static and dynamic modes are interesting because they enable a range of applications such as relaxation time measurement for bio-molecular recognition, optical modulators, and viscometers, in addition to the study of aggregation effects, chain formation, and clustering in the field [26]. It is impossible to generalize the precise process causing the magneto-optical effects in ferrofluids. It is believed to be the direction of moments in the applied field with no agglomeration in the case of non-interacting particles. The clustering of pre-existing tiny aggregates or short chains that are generated by the field is also investigated.

4.3 Surface plasmon-coupled emission of magneto-plasmonic structure

In the realm of material science and biology, there is a notable interest in fluorescent spectroscopy. Recently, optical sensors based on the plasmonic properties of nanomaterials have been introduced to improve the investigation of molecular interactions, especially for detecting low concentrations of molecules [27-29]. One such method is the surface plasmon-coupled emission (SPCE) technique, which is a precise and advantageous means to assess the interaction between nanomaterials and molecules [30]. One way to think of SPCE is as the surface plasmon resonance in reverse; excited fluorophores couple with surface plasmons close to the metal to produce directed radiation, and the coupling efficiency is dependent on the distance between the fluorophores and metallic layer [31–38]. Surface Plasmon Resonance, is a different technique that is closely connected to SPCE. Whereas SPCE is the angle-dependent emission of light by a thin metal film, SPR is the angular-dependent absorption of incoming light by a thin metal film. The near-field interaction of a radiating molecule with a layered structure that contains a thin metal film produces surface plasmon-coupled emission or SPCE [39, 40]. Benner [41] was the first to report on plasmon-mediated emission when he saw distinct emission peaks in the glass prism caused by molecules close to the metal layer when they were excited by a surface-plasmon field. Surface Plasmon Coupled Emission (SPCE) emerges from the fusion of two rapidly evolving research fields: plasmonics and fluorescence.

SPCE is caused by the near-field interaction of a radiating molecule with thin metal surfaces. The basic idea behind SPCE is to optimise fluorescence excitation and fluorescence collection for molecules at the surface by placing a semi-transparent thin metal sheet on a glass substrate [42]. It is well known that, for plane wave illumination from the glass side at an incidence angle close to the angle of surface-plasmon resonance, the local electric-field intensity at the surface can be significantly boosted compared to a similar setup without metal. Additionally, it was demonstrated that fluorescence emission can couple into the metal film's surface plasmon (SP) mode and then radiate back into the glass at angles that are close to the SPR angle [43]. Using SPCE, single-molecule detection has even been demonstrated [44]. SPEC has garnered significant attention since the dawn of the 21st century because of its enormous potential in a variety of fields. Promising applications for this field of study can be found in imaging, genomics and drug development, medical diagnosis, protein and DNA sensing, immunological detection, and other areas [45-50]. To reach new heights in the field, research is still ongoing today to completely investigate it. Thus far, numerous studies have been carried out in both experimental and theoretical settings. The three main attributes of SPCE are polarised emission, background suppression, and directed emission. Owing to these special qualities, SPEC has drawn a lot of interest from academics, especially in the areas of analysis and bioanalysis, where it is regarded as a sensitive and trustworthy method. The sensitivity and reliability of SPCE make it a valuable technique for studying biological systems at the molecular level. Both theoretical and experimental studies have been conducted to deepen our understanding of SPCE, contributing to ongoing efforts to unlock its full potential. Continued exploration holds the promise of uncovering new applications and refining SPCE's capabilities across various scientific and medical disciplines.

In SPCE, along the surface, the excited surface plasmons propagate as a wave, oscillating normal to the surface with the resonance of incident light. The intensity decreases exponentially both perpendicular and parallel to the surface due to the damped oscillation. [51] A distribution of evanescent fields around 200 nm beyond the surface is indicative of the plasmon wave [52-54]. Fluorophores can sense the energy field within the near-field distance, and when excited dipoles couple strongly with surface plasmons, energy is released from the prism as radiation. It is believed that wave-vector matching causes this phenomenon. The direction in which the surface wave vector and prism vectors are aligned determines the discharge of radiation with p polarization. An increased electric field will be felt by the fluorophores in the near field, and these excited dipoles will couple strongly to these oscillations, producing radiation in the direction of the prism side [55]. The two basic configurations in which we can achieve SPCE are as follows: either the prism side or the sample side excites the fluorophores [56]. In the first mode, light enters the metal film through a prism and strikes it, creating surface plasmons that excite the nearby fluorescent proteins. This structure, is called the Kretschmann (KR) configuration, (**Figure 4.1a**) In the second arrangement, incoming light directly excites the fluorophores, causing their excited dipoles to pair close to surface plasmons, resulting in a directed emission. Reverse Kretschmann (RK) configuration is the name given to this arrangement (**Figure 4.1b**) [57].

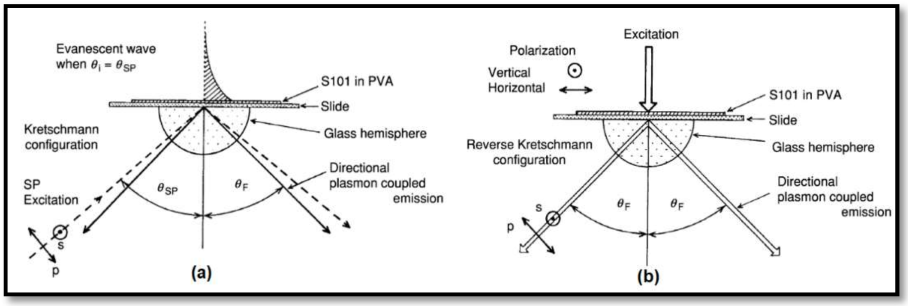

Figure 4.1 KR configuration and RK configuration to obtain SPCE [57]

Since the magnetic field is known to alter the optical characteristics of materials, it is one of the intriguing possibilities to regulate surface plasmons [58–62]. That is correct—the surface pasmon dispersion relation can be altered by applying a magnetic field in the right direction. When addressing the interaction between magnetic fields and optical properties, it is necessary to define optical characteristics using a dielectric tensor. We must use a dielectric tensor to characterize the optical properties while working with magnetic fields and optical characteristics. When there is no magnetic field, this tensor is diagonal or has the potential to become one. However, this dielectric tensor becomes non-diagonal when a magnetic field is added because it rotates the light electric fields. These non-diagonal elements generally termed magneto-optic constants, capture the impact of the magnetic field on the optical properties. The general dielectric tensor ε is given by [63]

$$\varepsilon = \begin{pmatrix} \varepsilon_{xx} & \varepsilon_{xy} & \varepsilon_{xz} \\ -\varepsilon_{xy} & \varepsilon_{yy} & -\varepsilon_{yz} \\ -\varepsilon_{xz} & \varepsilon_{yz} & \varepsilon_{zz} \end{pmatrix}$$

These constants are quite tiny and proportionate to the applied magnetic field for diamagnetic and paramagnetic materials [64]. Therefore, a strong magnetic field is required to achieve significant MO constants in those materials. On the other hand, for ferromagnetic materials, these MO constants are substantially greater and proportionate to the magnetization, allowing for the magnetic saturation of these materials and the achievement of larger MO constants at lower magnetic fields.

For magneto plasmonics, we want to combine both plasmonic and magnetic properties. The use of materials with good capabilities for plasmon propagation and MO constant of large value is necessary for the realization of magnetic field-induced modulation on plasmonic systems in the optical regime. Unfortunately, the MO constant of noble metals is quite tiny, and to boost this response, a magnetic substance must be added to the system. Because of their metallic character, ferromagnetic metals are an appropriate candidate for support. Nevertheless, because of their high optical coefficient of penetration, they cause an excessive dampening of SPP propagation, making them unsuitable for employment as the system's sole metallic component. As a result, noble and ferromagnetic metals have been combined to create appropriate magnetoplasmonic systems. The application of a magnetic field induces some modification in the dispersion relation of plasmons, it is given by [65]

$$\boldsymbol{k_x}(\vec{\boldsymbol{B}}) = \boldsymbol{k_x^0} + \Delta \boldsymbol{k_x m} \tag{4.9}$$

Where k_x^0 is the wave vector in the absence of an applied magnetic field, Δk_x is the modulation term, which is related to the dielectric constants of both materials at the interface. At the most basic level, the modulation expression may be obtained analytically as a function of the dielectric constants of the interface material by using the scattering matrix formalism on a single interface between two semi-infinite materials, a metal and a dielectric. This analytical approach provides insights into the dependence of the magnetic modulation of the surface plasmon wave vector on the dielectric constants of the materials at the interface, facilitating a comprehensive understanding of the phenomenon. For iron oxide-mediated magneto plasmonic structure, an analytical expression for the modulation factor Δk_x is expressed as [66]

$$\Delta \boldsymbol{k_x} \approx \frac{2tk_0^2\varepsilon_d^2 i\varepsilon_{yz}^{IO}}{-\varepsilon_{Nm}\varepsilon_{IO}} \boldsymbol{e}^{-2hk_z^{Nm}} \tag{4.10}$$

Where $t, \varepsilon_{yz}^{IO}, \varepsilon_{IO}$ represent the thickness, non-diagonal and diagonal elements of the complex dielectric permittivity tensor for iron oxide, $k_z^{Nm}, \varepsilon_{Nm}, h$ represent the surface plasmon field penetration in the noble metal layer, dielectric constant and thickness of the noble metal layer and ε_d, k_0 represent the dielectric constant of the dielectric layer and wave vector of light. Where $m = \frac{M_y}{M_{sat}}$, by providing magnetic fields large enough to saturate the sample and make m equal to 1 or -1, the maximal effect can be attained. The effect of magnetic field on surface plasmon coupled emission leads to a new perspective towards the kinetics and dynamics of biomolecules and it can also be used in biosensor applications.

Combining SPR with fluorescence technology produced one of the most intriguing uses for the technology. This interaction led to the emergence of a novel SPCE phenomenon and a notable increase in the degree of plasmonics applications. It is currently one of the most appealing study fields since it presents novel, intriguing possibilities for guiding and managing the passage of optical energy utilizing near-field effects rather than traditional far-field optical components. To fully explore this field's potential, investigations are underway. The present chapter discusses the iron oxide-mediated surface plasmon coupled emission in the presence of a magnetic field.

4.4 Characterization

In the present work, ferrofluids, magnetoplasmonic nanofluids based on silver nanoparticles and magnetoplasmonic nanostructures were synthesized. The structural characterization of synthesized iron oxide particles was carried out by the X-ray diffraction technique. (Bruker AXS D8 Advance X ray diffractometer employing Cu–Kα X-rays of wavelength 1.5406 Å). UV-visible spectrometer (Ocean Optics Maya 2000-Pro UV compact spectrometer, S10420, Sensitivity 0.32 counts/e,) was employed for studying the absorption properties. The magnetization measurement is carried out via SQUID, (Quantum design, VSM_HW_VERSION-3101-150 F0). The magneto-optical property of the hydrocarbon and aqueous-based iron oxide nanofluid was investigated by using a home-made setup.

4.5 Experimental

4.5.1 Synthesis of aqueous based ferrofluid

Aqueous-based ferrofluid was synthesized by a controlled co-precipitation method, as shown in **Figure 4.2**. Initially, anhydrous ferric chloride ($FeCl_3$) and ferrous sulphate heptahydrate ($FeSO_4.7H_2O$) are taken in the molar ratio of 2:1 is dissolved in 250 ml deionized water separately. Then the equimolar solution was mixed and homogenized by magnetic stirring for 20 minutes. Aqueous ammonia was added to this solution by constant stirring until the pH of the solution reached 12, and the blackish iron oxide nanoparticle was formed. Further, about 6 g of citric acid dissolved in 20 ml water was added to the solution to prevent agglomeration among the magnetic nanoparticles. The resultant mixture was maintained at 90 °C and subjected to continuous stirring for 90 minutes. Finally, the mixture was centrifuged for 30 minutes at 5000 rpm. After centrifugation, we obtained a black precipitate that dissolved in distilled water and was sonicated for 30 minutes at room temperature to obtain a stable ferrofluid. The fluid is then diluted with the carrier fluid to a known volume fraction (1 vol%).

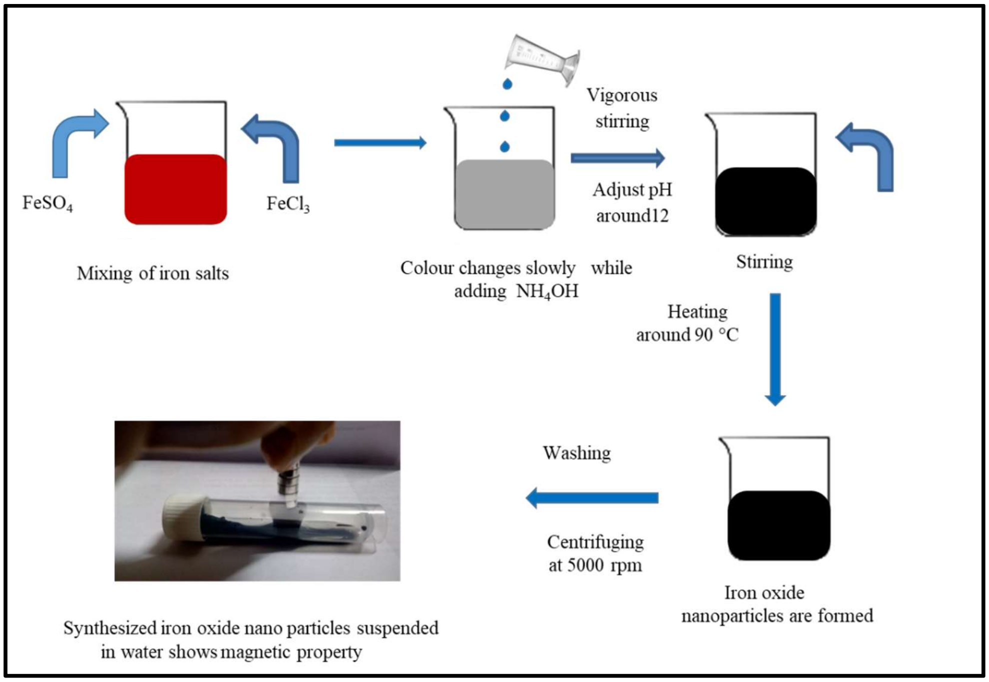

Figure 4.2 Schematic representation of the synthesis of aqueous based ferrofluid

4.5.2 Synthesis of silver nanoparticles

The neutral silver nanoparticles are synthesized through the reduction method using trisodium citrate as a reducing agent, is depicts in **Figure 4.3**. Silver nitrate and tri-sodium citrate were used for the production of silver nanoparticles. Two millimolar (2 mM) silver nitrate solution was heated at 90 °C for 5 minutes using a hot plate. The prepared twenty-millimolar (20 mM) tri-sodium citrate solution was added dropwise to this solution. The transformation of colour from translucent to pale yellow indicated the creation of silver nanoparticles.

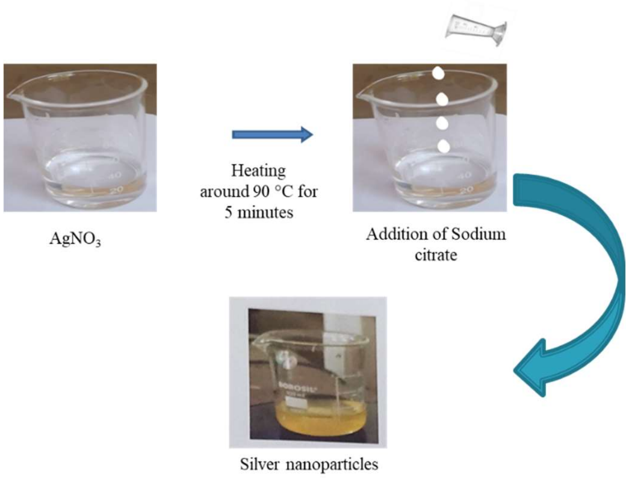

Figure 4.3 Schematic representation of synthesis of silver nanoparticles

4.5.3 Synthesis of magneto plasmonic nanofluid

The magnetic plasmonic nanofluid was prepared by mixing iron oxide nanofluid with silver nanoparticles, as shown in **Figure 4.4**. The neutral silver nanoparticles get attracted to the negatively charged citric acid-coated iron oxide particles [67]. The number density of silver nanoparticles can be tuned by altering the concentration of silver nanoparticles in the hybrid magneto plasmonic nanofluid. The prepared citric acid-coated ferrofluid and synthesized silver nanoparticles are mixed together and sonicated for 20 minutes. Here we have taken 1.5 ml ferrofluid with different concentrations of silver nanoparticles.

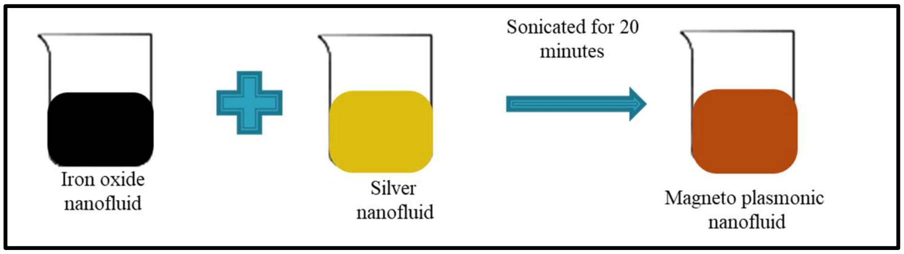

Figure 4.4 Schematic representation of synthesis of magneto plasmonic nanofluid

4.5.4 Fabrication of magneto plasmonic nanostructure

The magneto plasmonic nanostructure was fabricated through the spin coating method. In the fabrication of nanostructure, polyvinyl alcohol (PVA) was used as the dielectric. The PVA exists in powder form, particular weight percentage of PVA solution was made by dissolving PVA in deionized water and heating at 90 °C while continuously stirring. The Rhodamine B dye was used as an emitting material. Then .5 wt% Rhodamine dye and 25 µl iron oxide solution were mixed with 3 wt% PVA solution. This was deposited on top of the Ag film by the spin coating method. After that, the transmission spectra of the fabricated sample were recorded in the absence of a magnetic field and the presence of a magnetic field. The schematic representation of magneto plasmonic nanostructure fabrication was depicted in **Figure 4.5**.

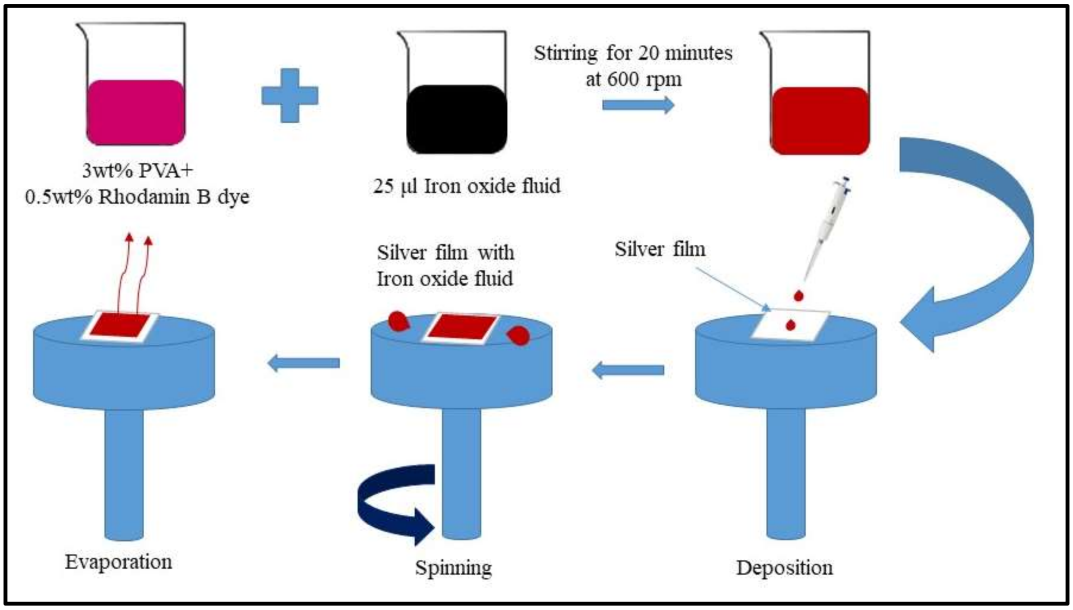

Figure 4.5 Schematic representation of magneto plasmonic nanostructure fabrication

4.5.5 Analysis techniques

The experimental setup for measuring the linear dichroism of ferrofluid is shown in **Figure 4.5**. The ferrofluid sample is taken in a quartz cuvette which is placed at the centre of the pole gap of an electromagnet, where the magnetic field is varied by changing the current passing through it using a dc power supply. A He-Ne laser of wavelength 633 nm with an output power of 10 mW is used as a light source. Light from a laser was adjusted for perpendicular and parallel linear polarization using a polarizer and fell normally on a fluid sample held between the pole pieces of an electromagnet. Light transmitted through the sample fall on a detector and the intensity of the transmitted light is measured. A gauss meter is used for measuring the field.

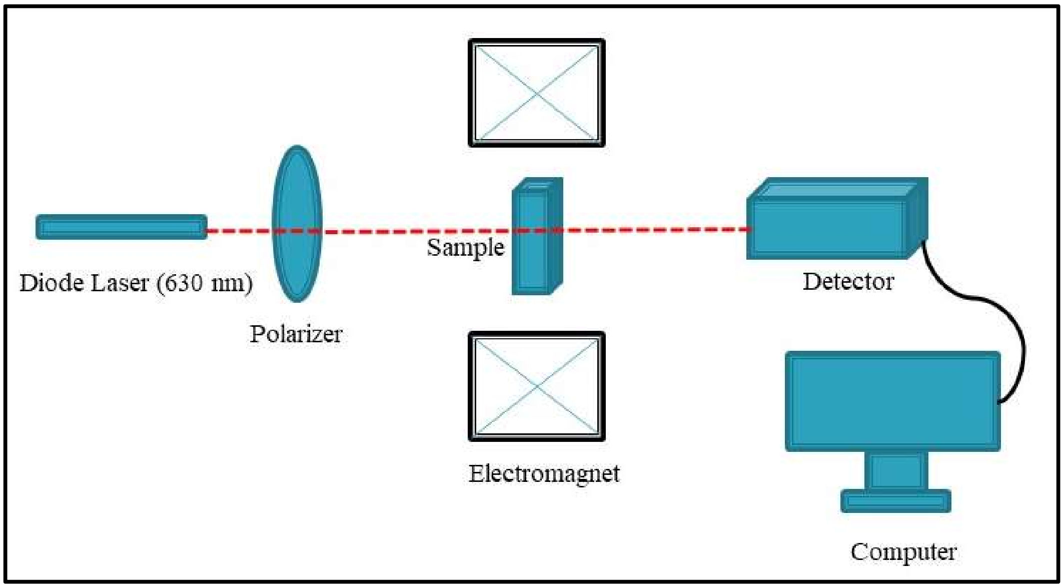

Figure 4.6 Experimental set up for linear dichroism study

An experimental setup based on the Reverse Kretschmann configuration (RK) (**Figure 4.7**) is utilized to investigate the fluorescence from plasmonic structures. Using glycerine (refractive index ~ 1.5) as a refractive index matching fluid, the sample is fixed on a hemicylindrical prism. The prism with the sample attached is set up on a rotating stage, enabling normal excitation and emission observation at any angle with the cylinder's normal. A diode laser source with a wavelength of 540 nm was used to illuminate the sample. The light emitted is collected from the prism side of the sample by an optical feed through and fiber to a high-sensitivity spectrometer (Ocean Optics Model No). The optical feedthrough is mounted on a rotating stage and the spectrum is constantly captured at one-degree intervals at angles ranging from 5° to 90°. A reference angle of 0° was determined by taking the direction opposite the laser's excitation direction. Using Ocean Optics Spectra Suite software, the emission spectra from the spectrometer were collected and controlled.

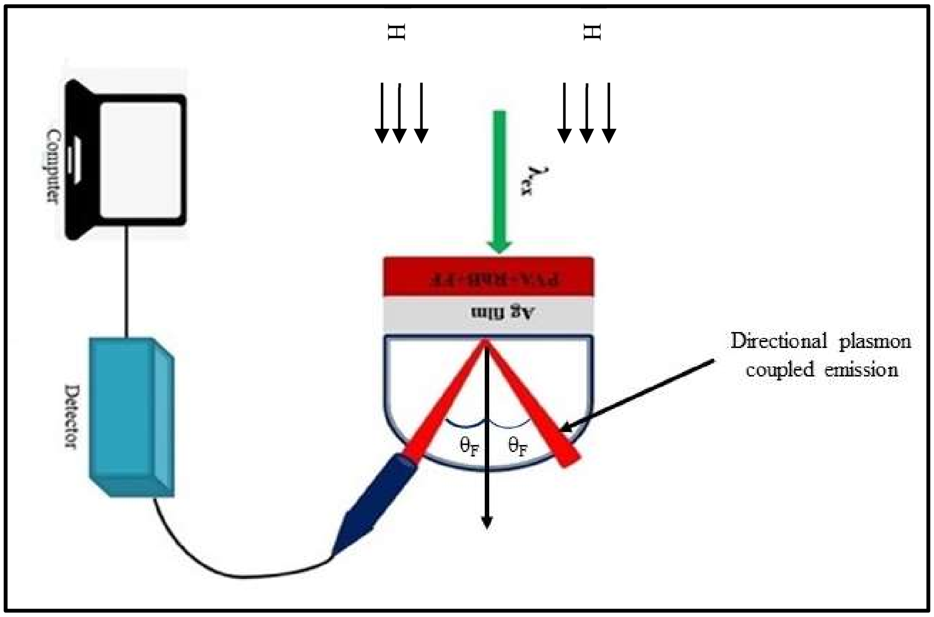

Figure 4.7 Experimental setup based on the Reverse Kretschmann configuration (RK)

4.6 Results and Discussions

4.6.1 Structural characterization

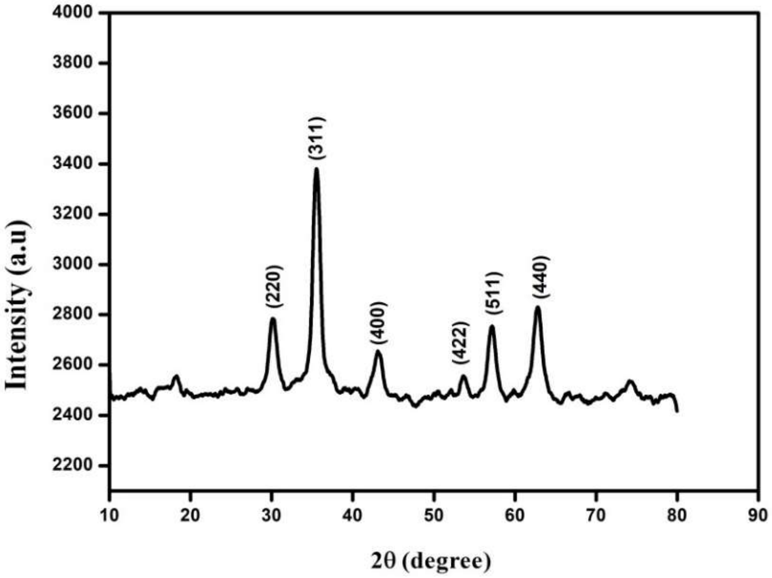

Figure 4.8 X-ray diffraction pattern of Fe_3O_4

The structural analysis of the prepared sample was done by X-ray diffraction technique. **Figure 4.8**, depicts the X-ray diffraction pattern of the synthesized particles. All the observed diffraction peaks match with the inverse spinel structure of Fe_3O_4 nanoparticles (JCPDS file no: 19-0629). The broad peak indicates the nanocrystalline nature of the particles [68]. The crystallite size was calculated using Debye Scherrer’s formula and was found to be 10 nm with a lattice parameter of 8.39 Å.

4.6.2 Optical study

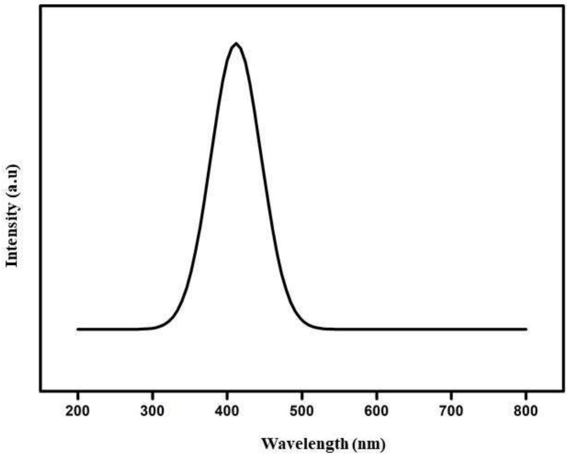

Figure 4.9.a UV-Visible absorption spectrum of Silver nanoparticles

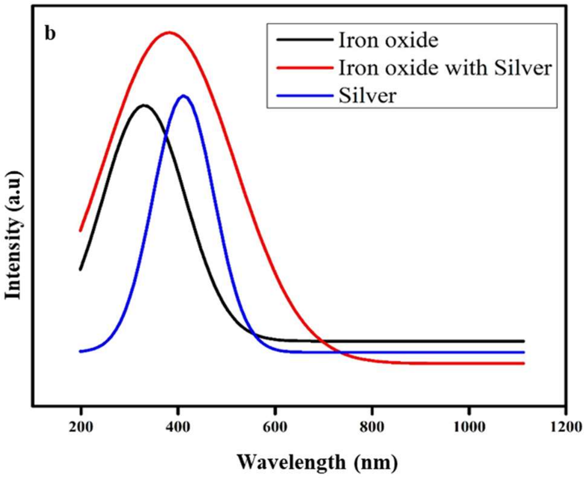

Figure 4.9.b UV-Visible absorption spectrum of iron oxide with silver nanoparticles

The conduction and valence bands of metal nanoparticles, such as silver, are relatively close to one another, allowing the electrons to move freely. This creates an SPR absorption band because the free electrons in the nanoparticles oscillate collectively in resonance with the light wave, which results in the vibrant colours seen in the dispersions of silver nanoparticles. A silver nanoparticle's electrons are traditionally polarised around its considerably heavier ionic core by an incoming wave of an electric field [69]. Every electron oscillates like a dipole in the same phase as a result of the restoring force generated. The combination of coherent electron mobility and the electromagnetic field results in a considerable absorption. **Figure 4.9a** shows the UV-Vis absorption spectra of silver nanoparticles. Particle characteristics such as size, shape, dielectric medium, and chemical environment, among others, greatly influence this absorption. Mie's scattering theory states that the surface plasmon resonance bands also affect the plasmonic fluid's particle-containing morphology. When there is only one SPR band, the particles are isotropic; when there are two or more bands, the particles are anisotropic [70]. There is just one SPR band visible in the spherically shaped nanoparticles. A single SPR band is observed around 412 nm. From the **Figure 4.9b** we can observe the absorption peaks at 325 nm (Iron oxide),412 nm (Silver) and 380 nm (Iron oxide with Silver). The shift in the absorption peak of Iron oxide with Silver arises due to the charge transfer effect that occurs between silver and iron oxide [71].

4.6.3 Magnetization measurement

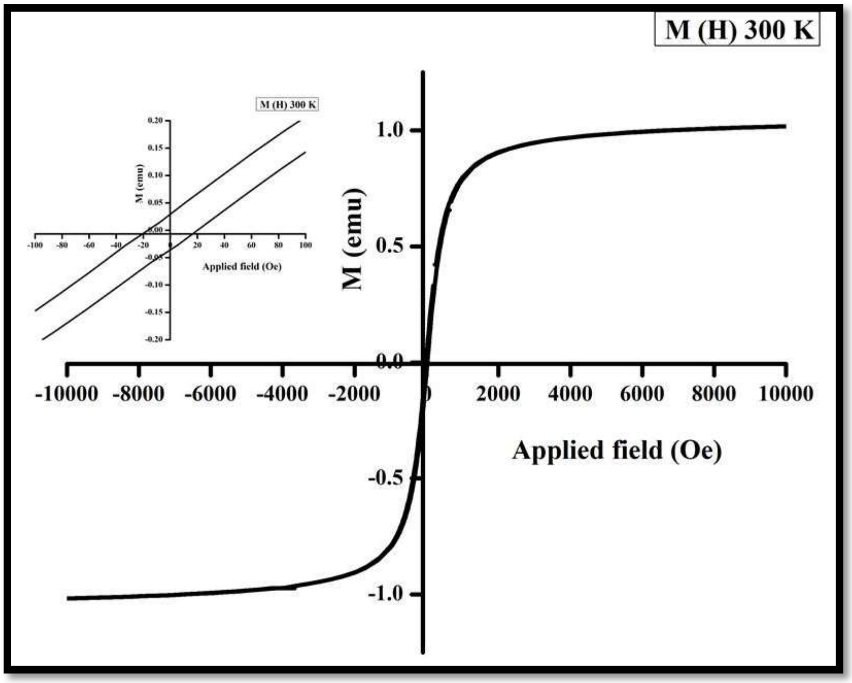

Figure 4.10 M-H Curve of magnetite nanoparticles

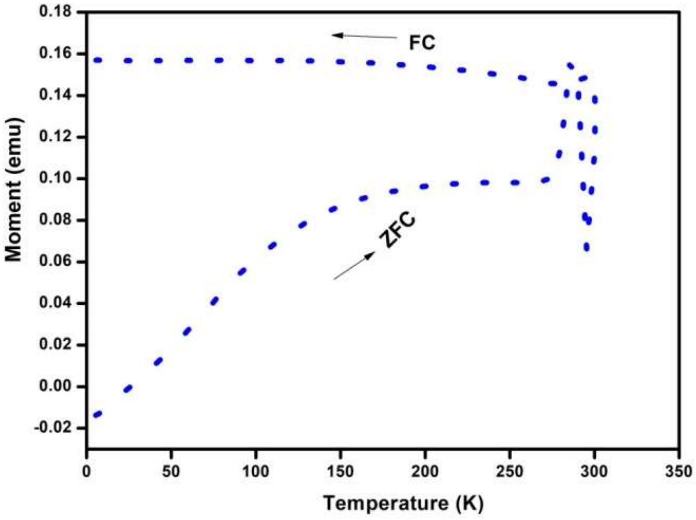

Figure 4.11 FC- ZFC Curve of magnetite nanoparticles

The magnetic measurement was carried out at room temperature and 5K using a SQUID magnetometer. After being removed from the fluid, iron oxide particles are examined using a vibrating sample magnetometer. **Figure 4.10** displays the magnetization curve of the prepared ferrofluid. The prepared nanoparticles exhibit a Langevin-like approach to saturation magnetization with negligible coercivity and remanence as observed in the M-H curve, which signifies the superparamagnetic nature of particles. The saturation magnetization of the bare Fe_3O_4 particles was measured by VSM and it is found to be 66.7 emu/g, which is slightly small compared to the bulk value. The reduction in saturation magnetization is due to the presence of a magnetically dead layer at the surface of the nanoparticles. Field-cooled (FC) and zero field-cooled (ZFC) moment measurements were used for the temperature-dependent relaxation investigations at a constant applied field of 10 mT, as indicated in **Figure 4.11**. Without using a magnetic field, the sample was cooled from 300 K to 5 K in a ZFC measurement. A 10 mT field was applied once the temperature reached 5K, and the magnetization was then monitored as a function of temperature when the material heated to 300K. The sample was cooled from 300K to 5K for an FC measurement while a 10 mT field was present, and the magnetization was noted as the temperature increased. The ZFC measurements exhibit a qualitative indication of the size distribution of the particles [72]. The broad maximum in ZFC reflects the relatively wide size distribution of magnetic nanoparticles. In ZFC measurement most of the particles are randomly oriented at low temperatures, but when the temperature is increased the particles have enough thermal energy to overcome the anisotropic barrier, hence the magnetization increases. Besides the broad peak in the ZFC magnetization, a cusp at around 275 K which associated with the freezing of carrier liquid [73].

4.6.4 Linear dichroism studies of iron oxide fluid

When there is no external magnetic field, ferrofluid is optically isotropic; however, when a magnetic field is applied, the small magnetic particles within the fluid will partially orient themselves along the direction of the magnetic field. As a result, the magnetic fluids exhibit structural anisotropy and exhibit magneto-optical phenomena like linear dichroism. Field-induced linear dichroism causes the magnetic fluids to absorb extraordinary and ordinary light beams differently if the direction of light propagation is perpendicular to the applied magnetic fields [74]. In linear dichroism measurements, the transmitted light intensity depends on the direction of polarization under the applied magnetic field. Particles impeding light passage decrease in number if the direction of polarisation is perpendicular to the applied magnetic field [75]. As a result, there is less absorption since fewer particles interact with the applied magnetic field, making particle transmission easier [76]. When the direction of polarization is parallel to the applied magnetic field, more particles interact with the field, which causes the intensity of transmitted light to be reduced and absorption to rise. Generally, a chain configuration is formed in a ferrofluid in the presence of an external magnetic field. These chains would spin their magnetic moment along the direction of the applied external magnetic field. The length of the chain changes dynamically as the strength of the field increases. If the applied field is zero, no clear chain arrangement forms because the ferrofluid is isotropic at that point. However, due of the comparatively lower particle-to-particle interactions, a configuration with shorter chains forms in the field direction when a smaller magnetic field is applied. A configuration with longer chains may arise if the field intensity is increased. The process tends to stop when the ferrofluid reaches its saturation magnetisation, at which point the chains are at their longest lengths [76].

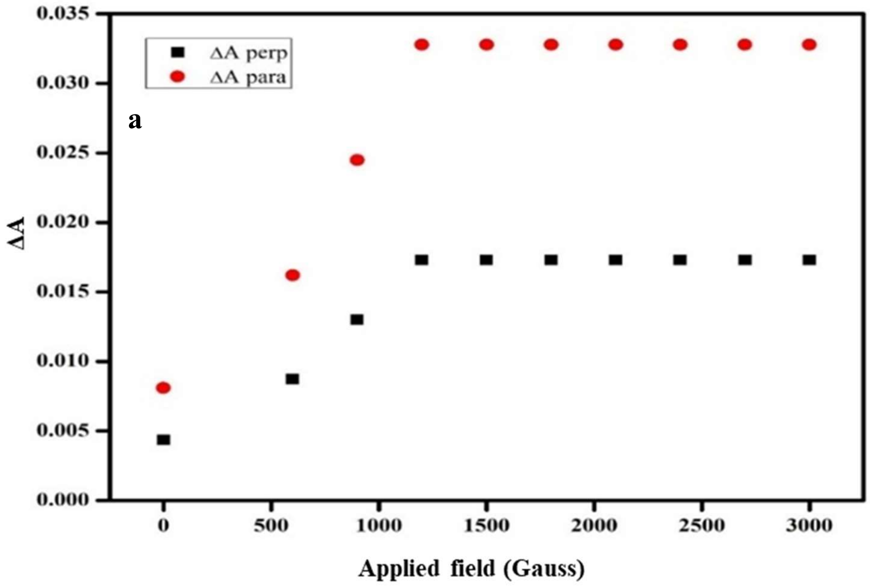

Figure 4.12 Linear dichroism in Fe_3O_4 (a) suspended in kerosene

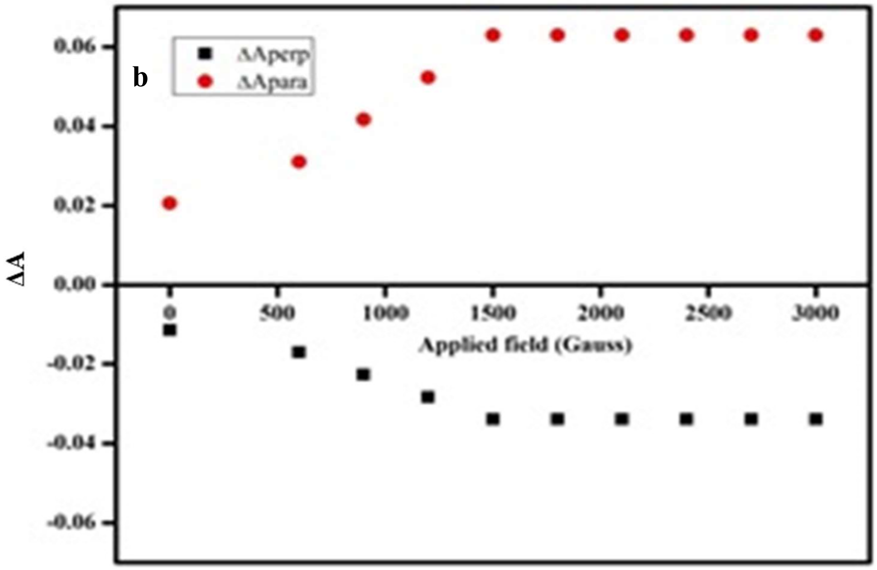

Figure 4.12 Linear dichroism in Fe_3O_4 (b) in water

The dichroism measurements are carried out in kerosene-based and aqueous-based ferrofluid is depicted in **Figure 4.12**. For the oleic acid-coated kerosene fluids, there is a noticeable increase in absorbance for light of both polarizations. This indicates that when light passes through these fluids, it is absorbed more significantly, regardless of its polarization. However, the citric acid-coated water-based fluids display dichroic behaviour. This means that these fluids exhibit different absorbance properties for light with varying polarizations. In other words, the extent of light absorption varies depending on the light's polarization. This behaviour suggests that the fluid's properties are anisotropic or non-uniform, leading to differential interactions with polarized light. When particles in surfacted fluids are coated with oleic acid, dipolar interactions come into play, causing the local clustering of particles. These local clusters then amalgamate to form macro clusters, which in turn lead to the scattering of light and, consequently, a reduction in light intensity irrespective of the polarization of the incoming light. In ionic fluid, this differential absorption can be attributed to the electrostatic repulsion of particles within the fluid. In diluted ionic fluids, there is limited particle clustering, allowing individual moments to align with the field direction and saturate independently.

4.6.5 Linear dichroism studies of magneto-plasmonic fluid

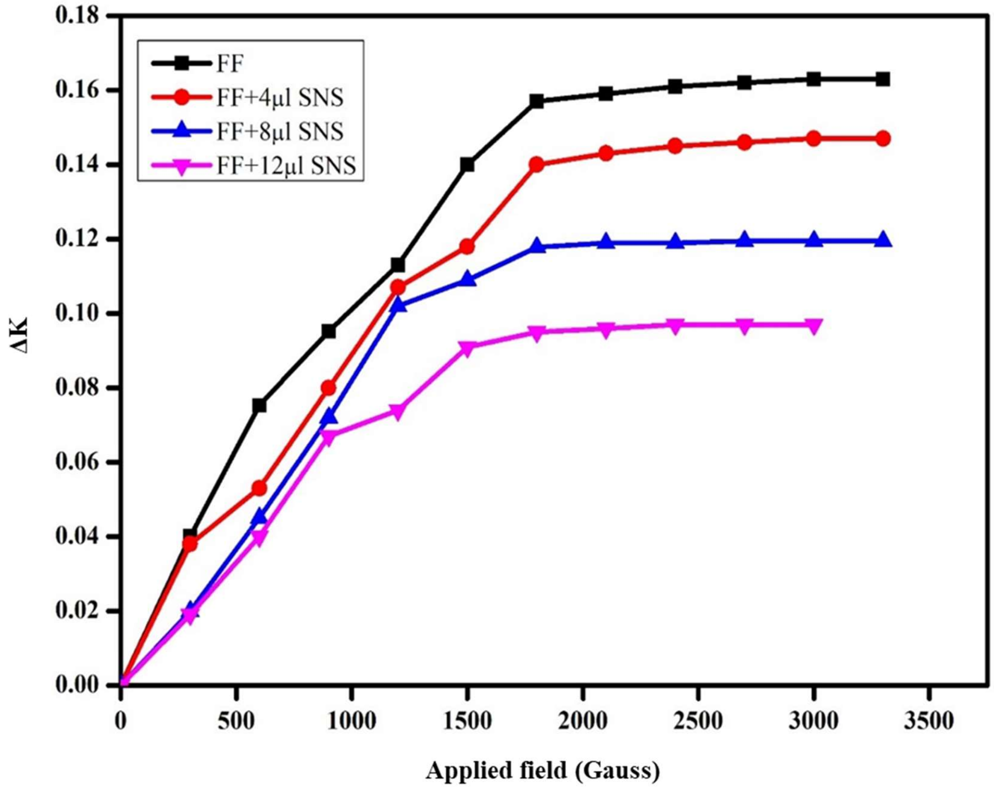

Figure 4.13 Magneto-optical study of ferrofluid with spherical-shaped silver nanoparticles

Figure 4.13 displays the hybrid magnetic nanofluid's linear dichroism measurement at varying quantities of spherical-shaped silver nanoparticles. It's observed that an increase in the concentration of silver nanoparticles leads to a reduction in the amplitude of intrinsic dichroism. This decrease can be attributed to the fact that spherical nanoparticles have a uniform structure and properties in all directions, resulting in reduced direction-dependent light absorption [77]. However, when a magnetic field is applied, the nanofluid exhibits magneto-optical anisotropy, causing its optical properties to vary with direction. In this case, the spherical nanoparticles align themselves along the magnetic field direction, forming chain-like structures. As the magnetic field strength increases, these chains become more prominent, leading to improved magneto-optical characteristics and a stronger dichroic effect. This behaviour is due to the alignment of spherical particles, which introduces optical anisotropy and results in differing light absorption along different directions. As a notable application, these magneto-plasmonic fluids can be used to combine magnetic hyperthermia and photodynamic therapy, offering a versatile approach to medical treatment by harnessing the heating properties of magnetic nanoparticles in the presence of a magnetic field and the light-sensitive properties of the magnetoplasmonic nanofluid for targeted cancer therapy.

4.6.6 Surface plasmon-coupled emission of magneto-plasmonic structure

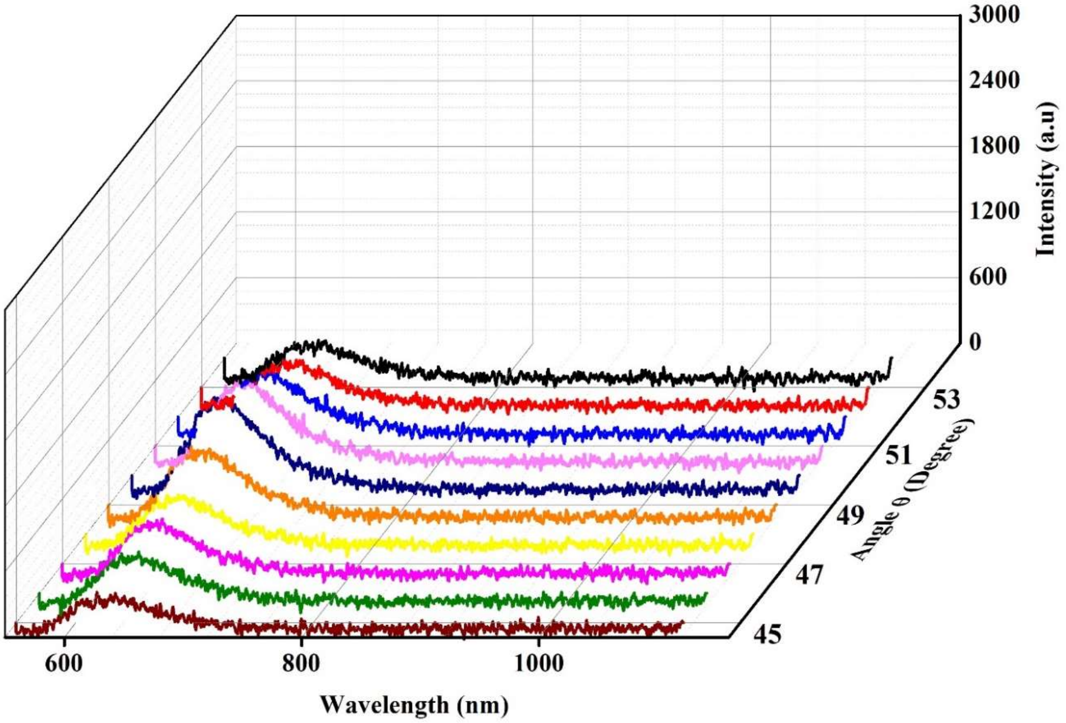

Figure 4.14 Iron oxide-mediated surface plasmon coupled emission in the absence of a magnetic field

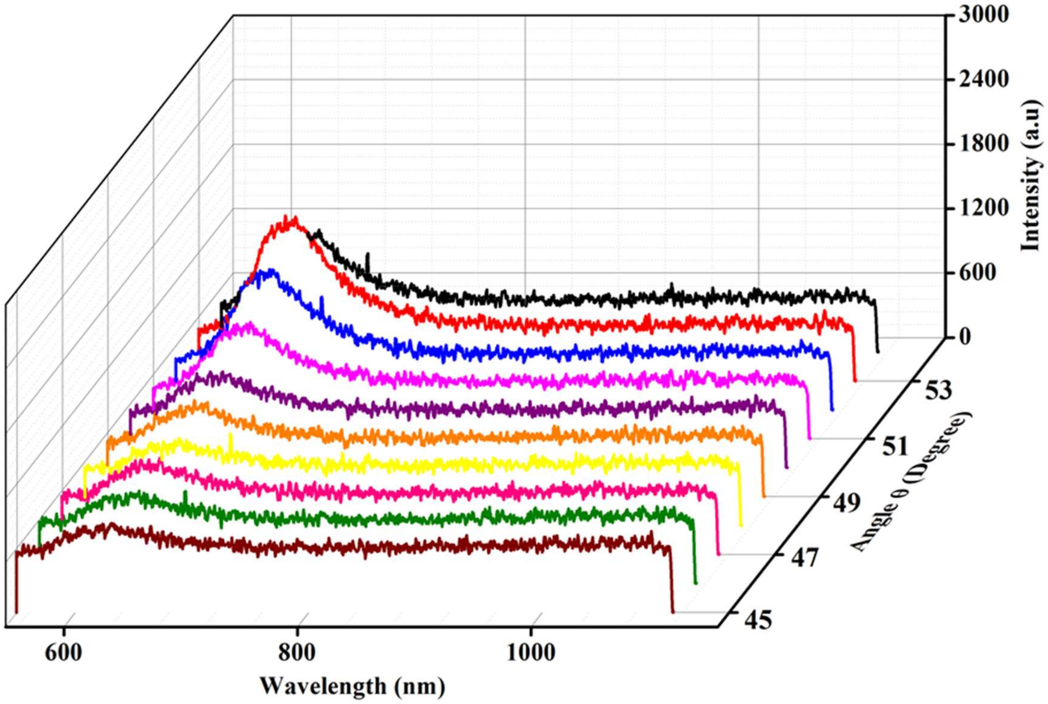

Figure 4.15 Iron oxide-mediated surface plasmon coupled emission in the presence of a magnetic field

The magnetic field control on the plasmonic property is investigated using a homemade reverse Kreschmann configuration setup. **Figure 4.14** depicts the iron oxide-mediated surface plasmon coupled emission in the absence of a magnetic field. Here we can observe that the emission occurs at a certain range of angle from 45° to 53°, the directional emission from fluorophore molecule. It can be explained on the basis that the attenuated total reflection due to SPR is excited by Kretschmann configuration. The SPR occurs at the prism interface when the angle of incidence is greater than the angle of total internal reflection and usually, we expect high reflectivity in this condition. However, as a result of evanescent waves, free electrons in a metal oscillate and produce surface plasmons, which pierce the sample's dielectric up to several hundred nanometres below the metal surface. However, the excited fluorophores present within this range create an electromagnetic field, which induces surface plasmons due to the strong interaction with free charges in the metal film. The plasmons and fluorophore’s emission frequencies are correlated. As a result, we observe a strong directional emission. The resulting SPCE is highly polarised with a clearly defined emission angle back into the glass substrate, although it displays the same spectral structure as the fluorophore emission. In SPCE, the interaction takes place between the layered structure containing metal film with near-field radiation. When a fluorescent molecule is placed close to an interface, it alters the emission profile and dynamics. SPCE is a reverse effect of SPR, the optimum thickness of film is 50 nm. In SPCE a radiating dipole can excite surface plasmon modes at the metal-dielectric interface, this again couple to light and is observed as a hollow cone of emission. The surface plsmon dispersion and fluorophore emission spectra determine the angular distribution of SPCE. In comparison to a simple dielectric, the metal induces a unique decay channel for the release of energy.

The response surface plasmon coupled emission of an iron oxide-mediated multilayer structure in the presence of a magnetic field is depicted in **Figure 4.15**. The influence of the magnetic field and the magneto-optical activity of the planar structure determine how the magnetic field modulates SPCE. To increase the magnetic field modulation impact of SPCE, it is possible to add strong response magnetic nanoparticles to the multilayer structure. In the present work, by the application of a magnetic field on an iron oxide-mediated multilayer structure, we can see the enhancement in emission intensity, which arises due to the improvement of MO activity of the multilayer structure. The generated plasmons are affected by applying a magnetic field on a multilayer structure with magnetic nanoparticles. These are evident from the dispersion relation for an interface made up of magnetic and metal film and it is given by [78]

$$k_{spp} = \frac{\omega}{C}\sqrt{\frac{\varepsilon_d \varepsilon_m}{\varepsilon_d + \varepsilon_m}}(1 + \alpha g_y)$$

$$\alpha = \frac{1}{\sqrt{-\varepsilon_d + \varepsilon_m}} \frac{1}{\left(1 - \frac{\varepsilon_d^2}{\varepsilon_m^2}\right)}$$

Where k_{spp},ω, ε_d, ε_m and g_y are surface plasmon momentum, incident light frequency, dielectric constants of the dielectric and metal layers and gyration vector (which is proportional to magnetization) respectively. The wave vector k_{spp} depends on the magnetization and thus on the applied magnetic field.

4.7 Conclusions

The water-based ferrofluid and magneto plasmonic nanofluid based on silver was synthesized and their structural, optical, magnetic and interaction of the electromagnetic field with the spherical-shaped silver nanoparticles was studied. Through the use of a superconducting quantum interference device, the magnetic characteristics have been examined. The measurement of magnetisation indicates that a particle is superparamagnetic. The temperature-dependent relaxation studies were carried out by field-cooled and zero-cooled moment measurements at a constant applied field. The magneto-optical property of the iron oxide nanofluid was investigated by linear dichroism measurements. In the absence of an external magnetic field, the suspensions were isotropic. Once the external field is applied, they show anisotropic behaviour and exhibit magneto-optic phenomena. From the study of linear dichroism of the hybrid magnetic nanofluid with spherical-shaped silver nanoparticles, we can observe that as the concentration of silver nanoparticles increases, the amplitude of intrinsic dichroism decreases. This arises due to the isotropic nature of spherical nanoparticles. The magneto-optical study of the different aspect ratios of silver nanoparticles with iron oxide nanofluid is a future prospect. The magneto plasmonic heterostructure was fabricated through the spin coating method. The surface plasmon-coupled emission was obtained using the Reverse Kretchmann configuration. In the present work, we can observe a direction-specific plasmon-coupled emission with and without a magnetic field in a fabricated heterostructure. But in the presence of a magnetic field emission enhancement with directional emission is obtained. This is due to the improvement of the magneto-optical activity of the metal substrate. The magnetic field modulation aided by magnetic nanoparticles offers the ability to create a universal technique for improving SPCE-based systems' signals. The wave vector of magnetic field-induced modulation on plasmonic materials depends on the off-diagonal elements of the dielectric tensor and magneto-optical constants of the materials. If there is ferromagnetic material nearby that can concentrate the electromagnetic field, the modulation will be greater when a magnetic field is applied. More electromagnetic fields spread along a dielectric than a metal if the ferromagnetic substance is dielectric. Magnetic field-controlled plasmonics can be extended to study the magnetic field effects on surface plasmon coupled emission, under varying concentrations and distance, leading to the sensing applications which is another future perspective.

References

[1]. Faraday, M., 1846. I. Experimental researches in electricity. —Nineteenth series. *Philosophical Transactions of the Royal Society of London*, (136), pp.1-20.

[2]. Landau, L.D. and Lifshitz, E.M., 2013. *Course of theoretical physics*. Elsevier.

[3]. Liu M. and Zhang X. (2013), Plasmon-boosted magneto-optics. Nature photonics, 7(6), 429-430

[4]. Kerr, J., 1877. XLIII. On rotation of the plane of polarization by reflection from the pole of a magnet. *The London, Edinburgh, and Dublin Philosophical Magazine and Journal of Science*, *3*(19), pp.321-343.

[5]. Erskine J L. and Stern E A. (1973). Magneto-optic kerr effect in Ni, Co, and Fe, *Physical Review Letters*, *30*(26), 1329.

[6]. Faraday M. (2008), Faraday's diary of experimental investigation, Vol. 7. *HR Direct*.

[7]. Pershan P S. (1967), Magneto-optical effects. *Journal of applied physics*, *38*(3), 1482-1490.

[8]. Du B., Yang D., Bai Y., Yuan Y., Mao D., Zhang W., and She X. (2017), Investigation of magneto-induced linear dichroism of magnetic fluid. *Applied Optics*, *56*(3), 739-742.

[9]. Nair S S., Rajesh S., Abraham V S., Anantharaman M R. and Nampoori V P N. (2006), Magnetic field-induced cluster formation and variation of magneto-optical signals in zinc-substituted ferrofluids. *Journal of magnetism and magnetic materials*, *305*(1), 28-34.

[10]. M. Xu and P.J. Ridler, Linear dichroism and birefringence effects in magnetic fluids, *J. Appl.Phys.,* vol. 82, pp. 326-332, 1997.
[11]. Sajanlal P R., Sreeprasad T S., Samal, A K., and Pradeep, T. (2011), Anisotropic nanomaterials: structure, growth, assembly, and functions. *Nano reviews*, *2*(1), 5883.
[12]. Stephens, P.J., 1970. Theory of magnetic circular dichroism. The Journal of Chemical Physics, 52(7), pp.3489-3516.
[13]. Piller, H., 1972. Faraday rotation. In Semiconductors and Semimetals (Vol. 8, pp. 103-179). Elsevier.
[14]. Lukins, P.B. and Ritchie, G.L., 1991. Magneto-optical Cotton—Mouton effect of molecular oxygen. A comparison. Chemical physics letters, 180(6), pp.551-555.
[15]. Horng, H.E., Hong, C.Y., Yang, H.C., Jang, I.J., Yang, S.Y., Wu, J.M., Lee, S.L. and Kuo, F.C., 1999. Magnetic field dependence of Cotton–Mouton rotation for magnetic fluid films. Journal of magnetism and magnetic materials, 201(1-3), pp.215-217.
[16]. Nairn, J.A., Friesner, R., Frank, H.A. and Sauer, K., 1980. A new approach to the theory of linear dichroism in partially ordered systems. Application to reaction centers and whole cells of photosynthetic bacteria. Biophysical Journal, 32(2), pp.733-753.
[17]. Yusuf N A., Ramadan A. and Abu-Safia, H. (1998), The wavelength and concentration dependence of the magneto-dielectric anisotropy effect in magnetic fluids determined from magneto-optical measurements. Journal of magnetism and magnetic materials, 184(3), 375-386.
[18]. Nordén, B., 1978. Applications of linear dichroism spectroscopy. Applied Spectroscopy Reviews, 14(2), pp.157-248.
[19]. Ferre, J. and Gehring, G.A., 1984. Linear optical birefringence of magnetic crystals. Reports on Progress in Physics, 47(5), p.513
[20]. Akyurekli, M., Gonulol, M., Bayram, A., Yarici, I., & Ozturk, Y. (2017, September). Investigation of optical properties of ferrofluid by using magneto-optical transmission and linear dichroism. In *2017 IEEE 7th International Conference Nanomaterials: Application & Properties (NAP)* (pp. 02MAN10-1). IEEE.
[21]. Blums E., Cebers A., and Maiorov M M., (2010), Magnetic fluids. Walter de Gruyter
[22]. Laskar J M., Philip J., and Raj, B. (2008), Light scattering in a magnetically polarizable nanoparticle suspension. *Physical Review E*, *78*(3), 031404.
[23]. Zhang Q., Wang J. and Zhu H. (1995). A theoretical consideration of the dielectric behaviors of ferrofluid subjected to a magnetic field. *Journal of applied physics*, *78*(6), 3999-4002.
[24]. Yusuf, N.A., Ramadan, A. and Abu-Safia, H., 1998. The wavelength and concentration dependence of the magneto-dielectric anisotropy effect in magnetic fluids determined from magneto-optical measurements. Journal of magnetism and magnetic materials, 184(3), pp.375-386.
[25]. Jennings, B. R., X u, M., & Ridler, P. J. (2000). Ferrofluid structures: a magnetic dichroism study. *Proceedings of the Royal Society of London. Series A: Mathematical, Physical and Engineering Sciences*, *456*(1996), 891-907.
[26]. Davies, H. W., & Llewellyn, J. P. (1980). Magneto-optic effects in ferrofluids. Journal of Physics D: Applied Physics, 13(12), 2327.
[27]. Shrivastav, A.M., Cvelbar, U. and Abdulhalim, I., 2021. A comprehensive review on plasmonic-based biosensors used in viral diagnostics. *Communications biology*, *4*(1), p.70.
[28]. Roh, S., Chung, T. and Lee, B., 2010, November. Overview of plasmonic sensors and their design methods. In *Advanced Sensor Systems and Applications IV* (Vol. 7853, pp. 25-36). SPIE.
[29]. Homola, J., 2008. Surface plasmon resonance sensors for detection of chemical and biological species. *Chemical reviews*, *108*(2), pp.462-493.
[30]. Xie, K., Cao, S., Zhai, Y., Chen, M., Pan, X., Watarai, H. and Li, Y., 2019. Enhanced modulation of magnetic field on surface plasmon coupled emission (SPCE) by magnetic nanoparticles. *Chinese Chemical Letters*, *30*(12), pp.2173-2176.
[31]. Xie, K.X., Cao, S.H., Liu, Q., Cai, W.P., Huo, S.X., Watarai, H. and Li, Y.Q., 2015. Modulation of surface plasmon coupled emission (SPCE) by a pulsed magnetic field. *Chemical Communications*, *51*(61), pp.12320-12323.
[32]. Cao, S.H., Xie, T.T., Cai, W.P., Liu, Q. and Li, Y.Q., 2011. Electric field assisted surface plasmon-coupled directional emission: an active strategy on enhancing sensitivity for DNA sensing and efficient discrimination of single base mutation. *Journal of the American Chemical Society*, *133*(6), pp.1787-1789.
[33]. Aslan, K., Previte, M.J., Zhang, Y. and Geddes, C.D., 2008. Surface plasmon coupled fluorescence in the ultraviolet and visible spectral regions using zinc thin films. *Analytical chemistry*, *80*(19), pp.7304-7312.
[34]. Lakowicz, J.R., 2004. Radiative decay engineering 3. Surface plasmon-coupled directional emission. *Analytical biochemistry*, *324*(2), pp.153-169.
[35]. Matveeva, E., Gryczynski, Z., Gryczynski, I., Malicka, J. and Lakowicz, J.R., 2004. Myoglobin immunoassay utilizing directional surface plasmon-coupled emission. *Analytical chemistry*, *76*(21), pp.6287-6292.

[36]. Geddes, C.D., Gryczynski, I., Malicka, J., Gryczynski, Z. and Lakowicz, J.R., 2004. Directional surface plasmon coupled emission. *Journal of fluorescence*, *14*(1), p.119.

[37]. Xie, K., Cao, S., Zhai, Y., Chen, M., Pan, X., Watarai, H. and Li, Y., 2019. Enhanced modulation of magnetic field on surface plasmon coupled emission (SPCE) by magnetic nanoparticles. *Chinese Chemical Letters*, *30*(12), pp.2173-2176.

[38]. Gryczynski, I., Malicka, J., Jiang, W., Fischer, H., Chan, W.C., Gryczynski, Z., Grudzinski, W. and Lakowicz, J.R., 2005. Surface-plasmon-coupled emission of quantum dots. *The Journal of Physical Chemistry B*, *109*(3), pp.1088-1093.

[39]. Geddes, C.D., Gryczynski, I., Malicka, J., Gryczynski, Z. and Lakowicz, J.R., 2004. Directional surface plasmon coupled emission. *Journal of fluorescence*, *14*(1), p.119.

[40]. Mishra, H., Dragan, A. and Geddes, C.D., 2011. UV to NIR surface plasmon coupled and metal-enhanced fluorescence using Indium thin films: application to intrinsic (label-less) protein fluorescence detection. *The Journal of Physical Chemistry C*, *115*(35), pp.17227-17236.

[41]. Benner, R.E., Dornhaus, R. and Chang, R.K., 1979. Angular emission profiles of dye molecules excited by surface plasmon waves at a metal surface. Optics Communications, 30(2), pp.145-149.

[42]. Enderlein, J. and Ruckstuhl, T., 2005. The efficiency of surface-plasmon coupled emission for sensitive fluorescence detection. *Optics express*, *13*(22), pp.8855-8865.

[43]. Weber, W.H. and Eagen, C.F., 1979. Energy transfer from an excited dye molecule to the surface plasmons of an adjacent metal. *Optics Letters*, *4*(8), pp.236-238.

[44]. Stefani, F.D., Vasilev, K., Bocchio, N., Stoyanova, N. and Kreiter, M., 2005. Surface-plasmon-mediated single-molecule fluorescence through a thin metallic film. *Physical review letters*, *94*(2), p.023005.

[45]. Cao, S.H., Zou, Z.X., Weng, Y.H., Cai, W.P., Liu, Q. and Li, Y.Q., 2014. Plasmon-mediated fluorescence with distance independence: From model to a biosensing application. *Biosensors and Bioelectronics*, *58*, pp.258-265.

[46]. Xie, K.X., Cao, S.H., Wang, Z.C., Weng, Y.H., Huo, S.X., Zhai, Y.Y., Chen, M., Pan, X.H. and Li, Y.Q., 2017. Graphene oxide-assisted surface plasmon coupled emission for amplified fluorescence immunoassay. *Sensors and Actuators B: Chemical*, *253*, pp.804-808.

[47]. Yuk, J.S., McDonagh, C. and MacCraith, B.D., 2010. Demonstration of a surface plasmon-coupled emission (SPCE)-based immunoassay in the absence of a spacer layer. *Analytical and bioanalytical chemistry*, *398*, pp.1947-1954.

[48]. Cao, S.H., Zou, Z.X., Weng, Y.H., Cai, W.P., Liu, Q. and Li, Y.Q., 2014. Plasmon-mediated fluorescence with distance independence: From model to a biosensing application. *Biosensors and Bioelectronics*, *58*, pp.258-265.

[49]. Tran, N.H.T., Trinh, K.T.L., Lee, J.H., Yoon, W.J. and Ju, H., 2018. Reproducible Enhancement of Fluorescence by Bimetal Mediated Surface Plasmon Coupled Emission for Highly Sensitive Quantitative Diagnosis of Double-Stranded DNA. *Small*, *14*(32), p.1801385.

[50]. Chen, M., Cao, S.H. and Li, Y.Q., 2020. Surface plasmon–coupled emission imaging for biological applications. *Analytical and Bioanalytical Chemistry*, *412*, pp.6085-6100.

[51]. Cao, S.H., Cai, W.P., Liu, Q. and Li, Y.Q., 2012. Surface plasmon–coupled emission: what can directional fluorescence bring to the analytical sciences?. *Annual Review of Analytical Chemistry*, *5*(1), pp.317-336.

[52]. Weber, W.H. and Eagen, C.F., 1979. Energy transfer from an excited dye molecule to the surface plasmons of an adjacent metal. *Optics Letters*, *4*(8), pp.236-238.

[53]. Yuk, J.S., Guignon, E.F. and Lynes, M.A., 2013. Highly sensitive grating coupler-based surface plasmon-coupled emission (SPCE) biosensor for immunoassay. *Analyst*, *138*(9), pp.2576-2582.

[54]. Badiya, P.K., Srinivasan, V., Naik, S.P., Rai, B., Reddy, N., Prathap Chandran, S., Sai Muthukumar, V., Molli, M. and Ramamurthy, S.S., 2018. Low-cost plasmonic carbon spacer for surface plasmon-coupled emission enhancements and ethanol detection: a smartphone approach. *Plasmonics*, *13*, pp.519-524.

[55]. Gryczynski, I., Malicka, J.B., Gryczynski, Z., Nowaczyk, K. and Lakowicz, J.R., 2004, June. Surface plasmon-coupled directional fluorescence emission. In *Plasmonics in Biology and Medicine* (Vol. 5327, pp. 37-44). SPIE.

[56]. Lakowicz, J.R., 2004. Radiative decay engineering 3. Surface plasmon-coupled directional emission. *Analytical biochemistry*, *324*(2), pp.153-169.

[57]. Gryczynski, I., Malicka, J., Gryczynski, Z. and Lakowicz, J.R., 2004. Radiative decay engineering 4. Experimental studies of surface plasmon-coupled directional emission. *Analytical biochemistry*, *324*(2), pp.170-182.

[58]. Manera, M.G., Ferreiro-Vila, E., Garcia-Martin, J.M., Garcia-Martin, A. and Rella, R., 2014. Enhanced antibody recognition with a magneto-optic surface plasmon resonance (MO-SPR) sensor. *Biosensors and Bioelectronics*, *58*, pp.114-120.

[59]. Zhang, H., Fu, C., Yi, Y., Zhou, X., Zhou, C., Ying, G., Shen, Y. and Zhu, Y., 2018. A magnetic-based SERS approach for highly sensitive and reproducible detection of cancer-related serum microRNAs. *Analytical Methods*, *10*(6), pp.624-633.

[60]. Wallis, R.F., Brion, J.J., Burstein, E. and Hartstein, A., 1974. Theory of surface polaritons in anisotropic dielectric media with application to surface magnetoplasmons in semiconductors. *Physical Review B*, *9*(8), p.3424.

[61]. Yu, Z., Veronis, G., Wang, Z. and Fan, S., 2008. One-Way Electromagnetic Waveguide Formed at the Interface between a Plasmonic Metal<? format?> under a Static Magnetic Field and a Photonic Crystal. *Physical review letters*, *100*(2), p.023902.

[62]. González-Díaz, J.B., García-Martín, A., Armelles, G., García-Martín, J.M., Clavero, C., Cebollada, A., Lukaszew, R.A., Skuza, J.R., Kumah, D.P. and Clarke, R., 2007. Surface-magnetoplasmon nonreciprocity effects in noble-metal/ferromagnetic heterostructures. *Physical Review B—Condensed Matter and Materials Physics*, *76*(15), p.153402.

[63]. Zvezdin, A.K. and Kotov, V.A., 1997. *Modern magnetooptics and magnetooptical materials*. CRC Press.

[64]. Armelles, G., Cebollada, A., García-Martín, A. and González, M.U., 2013. Magnetoplasmonics: combining magnetic and plasmonic functionalities. *Advanced Optical Materials*, *1*(1), pp.10-35.

[65]. Martín-Becerra, D., González-Díaz, J.B., Temnov, V.V., Cebollada, A., Armelles, G., Thomay, T., Leitenstorfer, A., Bratschitsch, R., García-Martín, A. and González, M.U., 2010. Enhancement of the magnetic modulation of surface plasmon polaritons in Au/Co/Au films. *Applied Physics Letters*, *97*(18).

[66]. Wallis, R.F., Brion, J.J., Burstein, E. and Hartstein, A., 1974. Theory of surface polaritons in anisotropic dielectric media with application to surface magnetoplasmons in semiconductors. *Physical Review B*, *9*(8), p.3424.

[67]. Sudhan, E.P.J. and Meenakshi, K.S., 2011. Synthesis of silver nanofluid by a novel one pot method for heat transfer applications. *Indian Journal of Science and Technology*, *4*(4), pp.417-21.

[68]. Archana, V.N., Sam, S.A., Balan, A.P. and Anantharaman, M.R., 2021. Magneto-optical properties of a magneto-plasmonic nanofluid based on superparamagnetic iron oxide and gold nanoparticles. *Journal of Magnetism and Magnetic Materials*, *536*, p.168092.

[69]. Reena Mary, A.P., Narayanan, T.N., Sunny, V., Sakthikumar, D., Yoshida, Y., Joy, P.A. and Anantharaman, M.R., 2010. Synthesis of bio-compatible spion–based aqueous ferrofluids and evaluation of radiofrequency power loss for magnetic hyperthermia. *Nanoscale research letters*, *5*, pp.1706-1711.

[70]. Garcia M A. (2011), Surface plasmons in metallic nanoparticles: fundamentals and applications. *Journal of Physics D: Applied Physics*, *44*(28), 283001.

[71]. Desai, R., Mankad, V., Gupta, S.K. and Jha, P.K., 2012. Size distribution of silver nanoparticles: UV-visible spectroscopic assessment. *Nanoscience and nanotechnology letters*, *4*(1), pp.30-34.

[72]. Ivashchenko O., Peplinska B., Gapinski J, Flak D., Jarek M., Zateski K., and Jurga, S. (2018), Silver and ultrasmall iron oxides nanoparticles in hydrocolloids: effect of magnetic field and temperature on self-organization. *Scientific Reports*, *8*(1), 4041.

[73]. Etemadi H., and Plieger, P G. (2020). Improvements in the Organic-Phase Hydrothermal Synthesis of Monodisperse M x Fe3–x O4 (M= Fe, Mg, Zn) Spinel Nanoferrites for Magnetic Fluid Hyperthermia Application. *ACS omega*, *5*(29), 18091-18104.

[74]. Babic-Stojic B., Jokanovic V., Milivojevic D., Jaglicic Z., Makovec, D., Jovic N., and Marinovic-Cincovic M. (2013). Magnetic and structural studies of $CoFe_2O_4$ nanoparticles suspended in an organic liquid. *Journal of Nanomaterials*, *2013*, 11-11.

[75]. Pu S., Dai M., Sun G., and Liu M. (2009, August), Linear birefringence and linear dichroism coupled optical anisotropy of magnetic fluids by external magnetic fields. In 2009 *Symposium on Photonics and Optoelectronics (pp. 1-6)*, IEEE.

[76]. Di Z., Chen X., Pu S., Hu X., and Xia, Y. (2006), Magnetic-field-induced birefringence and particle agglomeration in magnetic fluids. *Applied Physics Letters*, *89*(21).

[77]. Sajanlal P R., Sreeprasad T S., Samal A K., and Pradeep, T. (2011), Anisotropic nanomaterials: structure, growth, assembly, and functions. *Nano reviews*, *2*(1), 5883.

[78]. Achanta, V.G., 2020. Surface waves at metal-dielectric interfaces: Material science perspective. *Reviews in Physics*, *5*, p.100041.

Chapter 5

Hematite nanoparticles for photocatalytic and biological applications

The stability and relative lack of toxicity, make hematite nanoparticles highly pursued material which can provide significant contributions in both biomedical research and other interdisciplinary domains. The green method for synthesizing hematite nanoparticles is particularly promising, due to its low cost, biocompatibility and environment friendliness. Hematite nanoparticles are a potential candidate for photocatalytic application due to their adequate band gap, high surface-to-volume ratio and recyclability after the reaction. Among the various nanometal-oxides, hematite nanoparticles are promising compounds due to their wide range of applications as antioxidants, antibiofilm and antibacterial agents. This chapter deals with the photocatalytic, antibacterial property and cytotoxicity analysis of green synthesized hematite nanoparticles.

5.1 Introduction

Hematite is the most prevalent form of crystalline iron oxide and is also the most thermodynamically stable form under ambient conditions [1,2]. It is isostructural with corundum (α-Al_2O_3) structure. There are two formula units per unit cell in the hematite structure: the trigonal-hexagonal and the primitive rhombohedral. It is an n-type semiconductor and inert compound, insoluble in dilute acids. In numerous industries, including lithium-ion batteries, gas sensors, photocatalysis, water splitting and treatment for the production of H_2, anticorrosive agents, pigment, and biomedical applications, haematite is widely employed [3, 4]. Hematite is one of the most promising material as a potential photocatalyst due to several remarkable properties, such as abundance, low cost, non-toxicity, chemical stability, good visible light absorption, anti-corrosive property, biocompatibility etc. It is known that a number of metal oxide nanoparticles have antibacterial qualities. Their multifunctionality allows them to overcome drug resistance in bacteria. Inorganic oxide nanoparticles are more advantageous than organic antibacterial agents due to the potency of resistant strains of microbial pathogens as well as their durability and stability. In this regard, hematite is a good material as an antibacterial agent.

The most recent breakthrough in nanotechnology has increased the number of chemical and physical methods for the synthesis of nanoparticles. Using conventional methods for synthesizing nanomaterials such as template-assisted synthesis method, hydrothermal synthesis, vapour–solid growth techniques and sol-gel process [6-8] has several alluring advantages. These processes generate a wide range of nanoparticles with numerous uses: such as in electrical applications, and targeted disease therapy, some approaches have a wide range of scaling, great control over nanoparticle shape, extended scalability etc. But there's a big negative consequence with these traditional methods. The excessive use of organic solvents and the release of toxic and harmful chemicals during the synthesis of these nanomaterials poses a significant risk to neurobehavioral and reproductive health and the usage of high-pressure and heat conditions may also contribute to hazardous working conditions. Another unfavorable impact of these methods is the excessive creation of carbon dioxide, which significantly contributes to the greenhouse effect. However, these processes are damaging to the ecosystem and all living things. Therefore, it is essential to create nanoparticles in an environmentally friendly manner [9, 10]. When creating nanomaterials using a green process, metal atoms combine to create clusters, which then become nanoparticles. This technology's main objective is to produce metallic nanoparticles from various biological sources.

Throughout the synthesis process, microbial and phyto-constituents are involved in capping and stabilizing the surface of nanomaterials. The motivation for using the green method for the production of nanomaterials is the simplicity of handling and processing plant materials for extract collection, as well as the accessibility of plant materials in different geographical locations. Due to the use of non-toxic chemicals, environmentally friendly solvents, renewable resources, and easily scaled-up processes for large-scale production, green synthesis of nanoparticles is recognized as an environmental advantage technology [11].

The routine disposal of hazardous organic wastes causes irreversible and serious adverse effects, such as carcinogenic and mutagenesis consequences [12]. Many harmful and dangerous chemicals can be found in industrial effluent, including dyes, phenols, insecticides, metal ions, and so on. Among all of these toxins, dyes are the most persistent and difficult to break down. Because the mineralisation efficiency of these pollutants by standard mineralisation processes is insufficient. Many novel techniques are used for the removal of contaminants from water, like coagulation, ozonation, electrochemical degradation and photocatalytic degradation. Among them, photocatalytic degradation is one of the simplest and most efficient methods for purifying water. Magnetic nanoparticles have gained popularity as catalysts in organic transformations in recent years due to their greater surface area-to-volume ratio and retrievability and recyclability after the reaction [13].

The word photocatalysis combines photochemistry and catalysis, suggesting that both light and a catalyst are required to facilitate a chemical reaction. It can be broadly classified into two categories: heterogeneous photocatalysis, which occurs when it is present in a different phase than the reactant, and homogeneous photocatalysis, which occurs when it is present in the same phase as the reactant. Whereas the photocatalyst and the reaction medium are in a different phase in the latter scenario, they are in the same phase in the former. The surface area, porosity, defects, type of exposed planes, amount of dye, concentration of pollutants, reaction medium pH, calcination temperature, reaction temperature, light intensity, and presence of an oxidising agent are some of the factors that affect a material's photocatalytic properties and efficiency.

Photocatalysis involves the generation of electron-hole pairs in a conduction band through the oxidation and reduction process. To carry out oxidation and reduction reactions, photocatalysts use light energy. When an electron is stimulated from the valence band to the conduction band of the photocatalyst it is bombarded with light energy, leaving a photo-generated hole [14]. Conduction electrons reduce oxygen to superoxide radicals and valence band holes oxidize water to hydroxyl radicals. Oxidation and reduction activities are enabled by the photo-generated electrons and holes. Water and hydroxide ions react with photo-generated holes in aqueous solutions to yield hydroxyl radicals, which are the major oxidants in the photocatalytic oxidation of organic molecules. The oxidation potential of OH is higher than that of other oxidants such as ozone and hydrogen peroxide, and it has been demonstrated that repeated OH attacks on organic pollutants eventually lead to total oxidation. The production of OH can take one of two routes: first, O_2 in water is reduced to generate O_2, which then combines with H^+ to form OOH, which is then rapidly decomposed to OH. The oxidation of OH is the second route.

A significant contributor to chronic illnesses and mortality is bacterial infections. Antibiotics have been the primary form of treatment for bacterial illnesses due to their efficacy and effectiveness. However multidrug-resistant bacterial strains have evolved as a result of the widespread usage of antibiotics. The majority of bacteria exist as biofilms, which frequently contain different species that communicate with one another and their surroundings. Microbial clumps known as biofilms often depend on extracellular products and a solid surface. The bacteria can travel back and forth across the surface, but when the bacteria have settled, the synthesis of the bacterial flagellum is blocked, the bacteria multiply quickly, and a mature biofilm is created. At this point, the bacteria have formed a barrier that can withstand antibiotic treatment and serve as a source of systemic persistent infections. Biofilms pose a significant risk to human health. Additionally, the bacteria in biofilms can create superantigens to subvert the immune system. Therefore, despite the widespread use of antimicrobial medications and other contemporary antibacterial medicines, bacterial infections continue to be a significant problem. Metal nanoparticles have received a lot of attention as a potential treatment for antibiotic resistance due to their capacity to target several biomolecular characteristics of resistant strains. The interaction between hematite (α-Fe_2O_3) nanoparticles (NPs) and bacteria can occur through two potential mechanisms, because of their extreme stability in the natural environment, these haematite nanoparticles contribute little to the antibacterial action of metal ion release. But defective haematite nanoparticles can produce electron-hole pairs when exposed to UV or visible light. These electron-hole pairs are responsible for the production of reactive oxygen species (ROS), including hydroxyl radicals (OH^-), hydrogen peroxide (H_2O_2) and singlet oxygen (O_2*). These ROS are highly reactive and can have damaging effects on bacterial cells [15,16]. The generated free radicals can lead to various detrimental effects, such as the depolymerization of bacterial polysaccharides, inactivation of enzymes within the bacterial cells, induction of DNA strand breaks, potentially causing genetic damage, Initiation of lipid peroxidation, which can damage bacterial cell membranes. Ultimately, the accumulation of these harmful effects can lead to bacterial cell death. The other possible mechanism of interaction involves non-reactive interactions between hematite nanoparticles and bacteria. These interactions may include: electrostatic interactions: attraction or repulsion based on electrical charges, dipole-dipole interactions: interactions between molecules with permanent dipoles, hydrogen bonds: weak chemical bonds formed between hydrogen atoms and electronegative elements, hydrophobic interactions: interactions between hydrophobic regions of molecules, van der Waals interactions: weak forces of attraction between atoms and molecules. These non-reactive interactions can disrupt cellular functions and the organization of bacterial membranes [17, 18]. For example, electrostatic forces may lead to the binding of hematite nanoparticles to the bacterial cell surface, potentially interfering with membrane integrity or cellular processes. Hydrophobic interactions could also play a role in disrupting bacterial membranes.

Nanoparticles' unique and peculiar features allow them to be used in a variety of applications. At least 15% of the products available on the worldwide market today, such as cookware, food packaging, apparel, electrical gadgets, sunscreen, and so on, are expected to include nanotechnology into their manufacturing process [19-21]. One of the most serious concerns about human health is the emission of nanoparticles into the atmosphere. Because of their small size, they spend more time in the atmosphere, increasing the risk of respiratory exposure [22]. Hematite is one of the most commonly used nanoparticles in a variety of applications [23]. As a result, it was created in bigger quantities than other nanoparticles [24]. We now live in the world of nanotechnology. As a result, the toxicity investigation of hematite nanoparticles is more relevant in the current environment.

5.2 Characterization

The Bruker AXS D8 Advance X-ray diffractometer employing Cu–Kα X-rays of wavelength 1.5406 Å can be used to obtain the XRD pattern of synthesized nanoparticles. Diffraction pattern was collected in the range 10-90°. UV-visible spectrometer (Ocean Optics Maya 2000-Pro UV compact spectrometer) is employed for studying the absorption properties and assessing the photocatalytic activity of the synthesized sample. 5 mg of the prepared Hematite nanopowder was mixed with 40 ml of 20 ppm Methylene blue dye and stirred for 20 minutes. Then the solution is placed under solar illumination. The absorbance of the solution was taken every 30-minute time intervals. Using the agar well diffusion method, the synthesized haematite nanoparticles' antibacterial properties were investigated. The cell viability test was conducted on mouse fibroblast cell line L929. FTIR analysis was performed to identify the functional groups of the tea extract, using an FTIR Bruker spectrophotometer in the wavelength range of 3500–400 cm^{-1} with a resolution of 4 cm^{-1}, which are responsible for the reduction and stabilizing of the α-Fe_2O_3 nanoparticles. In addition, a phase study was performed by Raman spectroscopy using a 542 nm laser excitation on the Horiba Labram HR Evolution Raman spectrometer.

5.3 Experimental

5.3.1 Preparation of Tea extract

The tea extract was made by boiling 2 g of black tea powder in 100 mL of distilled water for 20 minutes at 60 °C. The broth is then cooled to room temperature and filtered to provide the extract, which is utilized to produce iron oxide nanoparticles.

5.3.2 Synthesis of Hematite nanoparticles

For synthesizing Hematite nanoparticles, 250 mM aqueous solution of ferric nitrate and the prepared tea extract were mixed in a ratio of 2:1. We obtained a dark greenish-black coloured solution, which was then stirred for 20 minutes. After that, this solution was transferred to a Teflon liner, properly sealed, and held in the autoclave for 2 hours at 300 °C. The autoclave was switched off and allowed to cool down to ambient temperature. To remove loosely attached organic content from the surface of the nanoparticles, the products were washed multiple times with ethanol and distilled water. The synthesized nanoparticles were then dried for 6 hours under a vacuum at 80 °C. **Figure 5.1** shows a schematic representation of nanoparticle synthesis.

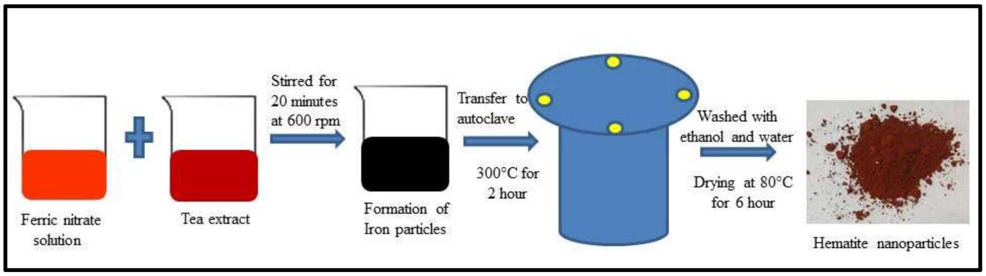

Figure 5.1 Schematic representation of hematite nanoparticles synthesis

5.3.3 Reduction Mechanism of Hematite Nanoparticles

The tea extract can be utilized as a reducing and capping agent while making Hematite nanoparticles. It contains a high quantity of polyphenols and other chemical elements. The polyphenols help in the reduction of the salt precursors into nanoparticles. Flavonols are the functional groups having the greatest biological significance. Tea contains four different flavanol derivatives: epicatechin (EC), epigallocatechin (EGC), epicatechin gallate (ECG), and epigallocatechin gallate (EGG). Epigallocatechin gallate is an active catechin that aids in the reduction process since it has a standard potential of 0.57 V and may reduce Fe^{3+} to Fe^{0}, whereas iron's standard potential is -0.036 V. When the precursor is injected, it initiates a complex by breaking the -OH bond and creating a partial bond with a metal ion [25, 26]. Finally, the partial link is broken, and electrons are transported to reduce metal ions to nanoparticles, which then oxidize to ortho-quinone. The steps involved in the reduction mechanism of hematite nanoparticle is shown in **Figure 5.2**.

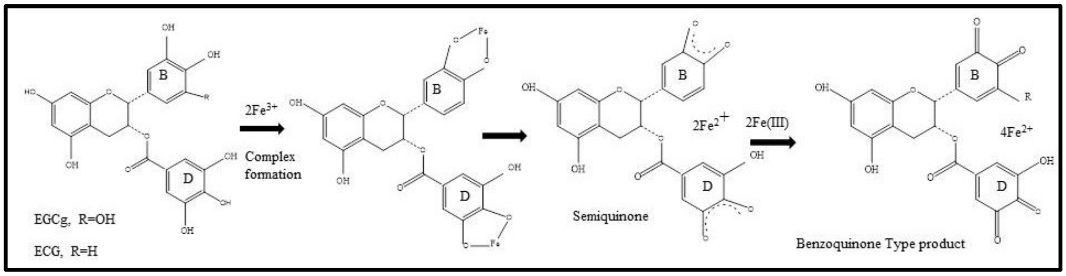

Figure 5.2 Reduction mechanism of hematite nanoparticles

5.3.4 Antibacterial study

The agar well diffusion method is used for investigating the antibacterial activity of synthesized hematite nanoparticles against gram-negative bacteria, Escherichia Coil. The cultured bacteria were injected into test tubes that contained a Muller-Hinton broth, which is placed in a rotating incubator at 37 °C for 24 hours. Then the Mueller-Hinton agar was transferred into a petri dish, where they were allowed to solidify under a sterile environment. The agar surface was bored using a sterile cork borer to make wells of approximately 6mm diameter and different concentrations of sample such as 1 mg/mL, 10 mg/mL and 100 mg/mL. The prepared samples are dissolved in 10% DMSO (Dimethyl sulfoxide) and sonicated to achieve uniform concentration. Then take 50 µL from this solution and it was loaded into each well. After a 24-hour incubation period at 37 °C, the diameter of the zone of inhibition on the plates was used to assess the antibacterial activity. Ampicillin was used as the positive control. The schematic representation of agar well diffusion method is shown in **Figure 5.3**.

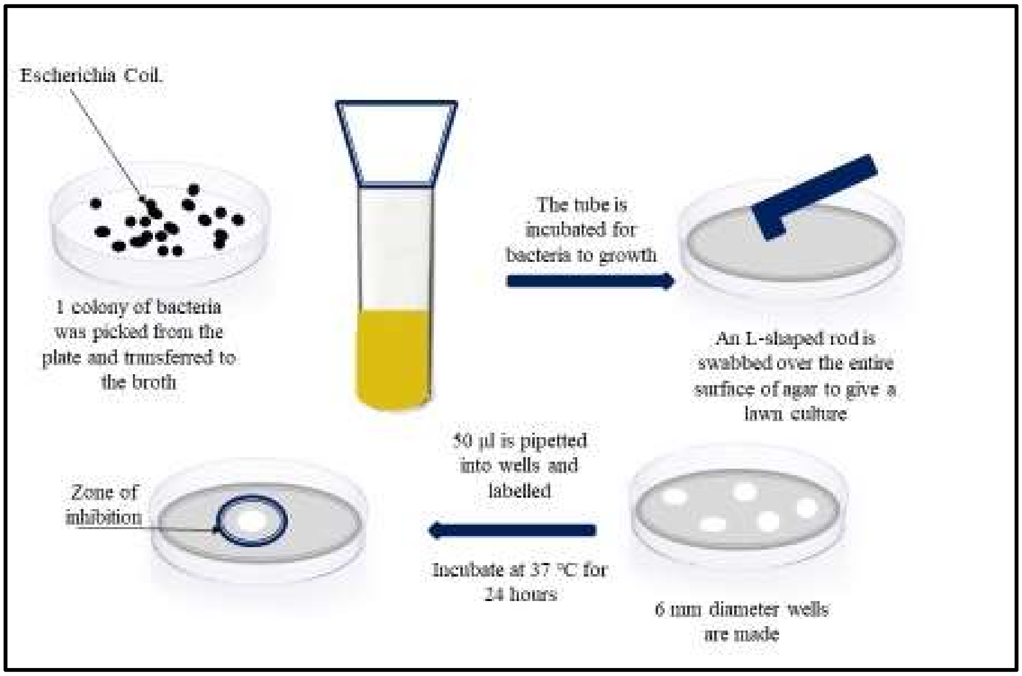

Figure 5.3 Schematic representation of agar well diffusion method

5.3.5 Cytotoxicity assay

The cytotoxicity of haematite nanoparticles is tested using the [3-(4,5-dimethylthiazole-2-yl)-2,5-diphenyltetrazolium chloride or bromide (MTT) assay. The cell viability test is conducted using Mosmann's suggested method. Cell viability was studied at various concentrations of haematite nanoparticles during a 24-hour time period. The assay was performed using mouse fibroblast cell line L929 obtained from ATCC (Manassas, Virginia, USA). The cells are cultured in RPMI (Gibco, UK) supplemented with 10% heat-inactivated foetal bovine serum (Charcol stripped FBS), pencilin (100 U/mL), and streptomycin (100 µg/mL) (Gibco, USA). The cells are incubated at 37°C in a humidified environment with 5% CO2. In this assay, the mitochondria hydrogenase enzyme in living cells breaks down the MTT reagent and converts it to the insoluble formamide molecule, which, when combined with dimethyl sulfoxide, creates a purple hue proportionate to the degree of cell viability. The cell viability was determined using an Elisa plate reader at 570 nm. In this test, the background absorbance of the generated MTT reagent in the unknown reactions with the surrounding cell was subtracted from the absorbance measured from the exposed cells. Cell viability is expressed using the formula [27]

$$\boldsymbol{Percentage\ of\ cell\ viability} = \frac{\boldsymbol{Average\ absorbance\ treated}}{\boldsymbol{Average\ absorbance\ of\ control}} \times \mathbf{100} \tag{5.1}$$

In the present study, the test was repeated 5 times to increase the accuracy.

5.4 Results and Discussions

5.4.1 Structural characterization

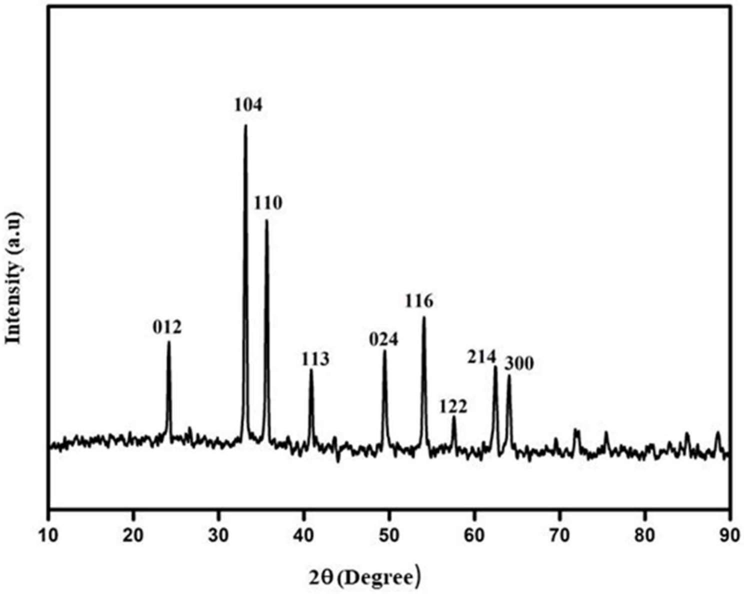

Figure 5.4 X-ray diffraction pattern of hematite nanoparticles

The XRD pattern of tea extract-mediated iron oxide nanoparticles are depicted in **Figure 5.4**. The diffraction pattern's major peaks may all be indexed using the JCPDS file number 85-0596, which is associated with rhombohedral symmetry hematite nanoparticles. The absence of any additional peaks in the diffraction pattern suggests that the green synthesised haematite nanoparticles were highly pure [28]. Based on the line width of the strongest peak, the average crystallite size of the synthesised particles was determined using the Debye-Scherrer equation.

$$D = \frac{K\lambda}{\beta cos\theta} \tag{5.2}$$

The variables D, K, λ, β, and stand for the mean crystallite size, Debye constant, radiation wavelength, full width at half maximum in radians, and Bragg angle, in that order. Based on calculations, the average size of a crystallite is approximately 35 nm. The average values of the lattice parameters are calculated for its rhombohedral structure using the equation,

$$d = \frac{1}{\sqrt{\frac{4(h^2+k^2+hk)}{3a^2}+\frac{l^2}{c^2}}} \tag{5.3}$$

Where d is interplanar distance, h, k, l are Miller indices and a, c are lattice parameters. The calculated values of a = 5.03 Å and c = 13.67 Å for the lattice parameters accord well with the stated values.

5.4.2 Optical study

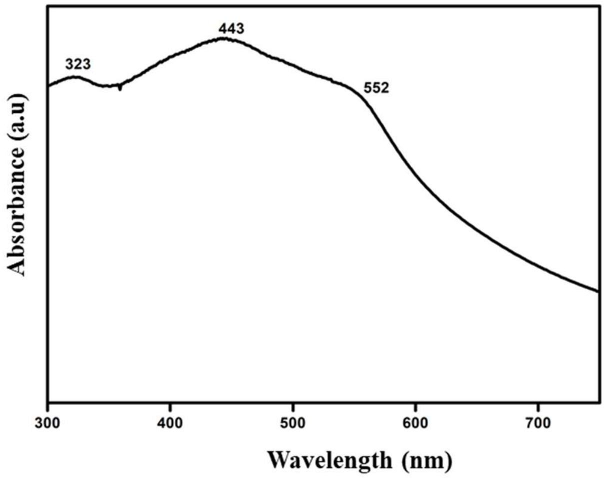

Figure 5.5a UV-visible absorption spectra of hematite nanoparticle

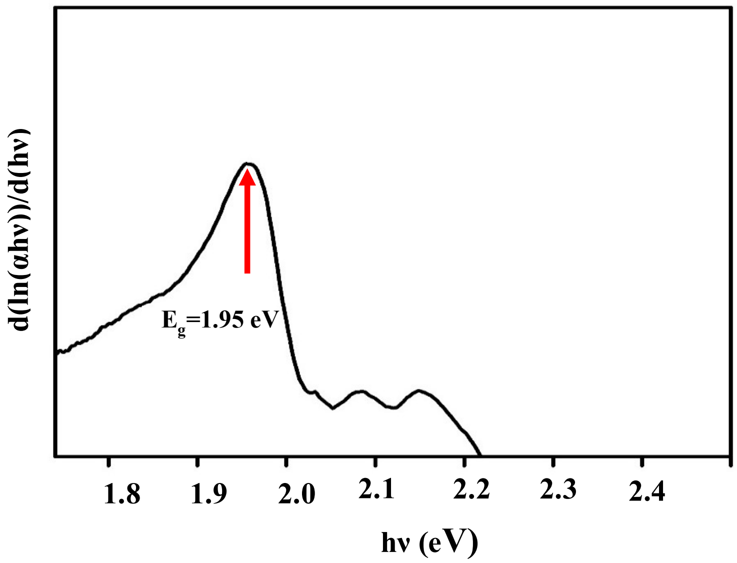

Figure 5.5b Derivative curve

The absorption spectrum of synthesized Hematite nanoparticles is shown in **Figure 5.5a**. Four absorption bands are observable in the near UV, near IR, and visible portions of the spectrum. The fourth zone is typically not taken into account due to its extremely low absorption coefficients. The absorption band around 323 nm arises due to ligand-to-metal charge transfer transitions. The second absorption band around 443 nm can be assigned to Fe^{3+} ligand field transitions or d–d transition. The absorption band at 552 nm, which is mainly responsible for hematite's red colour, is produced via the twofold excitation process. Using the Tauc Plot relationship,

$$(\boldsymbol{\alpha h v}) = \boldsymbol{A}(\boldsymbol{h v} - \boldsymbol{E_g})^{\boldsymbol{n}} \tag{5.4}$$

Where α, h, v, A, E_g and n stand for absorption coefficient, Planck’s constant, frequency of incident light, energy independent constant, band gap energy and type of electronic transitions respectively. The above equation can be rewritten in the following form [29],

$$\frac{\boldsymbol{d}(\ln(\boldsymbol{\alpha h v}))}{\boldsymbol{d}(\boldsymbol{h v})} = \frac{\boldsymbol{n}}{\boldsymbol{h v} - \boldsymbol{E_g}} \tag{5.5}$$

The plot of $d(\ln(\alpha h v))/d(h v)$ vs $h v$ will produce discontinuity at a particular value of [30]

$$h v = E \tag{5.6}$$

Where a possible electronic transition can occur corresponding to the band gap $E=E_g$. The derivative curve of hematite is depicted in **Figure 5.5b.**

5.4.3 Raman spectra

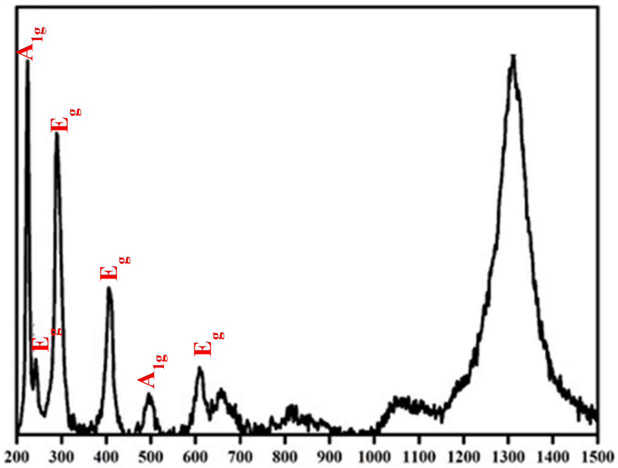

Figure 5.7 Raman spectra of hematite nanoparticles

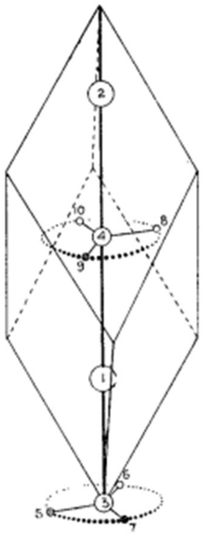

Figure 5.6 Unit cell of α-Fe_2O_3 [35]

Raman spectra can be used for structural, phase and compositional identification of the prepared particles. The hematite nanoparticles in **Figure 5.6** are members of the D_{3d}^{6} space group and have two Fe_2O_3 units, or ten atoms per rhombohedral unit cell, with unit cell parameters of a = 5.038 Å, b = 5.038 Å, and c = 13.772 Å. At the first Brillouin zone centre, the distribution of irreducible representations of Hematite particles among the various symmetry species is given by [31-34]

$$\Gamma_{vib} = 2A_{1g}(R) + 2A_{1u}(i.a) + 3A_{2g}(i.a) + 2A_{2u}(IR) + 5E_g(R) + 4E_u(IR)$$

Where R, IR, and i.a. refer to raman-active, infrared-active, and optically inactive modes, respectively. In fact, two A_{1g} modes and five $E_g$modes—or seven phonon lines—are anticipated in the raman spectrum. The raman spectra of hematite nanoparticles are depicted in **Figure 5.7**. The bands seen in the Raman spectrum of synthesized hematite nanoparticles at 222 and 495 cm^{-1} are attributed to the A_{1g} modes and the symmetric bending modes E_g can be seen at 241, 289, 407 and 609 cm^{-1} [34]. Another E_g mode at 299cm^{-1} is present in the Raman spectrum of hematite nanoparticles, but such bands are resolved only at 100 K or less [32]. However, the present study reports the Raman spectrum of hematite nanoparticles at room temperature. Being centrosymmetric, the Hematite nanoparticle is expected to have IR and Raman modes that are mutually exclusive, making the antisymmetric $2A_{2u}$and $4E_u$ modes are IR active. Optically passive modes include $2A_{1u}$and $3A_{2g}$. The additional peaks at 652 cm^{-1}, arise due to longitudinal optical mode E_u 826. Two-magnon scattering, which results from the interaction of two magnons generated on antiparallel near spin sites, is responsible for the peak at approximately 1306 cm^{-1}. The origin of the less intense peak at 1071 cm^{-1} is uncertain and there are fewer observations of it. The sharp and narrow peaks indicate the higher crystalline nature of the prepared sample.

5.4.4 FTIR spectra

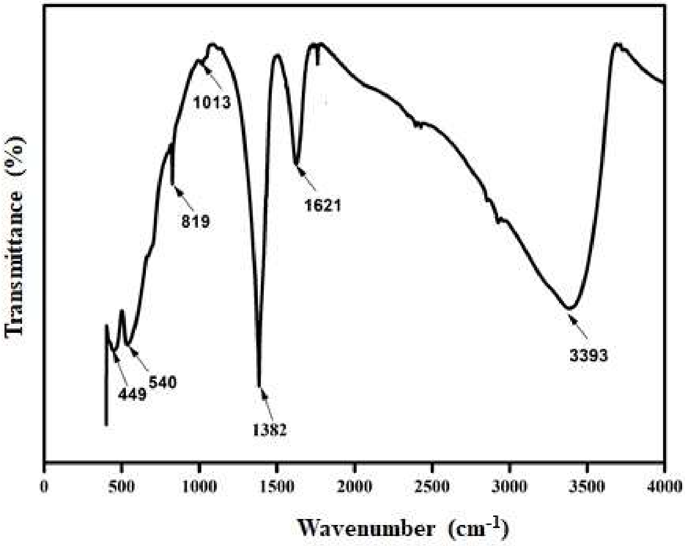

Figure 5.8 FTIR spectra of α-Fe_2O_3

The FTIR spectrum of Hematite nanoparticles is illustrated in **Figure 5.8**. The bands at 449 cm^{-1} and 540 cm^{-1} arises due to the vibrational intrinsic stretching of metal oxygen bond (Fe-O band vibrations), which indicated that the prepared nanoparticles are iron oxide. The peaks at 819 cm^{-1} and 1013 cm^{-1} corresponds to C-H bend of alkenes and C-O stretches respectively. The distinct peak located at 1382 cm-1 is accountable for the decrease in metal ions from the precursor. The peak at 1621 cm^{-1} and at 3393 cm^{-1} is attributed to bending vibration of absorbed water and hydroxyl groups [36].

5.4.6 Photocatalytic activity

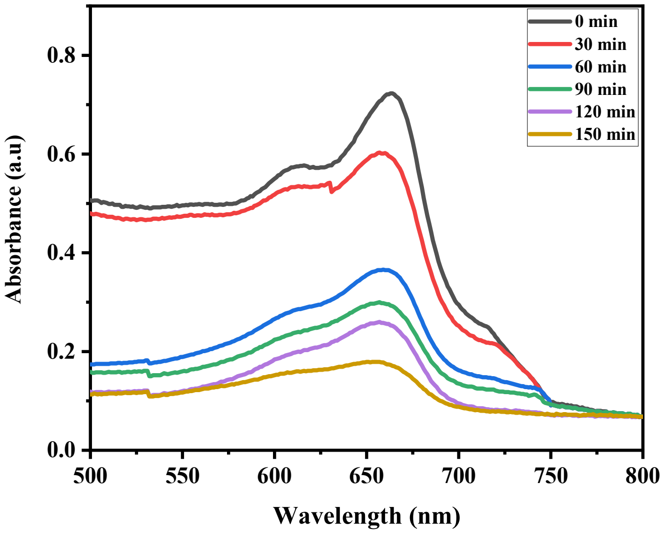

Figure 5.9(a) Absorption spectra of methylene blue with Hematite nanoparticles at different time intervals

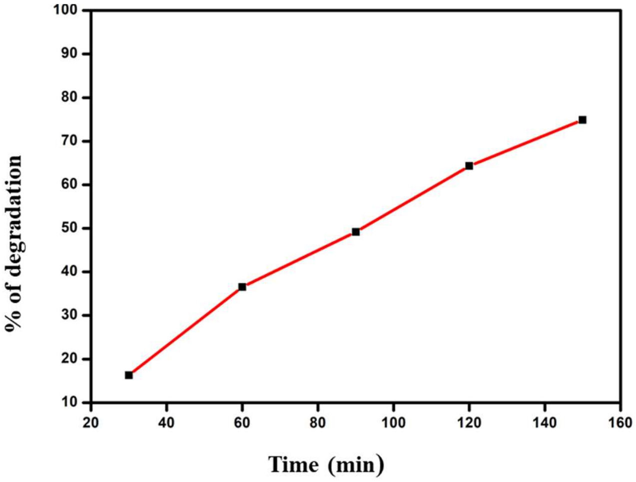

Figure 5.9(b). Variation of a percentage of degradation with time

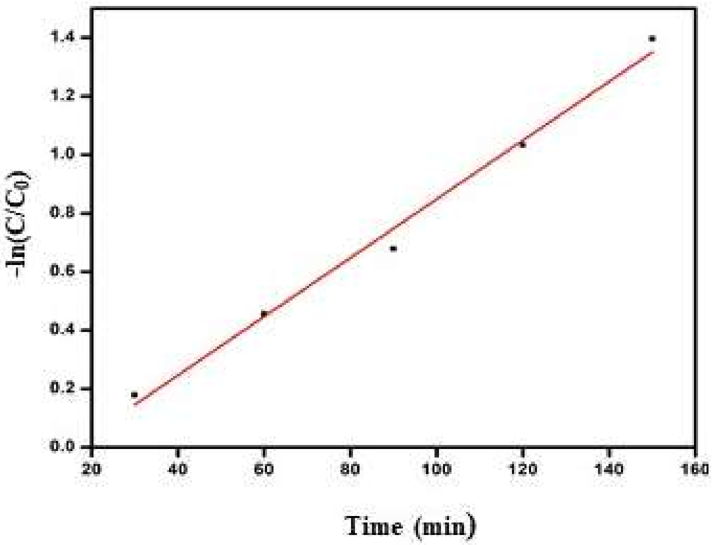

Figure 5.9(c) plot of -ln(C/C_0) versus irradiation time of α-Fe_2O_3

When the light of a suitable wavelength strikes a semiconductor, it stimulates the production of an electron-hole pair. On the surface of the particles, this charge separation can be exploited to accelerate redox processes. In comparison to other catalysts, hematite is well suited for visible light absorption due to its low bandgap. When photons strike the nanoparticles in the colloidal mixture during solar irradiation, electrons at the particle surface are energized. This causes holes to remain in the valence band as some electrons move from the valence band to the conduction band. While the conduction band electrons reduce oxygen to superoxide radicals and holes react with hydroxide ions, which decompose methylene blue into harmless gases such as carbon dioxide and water [37]. The degradation efficiency of hematite particle was determined using the equation,

$$D\% = \frac{C_0 - C}{C_0} \times 100 \tag{5.7}$$

Where C_0 and C are the initial and final concentrations of dye at time t=0 min and at a time t respectively. The first-order reaction kinetics is expressed by the equation

$$\ln\left(\frac{C}{C_0}\right) = -kt \text{ [38]} \tag{5.8}$$

The rate constant k was calculated using the equation,

$$k = 2.303 \times slope \tag{5.9}$$

In this case, slope is determined from the plot of the first-order kinetic graph.

The photocatalytic activity spectrum of hematite nanoparticles for the degradation of methylene blue dye at regular intervals is shown in **Figure 5.9(a)**. Here we can see that 75% of the dye was degraded after 150 minutes. The synthesised Haematite nanoparticles' huge surface area and size might be the cause of their increased photocatalytic activity. **Figure 5.9(b)** shows the change in the percentage of degradation over time. Hematite particles were utilised to investigate the Methylene blue degradation kinetics using order reaction kinetics. The **Figure 5.9(c)** depict the plot of -ln(C/C_0) versus irradiation time of methylene blue dye. It is observed that the degradation is a pseudo first-order reaction with rate constant .038 min^{-1} and correlation coefficient $R^2 = 0.9874$.

5.4.7 Antibacterial study

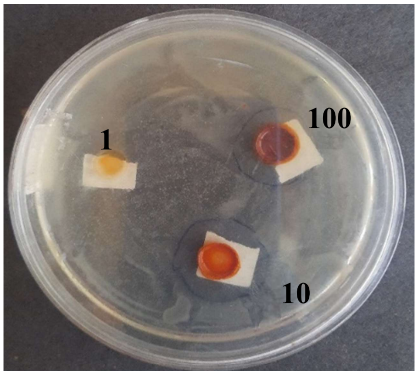

Figure 5.10(a) Zone of Inhibition image of Escherichia Coil

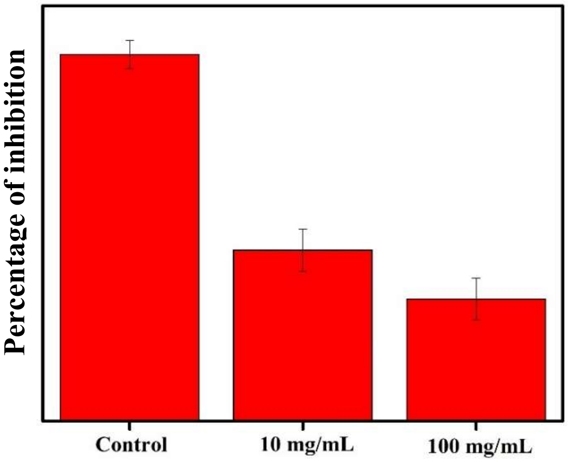

Figure 5.10(b) Effect of α-Fe_2O_3 on the growth of Escherichia Coil

Concentration (mg/mL)	Zone of inhibition (mm)
1	0
10	12
100	10

Table 5.1 The reduction of bacterial growth rate on different concentrations of hematite nanoparticles

The agar well diffusion method is used for investigating the antibacterial activity of synthesized hematite nanoparticles against gram-negative bacteria, Escherichia Coil, and significant zone of inhibitions are observed as shown in **Figure 5.10(a)**. The reduction of bacterial growth rate on different concentrations of hematite nanoparticles is evident from **Table 5.1** and graphical representation shown in **Figure 5.10(b)**. At a dosage of 1 mg/mL, the zone of inhibition was absent. 1mg/mL, because enough iron metal is not released. With increasing concentrations of hematite nanoparticles, the zone of inhibition was observed, but at high concentration the reduction ability of bacterial growth is reduced. The interaction between hematite nanoparticles and bacteria might occur through two different ways. Generation of Reactive oxygen species is one of the mechanisms for the interaction, which are free radicals that can injure cells differently. Bacterial mortality is caused by the severing of DNA strands, deactivation of enzymes and oxidation of membrane lipids. Molecules and reactive intermediates with a high positive redox potential are collectively referred to as ROS. The four distinct kinds of ROS, are the superoxide radical (O^{2*}), the hydroxyl radical (OH^-), hydrogen peroxide (H_2O_2), and singlet oxygen ($^1O_2$). Electron-hole pairs are produced when hematite nanoparticles are stimulated by UV or visible light. The holes can divide H_2O molecules into OH and H^+. Dissolved oxygen molecules are converted to superoxide radical anions (O^{2-}) by the addition of electrons. By depolymerizing polysaccharides, breaking DNA strands, deactivating enzymes, and starting lipid peroxidation, the free radicals O^{2-} and OH created in the processes might kill bacteria. The accumulation of nanoparticles in the cytoplasm or periplasm, which disturbs cellular function and disarrays membranes, is another possible route. Alternatively, nanoparticles may attach to bacterial cell membranes or cell membrane proteins through electrostatic interactions.

5.4.8 Cytotoxicity of hematite nanoparticles

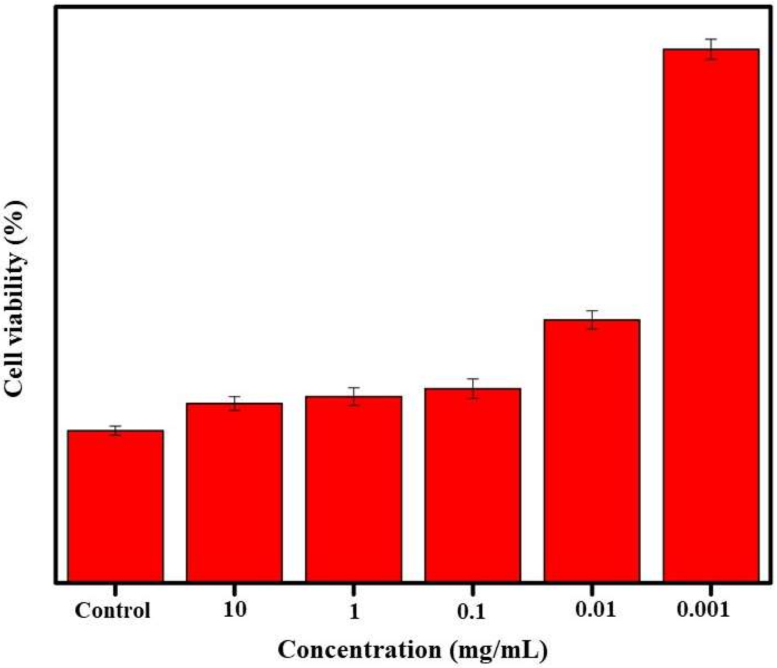

Figure 5.11 Cell viability for mouse fibroblast cell line L929 incubated with different concentrations of hematite nanoparticles

In vitro or in vivo applications of nanoparticles are determined by their non-toxicity as a necessary condition. **Figure 5.11** shows the mouse fibroblast cell line L929's vitality at various doses of artificially produced haematite nanoparticles in comparison to the control group. In the present work, we incubated mouse fibroblast cell line L929 with 0.001-10 mg/mL hematite nanoparticle concentrations were exposed for 24 hours, and the MTT assay was used to determine the viability in relation to the synthesis of the enzyme mitochondrial dehydrogenase. In this case, we have found that haematite nanoparticles are safe for cells cultured up to a concentration of 10 mg/mL. Cell viability is increased in all concentrations of hematite nanoparticles compared with the control group. Low cytotoxicity indicates that the synthesized hematite nanoparticles could be utilized as good drug carriers.

5.5 Conclusions

Stable Hematite nanoparticles were synthesized using Hydrothermal method. Different characterization techniques were performed to study the nature of synthesized particles; XRD, FTIR, UV-absorption spectra and Raman spectra. The enhancement of photocatalytic activity can be observed in α-Fe_2O_3 nanoparticles, which may be due to the size and large surface area of synthesized nanoparticles. About 75% of methylene blue dye was degraded after 150 minutes. Hence it can be used as a good candidate for waste water treatment. The concentration-dependent antibacterial effect of synthesized α-Fe_2O_3 nanoparticles on Escherichia Coli was studied and the zone of inhibition was found to be maximum at a concentration of 10 mg/mL. In the present study, we can see that, the hematite nanoparticles are not toxic to cells in culture up to a concentration of 10 mg/mL. The low cytotoxicity indicates that the synthesized nanoparticles could be utilized as drug carriers.

References

[1]. Gallon, T.E., 1966. *An investigation of the magnetic properties of hematite* (Doctoral dissertation, University of London).

[2]. Tamirat, A.G., Rick, J., Dubale, A.A., Su, W.N. and Hwang, B.J., 2016. Using hematite for photoelectrochemical water splitting: a review of current progress and challenges. *Nanoscale horizons*, *1*(4), pp.243-267.

[3]. Kefeni, K.K., Msagati, T.A., Nkambule, T.T. and Mamba, B.B., 2018. Synthesis and application of hematite nanoparticles for acid mine drainage treatment. *Journal of Environmental Chemical Engineering*, *6*(2), pp.1865-1874.

[4]. Wu, C., Yin, P., Zhu, X., OuYang, C. and Xie, Y., 2006. Synthesis of hematite (α-Fe2O3) nanorods: diameter-size and shape effects on their applications in magnetism, lithium ion battery, and gas sensors. *The Journal of Physical Chemistry B*, *110*(36), pp.17806-17812.

[5]. Pallela, P.N.V.K., Ummey, S., Ruddaraju, L.K., Gadi, S., Cherukuri, C.S., Barla, S. and Pammi, S.V.N., 2019. Antibacterial efficacy of green synthesized α-Fe2O3 nanoparticles using Sida cordifolia plant extract. *Heliyon*, *5*(11).

[6]. Ahmmad, B., Leonard, K., Islam, M.S., Kurawaki, J., Muruganandham, M., Ohkubo, T. and Kuroda, Y., 2013. Green synthesis of mesoporous hematite (α-Fe2O3) nanoparticles and their photocatalytic activity. *Advanced Powder Technology*, *24*(1), pp.160-167.

[7]. Fu Y Y., Wang R M., Xu J., Chen J., Yan Y., Narlikar A V., and Zhang, H (2003), Synthesis of large arrays of aligned α-Fe_2O_3 nanowires. *Chemical Physics Letters*, *379*(3-4), 373-379.

[8]. Wang X., Chen X., Gao L., Zheng H., Ji M., Tang C., and Zhang Z (2004), Synthesis of β-FeOOH and α-Fe_2O_3 nanorods and electrochemical properties of β-FeOOH. *Journal of Materials Chemistry*, *14*(5), 905-907.

[9]. Bibi I., Nazar N., Ata S., Sultan M., Ali A., Abbas A., and Iqbal M (2019), Green synthesis of iron oxide nanoparticles using pomegranate seeds extract and photocatalytic activity evaluation for the degradation of textile dye. *Journal of Materials Research and Technology*, *8*(6), 6115-6124.

[10]. Xu J K., Zhang F F., Sun J J., Sheng J., Wang F., and Sun M (2014), Bio and nanomaterials based on Fe_3O_4. *Molecules*, *19*(12), 21506-21528.

[11]. Shankar S. S., Rai A., Ankamwar B., Singh A., Ahmad A., and Sastry M (2004), Biological synthesis of triangular gold nanoprisms. *Nature materials*, *3*(7), 482-488.

[12]. Chahar, D., Taneja, S., Bisht, S., Kesarwani, S., Thakur, P., Thakur, A., & Sharma, P. B. (2021). Photocatalytic activity of cobalt substituted zinc ferrite for the degradation of methylene blue dye under visible light irradiation. *Journal of Alloys and Compounds*, *851*, 156878.

[13]. Qasim, M., Asghar, K., Singh, B. R., Prathapani, S., Khan, W., Naqvi, A. H., & Das, D. (2015). Magnetically recyclable Ni0. 5Zn0. 5Fe2O4/Zn0. 95Ni0. 05O nano-photocatalyst: Structural, optical, magnetic and photocatalytic properties. *Spectrochimica Acta Part A: Molecular and Biomolecular Spectroscopy*, *137*, 1348-1356.

[14]. Casbeer, E., Sharma, V. K., & Li, X. Z. (2012). Synthesis and photocatalytic activity of ferrites under visible light: a review. *Separation and Purification Technology*, *87*, 1-14.

[15]. Ahmmad, B., Leonard, K., Islam, M.S., Kurawaki, J., Muruganandham, M., Ohkubo, T. and Kuroda, Y., 2013. Green synthesis of mesoporous hematite (α-Fe_2O_3) nanoparticles and their photocatalytic activity. *Advanced Powder Technology*, *24*(1), pp.160-167.

[16]. Rufus, A., Sreeju, N. and Philip, D., 2016. Synthesis of biogenic hematite (α-Fe_2O_3) nanoparticles for antibacterial and nanofluid applications. *RSC advances*, *6*(96), pp.94206-94217.

[17]. Yoonus, J., Resmi, R. and Beena, B., 2021. Evaluation of antibacterial and anticancer activity of green synthesized iron oxide (α-Fe_2O_3) nanoparticles. *Materials Today: Proceedings*, *46*, pp.2969-2974.

[18]. Sajid, M.M. and Alomayri, T., 2022. Synthesis of α-Fe_2O_3 rhombus nanoplates for photocatalytic investigation of cationic and anionic dyes and antibacterial aspect. *Journal of Taibah University for Science*, *16*(1), pp.1192-1201.

[19]. Rafieepour, A., Azari, M.R., Khodagholi, F., Jaktaji, J.P., Mehrabi, Y. and Peirovi, H., 2021. Interactive toxicity effect of combined exposure to hematite and amorphous silicon dioxide nanoparticles in human A549 cell line. *Toxicology and Industrial Health*, *37*(5), pp.289-302.

[20]. Grégoire, V., Levendag, P., Ang, K.K., Bernier, J., Braaksma, M., Budach, V., Chao, C., Coche, E., Cooper, J.S., Cosnard, G. and Eisbruch, A., 2003. CT-based delineation of lymph node levels and related CTVs in the node-negative neck: DAHANCA, EORTC, GORTEC, NCIC, RTOG consensus guidelines. *Radiotherapy and oncology*, *69*(3), pp.227-236.

[21]. Dawson, G., 2008. Early behavioral intervention, brain plasticity, and the prevention of autism spectrum disorder. *Development and psychopathology*, *20*(3), pp.775-803.

[22]. Xiong, P., Huang, X., Ye, N., Lu, Q., Zhang, G., Peng, S., Wang, H. and Liu, Y., 2022. Cytotoxicity of metal-based nanoparticles: from mechanisms and methods of evaluation to pathological manifestations. *Advanced Science*, *9*(16), p.2106049.

[23]. Machala, L., Tucek, J. and Zboril, R., 2011. Polymorphous transformations of nanometric iron (III) oxide: a review. *Chemistry of materials*, *23*(14), pp.3255-3272.

[24]. Wang, Z., Lee, Y.H., Wu, B., Horst, A., Kang, Y., Tang, Y.J. and Chen, D.R., 2010. Anti-microbial activities of aerosolized transition metal oxide nanoparticles. *Chemosphere*, *80*(5), pp.525-529.

[25]. Nimisha, O.K., Ramanarayanan, R., Pradeesh, K. and Mary, A.P., 2023, September. Synthesis of iron oxide nanoparticles using black tea extract. In *AIP Conference Proceedings* (Vol. 2800, No. 1). AIP Publishing.

[26]. Gottimukkala, K.S.V., Harika, R.P. and Zamare, D., 2017. Green synthesis of iron nanoparticles using green tea leaves extract. *J. Nanomed. Biother. Discov*, *7*(1), p.151.

[27]. Kamiloglu, S., Sari, G., Ozdal, T. and Capanoglu, E., 2020. Guidelines for cell viability assays. *Food Frontiers*, *1*(3), pp.332-349.

[28]. Hua, J. and Gengsheng, J., 2009. Hydrothermal synthesis and characterization of monodisperse α-Fe_2O_3 nanoparticles. *Materials Letters*, *63*(30), pp.2725-2727.

[29]. Bhattacharyya, D., Chaudhuri, S. and Pal, A.K., 1992. Bandgap and optical transitions in thin films from reflectance measurements. *Vacuum*, *43*(4), pp.313-316.

[30]. Narayanan, T.N., Sakthi Kumar, D., Yoshida, Y. and Anantharaman, M.R., 2008. Strain induced anomalous red shift in mesoscopic iron oxide prepared by a novel technique. *Bulletin of Materials Science*, *31*, pp.759-766.

[31]. Marshall, C.P., Dufresne, W.J. and Rufledt, C.J., 2020. Polarized Raman spectra of hematite and assignment of external modes. *Journal of Raman Spectroscopy*, *51*(9), pp.1522-1529.

[32]. De Faria, D.L., Venâncio Silva, S. and de Oliveira, M.T., 1997. Raman microspectroscopy of some iron oxides and oxyhydroxides. *Journal of Raman spectroscopy*, *28*(11), pp.873-878.

[33]. Porto, S.P.S. and Krishnan, R.S., 1967. Raman effect of corundum. *The Journal of Chemical Physics*, *47*(3), pp.1009-1012.

[34]. Onari, S., Arai, T. and Kudo, K., 1977. Infrared lattice vibrations and dielectric dispersion in αFe_2O $_3$. *Physical Review B*, *16*(4), p.1717.

[35]. Bhagavantam, S. and Venkatarayudu, T., 1939, March. Raman effect in relation to crystal structure. In *Proceedings of the Indian Academy of Sciences-Section A* (Vol. 9, No. 3, pp. 224-258). New Delhi: Springer India.

[36]. Rufus, A., Sreeju, N. and Philip, D., 2016. Synthesis of biogenic hematite (α-Fe 2 O 3) nanoparticles for antibacterial and nanofluid applications. *RSC advances*, *6*(96), pp.94206-94217.

[37]. Abdelrahman, E.A., Hegazey, R.M., Kotp, Y.H. and Alharbi, A., 2019. Facile synthesis of Fe2O3 nanoparticles from Egyptian insecticide cans for efficient photocatalytic degradation of methylene blue and crystal violet dyes. *Spectrochimica Acta Part A: Molecular and Biomolecular Spectroscopy*, *222*, p.117195.

[38]. Puri, L.B., Sharma, L.R. and Pathania, M.S., 2013. *Principles of physical chemistry*. Vishal Publishing Co.

Chapter 6

Hematene-TiO_2 heterostructures for energy applications

The discovery of graphene in 2004 commenced the comprehensive investigation of 2D materials. The exfoliation of 2D material from a Van der Waal material is quite easy, but the peeling of non-Van der Waals material is very difficult. This chapter talks about the peeling of 2D Hematene from synthesized Hematite and investigates its structural and optical properties. Hematene has been predicted as a good material for photocatalytic and spintronic applications and they have distinct magnetic, as well as electronic properties concerning their bulk counterparts. Additionally, hematene's visible light photoelectrochemical activity is facilitated by heterojunction with a TiO_2 nanostructure.

6.1 Introduction

The rapid growth of industrialization and urbanization causes the increasing need for energy. Energy scarcity is a great problem in our society, hence the evolution of inexhaustible energy technologies grabbed the society's interest [1-4]. Solar energy is one of the best options, especially in areas with ample sunshine [5-8]. One of the promising technologies for addressing the energy dilemma is photoelectrochemical water splitting [9-12]. Photoactive semiconductors are an alternative to solar photovoltaics which can produce chemical solar fuels and transform sunlight into a chemical form that can be distributed and stored. A TiO_2 photoanode that can split water into H_2 and O_2 when exposed to UV light was found in 1972 by Fujishima and Honda [13-15]. This discovery leads to the expeditious development of photoactive semiconductors for energy applications. The morphology, crystallinity, dimensionality and band gap of the material should influence the efficiency of the PEC process [16, 17]. A semiconductor's valence band will have holes in it as a result of electrons being excited into the conduction band under light illumination. Conduction band electrons diffuse to the cathode's surface, where they convert H^+ to H_2 [9]. In parallel, water is oxidized to O_2 by the photogenerated holes as they move closer to the anode's surface. Generally, three geometric parameters facilitate hole transfer to the electrode-electrolyte interface, thickness of the material space charge region and diffusion length. In the PEC system, the semiconductor electrolyte interface creates a junction, which is similar to the Schottky diode. The built-in electric field, due to charge distribution in a semiconductor and the semiconductor electrolyte interface causes the separation of photo-excited carriers. The concept of band bending is used for studying the photoexcitation process in detail. For an n-type semiconductor, the fermi level is located near to its conduction band minimum and higher than the electrochemical potential of the electrolyte. Most carriers will move from the semiconductor to the electrolyte when they come into touch with each other until the electrochemical potential and fermi level line up [18]. The band edge of a semiconductor is also shifted due to the change in carrier concentration [7]. The band bending that occurs in this scenario is depicted in **Figure 6.1.**

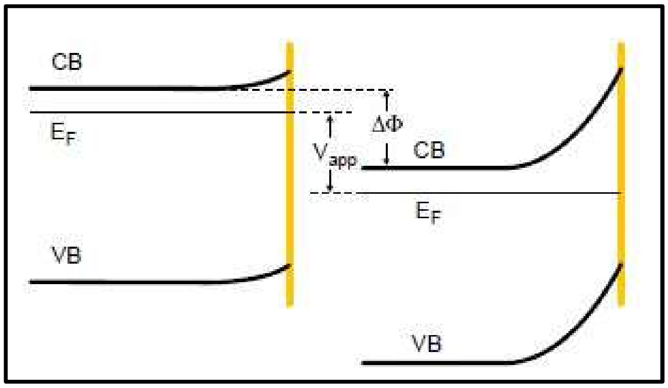

Figure 6.1 The band diagram of an n-type semiconductor with electrolyte before and after contact [19]

The positively charged area is created by the ionised donors remaining in the semiconductor, while the negatively charged areas focus on the electrolyte interface. Hence an electric field is formed at the interface. Which counterbalances the continuous flow of charges until a dynamic equilibrium is reached. When the light is incident on the semiconductor electrolyte interface, the electrons are stimulated from the valence band to the conduction band, as the majority carriers there is a little variation in the concentration of electrons. Hence the quasi-fermi level of electrons remains unchanged in comparison to the dark condition. But as the minority carrier, the concentration of holes increases significantly leading to a notable separation of its quasi-fermi level from that in the dark. This separation defines the magnitude of photovoltage. The important component in the PEC system is the photoanode. To obtain high efficiency the photoanode meets the following conditions: strong absorption capacity in the visible region, the band gap of the material in the range of 1.9 eV to 2.3 eV, proper band edge position to catalyze the reduction and oxidation of water, the material's conduction band level should be more negative than the H_2 production energy level and valence band should be more positive than the water oxidation potential, effective charge separation between electrons and holes in a semiconductor and the yield is abundant and cost-effective [20-23].

Iron oxides and their derivatives are unique due to their distinct magnetic electrical and optical properties. Hematite is the most thermodynamically stable form of iron oxide at ambient conditions. It is abundant, relatively inexpensive, highly sought after for environmental and energy applications and easily synthesized material [24]. Hematite is a small band gap semiconductor that exhibits a corundum structure belonging to D_{3d}^{6} space group with iron atoms octahedrally surrounded by six oxygen atoms [25, 26]. It is a well-known antiferromagnet with a Neel temperature of 961 K due to strong Fe^{3+}-Fe^{3+} interlayer superexchange [26]. Compared to other photo anodes with bigger bandgaps, haematite can harvest solar energy across a far wider spectrum, including both visible and ultraviolet light, making it a viable material for photo anodes. However, hematite's short excited state life span, which extinguishes photogenerated charges before they reach the surface, poor hole diffusion length, and unsatisfactory oxygen generation reaction kinetics pose the biggest challenges to the material's ability to convert solar energy into electricity [27, 28]. But when the hematite is made into a thinner 2D structure (hematene), the sufficient separation of charge carriers occurs due to the absorption of light on the surface. This is one of the efficient methods to enhance PEC water-splitting performance. The exfoliation of 2D material from a non-van der Waals material is very difficult [30]. Generally, bottom-up techniques are used to create 2D material due to strong bonds. Because of their tunable band gaps and dangling connections on the surface, ultrathin 2D non-layered materials may produce unique material properties [31–33]. However, due to the lack of generic synthesis methodologies, research on 2D non-layered materials is still in its very early stages. The three-dimensional chemical connections that connect the structural network of non-layered materials make it difficult to exfoliate and produce ultrathin nanoparticles. Traditional liquid phase exfoliation in appropriate organic solvents can even exfoliate covalent or ionic crystals, as shown by Balan et al [34]. This approach is a very new and significant development in this expanding field of study. Here, n-vdW exfoliation energetics play a significant role in determining whether or not n-vdW crystals may be exfoliated. Successful exfoliation of hematene would pave the way for new and exotic non-van der Waals 2D solids. In liquid exfoliation, it is based on the idea that a layered crystal must go through two steps to transform into a substantial amount of nanosheets in liquids: breaking the formation of linkages to detach the nanosheets from the crystal and stabilize the resulting nanosheets to prevent reaggregation. Pumping energy into the exfoliation liquid is important to separate the nanosheets from the parent crystal [35-37]. In the present work, we use bath sonication for the exfoliation of hematene. In bath sonication, ultrasonic waves propagating through the water cause pressure oscillations, which in turn cause microbubbles to develop and burst, producing strong shockwaves and regionally high shear rates [38, 39]. The rapid depletion of fossil fuels and uncontrolled global warming forced an urgent search for the development of photoactive materials for solar harvesting applications.

TiO_2 is a potential candidate for a photoelectrochemical process for water splitting [40]. It has many beneficial qualities like its abundance, low cost, photoactive nature, non-toxicity etc. But due to wide band gap limits its ability to absorb solar energy mostly to the UV region, which is about only 4% of the solar spectrum [41-43]. This is one of the major constraints of

TiO_2. Furthermore, the wide band gap makes the photogenerated electron-hole recombination more difficult, which reduces TiO_2's efficiency in converting solar energy. To overcome this difficulties researchers are actively exploring different strategies such as heterojunction creation, surface modification, band gap engineering etc [44]. The present chapter discusses the formation of hematene/TiO_2 heterostructure for water-splitting applications.

6.2 Characterization

The phase study was performed by Raman spectroscopy using a 540 nm laser excitation on the Horiba Labram HR Evolution Raman spectrometer. UV-visible spectrometer (Ocean Optics Maya 2000-Pro UV compact spectrometer) is employed for studying the absorption properties of the synthesized materials. FESEM images of the prepared samples were performed using JEOL JSM 6390. The photoelectron chemical measurements were performed in a standard three electrode setup at room temperature using the Bio-Logic potentiostat (model SP300). The hematene-TiO_2 heterojunction, Pt wire and Calomel electrode were used as the working, counter and reference electrode respectively. A He-Ne laser with 510 nm is used as a light source for illumination.

6.3 Experimental

6.3.1 Synthesis of Hematene

The synthesized hematite nanoparticles are used for the exfoliation of hematene. The preparation of hematite particles was discussed in chapter 5. In Hematite It is well known that crystals with specific atomic planes orientated in one direction typically have weaker bonding as compared to other directions. Hematite [001] has the highest broken bond density with a trigonal crystal structure. In addition to that, alternate anion and cation layers induce a dipole moment perpendicular to [001] and tend to be less stable. Thus, as we apply suitable ultrasonic energy, the hydrodynamic forces cleave the Hematite crystal along the [001] and [010] directions. Take 5 mg synthesized hematite particles and it was dispersed in 20 ml N, N dimethyl formamide (DMF). Then the suspensions were sonicated for 40 hours in a bath sonicator. The maximum temperature reached in this experiment was 50 °C. The resulting reddish-orange solution was then centrifuged at 5,000 rpm for 20 minutes to remove the un-exfoliated particles from the solution. Then the upper part of the supernatant solution was filtered using a Whatman filter paper to obtain a hematene sheet. A schematic representation of the exfoliation process is given in **Figure 6.2**. For haematite exfoliation, two different crystallographic planes are utilised. These two crystallographic planes' plane spacing and atomic arrangement are depicted, where the red spheres correspond to oxygen and the yellow spheres correspond to iron. The reddish-brown colour of hematene is due to its absorbance in the visible region.

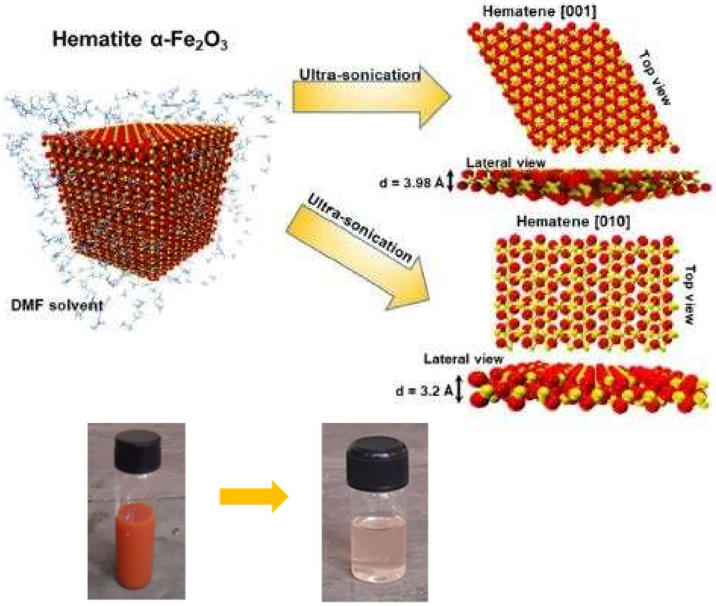

Hematite Hematene

Figure 6.2 Liquid phase exfoliation of Hematite to Hematene

6.3.2 Preparation of TiO_2 nano tubes

Electrochemical anodization is a relatively simple method for creating precisely engineered nanostructures. It is an electrolytic passivation process, where an oxide film can be grown on certain metals. Metals can develop a uniformly thick, thin, and dense barrier oxide when certain conditions are satisfied. The growth of the nanostructures was reported to be significantly influenced by variables like the electrolyte, temperature, applied voltage, and anodization period. The titanium foil was cleaned with acetone, isopropanol and de-ionized water for 10 minutes each and dried in air. Anodization of titanium foil was conducted using a two-electrode system with titanium foil as the working electrode and platinum (Pt) foil as the counter electrode is depicted in **Figure 6.3**. Both electrodes were kept at a distance of 2 cm and immersed in an electrolyte that contains 85 vol% ethylene glycol, 15 vol% of deionized water and dissolved 0.27 M NH_4F. The electrochemical process was carried out at 50 V for 45 minutes at room temperature. The titanium foil was taken out of the electrolyte after anodization, cleaned for three to five minutes with isopropanol to get rid of any debris that was on top of the nanotubes, and then left to air dry. Then the samples were annealed at 450 °C for 2 hours in a muffle furnace.

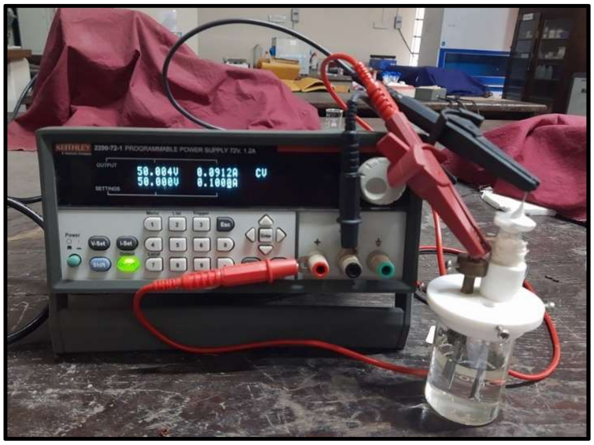

Figure 6.3 Experimental set up for anodization process

6.3.3 Formation of hematene/TiO_2 heterojunction

The Hematene/TiO_2 heterostructured photoanode is fabricated by hematene are coated on nanotube films by drop casting until its colour turned into brick-red. The hematene-loaded nanotube samples are heated at 200 °C for 25 minutes to remove the surface adsorbed organic compounds.

6.4 Results and Discussions

6.4.1 Raman spectra

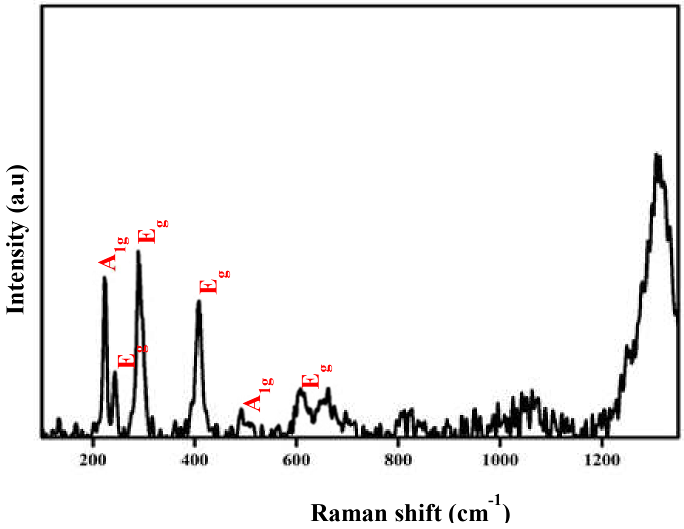

Figure 6.4 Raman spectra of Hematene

The formation of hematene is confirmed by Raman studies. Two exterior modes ($2E_g$) resulting from rotations and translations of these units and five internal vibrational modes ($2A_{1g}$+ $3E_g$) involving atomic motions within a single FeO_6 octahedral unit make up the bulk haematite Raman spectrum. The energies of these seven modes, which originate from the transverse optical branch, are roughly placed at two A_{1g} modes at 225 and 498 cm^{-1} and fiveE_g modes at 247, 293, 299, 412, and 613 cm^{-1}, respectively [50]. The intense peak at around 1300 cm^{-1} is arises due to two magnon scattering [51, 52]. Each of the prominent peaks of the hematene corresponds to a reported peak in the hematite spectrum, this validates the material's phase purity after exfoliation [53]. The successful exfoliation of hematene was determined by taking the relative intensity ratio $\frac{I_{Ag}}{I_{Eg}}$, for hematite the ratio was found to be greater than one and for hematene the ratio is less than one. After exfoliation some defects may occur in the exfoliated material, which may be the reason for a change in the ratio. In the present work the ratio was found to be 1.21 for hematite and 0.89 for hematene. The confirmation of hematene production is provided by the quantum confinement effects that cause the shift in peak positions between the exfoliated samle and the bulk material. When comparing the peak positions of exfoliated and bulk hematite, it is evident that the E_g modes undergo a blue shift while the A_{1g} modes undergo a redshift. The phonon momentum selection criteria q~ 0 fails, resulting in the observed redshift of A_{1g}[42]. **Table 6.1** provides an overview of each Raman mode's shift and intensity variation. The raman spectra of hematene is depicted in **Figure 6.4**.

Mode	Bulk		Exfoliated	
	Raman shift (cm^{-1})	Intensity (norm)	Raman shift (cm^{-1})	Intensity (norm)
A_{1g}	224.68	1	222.65	0.89
E_g	241.31	0.20	242.91	0.37
E_g	287.62	0.820	289.31	1
E_g	407.42	0.39	408.50	0.75
A_{1g}	495.60	0.11	491.42	0.19
E_g	607.08	0.18	608.74	0.27

Table 6.1 An overview of each Raman mode's shift and intensity variation

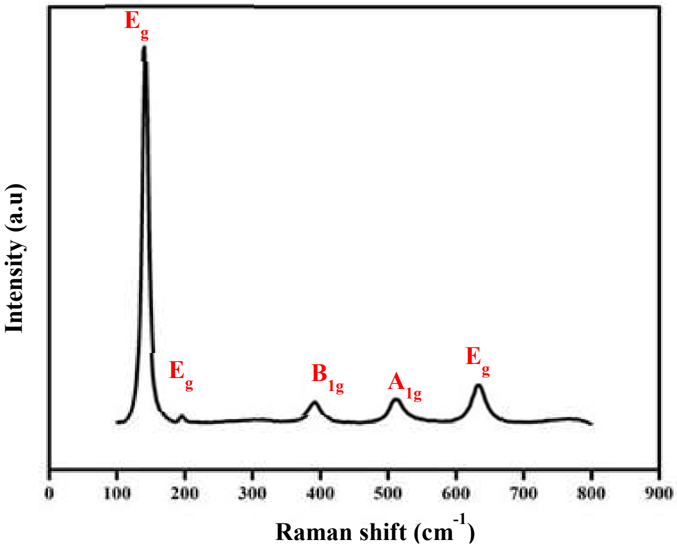

Figure 6.5 Raman spectra of anatase TiO_2

The room temperature Raman spectrum of anodized TiO_2 nanotube is depicted in **Figure 6.5**. Observing the spectra, we can see that it consists of five peaks, which indicates the anatase phase of TiO_2. Anatase is a member of the space group D_{4h}^{19} and is tetragonal. There are two TiO_2 chemical units in the primitive unit cell. We are able to determine 15 modes of vibration [54] based on the group theory analysis:

$$\mathbf{1A_{1g} + 1A_{2u} + 2B_{1g} + 1B_{1u} + 3E_g + 2E_u}$$

The Raman modes are $\boldsymbol{A_{1g}}$, $\boldsymbol{B_{1g}}$ **and** $\boldsymbol{E_g}$ while the infrared modes are $\boldsymbol{A_{2u}}$ **and** $\boldsymbol{E_u}$. The $\boldsymbol{B_{1u}}$ mode is not active in either the Raman or infrared spectra. The primitive cell of anatase phase of TiO_2 gives six active Raman mode of vibrations, three $\boldsymbol{E_g}$ modes approximately at 143, 197, 635 cm^{-1}. Similarly, two $\boldsymbol{B_{1g}}$ modes at 394 and 513 cm^{-1} and one $\boldsymbol{A_{1g}}$ mode at 519 cm^{-1} respectively. But $\boldsymbol{A_{1g}}$ mode occurs at low temperature around 73 K, the present study reports the spectrum at room temperature hence it is not observed in the given spectrum [52].

6.4.2 Optical properties

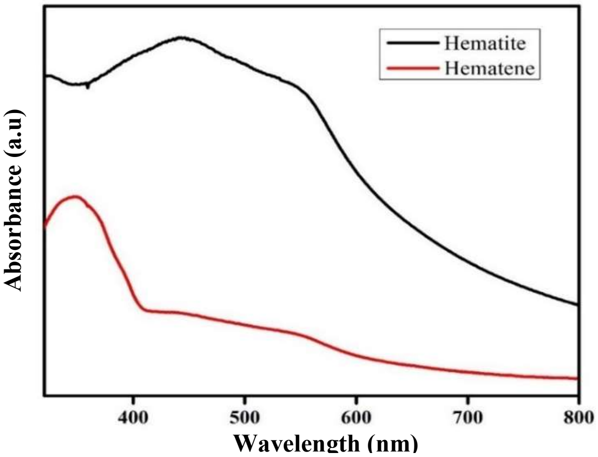

Figure 6.6a Absorption spectra

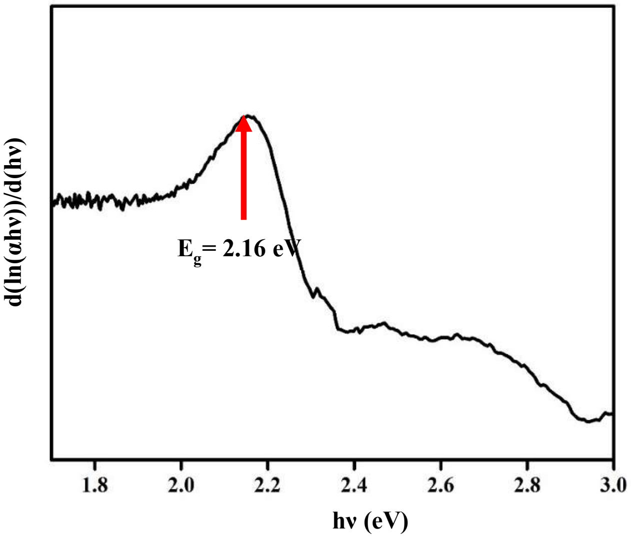

Figure 6.6b Derivative curve

The absorption spectra of hematite and hematene is depicted in **Figure 6.6a**. The exfoliated sample shows a blueshifted absorption edge and a restricted spectrum when co mpared to the bulk sample, which indicating a larger bandgap. Compared to pure hematite, which has a bandgap of 1.95 eV, hematene exhibits a larger bandgap of 2.15 eV. Because of the smaller size of the exfoliated sample, quantum confinement phenomenon can be responsible for the observed blue shift. Much of the absorption in the region below 400 nm can be attributed to ligand field (d-d) transition and ligand to metal charge transfer [55, 56]. Hematene's absorption spectra resemble those of haematite, however because of quantum con finement, the absorption maxima is blue shifted, suggesting that hematene is made up of nano structures with reduced thickness and lateral dimensions. The determination of band gap using derivative curve (**Figure 6.6b**) is explained in the previous chapter in detail. This band gap was determined to be 2.16 eV. After exfoliation, the band gap is increased.

6.4.3 Morphological analysis using FESEM

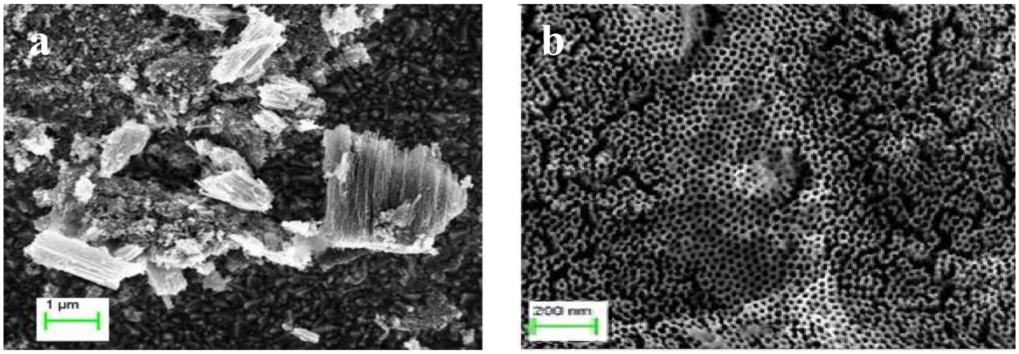

Figure 6.7 (a,b) FESEM image of Hematene

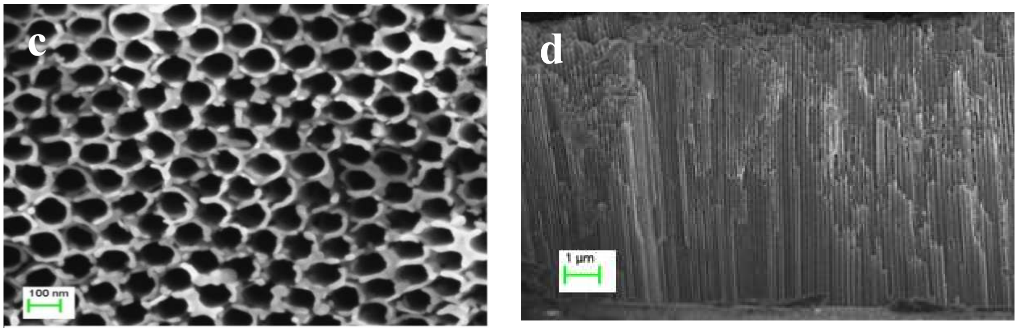

Figure 6.7 (c,d) FESEM image of TiO_2 nanotube

We have studied the morphology of Hematene and TiO_2 using field emission scanning electron microscopy (FESEM) (Top view and cross sectional view). The successful exfoliation process is indicated by a few large and numerous nano-sized flakes,depicted in **Figure 6.7 (a)**. The absence of creases in the nanoflakes is another intriguing finding. The lack of creases in the as-obtained sheets is especially noteworthy because wrinkles can seriously impair an electrical system's ability to transfer electrons smoothly. The nanotubes were found in well-aligned and homogenous order. The top of the tubes is clean and open. The side view of the titanium nanotube is also shown in **Figure 6.7 (d)** which shows the growth of uniformly aligned and densely packed TiO_2 nanotubes. The diameters of these nanotubes are about 92±7 nm with a length of 8±1 µm.

6.4.4 Photoelectrochemical measurement

Figure 6.8 Experimental set up for the Photoelectrochemical process

Figure 6.8 shows Experimental set up for the Photoelectrochemical process. A schematic illustration of the photoelectrochemical process with different mechanism is depicted in **Figure 6.9**. The photoelectrochemical process is an energy-demanding process, which converts water into hydrogen and oxygen in a chemical form that can be stored and distributed. This reaction requires an external source of energy for a substantial positive change in Gibbs free energy. This process is comparable to natural photosynthesis, in both cases the conversion of photon energy into chemical energy takes place. The complex electron transfer process and the band structure of the semiconductor determine the efficiency of PEC water splitting. To utilize the visible energy spectrum, the semiconductor must possess a specific band gap within the range of 1.23-3eV, to maximize the generation of H_2. Along with the suitable band gap, the precise band positioning of CB and VB is necessary to achieve equilibrium and guarantee the energy needs for water reduction and oxidation potential must be met. In contrast to the water reduction potential, the CB minima and VB maxima of semiconductors are expected to be more positive and negative respectively [45]. A key factor is the minimal band gap of approximately 1.23 eV required for effectively splitting water into H_2 and O_2 [46].

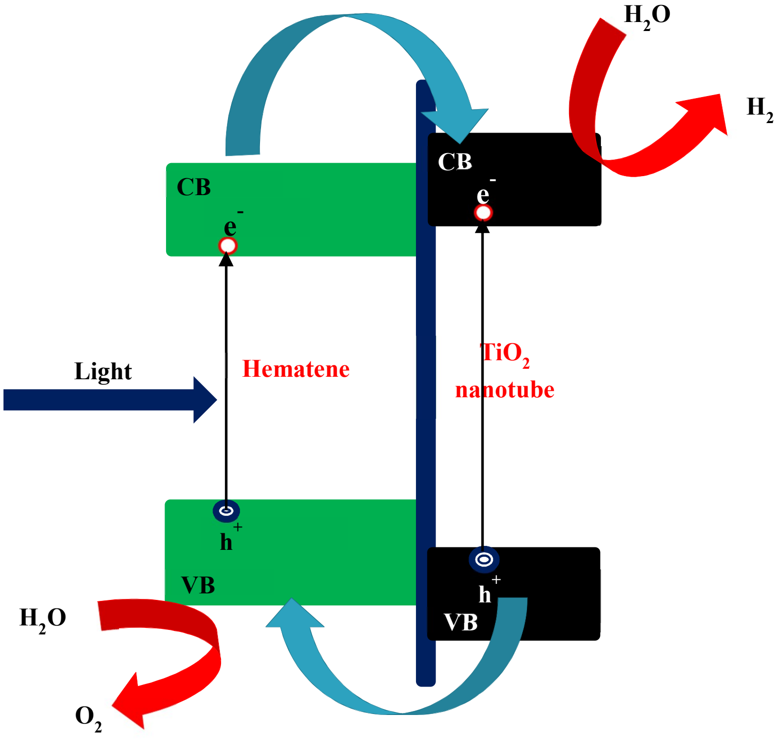

Figure 6.9 Schematic representation of the mechanism of the photoelectrochemical process

Pristine 2D material is a promising material for solar to chemical energy conversion. The fascinating property arises due to their exposed active surface, thickness-dependent physical and chemical properties, distinct electronic density of state spectrum etc [47,48]. Along with the positive advantages these materials have certain drawbacks that impede their application. Furthermore, the instability of certain semiconductors among 2D materials under experimental conditions, including exposure to an electrolyte solution and light illumination, poses a challenge due to their propensity for oxidation. Addressing these limitations is crucial to fully harness the potential of pristine 2D materials in the realm of photocatalysis. A semiconductor with a photoanode isolated from the cathode induces both the oxygen evolution reaction (OER) and the hydrogen evolution reaction (HER) at the same time when exposed to light.

An electron undergoes a transition from the valence band to the conduction band when the energy of the incident light is larger than E_g, creating a hole in the valence band with a positive charge. By providing a bias voltage, the holes and electrons of the photogenerated charge carrier on the photoanode are effectively separated. A small external potential is needed to encourage photochemical reactions since the conduction bands of the majority of metal oxide materials are less negative than the H_2 evolution potential for a PEC cell [45, 49]. The hole that is created, migrates to the surface of the photoactive material and then to an electrolyte solution, where it starts the water oxidation reaction that yields oxygen. In the electrolyte solution, the remaining electrons in the conduction band is transferred, aiding in the reduction of protons to generate H_2. The hematene-TiO_2 heterostructure the photogenerated electrons of hematene will be excited from VB to its CB at different energy levels under visible light irradiation. These energy levels comprise both high-energy and low-energy regions. Subsequently, electrons at the low-energy level promptly relax to the valence band of hematene, engaging in recombination with holes. On the other hand, high-energy electrons undergo thermodynamic transfer to the conduction band of TiO_2 conduction band, which extend the electron life times, reduces recombination and enlarge the separation between visible-excited charges. The holes generated in the TiO_2 nanotube are transferred to VB of hematene for oxidation of water. The transferred electrons from the hematene travel through the external circuit and reach to the counter electrode [34].

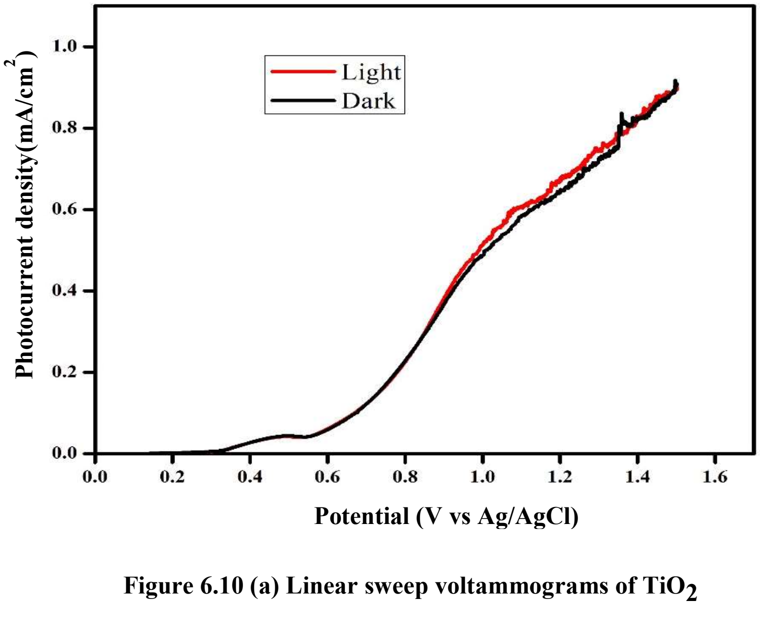

Figure 6.10 (a) Linear sweep voltammograms of TiO_2

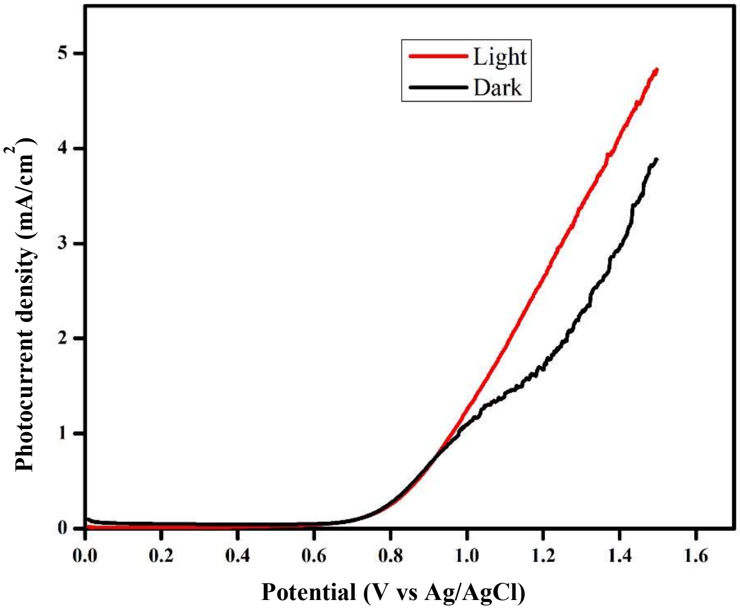

Figure 6.10 (b) Linear sweep voltammograms of Hematene loaded TiO_2

With the use of linear sweep voltammetry (LSV), one can assess a system's PEC performance by measuring its current density and hydrogen production rate. The LSV measurement of TiO_2 and hematene-loaded TiO_2 is shown in **Figure 6.10 (a, b)**. The hematene-loaded TiO_2 produces higher photocurrent density than pure TiO_2, producing a value of around 1.8 mA/cm^2 and 0.6 mA/cm^2 respectively. The magnitude of the photocurrent density indicates the number of generated electrons that will be involved in the H_2 production. The hematite, with a band gap ranging from 1.8 to 2.2 eV, exhibits promise for hydrogen generation through water photoelectrolysis. However, its utility is hindered by poor carrier transport properties, primarily attributable to intrinsic and surface defects acting as midgap trap centers. This limitation restricts the lifetime of photo-generated carriers to mere picoseconds, with a hole diffusion length typically below ~4 nm and hindered electron transport due to low mobility.

Another problem with sluggish water oxidation kinetics is that spontaneous water splitting is not expected because of the water reduction potential's greater positive flat band potential (in comparison to the normal hydrogen electrode, or NHE). To address these issues, hematene is introduced as a potential solution, leveraging its 2D geometry to enable efficient separation of electrons and holes at the surface, reducing recombination. The PEC methods are highly promising. In comparison to hematene, TiO_2 nanotube has a greater work function and the fermi level is located higher in hematene than TiO_2. But when a fermi level equilibrium is reached between hematene and TiO_2 electrons are transferred from hematene to TiO_2 across the interface. The holes in VB are left behind when electrons are stimulated from the VB to the conduction band under light irradiation. The internal, built-in electric field at the interface between hematene and TiO_2 facilitates the migration of photogenerated electrons from hematene's CB to TiO_2. The transmission of excited electrons and holes is facilitated by this kind of band alignment. Furthermore, positive potential forms at the surface of hematene and negative potential forms at the surface of TiO_2 when a photoanode remains in contact with the electrolyte until equilibrium states are reached. Hence an electric field is built at the electrode-electrolyte interface, which helps to increase the lifetime of carriers and separation between the photogenerated holes and electrons more effectively. The TiO_2 nanostructure with its vertically aligned structure also aids in electron migration, and the abundance of active sites in hematene expands the reaction area for PEC reaction. Photogenerated current density is a common parameter used to evaluate the PEC performance. The incorporation of hematene into TiO_2 (titanium dioxide) has been pursued to enhance the separation of charges in photoactive materials. At the core of this improvement is the critical role played by the interface between TiO_2 and hematene, which provides alternate positions for holes and electrons, thereby facilitating their separation. The movement of holes takes place from TiO_2's valence band (VB) to hematene and electrons from hematene's conduction band (CB) to TiO_2 when exposed to light radiation. This results in the effective separation of electron-hole pairs, thereby extending the lifetime of charges by suppressing recombination. The incident photon-to-electron conversion efficiency (IPCE) is given by [7]

$$\text{IPCE}=\left(\frac{\frac{1240}{\lambda}X(I_{light}-I_{dark})}{P}X100\%\right) \tag{6.1}$$

Where λ and P are the wavelength and power of light used, I_{light} and I_{dark} are the photocurrent density in the light and dark condition. The IPCE of the Hematene-TiO_2 heterostructure was significantly improved compared with the TiO_2 nanotube [34], the values are found to be 2.6% and 0.04% respectively at 510 nm.

6.5 Conclusions

A Stable wrinkle free hematene 2D structure has been successfully exfoliated from green synthesized non-layered hematite by the method of liquid exfoliation. TiO_2 nanotubes are fabricated using an optimised anodization process. The grown nanotubes are found to be thickly populated with uniform diameter and open on top as seen by FESEM images. The Raman spectra confirms the formation of phase pure titanium dioxide in the anatase structure. The photoelectrochemical analysis is carried out using Linear sweep voltammetry. The ability of hematene sheets to participate in the PEC water-splitting process is demonstrated through the formation of a heterojunction with TiO_2 nanotube array electrodes. This unique junction enhances the overall efficiency of the process. The band gap position must be consistent with the oxidation and reduction potential of water for successful water splitting through a semiconductor. The most suitable material for PEC is TiO_2, but due to the wide band gap, it is not suitable for visible light absorption. Significantly, hematene sheets exhibit the capability to sensitize TiO_2 nanotubes, allowing them to capture the visible portion of the solar spectrum ranging from 400 nm to 700 nm. This is particularly noteworthy as TiO_2 nanotubes typically show PEC activity in the UV region, specifically below 400 nm. Hematene is so thin that the charge carriers undergo recombination and hence reduces the current. Combining these two materials to form an interface can improve the performance by complementing the limitations of each material. The interface plays a critical role by providing alternate positions for charge carriers and enhancing their separation, thus improving the PEC performance. Through the extension of light absorption into the visible spectrum, the heterojunction plays a crucial role in optimising solar energy utilisation for the photoelectron chemical water splitting process. The PEC performance can be studied with varied thickness of the 2D layers and with added dopants that can catalyse the photoelectrochemical reaction for further enhancement.

References

[1]. Luan, P., Xie, M., Liu, D., Fu, X. and Jing, L., 2014. Effective charge separation in the rutile TiO_2 nanorod-coupled α-Fe2O3 with exceptionally high visible activities. *Scientific reports*, 4(1), p.6180.

[2]. Ling, Y., 2014. *Nanostructured Hematite for Photoelectrochemical Water Splitting* (Doctoral dissertation, UC Santa Cruz).

[4]. Jakhar, M., Singh, J., Kumar, A. and Pandey, R., 2020. First-principles study of the hexagonal T-phase PdSe2 monolayer and its application in solar cells. *The Journal of Physical Chemistry C*, 124(49), pp.26565-26571.

[5]. Qu, Y. and Duan, X., 2013. Progress, challenge and perspective of heterogeneous photocatalysts. *Chemical Society Reviews*, 42(7), pp.2568-2580.

[6]. Jakhar, M., Kumar, A., Ahluwalia, P.K., Tankeshwar, K. and Pandey, R., 2022. Engineering 2D materials for photocatalytic water-splitting from a theoretical perspective. *Materials*, 15(6), p.2221.

[7]. Ma, P. and Wang, D., 2018. The principle of photoelectrochemical water splitting. In *Nanomaterials for Energy Conversion and Storage* (pp. 1-61).

[8]. Nunes, B.N., Paula, L.F., Costa, I.A., Machado, A.E.H., Paterno, L.G. and Patrocinio, A.O.T., 2017. Layer-by-layer assembled photocatalysts for environmental remediation and solar energy conversion. *Journal of Photochemistry and Photobiology C: Photochemistry Reviews*, 32, pp.1-20.

[9]. Chang, J.H., Kumar, M. and Nayak, A.K., 2021. *Nanostructured materials for photoelectrochemical water splitting*. IOP Publishing.

[10]. Chen, Z., Jaramillo, T.F., Deutsch, T.G., Kleiman-Shwarsctein, A., Forman, A.J., Gaillard, N., Garland, R., Takanabe, K., Heske, C., Sunkara, M. and McFarland, E.W., 2010. Accelerating materials development for photoelectrochemical hydrogen production: Standards for methods, definitions, and reporting protocols. *Journal of Materials Research*, 25(1), pp.3-16.

[11]. Ozer, L.Y., Garlisi, C., Oladipo, H., Pagliaro, M., Sharief, S.A., Yusuf, A., Almheiri, S. and Palmisano, G., 2017. Inorganic semiconductors-graphene composites in photo (electro) catalysis: Synthetic strategies, interaction mechanisms and applications. *Journal of Photochemistry and Photobiology C: Photochemistry Reviews*, 33, pp.132-164.

[12]. White, J.L., Baruch, M.F., Pander III, J.E., Hu, Y., Fortmeyer, I.C., Park, J.E., Zhang, T., Liao, K., Gu, J., Yan, Y. and Shaw, T.W., 2015. Light-driven heterogeneous reduction of carbon dioxide: photocatalysts and photoelectrodes. *Chemical reviews*, 115(23), pp.12888-12935.

[13]. Fujishima, A. and Honda, K., 1972. Electrochemical photolysis of water at a semiconductor electrode. *nature*, 238(5358), pp.37-38.

[14]. Wu, H., Tan, H.L., Toe, C.Y., Scott, J., Wang, L., Amal, R. and Ng, Y.H., 2020. Photocatalytic and photoelectrochemical systems: similarities and differences. *Advanced Materials*, 32(18), p.1904717.

[15]. Phuan, Y.W., Ong, W.J., Chong, M.N. and Ocon, J.D., 2017. Prospects of electrochemically synthesized hematite photoanodes for photoelectrochemical water splitting: A review. *Journal of Photochemistry and Photobiology C: Photochemistry Reviews*, 33, pp.54-82.

[16]. Jimmy, C., 2006. Synthesis of hierarchical nanoporous F-doped TiO_2 spheres with visible light photocatalytic activity. *Chemical Communications*, (10), pp.1115-1117.

[17]. Grimes, C.A., 2007. Synthesis and application of highly ordered arrays of TiO_2 nanotubes. *Journal of Materials Chemistry*, 17(15), pp.1451-1457.

[18]. Park, S.Y., 2015. Photoelectrochemical water splitting: optimizing interfaces and light absorption.

[19]. Thorne, J.E., Li, S., Du, C., Qin, G. and Wang, D., 2015. Energetics at the surface of photoelectrodes and its influence on the photoelectrochemical properties. *The journal of physical chemistry letters*, 6(20), pp.4083-4088.

[20]. van de Krol, R., Liang, Y. and Schoonman, J., 2008. Solar hydrogen production with nanostructured metal oxides. *Journal of Materials Chemistry*, 18(20), pp.2311-2320.

[21]. Sivula, K., Le Formal, F. and Grätzel, M., 2011. Solar water splitting: progress using hematite (α-Fe_2O_3) photoelectrodes. *ChemSusChem*, 4(4), pp.432-449.

[22]. Misra, M. and Raja, K.S., 2010. Ordered titanium dioxide nanotubular arrays as photoanodes for hydrogen generation. *On Solar Hydrogen & Nanotechnology*, pp.265-290.

[23]. Ni, M., Leung, M.K., Leung, D.Y. and Sumathy, K., 2007. A review and recent developments in photocatalytic water-splitting using TiO_2 for hydrogen production. *Renewable and Sustainable Energy Reviews*, 11(3), pp.401-425.

[24]. Tamirat, A.G., Rick, J., Dubale, A.A., Su, W.N. and Hwang, B.J., 2016. Using hematite for photoelectrochemical water splitting: a review of current progress and challenges. *Nanoscale horizons*, 1(4), pp.243-267.

[25]. Hill, A.H., Jiao, F., Bruce, P.G., Harrison, A., Kockelmann, W. and Ritter, C., 2008. Neutron diffraction study of mesoporous and bulk hematite, α-Fe_2O_3. *Chemistry of Materials*, 20(15), pp.4891-4899.

[26]. Thejas Prasannakumar, A., U, R.F., Philip, R. and J Varma, S., 2022. Hematene Nanoflakes: A Non-van der Waals Material with Superior Nonlinear Optical Properties. ACS Applied Optical Materials, 1(3), pp.660-668.

[27]. Morin, F.J., 1950. Magnetic susceptibility of α Fe_2O_3 and α Fe_2O_3 with added titanium. *Physical Review*, 78(6), p.819.

[28]. Benjamin, K., Sixto, G., Francisco, F.S., Thomas, H. and Juan, B., 2012. Water Oxidation at Hematite Photoelectrodes: The Role of Surface States.

[29]. Franking, R., Li, L., Lukowski, M.A., Meng, F., Tan, Y., Hamers, R.J. and Jin, S., 2013. Facile post-growth doping of nanostructured hematite photoanodes for enhanced photoelectrochemical water oxidation. *Energy & Environmental Science*, 6(2), pp.500-512.

[30]. Balan, A.P., Puthirath, A.B., Roy, S., Costin, G., Oliveira, E.F., Saadi, M.A.S.R., Sreepal, V., Friedrich, R., Serles, P., Biswas, A. and Iyengar, S.A., 2022. Non-van der Waals quasi-2D materials; recent advances in synthesis, emergent properties and applications. *Materials Today*, 58, pp.164-200.

[31]. Wang, F., Wang, Z., Shifa, T.A., Wen, Y., Wang, F., Zhan, X., Wang, Q., Xu, K., Huang, Y., Yin, L. and Jiang, C., 2017. Two-dimensional non-layered materials: synthesis, properties and applications. *Advanced Functional Materials*, 27(19), p.1603254.

[32]. Zhou, N., Yang, R. and Zhai, T., 2019. Two-dimensional non-layered materials. *Materials Today Nano*, 8, p.100051.

[33]. Dou, Y., Zhang, L., Xu, X., Sun, Z., Liao, T. and Dou, S.X., 2017. Atomically thin non-layered nanomaterials for energy storage and conversion. *Chemical Society Reviews*, 46(23), pp.7338-7373.

[34]. Aravind, P.B., 2019. *Exfoliation of Non-van der Waals Materials and Investigations on the Magnetic Bistability of 2D Nanostructures on Curved Surfaces* (Doctoral dissertation, Cochin University of Science and Technology).

[35]. Kaur, H. and Coleman, J.N., 2022. Liquid-Phase Exfoliation of Nonlayered Non-Van-Der-Waals Crystals into Nanoplatelets. *Advanced Materials*, 34(35), p.2202164.

[36]. Huo, C., Yan, Z., Song, X. and Zeng, H., 2015. 2D materials via liquid exfoliation: a review on fabrication and applications. *Science bulletin*, 60(23), pp.1994-2008.

[37]. Hernandez, Y., Nicolosi, V., Lotya, M., Blighe, F.M., Sun, Z.Y., De, S., McGovern, I.T., Holland, B. and Byrne, M., 2008. YK Gun ko, JJ Boland, P. *Niraj, G. Duesberg, S. Krishnamurthy, R. Goodhue, J. Hutchison, V. Scardaci, AC Ferrari, JN Coleman, Nat. Nanotechnol*, *3*, p.563.

[38]. Backes, C., Higgins, T.M., Kelly, A., Boland, C., Harvey, A., Hanlon, D. and Coleman, J.N., 2017. Guidelines for exfoliation, characterization and processing of layered materials produced by liquid exfoliation. *Chemistry of materials*, 29(1), pp.243-255.

[39]. Flint, E.B. and Suslick, K.S., 1991. The temperature of cavitation. *Science*, 253(5026), pp.1397-1399.

[40]. Phuan, Y.W., Ong, W.J., Chong, M.N. and Ocon, J.D., 2017. Prospects of electrochemically synthesized hematite photoanodes for photoelectrochemical water splitting: A review. *Journal of Photochemistry and Photobiology C: Photochemistry Reviews*, 33, pp.54-82.

[41]. MINGGU, J. and KASSIM, M.B., 2022. Hydrogen Production from Water Splitting using TiO. Sains Malaysiana, 51(10), pp.3251-3259.

[42]. Puthirath Balan, A., Radhakrishnan, S., Woellner, C.F., Sinha, S.K., Deng, L., Reyes, C.D.L., Rao, B.M., Paulose, M., Neupane, R., Apte, A. and Kochat, V., 2018. Exfoliation of a non-van der Waals material from iron ore hematite. *Nature nanotechnology*, 13(7), pp.602-609.

[43]. Chen, X. and Mao, S.S., 2007. Titanium dioxide nanomaterials: synthesis, properties, modifications, and applications. *Chemical reviews*, 107(7), pp.2891-2959.

[44]. Krishnan, A. and Kannan, P., 2019. A Non-Van der Waals two dimensional material from microwave synthesized Cu2ZnSnS4 nanocrystal agglomerates. *Materials Research Express*, 6(11), p.1150a3.

[45]. Li, Y. and Zhang, J.Z., 2010. Hydrogen generation from photoelectrochemical water splitting based on nanomaterials. *Laser & Photonics Reviews*, 4(4), pp.517-528.

[46]. Miller, E.L., 2010. Solar hydrogen production by photoelectrochemical water splitting: the promise and challenge. *On Solar Hydrogen & Nanotechnology*, pp.1-35.

[47]. Tan, C. and Zhang, H., 2015. Wet-chemical synthesis and applications of non-layer structured two-dimensional nanomaterials. *Nature communications*, 6(1), p.7873.

[48]. Ling, T., Wang, J.J., Zhang, H., Song, S.T., Zhou, Y.Z., Zhao, J. and Du, X.W., 2015. Freestanding ultrathin metallic nanosheets: Materials, synthesis, and applications. *Advanced Materials*, 27(36), pp.5396-5402.

[49]. Bessegato, G.G., Guaraldo, T.T., de Brito, J.F., Brugnera, M.F. and Zanoni, M.V.B., Achievements and trends in photoelectrocatalysis: from environmental to energy applications, *Electrocatalysis* 6 (2015) 415–441.

[50]. Chernyshova, I.V., Hochella Jr, M.F. and Madden, A.S., 2007. Size-dependent structural transformations of hematite nanoparticles. 1. Phase transition. *Physical Chemistry Chemical Physics*, 9(14), pp.1736-1750.

[51]. McCarty, K.F., 1988. Inelastic light scattering in α-Fe2O3: Phonon vs magnon scattering. *Solid state communications*, 68(8), pp.799-802.

[52]. De Faria, D.L., Venâncio Silva, S. and de Oliveira, M.T., 1997. Raman microspectroscopy of some iron oxides and oxyhydroxides. *Journal of Raman spectroscopy*, 28(11), pp.873-878.

[53]. Koutsioukis, A., Florakis, G., Samartzis, N., Yannopoulos, S.N., Stavrou, M., Theodoropoulou, D., Chazapis, N., Couris, S., Kolokithas-Ntoukas, A., Asimakopoulos, G. and Gournis, D.P., 2023. Green synthesis of ultrathin 2D nanoplatelets, hematene and magnetene, from mineral ores in water, with strong optical limiting performance. *Journal of Materials Chemistry C*, 11(9), pp.3244-3251.

[54]. Narayanan, P.S., 1950, October. Raman spectrum of rutile (TiO 2). In *Proceedings of the Indian Academy of Sciences-Section A* (Vol. 32, pp. 279-283). Springer India.

[55]. Wheeler, D.A., Wang, G., Ling, Y., Li, Y. and Zhang, J.Z., 2012. Nanostructured hematite: synthesis, characterization, charge carrier dynamics, and photoelectrochemical properties. *Energy & Environmental Science*, 5(5), pp.6682-6702.

[56]. Thejas Prasannakumar, A., U, R.F., Philip, R. and J Varma, S., 2022. Hematene Nanoflakes: A Non-van der Waals Material with Superior Nonlinear Optical Properties. *ACS Applied Optical Materials*, 1(3), pp.660-668.

Chapter 7

Fundamental study of α-Fe_2O_3 using DFT

Over the past thirty years, enormous volumes of theoretical and experimental data have been produced in several fields of study. The success of density functional theory (DFT) and the rapid advancement of computational capabilities are primarily responsible for the quantity of data in the field of computational material research. Theoretical prediction of important properties such as band gap and density of states of hematite nanoparticles using Density functional theory is discussed in this chapter.

7.1 Introduction

A computer quantum mechanical modelling technique called density functional theory is used to calculate many different properties, including structural, magnetic, mechanical, optical, and so on. Based on the Hohenberg-Kohn theorem, it is categorised as an ab initio approach. The ground state charge density of a many-body system can determine all of the properties of the electrons in it, according to the 1964 Hohenberg-Kohn argument, which states that the electron density, a variable that is only dependent on three spatial variables, theoretically contains all information about the ground state properties of a system [1-3]. The theory comprises two parts [1]:

Theorem 1: The ground state energy of electrons in a system is a unique functional of the ground state density. There is a unique one-to-one relation between the external potential $V_{ext}(r)$ and the electron density $\rho(r)$

$$\boldsymbol{E} = \boldsymbol{E}\,[\boldsymbol{\rho}(\boldsymbol{r})] \tag{7.1}$$

Theorem 2: A universal functional for the energy $\boldsymbol{E}\,[\boldsymbol{\rho}(\boldsymbol{r})]$ can be defined in terms of the density. The exact ground state is the global minimum value of this functional

$$\boldsymbol{E}[\boldsymbol{\rho}(\boldsymbol{r})] > \boldsymbol{E_0}[\boldsymbol{\rho_0}(\boldsymbol{r})] \tag{7.2}$$

Combining these two theorems the energy $E[\rho(r)]$ can be expressed as

$$\boldsymbol{E}[\boldsymbol{\rho}(\boldsymbol{r})]=\int \boldsymbol{V_{ext}}(\boldsymbol{r})\,\boldsymbol{\rho}(\boldsymbol{r})\boldsymbol{dr} + \boldsymbol{F}[\boldsymbol{\rho}(\boldsymbol{r})] \tag{7.3}$$

There is nothing that the Hohenberg-Kohn theorems tell us about building a functional. Kohn and Sham (1965) presented a self-consistent set of equations that included exchange and correlation effects for determining the ground-state density ρ, using the one-electron Schrodinger equation. The problem can be solved using just the universal functional F[ρ(r)] according to the equation above; but unfortunately, an explicit expression for F[ρ(r)] is not known. This problem can be overcome by Kohn Sham's proposal. The universal functional F[ρ(r)], was separated into different forms, by claiming that the density of the hypothetical system of interacting electrons is equal to that of the actual system of interacting electrons.

$$F[\rho(r)] = T_0 + V_H + V_{xc} \tag{7.4}$$

Where T_0, V_H, V_{xc} represent the kinetic energy of the non-interacting electron gas, Hartee potential and exchange-correlation potential respectively. The Hartee potential arises due to the classical Coulombic interaction between the electrons. The exchange-correlation potential is defined as

$$V_{xc} = \frac{\delta E_{xc}}{\delta \rho} \ [2] \tag{7.5}$$

The exchange-correlation term includes both the non-classical effects of exchange and correlation as well as the difference between the precise and non-interacting kinetic energy. The validity of the entire theory depends on this term, which includes the complex inter-electron interactions.

According to Kohn and Sham's proposal, the Hamiltonian can be written as:

$$H[\rho(r)] = T_0 + V_H + V_{xc} + V_{ext} \tag{7.6}$$

Since the auxiliary system consists of non-interacting single particles, a set of single-particle wave functions can precisely describe the system's overall ground-state wave function. The single-particle wave functions $\varphi_i(r)$ are used to build the density of the N single-particle system. It is given by

$$\rho(r) = \sum_i^N |\varphi_i(r)|^2 \tag{7.7}$$

Once $H[\rho(r)]$ is known, we can solve relatively simple single-particle Schrodinger equations

$$H\varphi_i = \varepsilon_i \varphi_i \tag{7.8}$$

However, Kohn and Sham derived self-consistent, iteratively solvable equations that were eventually utilised in a real computer simulation. The Kohn-Sham approach is accurate up until this point. If the exchange-correlation term is known, the electronic structure of the majority of materials may be solved with accuracy. The issue currently lies in the fact that we do not yet know the exchange-correlation term, and in particular, we do not know one that appropriately models d-systems. In **Figure 7.1**, the Kohn-Sham scheme schematic depiction is shown.

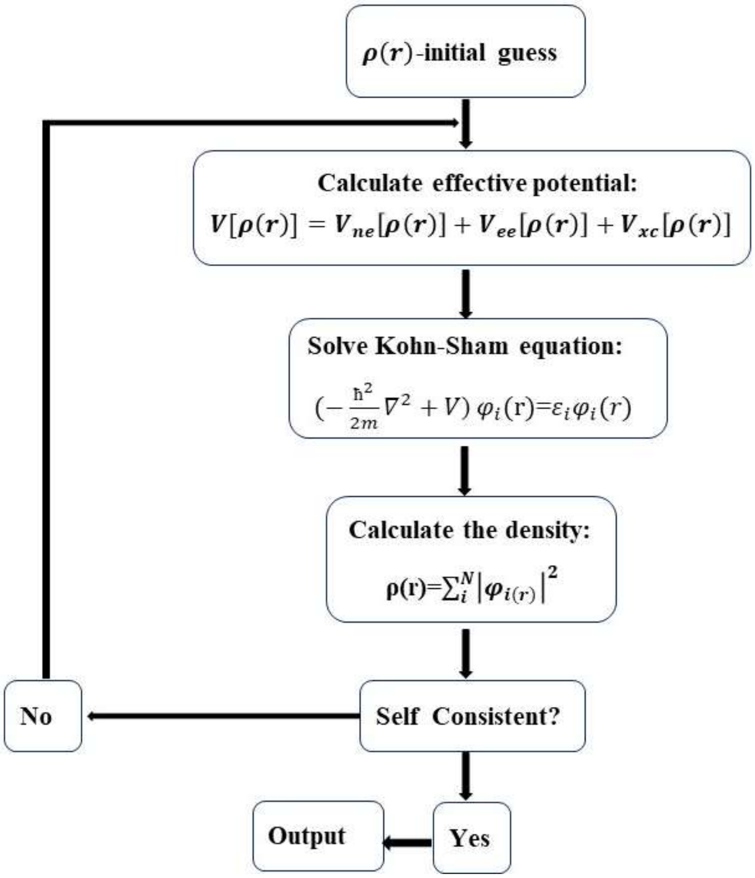

Figure 7.1. Schematic representation of the Kohn Sham scheme

7.2 Fundamental study of theoretical calculation using DFT

7.2.1 Exchange correlation functionals

Approximations for the so-called exchange-correlation potential serve as the foundation for the actual applications of DFT. The Pauli principle and Coulomb potential are described by the exchange-interaction potential [4], which goes beyond an electrical interaction between the electrons alone. It is clear that we have solved the many-body problem exactly because we have the exact exchange-correlation potential. The electron exchange-correlation energy can be approximated using a wide range of methods [5, 6]. Three categories mostly comprise the approximations:

7.2.2 Local Density Approximation (LDA)

The Local Density Approximation, which relies solely on the local electron density and is based on the uniform homogeneous electron gas, is among the most basic approximations [4-6]. Kohn-Sham's assumption is that each little volume in the system adds the same amount of energy to the exchange-correlation as would an equivalent volume of a uniformly dense electron gas. The local density estimate for exchange and interaction energy takes the following form [7]

$$E_{xc}^{LDA}[\rho(r)] = \int \varepsilon_{xc}(\rho)\rho(r))dr \qquad (7.9)$$

Where$\boldsymbol{\varepsilon_{xc}(\rho)}$ represents the exchange-correlation energy of each particle. Consequently, this method does a good job of characterising molecules, geometries, and vibration frequencies, but it does a bad job of forecasting binding energies [8]. In many systems, local density approximations work very well. However, they are not able to accurately forecast some systems' electrical characteristics, especially strongly correlated systems like the d-system. The d-electrons are typically localised, however LDA tends to delocalise them. Furthermore, these functionals undervalue semiconductor bandgaps.

7.2.3 Generalized Gradient Approximation

In order to enhance the LDA functional, the GGA has arisen [9, 10]. In the Generalised Gradient Approximation (GGA), the energy resulting from exchange and correlation is contingent upon the local densities and their gradients. In order to offset the inaccuracy resulting from the non-homogeneity of the actual electronic density, a density gradient is imposed. Furthermore, the GGA approximation enhances the ground-state energies and molecular geometries results over the LDA approximation. According to GGA approximation the exchange-correlation energy can be expressed as:

$$E_{xc}^{GGA} = \int \varepsilon_{xc}(\rho, \nabla\rho)\rho(r)dr \qquad (7.9)$$

PBE is the most widely used Generalised Gradient Approximation functional, which was created by Perdew, Burke, and Ernzerhof. To some extent, we can fix the underestimations by using this functional in conjunction with GGA. However, the systems with local strongly coupled d or f electrons are often not well described by this approximation.

7.2.4 DFT+U method

From the explanation above, it is clear that in systems with highly localised electrons, the system cannot be well described by the LDA or GGA approaches. Strong intra-atomic interactions can be introduced to get around this problem. The DFT+U method is the common name for this approach [11–13]. The DFT+U approach's main benefit is that it falls inside the purview of DFT, making it simple to incorporate in the current DFT codes and only somewhat costlier to compute than conventional DFT computations. The main purpose of the U correction is to enhance the strong on-site Coulomb interaction of localised electrons by introducing a Hubbard-like term. While handling the remaining valence electrons using the standard DFT assumptions, the Hubbard Hamiltonian represents the tightly coupled electronic states [14–18]. In the case of many strongly correlated materials and perovskites, where localised 3d or 4f orbitals are embedded in elongated s-p states, all open-shell orbitals, including the d and f orbitals for transition metal elements with localised orbitals present in extended states, can be described by DFT+U [19, 20]. The bandgap's localised orbitals, the d- and f-states, are too close to the Fermi energy. According to that viewpoint, these states should be pushed away from the Fermi level using the U value, such as that provided by the GGA+U theory, which adds a term to the Hamiltonian that raises the total energy and inhibits the undesired delocalisation of the d- or f-electrons when two of them are located on the same cation. Using excessively large values of U will, in particular, lead to an over-localization of the states, which will unphysically flatten the appropriate bands and impair the fit [21], in contrast to fitting to many other features. Additionally, because of the electronic interaction inaccuracy, an increase in the U value may lead to an incorrect estimate of the ground state energy and an overestimation of the lattice constants [22]. Consequently, in order to solve the bandgap problem and anticipate the properties of transition metal oxides, Hubbard correction must be applied.

7.2.5 Basis sets

The basic set for the expansion of the Kohn-Sham orbitals is plane waves. Bloch's theorem can be used to show that the union of a plane wave and a function with the lattice's periodicity can be used to express the wave function of an electron in a periodic solid [23, 24].

$$\varphi_{nk}(r) = exp(ik.r)u_{nk}(r) \tag{7.10}$$

Where r and k denote the position vector and wave vector respectively. Since there is no periodic unit cell in aperiodic systems, the relevant system region must be modelled as a supercell and then subjected to periodic boundary conditions in order to use a plane-wave basis set. Then, the supercell needs to be big enough to stop nearby supercell defects from interacting with one another. Once a supercell has been identified, Bloch's theorem can be applied to the newly created artificially periodic system. One needs an endless number of plane waves in order to obtain a perfect expansion. Thankfully, the coefficients of high-energy plane waves have to go to zero; otherwise, the energy of the wave function would increase eternally. This allows for the truncation of the plane wave basis set above cut-off energy. Bloch's theorem spares us from having to compute an endless number of wave functions since the unit (super) cell contains a finite number of electrons. An integral over the infinitely numerous discrete k points that still need to be considered is used to calculate the unit cell's energy. Since wave functions at k places that are close to one another turn out to be equivalent, an interpolation technique can use a finite number of k points. Furthermore, the integral of the energy is transformed into a sum over the k points, suitably weighted to take into consideration their finite quantity. The Monkhorst-Pack and Chadi-Cohen systems are the most widely used methods for producing k points.

7.2.6 Pseudopotentials

Plane wave basis sets are expensive to compute with because of the highly localised character of an atom's core electrons. According to this, a large number of plane waves are required in order to enlarge their wave functions [25]. Moreover, the contributions of the core electrons to bonding are frequently negligible in comparison to valence electrons. The function of the core electron wave functions is actually primarily concerned with preserving sufficient orthogonality between the valence electrons and core states [26, 27]. Therefore, replacing the atomic potential created by the core electron with a pseudopotential that has the same impact on the valence electrons would be beneficial. Essentially, there are two types of pseudopotentials: norm-conserving soft pseudopotentials and Vanderbilt ultra-soft pseudopotentials. In both cases, the pseudopotential function is obtained from an all-electron computation of an atom in a reference state. Make that the charge in the cut-off zone of norm-conserving pseudopotentials is the same as the charge in the core electrons. This promotes transferability by ensuring that the atom's core is not significantly impacted by its surroundings. This condition is loosened in ultra-soft pseudopotentials, and the discrepancy is compensated using charge augmentation functions. As the name suggests, this makes it possible to construct a "softer" pseudopotential, requiring fewer plane waves to expand it.

7.2.7 Band occupation number

At zero temperature, every band up to the Fermi level is populated, but every band above the Fermi level is empty [28]. These band occupancies are step functions with a clear definition. It is very difficult to calculate the electronic structures of metals compared to semiconductors and molecules. In semiconductors and molecules, the occupied and unoccupied states have different energies. Consequently, self-consistency cycles' fluctuations in energy have no effect on the occupancies. However, the density of states in metals is continuous at the Fermi level, and many states are close to the Fermi level in energy. Therefore, even minute changes in energy can have a significant impact on the occupation numbers, leading to instability and a challenging convergence to the occupation step function.

One related issue is that the Brillouin zone integral, which is calculated as the sum over a finite number of k points in practice, converges very slowly to the number of k points because of the discontinuity in occupancies in a continuous distribution of states for metals. There is a problem because the majority of DFT calculations use an absolute zero temperature. At higher temperatures, the DOS is distributed throughout the Fermi level, resulting in a continuous occupation function across the range of states. A developed finite-temperature version of DFT serves as one basis for solving this challenge. In this approach, the step function is replaced with a smoothly variable function, such as the Fermi-Dirac function at a low but non-zero temperature. The entire energy is then projected back to zero after that.

7.2.8 Electronic band structure

In solid-state physics, electronic band theory is a fundamental idea that provides understanding of how electrons behave in solid materials. The foundation of this theory is the idea of quantum mechanics, which holds that the energy levels of electrons are quantised and exist as discrete, non-continuous states. Examining a material's band structure can reveal important details about the many energy levels that electrons can occupy. According to the laws of solid-state physics, electrons normally occupy energy bands that range from the lowest possible energy levels to higher energy levels. The valence band and the conduction band are the two important sections that make up the energy band itself.

The valence band is primarily occupied by electrons that are closely bound to atoms and therefore do not participate in electrical conduction. Higher energy electrons, on the other hand, can reside in the conduction band where they can easily migrate and aid in electrical conduction. The band gap (Eg), which denotes the energy difference between the top of the valence band and the bottom of the conduction band, is a key idea in electronic band theory. The lowest energy needed to move an electron from the valence band to the conduction band is shown by this band gap. Materials are categorized as conductors, semiconductors, and insulators based on the size of their band gap, which also defines their electrical characteristics [29]. Semiconductors are in the middle with a moderate band gap, while conductors have very small or non-existent band gaps. Insulators have enormous band gaps. Designing and developing materials and electronic devices for a variety of purposes, such as semiconductors used in electronic circuits and solar cells, requires an understanding of electronic band theory, the band structure, and the band gap.

7.2.9 Density of states

In solid-state physics, the quantum states of the electrons within a crystal lattice are represented in k-space, which is also referred to as momentum space. Every electron has a unique quantum state that is defined by its momentum, or k-vector. In k-space, these states are shown as points. The permissible wavelengths and directions of electron propagation are determined by the allowed electron states in the crystal. Certain materials only permit certain electron wavelengths because of their charge distribution and interatomic distances. Which electron states are permitted depends critically on a material's crystalline structure [30]. Atoms in a crystal lattice are arranged periodically to form energy bands where electrons can reside and band gaps, which are areas devoid of electron states. The distribution of electronic states with respect to their energy is referred to as the density of states. At a particular energy level, it quantifies the number of electronic states per unit energy range. The following is a general definition of DOS [31]:

$$D(E) = \frac{d\Omega(E)}{dE} \tag{7.11}$$

Where $\Omega(E)$ is the number of states per volume.

7.3 Characterization

Theoretically, basic features including the density of states and optical band gap were predicted using DFT calculations. The simulation program Quantum Espresso was used to obtain the current work's results. Pseudopotentials are used to simulate electron-ion interactions in Quantum Espresso, an integrated suite of computer algorithms for electronic-structure calculations and materials modeling based on density-functional theory and plane wave basis sets. The DFT calculations in this work were carried out utilizing the Quantum Espresso's generalized gradient approximation (GGA) with Perdew Burke Ernzerhof (PBE) parametrization for the exchange functional. DFT provides an inadequate description of the effects of the coulomb repulsion of the 3d localised electrons of iron atoms in oxide systems. Hybrid DFT or DFT+U can address these problems, although the former is costlier and the latter only takes into account interactions that occur on-site. Thus, in order to take into consideration, the impact of local correlations, we ran DFT+U computations. By comparing the band gap value of bulk haematite, an effective Hubbard value U_{eff} of 4 eV was selected for Fe atoms. The frozen nuclei and electrons of each atom were represented using projector-augmented wave (PAW) potentials. For the Brillouin zone integration, dense Γ-centered k point meshes (Monkhorst-Pack k point grid) with a 4 × 4 × 1 cutoff energy of 550 eV were employed to guarantee converged structural parameters and total energies within meV precision for the GGA+U method.

7.4 Results and Discussions

7.4.1 Band structure using DFT

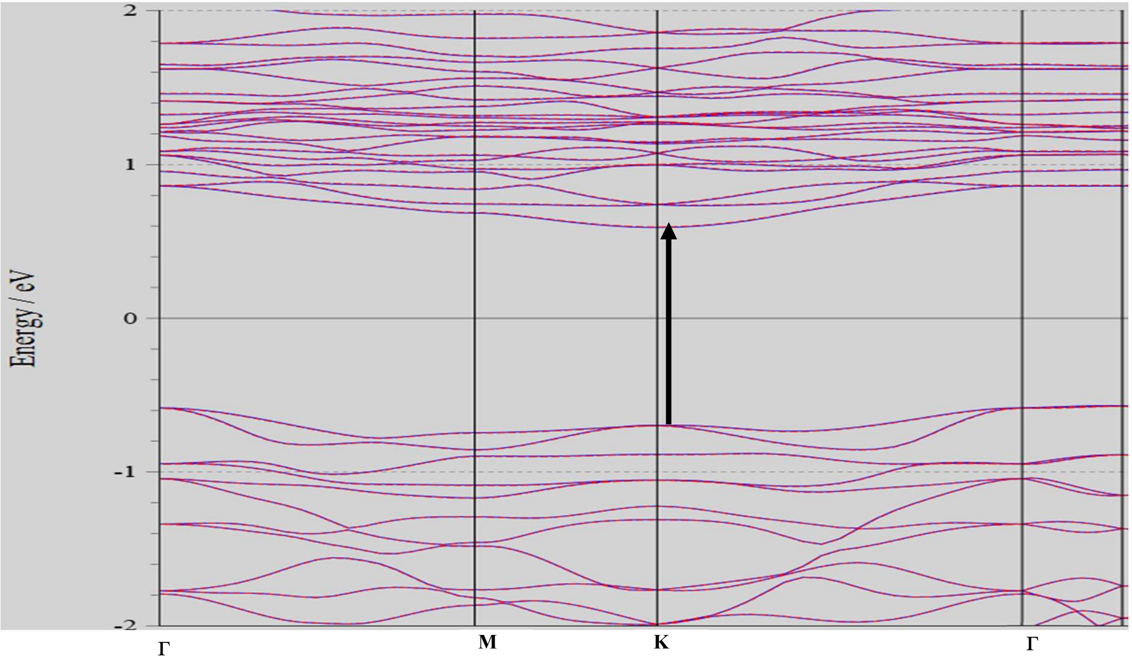

Figure 7.2 Band structure of α-Fe_2O_3

Hematite's band structure has been computed using DFT+U, GGA, and LDA. Nonetheless, when compared to the experimental value, DFT+U produced good results. **Figure 7.2** displays the hematite band structure. The band gap was found to be 1.3 eV. The valence band is found to be clean and separated as compared to conduction band. Because the valence band primarily consists of oxygen 2p orbitals. To some extent, the 2p orbitals hybridise with Fe 3d but they remain comparatively distinct and sharp. The conduction band primarily composed of Fe 3d orbitals. These states are more delocalized and complex; hence the conduction band is found to be congested.

7.4.2 Density of states using DFT

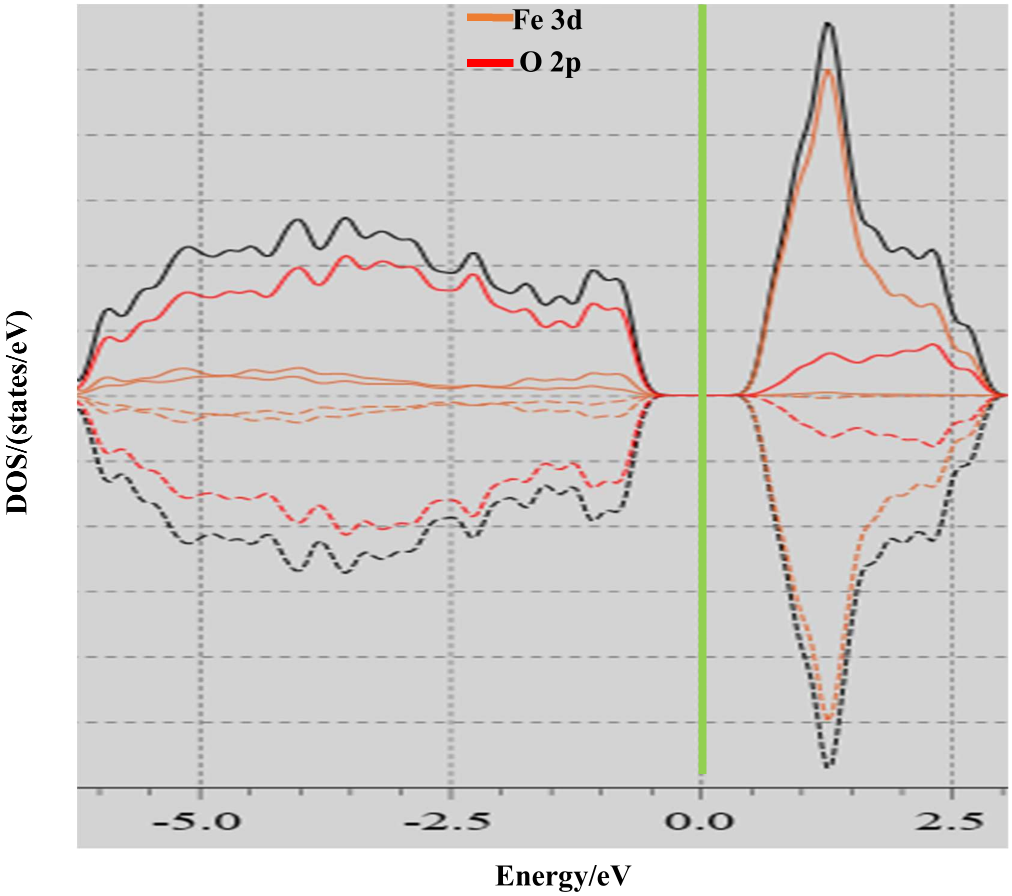

Figure 7.3 Density of states of α-Fe_2O_3

The band structure and density of states (DOS) may offer comparable insights on bandgap and conductivity. In particular, DOS can offer more details on the amount that occupies at a given energy level and the areas where electrons are permitted to occupy than band structure. An abundance of energy states that are available for occupation is indicated by a high DOS value. The state density will be zero if there are no states at that energy level. The fermi level is set to zero, the valence band and conduction band energy range is below and above the fermi level respectively. In the valence band the Fe 3d orbitals show splitting due to the crystal field and exchange splitting. At the same time O 2p orbitals are not show splitting, because the 2p orbitals of oxygen atoms are not split by the crystal field; they are ligands rather than metal centres. In the conduction band the Fe 3d orbitals are mostly antibonding, less hybridized and more delocalized, hence the crystal field and exchange effects are less effective, so the splitting becomes harder to see in DOS.

7.5 Conclusions

Researchers can now quantitatively study the properties of materials in a variety of systems from fundamental principles, that is, without any input parameters other than the atoms that comprise the substance, thanks to significant advances in theoretical methodology and computer technology over the past few decades. Significant progress has been made in theory. Theory has effectively reduced an apparently intractable quantum manybody problem to a computationally tractable problem while retaining the essential physics. Today, fundamental principles may anticipate the ground and excited states of severa materials. Because the DFT+U approach improves accuracy over normal LDA and GGA functionals and has a lower computing cost, it is a good method for addressing transition metal complexes. Here the DFT+U technique was used to study the band structure and density of states. The band gap was determined to be 1.3 eV, which is more or less consistent with the experimental result.

References

[1]. Hohenberg, P. and Kohn, W., 1964. Inhomogeneous electron gas. *Physical review*, *136*(3B), p.B864.

[2]. Kohn, W. and Sham, L.J., 1965. Self-consistent equations including exchange and correlation effects. *Physical review*, *140*(4A), p.A1133.

[3]. Kohn, W., 1999. Nobel Lecture: Electronic structure of matter—wave functions and density functionals. *Reviews of Modern Physics*, *71*(5), p.1253.

[4]. Thomas, L.H., 1927, January. The calculation of atomic fields. In *Mathematical proceedings of the Cambridge philosophical society* (Vol. 23, No. 5, pp. 542-548). Cambridge University Press.

[5]. Rowsell, J.L., Millward, A.R., Park, K.S. and Yaghi, O.M., 2004. Hydrogen sorption in functionalized metal–organic frameworks. *Journal of the American Chemical Society*, *126*(18), pp.5666-5667.

[6]. Dirac, P.A., 1930, July. Note on exchange phenomena in the Thomas atom. In *Mathematical proceedings of the Cambridge philosophical society* (Vol. 26, No. 3, pp. 376-385). Cambridge University Press.

[7]. Fermi, E., 1927. Statistical method to determine some properties of atoms. *Rend. Accad. Naz. Lincei*, *6*(602-607), p.5.

[8]. Perdew, J.P. and Levy, M., 1983. Physical content of the exact Kohn-Sham orbital energies: band gaps and derivative discontinuities. *Physical Review Letters*, *51*(20), p.1884.

[9]. Sahni, V., Bohnen, K.P. and Harbola, M.K., 1988. Analysis of the local-density approximation of density-functional theory. *Physical Review A*, *37*(6), p.1895.

[10]. Perdew, J.P., Burke, K. and Ernzerhof, M., 1996. Generalized gradient approximation made simple. *Physical review letters*, *77*(18), p.3865.

[11]. Perdew, J.P., Kurth, S., Zupan, A. and Blaha, P., 1999. Accurate density functional with correct formal properties: A step beyond the generalized gradient approximation. *Physical review letters*, *82*(12), p.2544.

[12]. Wang, Y. and Perdew, J.P., 1991. Correlation hole of the spin-polarized electron gas, with exact small-wave-vector and high-density scaling. *Physical Review B*, *44*(24), p.13298.

[13]. Anisimov, V.I., Zaanen, J. and Andersen, O.K., 1991. Band theory and Mott insulators: Hubbard U instead of Stoner I. *Physical Review B*, *44*(3), p.943.

[14]. Liechtenstein, A.I., Anisimov, V.I. and Zaanen, J., 1995. Density-functional theory and strong interactions: Orbital ordering in Mott-Hubbard insulators. *Physical Review B*, *52*(8), p.R5467.

[15]. Dudarev, S.L., Botton, G.A., Savrasov, S.Y., Humphreys, C.J. and Sutton, A.P., 1998. Electron-energy-loss spectra and the structural stability of nickel oxide: An LSDA+ U study. *Physical Review B*, *57*(3), p.1505.

[16]. Anisimov, V.I., Poteryaev, A.I., Korotin, M.A., Anokhin, A.O. and Kotliar, G., 1997. First-principles calculations of the electronic structure and spectra of strongly correlated systems: dynamical mean-field theory. *Journal of Physics: Condensed Matter*, *9*(35), p.7359.

[17]. Dudarev, S.L., Botton, G.A., Savrasov, S.Y., Humphreys, C.J. and Sutton, A.P., 1998. Electron-energy-loss spectra and the structural stability of nickel oxide: An LSDA+ U study. *Physical Review B*, *57*(3), p.1505.

[18]. Timrov, I., Marzari, N. and Cococcioni, M., 2018. Hubbard parameters from density-functional perturbation theory. *Physical Review B*, *98*(8), p.085127.

[19]. Kirchner-Hall, N.E., Zhao, W., Xiong, Y., Timrov, I. and Dabo, I., 2021. Extensive benchmarking of DFT+ U calculations for predicting band gaps. *Applied Sciences*, *11*(5), p.2395.

[20]. Naveas, N., Pulido, R., Marini, C., Hernández-Montelongo, J. and Silván, M.M., 2023. First-principles calculations of hematite (α-Fe2O3) by self-consistent DFT+ U+ V. *Iscience*, *26*(2).

[21]. Kulik, H.J., Cococcioni, M., Scherlis, D.A. and Marzari, N., 2006. Density Functional Theory in Transition-Metal Chemistry:<? format?> A Self-Consistent Hubbard U Approach. *Physical Review Letters*, *97*(10), p.103001.

[22]. Kirchner-Hall, N.E., Zhao, W., Xiong, Y., Timrov, I. and Dabo, I., 2021. Extensive benchmarking of DFT+ U calculations for predicting band gaps. *Applied Sciences*, *11*(5), p.2395.

[23]. Aryasetiawan, F., Karlsson, K., Jepsen, O. and Schönberger, U., 2006. Calculations of Hubbard U from first-principles. *Physical Review B—Condensed Matter and Materials Physics*, *74*(12), p.125106.

[24]. Hu, Z. and Metiu, H., 2011. Choice of U for DFT+ U calculations for titanium oxides. *The Journal of Physical Chemistry C*, *115*(13), pp.5841-5845.

[25]. Blochl, P.E., 1994. Projector augmented-wave method. *Physical review B*, *50*(24), p.17953.

[26]. Kresse, G. and Joubert, D., 1999. From ultrasoft pseudopotentials to the projector augmented-wave method. *Physical review b*, *59*(3), p.1758.

[27]. Chelikowsky, J.R., Derby, J.J., Godlevsky, V.V., Jain, M. and Raty, J.Y., 2001. Ab initio simulations of liquid semiconductors using the pseudopotential-density functional method. *Journal of Physics: Condensed Matter*, *13*(41), p.R817.

[28]. Chelikowsky, J.R., 2000. The pseudopotential-density functional method applied to nanostructures. *Journal of Physics D: Applied Physics*, *33*(8), p.R33.

[29]. Valiev, M.M. and Fernando, G.W., 1995. Occupation numbers in density-functional calculations. *Physical Review B*, *52*(15), p.10697.

[30]. Tsidilkovski, I.M., 2016. *Band Structure of Semiconductors: International Series on the Science of the Solid State* (Vol. 19). Elsevier.

[31]. Wolfram, T. and Ellialtioglu, S., 2006. *Electronic and optical properties of d-band perovskites*. Cambridge University Press.

Chapter 8

Thesis Conclusions and recommendations

Research is a perpetual journey to untangle the mysteries of nature and every researcher contributes something to this wide community of research. Despite its infinitesimally small size, this embodies the proverb 'Tiny drops of water make a mighty ocean'. This study may be considered as such a very small drop in the vast knowledge of science. Along with the positive outcomes of this study, there are some lacunae and gaps in the present study which can be addressed further by other researchers. This chapter discusses the interference drawn from this study and also will talk about the prospects for further investigation.

8.1 Conclusions

After six years of investigation, I feel that the voyage has only just begun and that many more kilometers must be covered to reach the objective. It is common to feel blanked out at the end of a lengthy journey. Because most of the time we think about our work from the first day to till the thesis is completed. To tell the truth, I felt completely lost when the event abruptly ended. The research journey has not been easy; many challenges have been encountered. Nevertheless, every barrier might offer a chance for creative problem-solving and a distinct angle on issues. In addition to highlighting the promising findings of this study with several shortcomings and the need for more research is also dealt with in this chapter.

Since ferrofluids behave like ferromagnetic materials and have fluid characteristics while being able to be moved by a magnetic field, they are quite interesting. Ferrofluid provides a perfect environment to study pattern generation and instability from a fundamental point of view. The investigations of instability in magnetic fluids are a great way to learn more about the physics behind the fluids. Many technical applications, where stability is crucial, are aggravated by the instability of a fluid surface. Nevertheless, the research results in a thorough understanding of the fluid's basic characteristics. Therefore, exploring the normal magnetic field on a fluid's free horizontal surface opens up new technical possibilities. Because field-induced instability studies are simpler to execute and can be controlled by adding an external field, Rosensweig instability studies are a great option for studying surface pattern generation in the equilibrium system. Only when the applied magnetic field is greater than the stabilizing forces brought on by surface tension and gravitational force does the instability mechanism take place. The surface assumes a pattern of hexagons when the applied field increases beyond the critical field, and squares when the applied field crosses a second barrier. A pattern of distinctive spikes is created by the interaction of surface tension, gravity force, and an external magnetic field.

Since ferrofluids cause some anisotropy when magnetic nanoparticles interact with a magnetic field, they are suggested for application in magneto-controlled optical switches, optical modulators, sensors, and other devices. To investigate the interaction effects, dichroism measurements are performed in various ferrofluids and magneto-plasmonic fluids. By using linear dichroism measurements, the magneto-optical property of the iron oxide nanofluid was examined. The suspensions were isotropic when there was no outside magnetic field. They display magneto-optic phenomena and anisotropic behaviour once the external field is applied.

Particles aligned along the direction of the magnetic field form a chain formation along the field direction when a magnetic field is applied. The strengthening of magneto-optical properties is attributed to these linear head-to-tail chains, which grow to form long periodic chains when the magnetic field increases. The magneto plasmonic nanofluid functions as a dual-purpose substance. In the field of medicine, the combined effects of magnetism and plasmonics are crucial, particularly in the case of magnetic hyperthermia. We can see that the amplitude of intrinsic dichroism reduces with increasing concentration of spherical-shaped silver nanoparticles in the hybrid magnetic nanofluid by analysing its linear dichroism. The reason for this is that spherical nanoparticles are isotropic. By varying the aspect ratio, the magnetoplasmonic fluid's absorption wavelength can be modified.

Iron oxide's unique physical and chemical properties make it an interesting candidate for further research. As a consequence of the most recent breakthroughs in nanotechnology, there are now more chemical and physical methods available for producing nanoparticles. However, these therapies harm the ecosystem and living things since the unreacted toxins are discharged into the environment. Therefore, creating nanoparticles in an environmentally friendly way is essential. In the green method of producing nanomaterials, metal atoms unite to form clusters, which then create nanoparticles. The primary objective of this method is to synthesise metallic nanoparticles from diverse biological sources. A well-known semiconductor with strong electron-phonon and electron-electron correlation is haematite. Haematite is the most stable iron oxide in ambient conditions and the most environmentally benign of all the iron oxides. Haematite is a promising material with many potential uses because of its good chemical stability, capacity to absorb visible light, low cost, suitable band gap, etc. Tea extract can be employed as a reducing and stabilising agent. In the current study, stable haematite nanoparticles were synthesised using the environmentally beneficial Hydrothermal technique. Hematite nanoparticles have enhanced photocatalytic activity, which could be attributed to their increased surface area and size during synthesis. After 150 minutes, around 75% of the methylene blue dye had been lost. As a result, it makes sense to consider it for waste water treatment. The antibacterial activity of synthesized α-Fe_2O_3 nanoparticles on Escherichia Coli was examined in relation to concentration, and it was discovered that the highest zone of inhibition occurred at a concentration of 10 mg/mL. Due to insufficient safety features and the availability of bacteria, the broader use necessitates a response to various forms of bacteria, which could not be executed. With the right modifications, iron oxide nanoparticles that respond to a magnetic field may eventually be used for targeted medicine delivery.

Surface plasmon coupled emission is the result of combining two fast developing fields of study: fluorescence and plasmonics. This is a technique for detection in which electron oscillations in metal films caused by plasmon resonance are connected with excited fluorophores. SPR sensors, or surface plasmon resonance-based sensors, are an effective technique for researching biomolecular interactions. The resolution of complicated samples, highly diluted concentrations, and small molecular weight are limitations of conventional SPR sensors. In the presence of a magnetic field, the sensitivity of surface plasmon resonance can be increased by using a magnetoplasmonic material. In this work, the spin coating technique was used to create the magnetoplasmonic heterostructure.

The Reverse Kretchmann setup was used to produce the surface plasmon-coupled emission. One of the key features of SPCE is directional emission, which denotes that almost all signals are focused in a single direction. In the current work, a plasmon-coupled emission that is direction-specific is observed in a manufactured heterostructure both in the presence and absence of a magnetic field. However, directed emission is obtained along with emission increase in the presence of a magnetic field. The dielectric tensor's off-diagonal elements and the materials' magneto-optical constants determine the wave vector of magnetic field-induced modulation on plasmonic materials. If the ferromagnetic material has more electromagnetic field spread on it when a magnetic field is applied, the modulation will be greater. More electromagnetic field will propagate along a dielectric than a metal if the ferromagnetic substance is dielectric. Another future possibility for magnetic field-controlled plasmonics is to investigate the effects of magnetic fields at different concentrations and distances on surface plasmon coupled emission. This could lead to sensing applications.

Our civilisation suffers greatly from energy scarcity, which is why people's attention has been drawn to the development of sustainable energy technology. One viable method for resolving the energy challenge is photoelectrochemical water splitting. The first report of PEC water splitting was made in 1972 by Fujishima and Honda using a TiO_2 semiconductor as a photoelectrode. But a significant disadvantage is that its comparatively large bandgap of about 3.2 eV limits its ability to absorb solar energy mostly to the ultraviolet, which makes up about 4% of the solar spectrum. This constraint is important since there is still a large amount of solar energy that is unutilized, mostly in the visible light spectrum. Additionally, the large bandgap makes photogenerated electron-hole recombination more difficult, which reduces TiO_2's efficiency in solar energy conversion. Researchers are constantly investigating ways to reduce these drawbacks and improve TiO_2's overall performance in solar applications, including bandgap engineering, surface modifications, heterojunction creation, nanostructuring, and sensitisation. Creating heterojunctions with materials having narrow band gaps helps get around this problem. Haematite is a material for a prospective photo anode because, in contrast to other photo anodes with bigger bandgaps, it can harvest solar energy over a considerably wider spectrum, including both visible and ultraviolet light. The short excited state life span of haematite, which causes photo-generated charges to be extinguished before they reach the surface, its poor hole diffusion length, and its unsatisfactory oxygen generation reaction kinetics, which result in an unsatisfactory photoelectrochemical (PEC) efficiency, pose the main challenges to the material's use in solar energy conversion.

The photogenerated charges are within a few atoms of the surface when hematite is made thinner with a two-dimensional structure (Hematene), which leads to a more efficient separation of charge carriers upon light absorption on the surface. This may prove to be a helpful strategy in improving PEC water-splitting performances. The discovery of graphene in 2004 set the stage for a great deal of 2D material research. Aravind et al. successfully exfoliated bulk haematite material into freestanding 2D sheets with intrinsic magnetic in 2018. Exfoliated from haematite particles, hematene is a 2D material. Quantum confinement in the 2D regime modifies the optical bandgap, making it a potentially valuable material for water splitting. In the current work, it was discovered that, in the visible area, the Hematene-loaded TiO_2 had a greater boost in photocurrent density than TiO_2 heterostructures. In the future, different changes such as TiO_2 nanostructures with changing hematene thicknesses and tweaking the characteristics of TiO_2 nanostructures containing hematene could be used to improve the photocurrent generated in the hematene-loaded TiO_2 nanostructure.

An investigation is never the end; rather, it is the start of a new journey. The insights gathered from this expedition will function as a roadmap for additional research. Still, there is considerable work to be done and this thesis is not yet complete. I went through a range of emotions while pursuing my PhD, including anticipation and boredom, patience and impatience, despair, and diversions with unanticipated turning points. As I went along, I came to understand that the secret to finishing a PhD successfully is patience, methodical study, and supervisor assistance. I also gained an appreciation for tenacity and resilience. The search for the complete truth is an ongoing endeavour, and this thesis is regarded as just one more attempt to discover the truth. In the universe, the one constant is called "change." The researchers are always looking for these shifts that could influence the way they shape notions and see reality.

8.2 Recommendations

In ferrofluid research, the Surface Instability studies have become something of a symbol. Thoroughly examining Rosensweig instabilities can provide insight into the mechanics of ferrohydrodynamics. In the future, we could investigate the combined impact of electric and magnetic fields on the instability of ferrofluid for thruster applications by extending our investigation into the phenomenon of Rosensweig instabilities. Numerous applications exist for the study of fluid characteristics in an external magnetic field, particularly in ferrofluid actuator design. Further forward-thinking ideas are the investigations of Rosensweig instability on various non-magnetic interfaces and the relationship of spike height on field strength.

Numerous applications may result from combining the properties of plasmonic structure and magnetism. Much more needs to be learnt about the role of liquid-solid interfaces and the dipolar effect from a fundamental standpoint. Such fluids can combine magnetic hyperthermia and photodynamic therapy in a single magnetic nanofluid if biocompatible plasmonic particles with a λmax that fits the optical window suitable for photodynamic therapy can be added to the hybrid fluid. By varying the aspect ratio, the plasmonic fluid's absorption wavelength can be adjusted. Thus, integrating several plasmonic materials with varying aspect ratios into a magnetic fluid is a promising avenue for future research.

SPR sensors, or surface plasmon resonance-based sensors, are an effective technique for researching biomolecular interactions. Nevertheless, the resolution of complicated samples, very diluted concentrations, or small molecular weight is restricted by the traditional SPR sensor. This study also explores the phenomenon of surface linked emission, which can be used to increase the sensitivity of surface plasmon resonance when there is a magnetic field present. Another future possibility for magnetic field-controlled plasmonics is to investigate the effects of magnetic fields at different strengths and orientation on surface plasmon coupled emission. This could lead to sensing applications.

The most stable form of iron oxide in the atmosphere at room temperature is haematite. It is one of the materials that is most frequently utilised in industrial, scientific, and medicinal applications. This study examines the cytotoxicity, photocatalytic activity, and antibacterial characteristics of bio-synthesised haematite nanoparticles. α-Fe_2O_3 nanoparticles have enhanced photocatalytic activity, which could be attributed to their increased surface area and size during synthesis. The investigation of α-Fe_2O_3 nanoparticles' photocatalytic impact on various dyes can be further upon. The antibacterial impact of synthesised α-Fe_2O_3 nanoparticles on Escherichia Coli is investigated in relation to concentration. Due to insufficient safety features and the availability of bacteria, the broader use necessitates a response to various forms of bacteria, which could not be executed. With the right modifications, iron oxide nanoparticles that respond to a magnetic field may eventually be used for targeted medicine delivery.

One method that assures a solution for addressing the energy challenge is photoelectrochemical water splitting. In the visible region, the hematene-loaded TiO_2 was observed to exhibit a greater boost in photocurrent density than TiO_2 heterostructures. In the future, different changes such as TiO_2 nanostructures with changing hematene thicknesses and tweaking the characteristics of TiO_2 nanostructures containing hematene could be used to improve the photocurrent generated in the hematene-loaded TiO_2 nanostructure.

Only the fundamental calculations in this study are made theoretically using DFT. In actuality, the role of simulations in understanding and forecasting unique properties of materials has grown. Thus, 2D material research can benefit from the extension of DFT computations with advanced computational facilities.

Due to their many potential uses, magnetic nanostructures have garnered a great deal of attention from researchers in light of recent developments in magnetism and magnetic materials. Combining different properties in a single material by making composites or hybrid heterostructures will add synergy to technological development.